Structure, Electronic Correlations and Magnetism in 2D Layers and 2D Layer Stacks on Iridium Substrates

Inaugural-Dissertation
zur
Erlangung des Doktorgrades
der Mathematisch-Naturwissenschaftlichen Fakultät
der Universität zu Köln

vorgelegt von
Timo Knispel
aus Köln

Köln 2021

Erster Berichterstatter: Prof. Dr. Thomas Michely
Zweiter Berichterstatter: Priv.-Doz. Dr. Daniel Bürgler

Vorsitzender der Prüfungskommission: Prof. Dr. Klas Lindfors
Tag der mündlichen Prüfung: 23.03.2022

Die vorliegende Dissertation wurde von der Mathematisch-Naturwissenschaftlichen Fakultät der Universität zu Köln angenommen.

Abstract

Physical phenomena like electronic correlations and magnetism are present in many layered three-dimensional bulk crystals, but thinning these materials down to the two-dimensional limit offers a new field of exceptional properties to study. The scope of this thesis ranges from the electronic correlation effects in monolayer transition metal dichalcogenides, over the synthesis and structural analysis of intercalated heterostacks of monolayer van der Waals materials including transition metal dichalcogenide sheets, to the investigation of magnetism in ultrathin metal layers.

The layer dependence of electronic correlation effects, like charge density waves and superconductivity in transition metal dichalcogenides, is subject to ongoing research and discussion. In this thesis the electronic properties of NbS_2 monolayers grown in situ on a graphene/Ir substrate are investigated by high-resolution scanning tunneling microscopy and scanning tunneling spectroscopy at low temperatures. A 3×3 superstructure is present at the surface of NbS_2 and by analyzing its electronic footprints, it is identified as a charge density wave in the picture of a weak-coupling electron-lattice system featuring nesting of the Fermi surface. The electronic structure in the occupied and unoccupied states is found to be largely unaffected by the charge density wave instability, resembling the results of density functional theory calculations for freestanding NbS_2 monolayers in literature. Edges of NbS_2 monolayer islands influence the electronic structure and superconductivity is found absent, the latter explained by the limited lateral size of the monolayer islands obtained by molecular beam epitaxy.

Intercalation of foreign species into the van der Waals gap of two layers is known to strongly influence the properties of layered materials. Combining intercalation of layered materials and the interest into atomically thin two-dimensional materials, in this thesis a new method to intercalate vertical 2D layer heterostacks consisting of two different monolayer van der Waals materials, namely graphene and monolayer NbS_2 on an Ir substrate, is demonstrated under ultra-high vacuum conditions. Nb intercalation into the van der Waals gap between the layers is achieved by post-growth annealing of the heterostack, causing partial dissociation of NbS_2, and by deposition of Nb from the vapor phase. The latter method can also be applied to the intercalation of species distinct from the constituents of the heterostack, here demonstrated for the intercalation of Fe, thereby possibly inducing magnetic behavior in the NbS_2 monolayer. The compounds resulting from intercalation are investigated by scanning tunneling microscopy and scanning tunneling spectroscopy, giving insight into different emerging structural phases and the influence of intercalation on the electronic structure of NbS_2.

Scanning tunneling microscopy is a method of surface investigation used for a long time in our group. To extent this method, the UNISOKU USM1300 system was introduced, enabling to conduct spin-polarized scanning tunneling microscopy and spin-polarized scanning tunneling spectroscopy at low temperatures in a vector magnetic field, useful tools for the investigation of non-collinear magnetism on the atomic scale at surfaces.

Non-collinear magnetic structures are of high relevance for the realization of spintronic devices and are subject to intense research regarding stabilizing magnetic interactions. Using spin-polarized scanning tunneling microscopy and scanning tunneling spectroscopy, the spin texture of ultrathin Fe films on Ir(110) is investigated. A magnetic stripe pattern of short period is revealed along the close-packed direction of the in situ grown Fe film. By employing the vector magnetic field, the pattern is identified as a Bloch type spin helix, with the rotation axis of the helix being parallel to the propagation. The rotational sense is found to be degenerate. These results indicate that the non-collinear spin texture in ultrathin Fe on Ir(110) cannot be driven by the Dzyaloshinskii-Moriya interaction, usually playing an important role at interfaces with heavy elements like Ir. Including theoretical considerations, the spin helix is discussed to be driven by exchange interactions.

Deutsche Kurzzusammenfassung
(German Abstract)

Physikalische Phänomene wie elektronische Korrelationseffekte und Magnetismus sind in vielen dreidimensionalen, geschichteten Kristallen präsent, aber die Reduktion dieser Materialien auf zweidimensionale Form eröffnet die Möglichkeit der Erforschung einer neuen Bandbreite außergewöhnlicher Eigenschaften. Der Umfang dieser Arbeit reicht von elektronischen Korrelationseffekten in Übergangsmetall-Dichalkogenid-Monolagen, über die Herstellung und strukturelle Analyse von interkalierten Monolagen-Heteroschichten bestehend aus Van-der-Waals-Monolagen und im speziellen Übergangsmetall-Dichalkogenid-Monolagen, bis hin zur Untersuchung von Magnetismus in ultradünnen Metallschichten.

Die Lagenabhängigkeit von elektronischen Korrelationseffekten, wie zum Beispiel dem Phänomen der Ladungsdichtewellen und der Supraleitung in Übergangsmetall-Dichalkogeniden, ist Gegenstand fortlaufender Forschung und Diskussion. In dieser Arbeit werden die elektronischen Eigenschaften von in situ auf einem Graphen/Ir-Substrat gewachsenen NbS_2-Monolagen durch hochaufgelöste Rastertunnelmikroskopie und Rastertunnelspektroskopie bei niedrigen Temperaturen untersucht. Auf der Oberfläche der NbS_2-Monolagen ist eine 3×3-Überstruktur erkennbar, welche durch die Analyse ihrer elektronischen Signatur eindeutig einer Ladungsdichtewelle im Sinne eines schwach wechselwirkenden Elektron-Phonon-Systems mit Fermiflächen-„Nesting“ zugeordnet werden kann. Die elektronische Struktur in den besetzten und unbesetzten Zuständen stimmt mit den Ergebnissen Dichtefunktionaltheoretischer Rechnungen in der Literatur bezüglich freistehender NbS_2-Monolagen überein und scheint durch die Ladungsdichtewelle kaum beeinflusst zu sein. Die Ränder der NbS_2-Monolagen-Inseln beeinflussen die elektronische Struktur der Inseln und Supraleitung ist nicht vorhanden, wobei letzteres durch die begrenzte laterale Größe der durch Molekularstrahlepitaxie synthetisierten Inseln bedingt zu sein scheint.

Die Interkalation von außen hinzugefügter Materialien in die Van-der-Waals-Lücke zweier Lagen ist bekannt dafür die Eigenschaften geschichteter Materialen stark zu beeinflussen. Um die Interkalation geschichteter Materialien mit dem Interesse an einzelnen zweidimensionalen Lagen zu kombinieren, wird in dieser Arbeit einen neues Verfahren zur Interkalation von aus zwei verschiedenen Van-der-Waals-Monolagen (Graphen und NbS_2) bestehenden vertikalen Heteroschichten auf einem Ir Substrat unter Ultrahochvakuum-Bedingungen demonstriert. Interkalation von Nb in die Van-der-Waals-Lücke zwischen den Lagen wird sowohl durch das Aufheizen der Heteroschicht und dadurch verursachter partieller Dissoziation von NbS_2 erreicht, als auch durch Nb-Deposition aus der Gasphase. Letztere Methode kann auch auf die Interkalation von Materialien, welche kein Bestandteil der ursprünglichen Heteroschicht sind, angewendet werden, was hier für die Interkalation von Fe demonstriert wird. Dadurch könnten möglicherweise magnetische Wechselwirkungen in der NbS_2-Monolage induziert werden. Die durch die Interkalation entstehenden Verbindungen werden durch Rastertunnelmikroskopie und Rastertunnelspektroskopie untersucht. Dadurch wird ein Einblick in verschiedene strukturelle Phasen und den Einfluss der Interkalation auf die elektronische Struktur von NbS_2 gewonnen.

Rastertunnelmikroskopie ist eine Methode der Oberflächenuntersuchung, welche in unserer Arbeitsgruppe seit langer Zeit angewendet wird. Um diese Methode zu erweitern, wurde das UNISOKU USM1300-System eingeführt, welches spinpolarisierte Rastertunnelmikroskopie und Rastertunnelspektroskopie in einem Vektormagnetfeld bei sehr niedrigen Temperaturen ermöglicht; nützliche Werkzeuge für die Untersuchung von nicht-kollinearem Magnetismus auf der atomaren Skala an Oberflächen.

Nicht-kollineare magnetische Strukturen sind von hoher Relevanz für Realisierung von spintronischen Nano-Geräten und daher Gegenstand der Forschung bezüglich der dafür verantwortlichen magnetischen Wechselwirkungen. In dieser Arbeit wird die Spin-Textur ultradünner Fe-Schichten auf Ir(110) durch spinpolarisierte Rastertunnelmikroskopie und Rastertunnelspektroskopie untersucht. Auf dem in situ gewachsenen Fe-Film wird ein magnetisches Streifenmuster mit kurzer Periodizität entlang der dicht-gepackten Kristallrichtung entdeckt. Durch die Anwendung des Vektormagnetfelds wird das Streifenmuster als Bloch-artige Spin-Helix mit zur Ausbreitungsrichtung paralleler Drehachse identifiziert. Der Drehsinn der Helix ist in beide Richtungen entartet. Die Resultate deuten darauf hin, dass die nicht-kollineare Spin-Textur in dünnen Fe-Schichten auf Ir(110) nicht, wie bei vielen Grenzschichtsituationen mit schweren Materialien wie Ir üblich, durch die Dzyaloshinskii-Moriya-Wechselwirkung verursacht wird. Mithilfe theoretischer Erwägungen wird die Spin-Helix als Resultat von Austauschwechselwirkung diskutiert.

Frequently used Acronyms and Abbreviations

1D - one-dimensional
2D - two-dimensional
3D - three-dimensional
TMDC - transition metal dichalcogenide
Gr - graphene
vdW - van der Waals
CDW - charge density wave
PLD - periodic lattice distortion
CVD - chemical vapor deposition
MBE - molecular beam epitaxy
vdWe - van der Waals epitaxy
UHV - ultra-high vacuum
LEED - low-energy electron diffraction
STM - scanning tunneling microscopy
SP-STM - spin-polarized STM
STS - scanning tunneling spectroscopy
FFT - fast Fourier transform
DFT - density functional theory
QPI - quasi-particle interference
SOC - spin-orbit coupling
DMI - Dzyaloshinskii-Moriya interaction
DOS - density of states
LL - load-lock
e-beam - electron beam
prc - preparation chamber
exc - exchange chamber
IVC - isolation vacuum space
HV - high voltage

Contents

CHAPTER 1

Introduction

Layered materials are a special case of three-dimensional (3D) crystals investigated in condensed matter physics. They are formed by stacks of individual ultrathin sheets like a stack of paper. Often, like in the case of graphite, between the covalently-bound layers a van der Waals (vdW) gap is present, rendering the interlayer interaction weak. This is apparent in everyday life as grinding a graphite pencil on paper, layers are easily ripped of. The isolation of single layers, first achieved for single graphene (Gr) sheets from a layered 3D graphite crystal, started a new era for scientific research of two-dimensional (2D) materials [1,2]. The interest in 2D materials is driven by their unique properties different from their bulk counterparts, like Gr featuring the anomalous room-temperature quantum Hall effect [3]. In 2D, electronic screening is generally reduced and electronic correlation effects can be enhanced [4,5].

The layer dependence of correlation effects is prominently demonstrated in layered metallic transition metal dichalcogenides (TMDCs). In 3D form, these compounds are long known to possess charge density wave (CDW) phases [6] and superconductivity [7]. Thinning down such materials to the 2D limit strongly affects these phenomena, like in the case of the metallic group V TMDC 2H-TaS_2. While being superconducting in the bulk [6,8,9] and also featuring a CDW phase [10,11], in the monolayer limit the superconducting critical temperature is enhanced [9,12,13], while the transition temperature of the CDW phase is contradictory reported to be both reduced [13] or enhanced [14]. The layer dependence and competition of the electronic correlation effects in TMDCs remains an ongoing challenge in general. Especially the CDW phases with their driving forces and mechanisms often remain elusive [15,16]. As another example, the metallic group V TMDC 2H-NbS_2 is superconducting in the bulk [7,17,18], but no CDW phase appears to be present [17,19,20]. In the monolayer limit, even though a 3×3 superstructure reminiscent of a CDW was reported before [21], the electronic correlation effects including superconductivity are largely uninvestigated experimentally. The first manuscript of this thesis (chapter 7) is therefore focused on the CDW phase and possible superconductivity in quasi-freestanding H-NbS_2 monolayers grown in situ on Gr/Ir(111).

The properties of 3D layered materials can be influenced strongly by incorporation of atoms or molecules into the vdW gap [22–24], called intercalation. To give an example, intercalation of alkali atoms into semiconducting black phosphorus (BP) can make it superconducting [25]. Also functionalization of layered materials by intercalation is possible, for example enabling to write information with current pulses into Fe-intercalated bulk NbS_2 by switching the antiferromagnetic order [26]. Furthermore, intercalation of single monolayers placed on a substrate was shown to modify the properties of the layer and also decouple it to a quasi-freestanding state [27–30]. Intercalation of layered materials combined with the interest into atomically thin 2D layers, to obtain intercalation of 2D layer heterostacks consisting of two different monolayers, offers the prospect to modify the properties and create new functions of 2D layer heterostacks, which are currently an important focus field in research [31, 32].

Another phenomenon offering fascinating properties in ultrathin structures is magnetism. The interface of an ultrathin magnetic film with a substrate gives rise to new magnetic interactions like the Dzyaloshinskii-Moriya- and beyond-Heisenberg interactions, that interplay to cause non-collinear spin structures [33]. One of these structures are skyrmions [34–36], vortex-like, topologically protected spin configurations with chiral boundaries and particle-like properties [37–39]. These are of interest for spintronic applications [40, 41]. For example the so called "racetrack memory" [42], an information storage device originally proposed to use a spin-coherent current to move magnetic domain walls through a nanowire, could be realized by skyrmions in a nanoribbon [36,41]. It could potentially offer significant advantages regarding information storage densities, addressing times and energy consumption over conventional information storage devices like hard disk drives, known to have reached their limit in information density [43, 44]. The racetrack memory realized by skyrmions however offers several challenges like the skyrmion Hall effect, leading to the movement of skyrmions to the edge of a nanoribbon and subsequent annihilation [45, 46]. Antiskyrmions with vanishing Hall effect [47, 48] and increased thermal stability [49] could offer an alternative to conventional skyrmions. So far these have been observed in bulk Heusler materials [49, 50]. Even though antiskyrmions have not been observed on surfaces, their presence in ultrathin films on C_{2v}-symmetry substrates was proposed theoretically [51]. Such systems are therefore of high interest for experimental research and in the third manuscript of this thesis (chapter 9) the magnetic structure and the interplay of magnetic interactions in an ultrathin Fe film on the C_{2v}-symmetry surface of Ir(110) is investigated.

This thesis is structured as follows: in chapter 2, first TMDCs and the phenomenon of CDWs are introduced, followed by an overview of the CDW phases in group V TMDCs. Chapter 3 focuses on the properties of NbS_2 in particular, including the structure and layer-dependent electronic properties reported in literature, as well as preparation methods. In chapter 4, the topic of intercalation of layered materials is introduced, focusing on TMDC self-intercalation, intercalation of magnetic materials into TMDCs and intercalation of 2D monolayer heterostacks containing TMDC monolayers. Magnetic interactions and non-collinear magnetism at surfaces are discussed in chapter 5, followed by a description of spin-polarized scanning tunneling microscopy (SP-STM) and the set-up of the new UNISOKU USM1300 system at the University of Cologne in chapter 6. The chapters 7, 8 and 9 are the manuscripts mentioned above containing the results, which are then subsequently summarized and discussed in chapter 10. The three manuscripts are in the phase of preparation for submission to a publishing journal.

CHAPTER 2

Transition Metal Dichalcogenides and the Concept of Charge Density Waves

In this chapter, transition metal dichalcogenides with their basic structural properties and phases are introduced. One phenomenon present in many of these materials are charge density waves. The concept of charge density waves is explained in the basic picture of a Peierls transition and the applicability of the Peierls picture, as well as example cases of charge density wave phases in different transition metal dichalcogenides are discussed.

Layered transition metal dichalcogenides (TMDCs) represent a family of materials known and popular for their diverse properties and interplay of electronic phenomena like Mott insulating phases, superconductivity and charge density waves (CDWs) [6, 8, 52]. Application opportunities range from energy storage like in the case of Li batteries [53] and even environmental matters [54], to electronic, optoelectronic and photonic devices [55, 56]. TMDCs are long known to exist in three-dimensional (3D) bulk form [57], as well as in the form of two-dimensional (2D) materials [58]. The electronic properties are often strongly layer-dependent like in the case of the semiconducting MoS_2 [59–61] and especially the CDW phases in many metallic TMDCs are subject to an ongoing discussion in literature regarding their origin and driving forces [16, 62], therefore constituting an appealing field of research.

2.1 Crystal Structure and Phases of Transition Metal Dichalcogenides

The structural hallmark of TMDCs is that they consist of X-M-X planes, with a hexagonal transition metal layer (M from group IV–VII) sandwiched in between two hexagonal chalcogen layers (X: S, Se, Te). Single planes are then stacked on top of each other, with a van der Waals (vdW) gap in between. The stoichiometry is denoted as MX_2, with the oxidation state of the metal atoms being +4 and the one of the chalcogens -2. Each TMDC plane possesses a thickness of $0.6 - 0.7\,\mathrm{nm}$ and the atoms within are bound covalently. In the two most common phases, the transition metal atoms either feature trigonal-prismatic coordination of D_{3h} symmetry (H-phase), or octahedral coordination of D_{3d} symmetry (T-phase). The structure of the two phases is depicted in Fig. 2.1 (a) and (b) (topview) and Fig. 2.1 (c) and (d) (sideview).

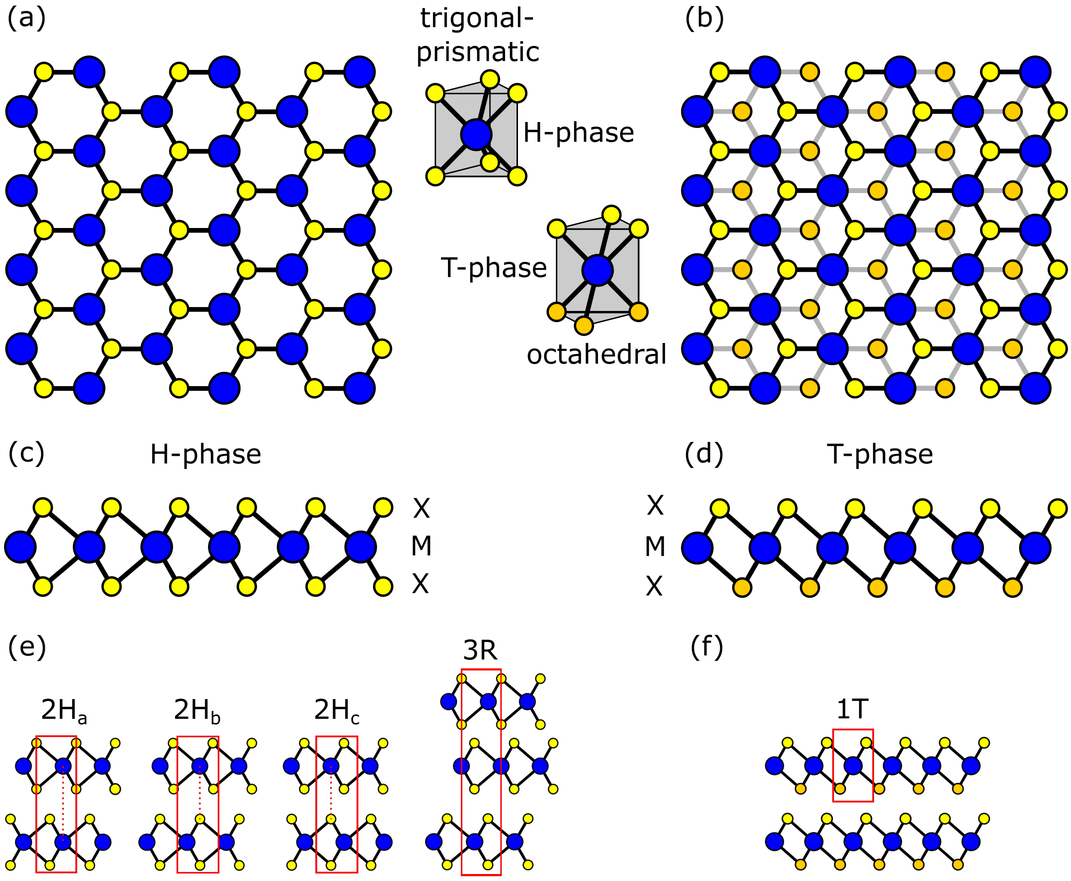

Figure 2.1: Crystal structure and phases of TMDCs. (a) Top view of the H-phase structure and illustration of the trigonal-prismatic coordination of the M atoms. (b) Top view of the T-phase structure and illustration of the octahedral coordination of the M atoms. (c) Side view of the H-phase structure. (d) Side view of the T-phase structure. (e) Different polytypes of the H-phase. (f) 1T-polytype of the T-phase. Transition metal atoms (M) are shown in blue, chalcogen atoms (X) are shown in yellow and orange. The polytype unit cells are marked red. Figures partially adapted from Ref. [22, 57, 63].

Different polytypes arise when stacking the sandwich layers on top of each other. Fig. 2.1 (e) shows the stacking possibilities of the H-phase. $2H_{a,b,c}$ represent the family of 2H-polytypes, for which always two layers are necessary to construct the 3D unit cell of hexagonal symmetry. The 3R-polytype requires three H-layers to construct a rhombohedral unit cell. The trivial stacking of the T-phase is displayed in Fig. 2.1 (f). Metal atoms lie on top of each other and the trigonal unit cell can be constructed by just one layer. Some materials can exist in different phases and polytypes depending on the environment and the conditions during synthesis, but usually one of them is thermodynamically preferred. A more detailed description of TMDCs featuring other phases, structures and properties in general, can be found in literature [57, 64, 65].

2.2 Charge Density Waves in the Picture of a Peierls Transition

Metals usually consist of atoms forming a periodic lattice with the ions sitting in equilibrium positions. In this case the electron (charge) density is evenly distributed over the lattice. Under certain conditions, this arrangement of ions and charge density can become unstable and the system undergoes a transition to a CDW phase. TMDCs are one prototype class of material long known to feature such transitions [6]. Regarding the driving forces, the so called "Peierls transition" [66] was initially identified as the dominant mechanism, but until today there is an ongoing controversy discussing other driving forces beyond the initially assumed Peierls picture [16, 67–69]. The following description loosely follows Ref. [62] and Ref. [63].

The concept of a Peierls transition [66] was developed to describe CDWs in a monoatomic, one-dimensional (1D) chain with lattice constant a. Fig. 2.2 (a) shows such a chain in the equilibrium case. The ionic cores possess a weak periodic potential U and the nearly free-electrons can be described as Bloch wave functions ψ. The electron probability density $|\psi|^2$ of periodicity a results from standing waves, caused by interference of Bloch electron waves after scattering at the Brillouin zone boundary under fulfillment of the Bragg condition. Two antiphase solutions $|\psi^+|^2$ and $|\psi^-|^2$ emerge as marked in the drawing. One solution, the $|\psi^+|^2$ one, is energetically favorable since in this case the electron probability density is highest at the nuclei where the potential is the lowest. In k-space the difference in energy of the two solutions opens a band gap E_g at the Brillouin zone boundary $k = \pm\pi/a$ in the parabolic band, as visible in Fig. 2.2 (b).

The situation changes when introducing a periodic lattice distortion (PLD) into the system, illustrated in Fig. 2.2 (c). The atom cores are moved slightly from their equilibrium positions by Δa, causing a new lattice periodicity of $2a$ with a changed periodic potential U'. For the reasons discussed before, U' again gives two solutions $|\phi^+|^2$ and $|\phi^-|^2$ for the electron probability density $|\phi|^2$, causing the opening of a band gap (2Δ) at the new Brillouin zone boundary at $k = \pm\pi/2a$ [Fig. 2.2 (d)]. The PLD causing the band gap is energetically favorable if the Fermi energy E_F for a half filled metallic band is located inside the gap, since in this case electron states directly at E_F are lowered. Electrons at E_F then occupy the energetically favorable solution $|\phi^+|^2$ for the electron probability density [Fig. 2.2 (c)], causing a charge modulation of periodicity $2a$ in real space following the new periodicity of the potential U'. The charge modulation is related to the wave vector $q_{CDW} = 2k_F$ indicated in Fig. 2.2 (d) by $2a = 2\pi/q_{CDW}$. One can conclude that the PLD conditions the opening of a band gap and vice versa, therefore both can only appear together [70]. This state of a connected PLD and band gap is then called the CDW phase, with the CDW denoting the charge modulation in the real space lattice.

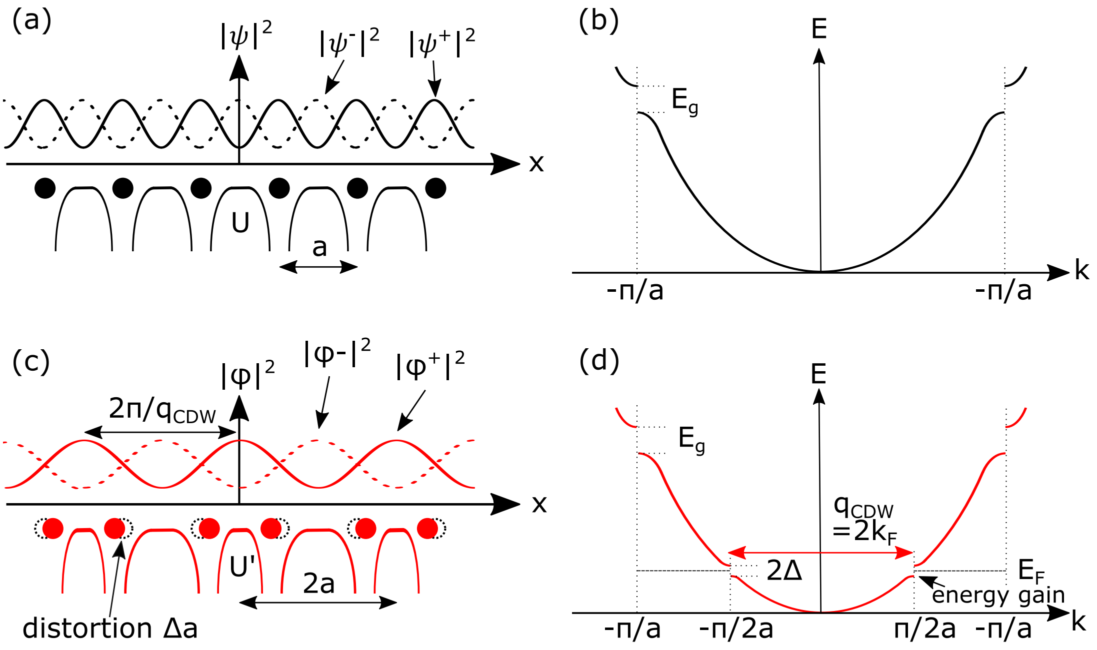

Figure 2.2: Illustration of the Peierls transition in a 1D atomic chain. (a) 1D chain with equilibrium atom positions, the corresponding electron probability density $|\psi|^2$ with solutions $|\psi^+|^2$ and $|\psi^-|^2$ and the periodic ionic potential U. (b) Parabolic band structure of the equilibrium lattice with a band gap E_g at the Brillouin zone boundary $k = \pm\pi/a$, caused by the periodic ionic potential. (c) Distorted metallic chain with out-of-equilibrium atom positions, the corresponding electron probability density $|\phi|^2$ with solutions $|\phi^+|^2$ and $|\phi^-|^2$ and the new periodic ionic potential U'. (d) Metallic band structure with a small gap 2Δ opening at the new Brillouin zone boundary $k = \pm\pi/2a$ and Fermi energy E_F upon the distortion of the chain. Figures partially adapted from Ref. [62] and Ref. [63].

To understand under which conditions a connected PLD/CDW is energetically favorable, the so called "Fröhlich Hamiltonian" [71, 72] is used to describe a system with electron-lattice coupling in the weak-coupling limit ($\Delta/E_\mathrm{F} << 1$ and $\Delta a/a << 1$) using a mean-field approach:

$$\mathcal{H} = \sum_k \underbrace{\epsilon_\mathbf{k} a^\dagger_\mathbf{k} a_\mathbf{k}}_{\text{free-electron gas}} + \sum_\mathbf{q} \underbrace{\hbar\omega_\mathbf{q} b^\dagger_\mathbf{q} b_\mathbf{q}}_{\text{lattice vibrations}} + \frac{1}{\sqrt{N}} \sum_{\mathbf{k},\mathbf{q}} \underbrace{g_\mathbf{q} a^\dagger_{\mathbf{k}+\mathbf{q}} a_\mathbf{k} (b^\dagger_{-\mathbf{q}} + b_\mathbf{q})}_{\text{electron-phonon coupling}} . \tag{2.1}$$

The Hamiltonian describes the lattice distortion as a phonon mode coupled to an electronic response in the picture of a free-electron gas. $a^\dagger_\mathbf{k}$ and $a_\mathbf{k}$ are the creation and annihilation operators of an electron state with wave vector **k** and energy $\epsilon_\mathbf{k}$, $b^\dagger_\mathbf{q}$ and $b_\mathbf{q}$ the creation and annihilation operators for a phonon with wave vector **q** and frequency $\omega_\mathbf{q}$ and therefore energy $\hbar\omega_\mathbf{q}$, and $g_\mathbf{q}$ the electron-phonon coupling constant assumed to be independent of **k**. N is the number of lattice sites. A static displacement $u_\mathbf{q}$ of the phonon mode **q**, relating to the before described

PLD, can be then understood as a perturbation in the equilibrium lattice, causing a potential $v_{\mathbf{q}} = g_{\mathbf{q}} u_{\mathbf{q}} \sqrt{(2\omega_{\mathbf{q}} M/\hbar)}$ resulting from the 1D-chain equation of motion

$$\ddot{u}_{\mathbf{q}} = -\omega_{\mathbf{q}}^2 u_{\mathbf{q}} - g_{\mathbf{q}} \left(\frac{2M\omega_{\mathbf{q}}}{\hbar}\right)^{1/2} \rho_{\mathbf{q}}, \tag{2.2}$$

with M being the ionic mass. The response of a free-electron gas to a potential can be treated within the framework of linear response theory. The resulting charge density takes the form $\rho^{\text{ind}}(\mathbf{q}) = \chi(\mathbf{q}) v_{\mathbf{q}}$, with $\chi(\mathbf{q})$ being the Lindhard response function [73]

$$\chi(\mathbf{q}) = \frac{1}{L} \sum_{\mathbf{k}} \frac{f_{\mathbf{k}+\mathbf{q}} - f_{\mathbf{k}}}{\epsilon_{\mathbf{k}} - \epsilon_{\mathbf{k}+\mathbf{q}}} \tag{2.3}$$

in the case of a static potential, as the PLD is assumed to be static. This response function is also described as the non-interacting electronic susceptibility. $f_{\mathbf{k}}$ is the Fermi function $f(\epsilon_{\mathbf{k}})$ at the energy $\epsilon_{\mathbf{k}}$ and L the length of the atomic chain. To now understand under which conditions a PLD together with the opening of a band gap is energetically favorable, one has to compare static lattice energy cost in case of a distortion $u_{\mathbf{q}}$ and the band energy gain from the electronic response to the potential $v_{\mathbf{q}}$, derived within second-order perturbation theory [74]. The energies are given as:

$$\delta E_{\text{lattice}} = \frac{1}{2} M \omega_{\mathbf{q}}^2 u_{\mathbf{q}}^2 \quad \text{and} \quad \delta E_{\text{band}} = -|v_{\mathbf{q}}|^2 \chi(\mathbf{q}). \tag{2.4}$$

For the system to gain energy by creating a PLD of wave vector $\mathbf{q}$ and the connected change in the energy bands (gap), the condition $\delta E_{\text{lattice}} + \delta E_{\text{band}} < 0$ must be fulfilled, leading to:

$$4g_{\mathbf{q}}^2/\hbar\omega_{\mathbf{q}} > 1/\chi(\mathbf{q}). \tag{2.5}$$

The condition is fulfilled for large, non-interacting electron susceptibilities $\chi(\mathbf{q})$, given when many electronic states take part in the response, which is the case for systems in which a large number of electronic states is separated by a single wave vector $\mathbf{q}$. This corresponds to Fermi surface topologies featuring large parallel surface areas separated by $\mathbf{q}$ and is called Fermi surface nesting [75]. The principle of nesting is illustrated in Fig. 2.3. Fig. 2.3 (a) displays the ideal case of a 1D free-electron gas. The 1D Fermi surface consists of two exactly parallel lines due the 1D dispersion of the band structure, with all states being connected by a single nesting vector. In this case the susceptibility $\chi(\mathbf{q})$ diverges at $\mathbf{q} = 2\mathbf{k}_F$ as shown in Fig. 2.4 (a). In higher dimensions, the nesting can be completely absent like in the case shown in Fig. 2.3 (b) for a 2D free-electron gas in which case the 2D Fermi surface is given as a circle, or be partial like for Fermi surfaces of other shapes [Fig. 2.3 (c)]. For partial nesting in the 2D or 3D electron gas, the susceptibility curves feature a step-like (2D) or washed-out-step-like (3D) behavior as shown in Fig. 2.4 (a). It should be noted that nesting, instead of requiring parallel segments of the Fermi surface, can also be evident in the case of saddle points in the Fermi surface [76].

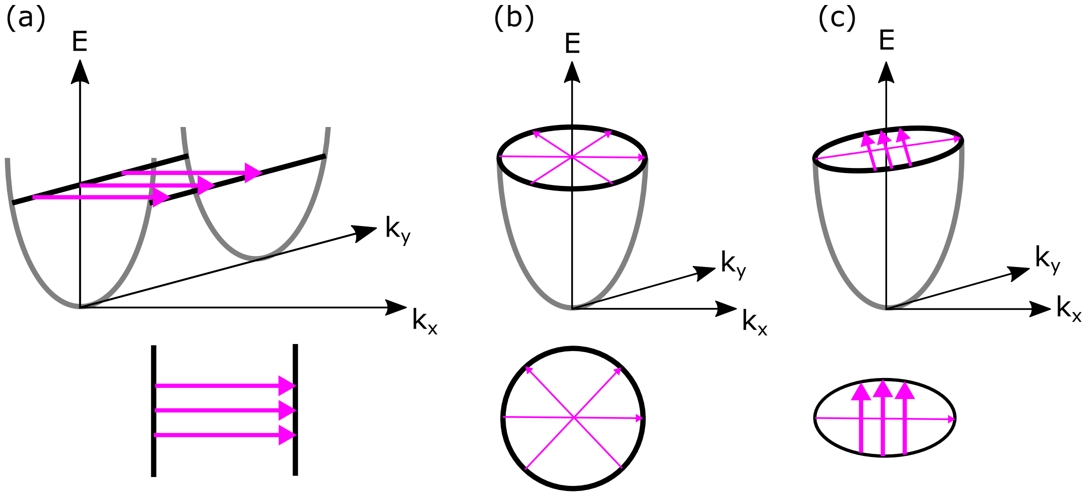

Figure 2.3: Illustration of Fermi surface nesting. (a) 1D free-electron gas, the nesting condition is always fulfilled due to the 1D Fermi surface. (b) 2D free-electron gas. In this case, nesting is not favorable. (c) Partial 2D Fermi surface nesting in the case of a close to parallel section in the Fermi surface. The Fermi surfaces are shown in black, the band structure in grey. Strong nesting contributions are indicated by thick pink arrows, weak contributions by thin pink arrows. The lower figures are a top view of the Fermi surfaces in the $k_{x,y}$ plane. Figure adapted from Ref. [63].

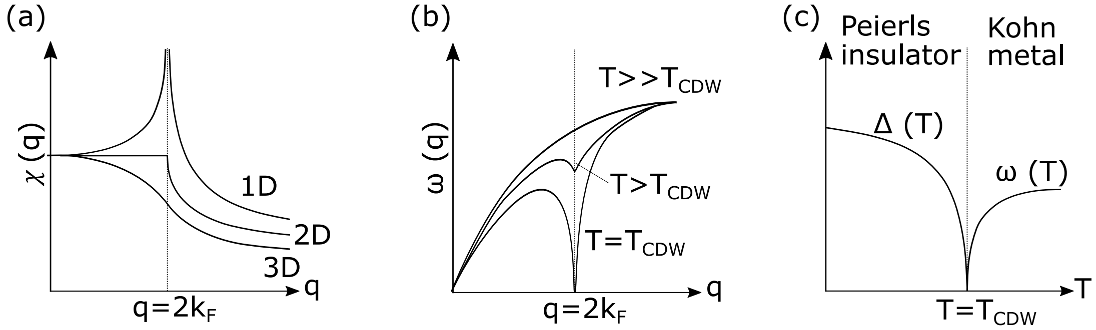

Figure 2.4: (a) Susceptibility $\chi(\mathbf{q})$ of the free-electron gas in different dimensions. Figure adapted from Ref. [75]. (b) Temperature dependence of 1D phonon frequencies ω featuring a Kohn anomaly. Figure adapted from Ref. [72]. (c) Transition from a Peierls insulator to a Kohn metal. Figure adapted from Ref. [77].

Just like the electron system responding to the introduced perturbation, also the phonon system reacts to the electronic perturbation. This reaction is called a Kohn anomaly [78]. The before described equation of motion (2.2) results in a renormalized phonon frequency [72]:

$$\tilde{\omega}_{\mathbf{q}}^2 = \omega_{\mathbf{q}}^2[1 - \frac{4g_{\mathbf{q}}^2}{\hbar\omega_{\mathbf{q}}}\chi(\mathbf{q})]. \tag{2.6}$$

The effect of a diverging susceptibility $\chi(\mathbf{q})$ on the renormalized phonon frequency is illustrated in Fig. 2.4 (b). For a fulfilled nesting condition at $\mathbf{q} = 2\mathbf{k}_\mathrm{F}$, the phonon frequency softens completely, thereby becoming imaginary with $\omega < 0$. This translates to a PLD, a frozen-out lattice distortion. The scope of softening is temperature-dependent and is only complete at/below the critical temperature T_CDW. The temperature-dependent behavior of the PLD/CDW system is further illustrated in Fig. 2.4 (c). Below the critical temperature T_CDW the system becomes an insulator with a gap opening at the Fermi energy. The size of the gap is also temperature-dependent and results in relation to the displacement $u_{\mathbf{q}}$, the electron-phonon coupling $g_{\mathbf{q}}$ and the phonon frequency $\omega_{\mathbf{q}}$ with $\mathbf{q} = 2\mathbf{k}_\mathrm{F}$ as [72]

$$\Delta(T = 0) = u_{\mathbf{q}}g_{\mathbf{q}}\sqrt{\frac{2M\omega_{\mathbf{q}}}{\hbar}} = 3.52k_\mathrm{B}T_\mathrm{CDW}, \tag{2.7}$$

which is the well know BCS relation for zero-temperature band gaps and the corresponding mean-field transition temperature.

To summarize, the key features of the Peierls transition causing a connected PLD/CDW, are a sharp peak in the Lindhard-function in the case of a fulfilled Fermi surface nesting condition and a corresponding lattice response in the form of a Kohn anomaly, resulting in a structural metal-insulator transition.

2.3 Applicability of the Peierls Model

In the Peierls model several assumptions are made, that do not always hold true in real materials [16]. The first problem is the non-interacting Lindhard function, used to describe the response of the electron system to an external potential $v_{\mathbf{q}}$. This function might not be suited to describe systems with strong electron-electron correlations, even in 1D [79]. In this case the Fröhlich Hamiltonian is not sufficient and both the Coulomb- and exchange interaction of charge carriers have to be considered [70], resulting in a modified condition 2.5 for a energetically favorable CDW/PLD:

$$4g_{\mathbf{q}}^2/\hbar\omega_{\mathbf{q}} - 2U_{\mathbf{q}} + V_{\mathbf{q}} \geq 1/\chi(\mathbf{q}). \tag{2.8}$$

$U_\mathbf{q}$ denotes the Coulomb interaction and $V_\mathbf{q}$ the exchange interaction. The consequence is that when the exchange interactions dominate, a spin density wave can arise [70].

The second problem is that in the Peierls model the interactions like the electron-phonon coupling $g_\mathbf{q}$ are assumed to be wave-vector-independent. The wave vector at which the PLD/CDW combination takes place is solely determined by the Fermi surface nesting condition and therefore exclusively ruled by the electronic response. This does generally not hold true in reality, with $g_\mathbf{q}$ showing variation along the Brillouin zone. One prominent example of a CDW insufficiently explained by a Peierls transition is 2H-NbSe$_2$ [67,68]. In this case, the Lindhard response function does not diverge at q_CDW [67,80]. The CDW in that system is therefore assumed to be at best assisted by Fermi surface nesting, which especially in higher dimensions (2D or 3D), can only be partial as described above. Instead, strong wave-vector-dependent electron-phonon coupling is driving the lattice distortion and leads to an energy softening of phonon modes on a broader range than expected for a sharp Kohn anomaly [68,81]. As a consequence, this can affect the band structure on a broader scale [62] and might lead to energy gaps away from the Fermi energy [82,83].

2.4 Charge Density Waves in Group V Transition Metal Dichalcogenides

Even though the phenomenon of CDWs is long known, its discovery in the metallic group V TMDCs TaS$_2$, TaSe$_2$ and NbSe$_2$ [6] made the topic emerge again. The exact mechanisms, driving forces and layer-dependence are still subject to an ongoing discussion. While CDWs are also present in the group IV TMDCs, for example TiSe$_2$ [84–87], or main group dichalcogenides like SnSe$_2$ [88–90], the following overview is mainly focused on the CDW phase and its coexistence with superconductivity in group V H-phase TMDCs, to which the TMDC treated in this work, H-phase NbS$_2$, belongs.

Starting with the Ta based compounds, bulk 2H-TaS$_2$ features an incommensurate CDW with a close to 3×3 periodicity of the CDW superlattice and a critical temperature of T_CDW = 75 K [10,11]. As becoming evident in the following, the 3×3 periodicity is typical for the CDW phases in group V H-phase TMDCs. On the one hand, the CDW phase in TaS$_2$ has experimentally been found to be accompanied by a partial gap in the band structure [91–94], consistent with the picture of Fermi surface nesting. On the other hand, theoretical works suggest higher-order phonon fluctuations and strong, momentum-dependent electron-phonon coupling as important driving forces of the CDW [95,96], supported by experimental results [97,98] also for example showing that short range CDW order can persist above T_CDW [99]. Like for other TMDCs, the discussion remains controversial regarding the CDW mechanisms. 2H-TaS$_2$ is found to be superconducting below or around T_c = 1 K [6,8,9]. Regarding the coexistence of the superconducting phase and the CDW phase, it has been found that an enhancement of superconductivity (e.g. by doping) is connected to a weakening of the CDW [100–106].

In the monolayer limit, H-TaS_2 features a commensurate 3×3 CDW when grown quasi-freestanding on graphene (Gr) [21, 107], while bilayers possess a disordered 2×2 CDW [107]. The results of Hall et al. [107] are a good example of the layer-dependent properties in TMDCs. In their work, the monolayer CDW features a partial gap at the Fermi energy [107], which on first sight points towards Fermi surface nesting, but theoretical works similar to the discussion regarding bulk 2H-TaS_2 propose electron-phonon coupling matrix elements controlling the lattice instability [69]. This is supported by the experimental finding that the transition temperature is enhanced to $\mathrm{T}_{\mathrm{CDW}}$ = 140 K for exfoliated monolayers on SiO_2 [14], suggesting a stronger driving force, since high transition temperatures are usually the result of large coupling constants in disagreement with CDWs driven by Fermi surface nesting [62]. On stronger interacting substrates like Au(111), the CDW phase in monolayer H-TaS_2 is suppressed due to substrate effects [108–111]. Regarding superconductivity in the 2D limit, 2H-TaS_2 features an increase of the critical temperature to T_{c} = 2.2 K [9] for 3.5 nm thick films and T_{c} = 3.0 K [12] in the monolayer limit. While Yang et al. [13] also reported an increase of the superconducting transition temperature to T_{c} = 3.4 K in the monolayer limit, they report a suppression of the CDW measured in transport, in contrast to [14].

Different from 2H-TaS_2, 2H-$TaSe_2$ features two CDW transition temperatures. The first transition happens below 122 K to a non-commensurate, near 3×3 CDW, which locks-in on the lattice and becomes a commensurate 3×3 CDW at T_{CDW} = 90 K [6, 112, 113]. Regarding the driving force in the commensurate phase, Fermi surface nesting is discussed in literature [76, 114], but a significant influence of wave-vector-dependent electron-phonon coupling is considered [21]. 2H-$TaSe_2$ has been found to be superconducting at very low transition temperatures of $\mathrm{T}_{\mathrm{c}} \approx 0.2$ K [115, 116]

In the monolayer limit, the 3×3 CDW persists [117], featuring an increased transition temperature of $\mathrm{T}_{\mathrm{CDW}}$ = 125 K [118], with the CDW even being present on Au(111) substrates [118], different to TaS_2. Superconductivity is expected from theory to possess an increased critical temperature of T_{c} = 2.2 K [119]. The more robust CDW and superconducting phase in the monolayer limit is attributed to an enhancement of electron-phonon coupling [119]. The increase of interactions is similar to the case of 2H-TaS_2.

Regarding Nb based TMDCs, the sister compound of 2H-NbS_2, bulk 2H-$NbSe_2$, possesses a nearly commensurate 3×3 superlattice below T_{CDW} = 33 K [112, 120–122]. Even though also some works attribute the CDW formation to Fermi surface nesting [123], in general stronger, wave-vector-dependent electron-phonon coupling is considered as the main driving force [67,68, 81,124–126]. Additional to the CDW phase, superconductivity was found below T_{c} = 7.2 K [127]. The coexistence of CDW and superconductivity is explained by the fact that the Fermi surface is mostly unaffected by the CDW and the competition between the two phenomena is quite low [126].

Different to the bulk, the 3×3 CDW is commensurate in the monolayer limit, for example in H-$NbSe_2$ monolayers grown on bilayer Gr/6H-SiC(0001) [128]. In that system, the CDW phase features a critical temperature between $T_{\mathrm{CDW}} = 25\,\mathrm{K}$ and $T_{\mathrm{CDW}} = 45\,\mathrm{K}$, very similar to the bulk case. A small gap of $2\Delta = 8\,\mathrm{meV}$, correlated with the amplitude of the CDW, is present at the Fermi energy in scanning tunneling spectroscopy (STS) measurements and therefore Fermi surface nesting seems to be a possible driving force. On the other hand in theoretical works, similar to the bulk case, the absence of Fermi surface nesting is discussed and stronger, wave-vector-dependent electron-phonon coupling has been assumed to be the driving force of the CDW [129, 130]. This is supported by the fact, that for exfoliated monolayer samples of $NbSe_2$ on sapphire, an enhanced T_{CDW} of about 145 K was found [131, 132], pointing to a stronger interaction mechanism than Fermi surface nesting since like in the above described case of monolayer H-TaS_2, the enhanced T_{CDW} relates to a coupling constant λ of the CDW in conflict with the weak-coupling limit of Fermi surface nesting [62, 131]. The enhancement of T_{CDW} has again been questioned by theory [133] and the topic remains under discussion, as Lin et al. [132] explain that the T_{CDW} in the case of $NbSe_2$ monolayers on Gr/6H-SiC(0001) [128] is actually suppressed by charge transfer from Gr. The before described coexistence of the superconducting phase and the 3×3 CDW phase in bulk 2H-$NbSe_2$ also prevails in the monolayer, with a reduced T_c of about 2 K in the superconducting phase [128, 134, 135]. This reduction is in contrast to the behavior of superconductivity in TaS_2 and $TaSe_2$ and was attributed to the competition of CDW and superconductivity [136, 137].

CHAPTER 3

The Transition Metal Dichalcogenide Niobium Disulfide

This chapter introduces H-phase NbS_2*, the group V TMDC addressed by the manuscripts in the chapters 7 and 8. First the structural features are briefly discussed, followed by a description of the layer-dependent electronic properties down to the monolayer limit, including a possible monolayer CDW phase. Afterwards different TMDC synthesis methods with a focus on the preparation of* NbS_2 *are presented.*

As described in chapter 2, many metallic group V TMDCs possess CDW phases with often varying properties depending on the thickness of the materials. 2H-NbS_2, also a group V TMDC, is a material structurally characterized long ago [17, 138] and several experimental reports regarding the bulk electronic properties are present for example in Ref. [7, 18, 19, 139], but investigations regarding the monolayer limit are mostly limited to theoretical works for example in Ref. [20, 140–142] and only sparse experimental reports exist for quasi-freestanding NbS_2 monolayers [21], lacking electronic characterization.

3.1 Structure

Like its sister compound $NbSe_2$, NbS_2 is a metallic group V TMDC with Nb metal atoms sandwiched between two S layers as shown in Fig. 2.1 in chapter 2. The preferred structural phase of TMDCs mainly depends on the *d*-electron count of the metal atoms [65]. Regarding NbS_2, first principle calculations indicate that the H-phase is energetically favorable over the T-phase [21], experimentally confirmed by the presence of the H-phase in CVD-grown thin films down to monolayer thickness [143]. The favored stacking sequences of the H-phase bulk compounds are reported to be either $2H_a$ or 3R [17, 138, 143, 144] (compare Fig. 2.1 in chapter 2). Nevertheless, the unpreferred 1T-phase can be present as occasional layers in bulk 2H-crystals [145], presumably located at rotational domains of the 2H-layers [146]. It can also be grown as thin films under special circumstances [147]. Both the 3R- and the 1T phase are not treated in further detail in this work.

3.2 Layer-Dependent Electronic Properties

The electronic properties of TMDCs depend on the *d*-electron count and the coordination of the metal atoms in the sandwich layer [65]. Regarding group V TMDCs, in the case of trigonal-prismatic coordination (H-phase) the *d*-orbitals split into three groups (d_{z^2}, $d_{x^2-y^2,xy}$ and $d_{yz,xz}$), as sketched in Fig. 3.1 (a). Since the *d*-orbitals are partially filled, the group V H-phase TMDCs generally possess metallic behavior [65].

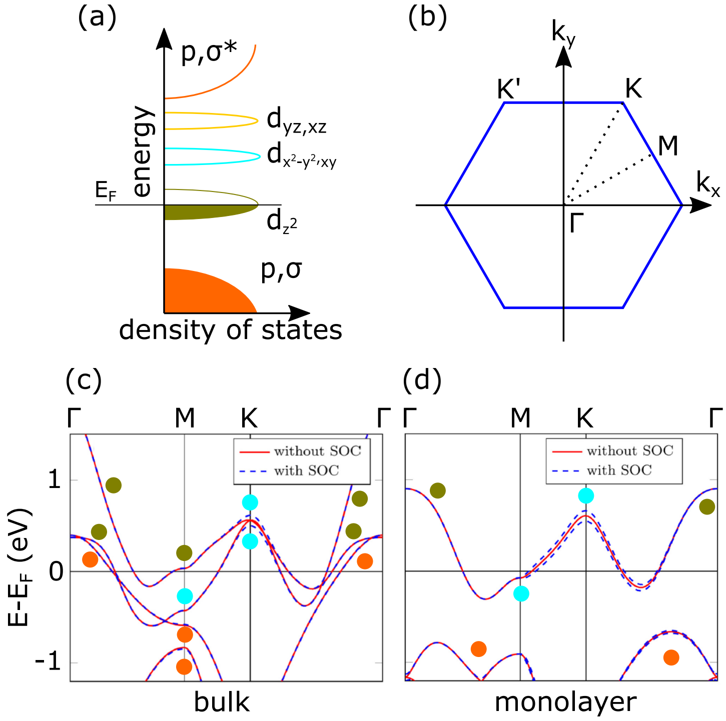

Figure 3.1: Layer-dependent band structure of NbS_2. (a) Schematic depiction of orbitals in group V H-phase TMDCs. Figure adapted from Ref. [63] and Ref. [65]. (b) Hexagonal Brillouin zone of NbS_2 with high-symmetry points. (c) DFT calculated bulk band structure of NbS_2. (d) DFT calculated monolayer band structure of NbS_2. Figures (c) and (d) adapted with permission from Ref. [139] © 2018 APS.

The hexagonal arrangement of the NbS_2 layers yields a hexagonal Brillouin zone in *k*-space [Fig. 3.1 (b)], featuring the high-symmetry points Γ, M and K. A density functional theory (DFT) calculated band structures of bulk 2H-NbS_2 along the high-symmetry directions is depicted in Fig. 3.1 (c), with the colored dots relating to the orbital character of the bands [compare colors to Fig. 3.1 (a)]. Following the description in Ref. [139], in the bulk between Γ and M, three bands cross the Fermi energy E_F, showing that 2H-NbS_2 is indeed metallic. Close to Γ, the upper two bands depicted stem from Nb d_{z^2}-states (khaki), while the lowest one originates from the S p_z-orbital (orange), showing that in 2H-NbS_2 also the S bands partially contribute to the conduction. The upper *d*-band crosses the Fermi energy again close M, changes its character to $d_{x^2-y^2,xy}$ (in-plane orbitals of Nb, turquoise) towards K and makes up a hole-like pocket around K. The lower d-band behaves similarly crossing the Fermi energy between M and K, but already changes its orbital character to $d_{x^2-y^2,xy}$ towards M. Again towards Γ, the two mentioned d-bands cross the Fermi energy two more times, changing their character back to d_{z^2} and complete two hole-like pockets around Γ. Here also the orange S p_z-band again comes up, crosses the Fermi energy and makes up the third hole-like pocket around Γ.

It is well known that the band structure in TMDCs is layer-dependent. This is prominently shown for the group VI TMDC MoS_2, featuring an indirect to direct band-gap-transition upon thinning the material down to the monolayer limit [59–61]. Also in the monolayer limit of NbS_2, the band structure [Fig. 3.1 (d)] undergoes changes. Here compared to the bulk, the S p_z-bands are moved to lower energies away from the Fermi energy due to the absence of S-S interactions along z [139]. The Fermi surface is made up by only one band originating from in-plane- and out-of-plane d-orbitals of Nb. Again hole-like pockets are present around Γ and K.

As discussed in chapter 2, another layer-dependent electronic property of many TMDCs are CDWs. Different to other group V H-phase TMDCs, in bulk 2H-NbS_2 the CDW order has been found absent in macroscopic measurements [6, 17], confirmed by scanning tunneling microscopy (STM) investigations [19]. The softening of a phonon mode near $q_{CDW} = 2/3\overline{\Gamma M}$ expected for a 3×3 CDW is reported, but anharmonic effects seem to suppress the CDW and the energy of the phonon mode remains finite [20, 140, 141]. Nevertheless, one STM work reported an incommensurate CDW in bulk 2H-NbS_2 pinned to defects [148], but the found q of the CDW appears to be unrelated to the described phonon-mode-softening, indicating a different origin. 2H-NbS_2 was also found to feature traces of a Star-of-David $\sqrt{13} \times \sqrt{13}$ CDW pattern in x-ray scattering, attributed to the presence of dilute 1T-layers [146]. The Star-of-David $\sqrt{13} \times \sqrt{13}$ CDW phase was theoretically studied both for monolayer [149] and bulk 1T-NbS_2 [150].

Just as the sister compound 2H-$NbSe_2$, bulk 2H-NbS_2 possesses a superconducting phase with a critical temperature of $T_c \approx 6\,\mathrm{K}$ [7, 17, 18].

Despite the absence of CDW order in the bulk, a 3×3 superstructure, very similar to the CDW pattern in monolayer H-$NbSe_2$, is observed experimentally in STM on quasi-freestanding NbS_2 monolayers on Gr/6H-SiC(0001) [21]. A comprehensive experimental investigation of the driving forces and electronic mechanisms is not offered yet. Van Loon et al. [142] presented a theoretical description regarding the electronic structure of freestanding NbS_2 monolayers. Fermi surface nesting in the picture of a classical Peierls transition is discarded and instead the system is described being subject to a strain-induced competition of long-range Coulomb- and electron-phonon interaction, making the system stay at the edge between charge- and spin order. As a possible mechanism to drive the system towards charge order, an enhancement of electron–phonon coupling appears to be necessary, with strain effects being a way to manipulate the coupling. Bianco et al. [140] found an enhancement of phonon-mode-softening in monolayer H-NbS_2 compared to the bulk, but also report that even small anharmonic effects like compression or dilatation can allow or inhibit the CDW order. The substrate on which the NbS_2 monolayer rests appears to have a significant influence, since different to the described case of a 3×3 superstructure in NbS_2 monolayers on Gr [21], no signs of such a pattern are present in NbS_2 monolayers grown on Au(111) [151], a much more strongly interacting substrate compared to Gr. Regarding the topic of spin order, theoretically a tendency to form a spin density wave was described for monolayer NbS_2 [152], as well as the switching of magnetic states due to strain [153, 154].

Superconductivity remains unreported in quasi-freestanding monolayer H-NbS_2 so far. The superconducting behavior reported for 2H-bulk samples has been shown to vanish in samples thinner than 6 nm due to oxidation [155]. In another work it was shown that for samples thinner than 4 nm the non-superconducting metallic 3R-phase dominates under the applied growth conditions [144]. This leaves the question of superconductivity in the monolayer unsolved in general. One special case is superconducting behavior in bulk van der Waals superlattices of alternating Ba_3NbS_5/NbS_2 [156] and $SnS_{1.7}/NbS_2$ [157] structure, showing a $T_c = 1.6\,K$ and $T_c = 2.8\,K$ correspondingly.

The electronic features and structure of quasi-freestanding H-NbS_2 on Gr/Ir(111) at low temperatures and especially the CDW phase are characterized in the manuscript of chapter 7.

3.3 Preparation and Synthesis

Different methods to synthesize TMDCs and 2D materials in general are available, with individual advantages and drawbacks [158–160]. In general, the fabrication methods can be divided into top-down approaches like exfoliation, as well as bottom-up approaches like chemical vapor deposition and molecular beam epitaxy. In the following a brief insight into the different methods is given with a focus on NbS_2, starting with the top-down synthesis.

Exfoliation

The most basic way to obtain highly crystalline 2D materials is the top-down method of exfoliation. Exfoliation means to remove a number of layers down to the single layer limit from a layered bulk crystal, for example by adhesive tape, and to place them on a substrate. It is the method that first enabled the preparation of 2D materials, with Gr being a famous example [1], but also other materials like TMDCs are possible [161]. Beyond exfoliation by mechanical cleaving, chemical exfoliation for example by liquid-phase procedures like intercalation of ions is possible, featuring higher yield [162, 163]. Some advantages of exfoliation, especially the chemical exfoliation, are versatility and low cost, therefore offering a possible pathway for industrial production of 2D TMDCs. Nevertheless, several challenges remain like finite flake size scalability, controlling flake thickness, yield rate and phases, as well as purity and surface features [164].

The method of chemical exfoliation can be applied in order to obtain thin flakes of NbS_2 , but contamination is inevitable [165] and the number of layers and therefore crystal thickness is difficult to control. Another problem also in the case of mechanical exfoliation is that thin flakes tend to oxidize if the exfoliation process is conducted in an ambient environment, a possible reason for the disappearance of superconductivity in flakes thinner than 6 nm [155].

Chemical Vapor Deposition

Another way to synthesize 2D TMDCs is the bottom-up method of chemical vapor deposition (CVD) [166]. In this method usually solid precursors are used, for example S or Se on the chalcogen site and metal oxide powders on the metal side. The precursors are placed in a furnace and by heating and the presence of a transport gas, the desired compound is formed on a substrate. Although being a relatively easy way to grow large scale TMDCs with controllable thickness and size, the growth taking place at close to ambient pressures and the fact that transfer has to occur ex-situ can introduce contaminants [167] and many of the CVD-grown compounds show limited uniformity [168, 169], effects that can have a significant impact on the physical properties [167, 170]. These limitations are subject to current research and ongoing improvements to the CVD methods [171].

Beside the mentioned exfoliation, also CVD can be applied for the synthesis of NbS_2. Epitaxial growth with the substrate determining the orientation of the grown crystal is possible down to the monolayer limit [143, 172–174], but for multilayer structures often several polytypes like 3R and 2H coexist [144]. Also achieving an exact stoichiometry is not always possible [175]. The fact that in this work STM and STS investigations are conducted under ultra-high vacuum (UHV) conditions renders CVD growth of NbS_2 unsuitable since as mentioned above, CVD-grown samples have to be transferred ex situ possibly giving rise to contamination as described for exfoliation [155].

Molecular Beam Epitaxy

One way to overcome some of the stated limitations regarding CVD is to utilize another bottom-up method called molecular beam epitaxy (MBE) [176]. It is a method of vacuum synthesis, for which a substrate is subjected to a beam of atomic or molecular species under UHV conditions, allowing epitaxial growth. In these very clean environments, the contamination of the grown materials often experienced for exfoliation and CVD can be avoided. Also the temperatures used when conducting this method are often significantly lower than in the CVD case, enabling to synthesize thermally sensitive compounds [177]. By supplying two different reactive species, growth of compound materials like TMDCs is achieved, for example shown for the synthesis of highly oriented H-NbS_2 monolayers on Au(111) upon supplying the metal Nb and the chalcogen S [151], among many other examples.

TMDC growth by MBE can also be achieved on another vdW material lacking reactive dangling bonds at the surface just as the TMDC itself. This growth method is called van der Waals epitaxy (vdWe) [178] and became of increasing interest with the rise of 2D materials, including 2D TMDCs [177,179]. It is for example demonstrated for the growth of many quasi-freestanding, weakly bound monolayer TMDCs on Gr/Ir(111) [180], in which case a vdW gap between the TMDC and Gr is present. Even though being weak, the vdW interaction can be strong enough to impose orientation on the grown material.

As will be shown in the manuscript of chapter 7, different to NbS_2/Au(111) featuring significant interaction of the TMDC with the metal substrate and no CDW order [151], NbS_2/Gr/Ir(111) resembles the band structure calculated for freestanding NbS_2 monolayers [142] and possesses a 3×3 CDW, showing the effective decoupling from the substrate as a result of vdWe.

CHAPTER 4

Intercalation of Transition Metal Dichalcogenides

This chapter serves as an introduction to the subject of chapter 8, the post-growth intercalation at the interface of Gr and monolayer NbS_2*. It starts with a discourse on the relevance of intercalation of layered materials. Afterwards the process of TMDC-self-intercalation and the intercalation of TMDCs by magnetic materials are discussed. Lastly the intercalation of 2D layer heterostacks containing a TMDC monolayer, the actual topic of the manuscript in chapter 8, is treated.*

The vdW gap of layered materials offers the possibility to incorporate atoms or molecules in between the layers, called intercalation [22–24]. Intercalation possesses the power to strongly alter the characteristics of layered bulk crystals, including the electrical and optical properties [181]. Semiconducting black phosphorus (BP) for instance becomes superconducting when alkali atoms are incorporated [25]. Layered topological insulators like Bi_2Se_3 feature drastically changed optical behavior like strongly enhanced transmission and increased carrier density by intercalation of Cu atoms [182], offering the prospect of transparent conducting electrodes [183]. Furthermore, intercalation is of great importance for energy storage devices like Li ion batteries [53], where reversible intercalation of both the cathode, e.g. TiS_2 [184] and the anode, e.g. graphite [185] is used. Intercalation of layered materials has not only been shown for bulk crystals, but also for thin, few layer 2D-materials [186–189]. Even for monolayer 2D materials where a vdW gap between the layer and the substrate is present intercalation is possible, causing a change in the properties of the monolayer and further decoupling it from the substrate, achieving a quasi-freestanding state [27–30].

TMDCs offer an ideal playground to investigate intercalation effects, due to the vdW gap present in between the sandwich layers. A large range of different bulk TMDC compounds arises upon intercalating additional metal atoms into the gap [22, 190–192]. As displayed in Fig. 4.1, dependent on the stacking sequence, H-phase TMDCs can generally offer trigonal-prismatic, tetragonal and octahedral coordination sites [191, 193, 194] that can be occupied by the incorporated material. The stacking sequence of Fig. 4.1 (c), (d) and (e), (f) ($2H_a$, compare

Fig. 2.1 in chapter 2), being the stacking sequence of for example 2H-NbS_2 [17, 138, 195], features both tetragonal and octahedral lattice sites for intercalation with the octahedral ones being favored in general [187, 190, 193, 195].

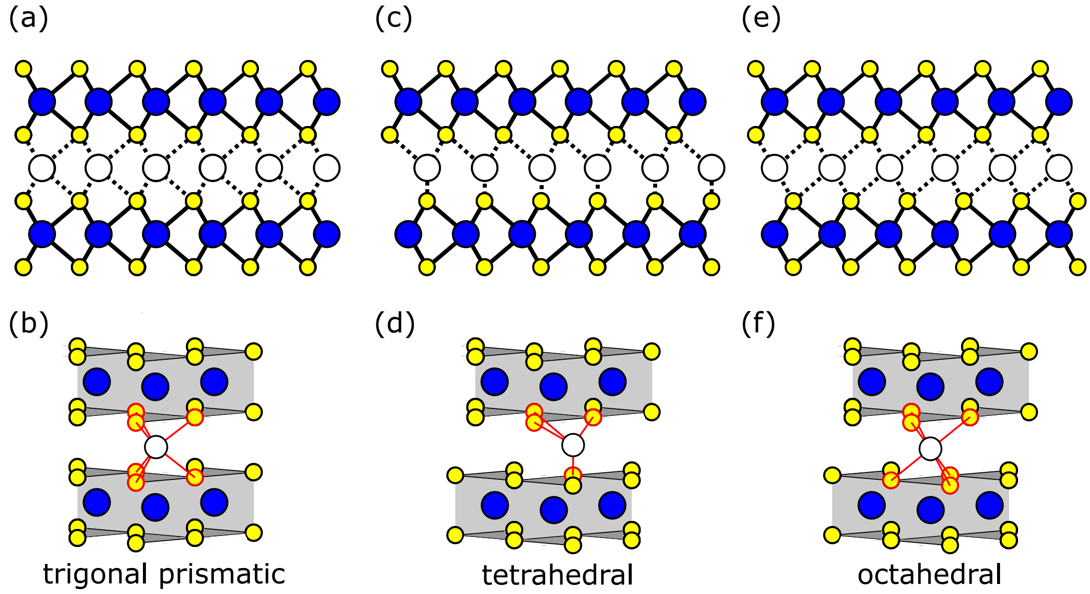

Figure 4.1: Intercalation sites of H-phase TMDCs. (a), (b) Intercalants featuring trigonal-prismatic coordination. (c), (d) Intercalants featuring tetrahedral coordination. (e), (f) Intercalants featuring octahedral coordination. Pristine metal atoms are indicated blue, pristine sulfur atoms yellow and intercalated atoms white. Figure (a), (b) adapted from Ref. [194] and Ref. [187], Figures (c)-(f) adapted from Ref. [193].

4.1 Self-Intercalation

One specific way of changing a TMDC compound by intercalation, is to incorporate native metal atoms into the vdW gap [138, 187, 195–199], called self-intercalation. Self-intercalation was for instance shown for the 1T-materials VTe_2, $TiTe_2$ and $CrTe_2$, featuring 2×1 intercalation structures caused by native metal atoms residing in octahedral adsorption sites in compounds thicker than bilayers [198].

A quite recent study demonstrated Ta intercalation of 2H-TaS_2, 2H-$TaSe_2$, as well as the self-intercalation of other 1T-and 2H-TMDC materials, altering the stoichiometry of the pristine compound and also introducing magnetic interactions like ferromagnetism and the formation of a spin frustrated Kagome lattice [187]. The intercalated materials mostly occupy octahedral adsorption sites between two TMDC layers, creating different intercalation structures depending on the stoichiometry of the compound like a $\sqrt{3} \times \sqrt{3}$ R30° superlattice. Also self-intercalated ternary $V_8(S_{1-x}Se_x)_{15}$ compounds have been found to possess magnetic behavior, in this case spin Hall magnetoresistance [199].

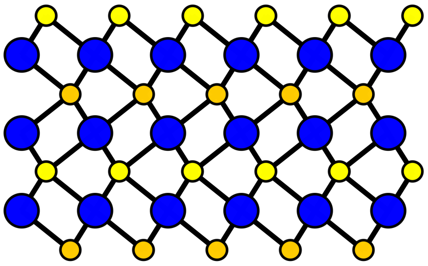

Figure 4.2: Side view of a NiAs structure in the case of $Nb_{2-y}S_2$. Nb atoms: blue, S atoms: yellow/orange. Figure adapted from Ref. [200].

For self-intercalation of bulk NbS_2 crystals, Jellinek et al. reported compounds with the composition $Nb_{1+x}S_2$ both in the rhombohedral 3R- and the hexagonal 2H-phase as early as 1960 [138, 201]. The compounds are stable in the range $0.3 \leq x \leq 0.43$ with the H-phase being preferred for thin crystals of that stoichiometry and are excellent catalysts for the hydrogen evolution reaction [195]. The additional Nb occupies the octahedral sites in the vdW gap. For very metal-rich compounds with the stoichiometry $Nb_{2-y}S_2$ and stability range $0 \leq y \leq 0.3$ the NiAs structure was reported (Fig. 4.2), with (depending on the temperature) two different phases and slight deviations from the ideal structure in the form of Nb atom-trimerization, giving rise to a $\sqrt{3} \times \sqrt{3}$ R30° superstructure [201]. The NiAs structure can be considered as the TMDC 1T-phase (see Fig. 2.1 in chapter 2), except lacking a vdW gap between the layers. This NiAs structure has for example also been reported for FeS compounds, including trimerization effects [202].

4.2 Intercalation of Magnetic Materials

Magnetism in TMDCs is a widely studied phenomenon, often reported to be the result of structural features, e.g. edges [203, 204], vacancies [205, 206] and the presence of impurities [207, 208]. One example of TMDCs claimed to feature intrinsic magnetic behavior are ultrathin V based compounds [209–214], although the magnetic ground state is reported to compete or correlate with a CDW phase [83, 215–218]. As mentioned in chapter 3, a tendency towards a spin density wave was predicted for monolayer H-NbS_2 [152], as well as the switching of magnetic states due to strain [153, 154]. Very recently, Kondo scattering was reported for 2H-NbS_2 bulk samples due to the presence of local 1T-layers [145]. Nevertheless, most TMDCs are not intrinsically magnetic and in the V based compounds the intrinsic magnetic behavior is still subject of discussion, calling for an alternative way of achieving magnetic interactions in TMDCs.

The intercalation of magnetic materials into the TMDC vdW gap has been discussed early on in literature [219]. The intercalated magnetic species usually occupy the octahedral sites in between the TMDC layers [190, 192, 220] and in the following a few examples of magnetically intercalated H-phase group V TMDCs are given, showing that magnetic interactions can indeed be successfully induced by intercalation. In the case of 2H-TaS_2, the incorporation of Fe was shown to introduce ferromagnetism [205, 221–229], while antiferromagnetism was demonstrated for Fe intercalation of 2H-NbS_2 [26, 190, 192, 230–233]. In the latter, information can be written to the material by switching the antiferromagnetic order with current pulses [26]. Cr intercalation in 2H-NbS_2 was found to cause a helimagnetic structure [192, 231, 232, 234, 235].

The variety of the introduced magnetic interactions demonstrates that the incorporation of other elements than those present in the TMDC is a wide playground to study intercalation effects.

4.3 Intercalation of 2D layer heterostacks

As described in chapter 2 and 3, electronic correlation effects like CDWs in TMDCs often change upon thinning down materials to the monolayer limit, as evident for NbS_2 featuring a 3×3 CDW in the monolayer (see manuscript in chapter 7]) but not in the bulk. The peculiar properties of monolayer materials has raised the interest into stacking single 2D layers of different composition, e.g. different semiconducting TMDCs, which has become an important field of research [31, 32]. Incorporation of material into the vdW gap of such 2D layer heterostacks by intercalation acts as a strong lever to tune the properties of such compounds. In literature, a lot of theoretical studies regarding the intercalation of heterostacks with a strong focus on Li intercalation for energy storage are available [111, 236–241], but as of yet, only few experimental works on the electrochemical Li intercalation of MoS_2/Gr/h-BN, MoS_2/h-BN and h-BN/Gr heterostacks exist [242–244]

The procedure of electrochemical heterostack intercalation is extended in the manuscript of chapter 8 to the post-growth intercalation of a H-NbS_2 monolayer, resting on a layer of Gr on Ir(111), by *d*-metals under UHV conditions, thereby greatly enlarging the possibilities to tune the properties of such hetero-compounds. The procedure is conducted both for native metal atoms (self-intercalation by Nb), as well as for the chemically dissimilar species Fe.

CHAPTER 5

Non-Collinear Magnetism at Surfaces

In this chapter, the basic principles of non-collinear magnetism in the 2D limit are discussed, necessary to understand the results presented in the manuscript of chapter 9 regarding the non-collinear spin structure in an ultrathin Fe film on Ir(110). The first part focuses on the most important magnetic surface interactions as well as on the role of the substrate. The second part then is a discourse on different non-collinear spin systems discussed in literature.

Magnetism plays an important role in the field of information storage. One long known example are hard disk drives (HDDs), encoding information in bits of possible states "0" and "1". Bits in this case consist of ferromagnetic domains, magnetized in two different directions. These HDDs reach information densities of 155 Gbit/cm^2 [44], but the density is partly restricted by the super-paramagnetic limit, determining the minimum size of magnetic domains [43]. Trying to overcome the limitations in information storage, concepts like the so called "magnetic racetrack memory" have been proposed [42], utilizing non-collinear spin configurations of magnetic domains in 1D nanowires. Also other non-collinear magnetic structures like skyrmions in ultrathin films are of interest for spintronic applications, including the realization of the mentioned racetrack memory [40,41]. The stabilizing interactions and mechanisms of non-collinear magnetism in general are therefore of high relevance for scientific research [33–35,245].

5.1 Magnetic Interactions and the Role of the Substrate

Non-collinear spin structures are the result of different magnetic interactions acting on magnetic spin moments $\mathbf{S}_i$ placed at site i in an ordered atomic configuration. In the following the description will be restricted to interactions most relevant for the results in the manuscript of chapter 9.

The first important interaction is the isotropic Heisenberg exchange, mediated by the hopping of itinerant spin-polarized electrons [33, 246]. It is a consequence of Coulomb interaction and the Pauli exclusion principle, and is determined by the Heisenberg Hamiltonian:

$$\mathcal{H}_{\text{exc}} = -\sum_{i,j}{}' J_{ij}\mathbf{S}_i \cdot \mathbf{S}_j. \tag{5.1}$$

$\sum{}'$ here and in the following denotes the summation over unequal indices. Heisenberg exchange favors the collinear alignment of magnetic moments, with the interaction term $J > 0$ in the case of ferromagnetism and $J < 0$ in the case of antiferromagnetism. The ferromagnetic case is illustrated in Fig. 5.1 (a) for the case of a 1D chain of atoms featuring magnetic spin moments. In a scenario in which J_1 is positive for the nearest-neighbor- and J_2 is negative for the next-nearest-neighbor distance, the competition between these two interactions renders the system frustrated if $J_1 < J_2/4$ [247]. The condition is generally dependent on the distance from the magnetic spin moment $\mathbf{S}_1$ by $J_1 < J_N/N^2$, with $N = 1$ being the nearest-neighbor and $N = 2$ being the next-nearest-neighbor etc.. For the given case of the next-nearest-neighbor with $N = 2$ and $J_1 < J_2/4$, the resulting spin texture features a canted alignment of magnetic moments as illustrated in Fig. 5.1 (b).

When the inversion symmetry assumed in the Heisenberg model is absent, for example at interfaces, spin-orbit coupling (SOC) connecting the lattice with the spin symmetry comes into play. The resulting interaction is named after Dzyaloshinskii and Moriya [Dzyaloshinskii-Moriya interaction (DMI)], who described it in 1958 and 1960 correspondingly [248,249]. DMI describes spin-orbit scattering of electrons in a system lacking inversion symmetry. It is given as a cross product of two magnetic spin moments $\mathbf{S}_i$ and $\mathbf{S}_j$:

$$\mathcal{H}_{\text{DMI}} = -\sum_{i,j}{}' \mathbf{D}_{ij}(\mathbf{S}_i \times \mathbf{S}_j). \tag{5.2}$$

$\mathbf{D}_{ij}$ is the Dzyaloshinskii vector (or DMI vector) proportional to the strength of SOC and $(\mathbf{S}_i \times \mathbf{S}_j)$ is the vector chirality between two magnetic spin moments. The cross product favors orthogonal alignment of spin moments, thereby reducing the total energy of the system and leading to non-collinear magnetic structures [33, 250]. The DMI can be understood as a 3-site indirect exchange mechanism between an atom with large SOC (generally heavy atoms with a large Z) and two magnetic spin moments $\mathbf{S}_1$ and $\mathbf{S}_2$ [36, 251]. The situation is illustrated in Fig. 5.1 (c), with the interaction causing canting of magnetic moments and therefore a non-collinear magnetic structure. In the case of an ultrathin magnetic film at an interface, the direction of the DMI vector $\mathbf{D}_{ij}$ is determined by the substrate symmetry and the magnitude by the strength of SOC [249]. It is therefore clear that the choice of substrate is decisive for the role DMI plays for magnetic structures at surfaces.

As described above, non-collinear magnetic structures and canting of magnetic moments can

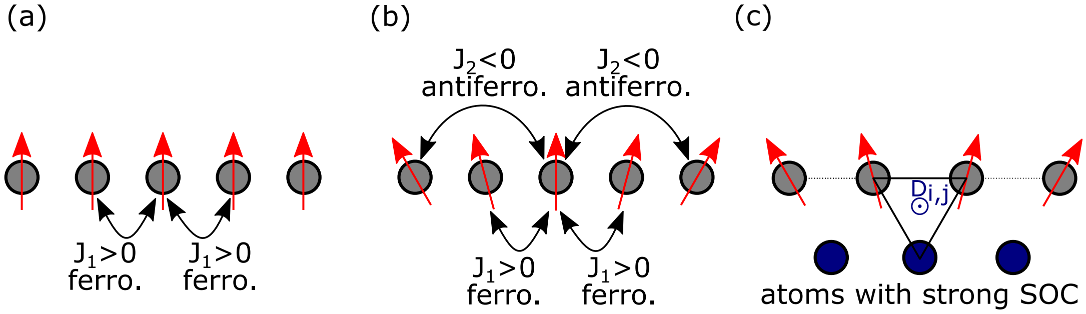

Figure 5.1: Illustration of magnetic interactions in a 1D chain of atoms possessing magnetic spin moments. (a) Ferromagnetic Heisenberg interaction causing a collinear alignment of magnetic moments. (b) Heisenberg interaction with partially antiferromagnetic coupling leading to canted alignment of magnetic moments. (c) DMI also causing canting.

generally also arise from Heisenberg exchange, but in many cases the simple bilinear Heisenberg term (equation 5.1) may not be a sufficient explanation and for 2D magnets on certain substrates, higher-order terms have to be considered [245,252–258]. For spins $S \geq 1/2$, a contribution from the interplay of four magnetic spin moments at four sites, called 4-spin-interaction, arises from fourth-order perturbation theory:

$$\mathcal{H}_4 = -\sum_{i,j,k,l}{}' K_{ijkl}[(\mathbf{S}_i \cdot \mathbf{S}_j)(\mathbf{S}_k \cdot \mathbf{S}_l) + (\mathbf{S}_i \cdot \mathbf{S}_l)(\mathbf{S}_j \cdot \mathbf{S}_k) - (\mathbf{S}_i \cdot \mathbf{S}_k)(\mathbf{S}_j \cdot \mathbf{S}_l)]. \tag{5.3}$$

In case of larger spins $S \geq 1$, two more higher-order terms are important. One is the biquadratic exchange. The term arises from fourth-order perturbation theory for four magnetic spin moments on two lattice sites (two orbitals per site) as:

$$\mathcal{H}_2 = -\sum_{i,j}{}' B_{ij}(\mathbf{S}_i \cdot \mathbf{S}_j)^2. \tag{5.4}$$

The other is the interplay of four magnetic spin moments at three sites (one site featuring two orbitals and two other sites featuring one each), called 3-spin-interaction:

$$\mathcal{H}_3 = -2\sum_{i,j,k}{}' Y_{ijk}(\mathbf{S}_i \cdot \mathbf{S}_j)(\mathbf{S}_i \cdot \mathbf{S}_k). \tag{5.5}$$

The extended Heisenberg Hamiltonian can be written as [245]:

$$\mathcal{H}'_{\text{exc}} = (\mathcal{H}_{\text{exc}} + \mathcal{H}_4)\{\text{for } S \geq 1/2\} + (\mathcal{H}_2 + \mathcal{H}_3)\{\text{for } S \geq 1\}. \tag{5.6}$$

The higher-order terms scale with the magnetic moment to fourth-order and because of that, their relative importance increases the larger the moments are [245]. The terms can lift the degeneracy of magnetic states in the Heisenberg model.

5.2 Non-Collinear Spin Systems

The competition of different magnetic interactions can stabilize non-collinear spins textures in 2D magnetic films at surfaces. As an example, the coexistence of exchange interaction and DMI in a Mn monolayer on W(110) led to the observation of chiral magnetic order [33]. The spin texture is a spin helix, where the magnetization rotates as a function of position from out-of-plane to in-plane.

Another famous example of a non-collinear spin structure at a surface, driven by the interplay and competition of Heisenberg exchange and DMI, is the square nanoskyrmion lattice in an Fe monolayer on Ir(111) [35]. A nanoskyrmion lattice is an array of skyrmions, with skyrmions being vortex-like, topologically protected spin configurations with chiral boundaries and particle-like properties [37–39]. A simple sketch of such a skyrmion structure is shown in Fig. 5.2 (a). In the case of the nanoskyrmion lattice, in addition to the Heisenberg exchange and DMI an additional interaction participates, namely the 4-spin beyond-Heisenberg interaction. The total Hamiltonian is given by [35]:

$$\begin{aligned}\mathcal{H} = &-\sum_{i,j}{}' J_{ij}\mathbf{S}_i \cdot \mathbf{S}_j - \sum_{i,j}{}' \mathbf{D}_{ij}(\mathbf{S}_i \times \mathbf{S}_j) \\ &- \sum_{i,j,k,l}{}' K_{ijkl}[(\mathbf{S}_i \cdot \mathbf{S}_j)(\mathbf{S}_k \cdot \mathbf{S}_l) + (\mathbf{S}_i \cdot \mathbf{S}_l)(\mathbf{S}_j \cdot \mathbf{S}_k) - (\mathbf{S}_i \cdot \mathbf{S}_k)(\mathbf{S}_j \cdot \mathbf{S}_l)].\end{aligned} \tag{5.7}$$

The two first terms establish the non-collinear character of the spin texture and the third term provides the directionality of the square lattice. The skyrmion lattice with a periodicity of about 1 nm in Fe/Ir(111) has been shown to be very stable and difficult to drive into a different topological state. The influence of DMI and the interplay of interactions can be tuned not only by the choice of substrate, but also by adding a second interface in the form Pd layer on top of the Fe/Ir(111) layer [259]. An additional contribution of the DMI arising from the second interface reduces the total DMI in the Fe layer, effectively changing the ground state to a Néel type spin helix. The resulting ground state is soft and upon applying an external magnetic field, the spin helix breaks up into a hexagonal skyrmion lattice, eventually ending up in a field-polarized state. These examples from literature illustrate the important role the competition of magnetic interactions plays to stabilize a non-collinear spin texture and how to tune the magnetic interactions in order to drive the lowest energy state into a different minimum.

The spin rotation in non-collinear spin textures can be of different types. In the skyrmion shown in Fig. 5.2 (a), the magnetization rotates as a function of position along the radial direction from pointing down in the center to pointing up around. By following the displayed cross sections shown in Fig. 5.2 (b), one can make out that the type of spin rotation is the so called Néel type, with the spins rotating around an axis normal to the propagation direction. For interfacial DMI-driven spin canting, this type of rotation is conditioned by the Moriya rules [249], valid for high-symmetry surfaces. Fig. 5.2 (c) displays a C_{3v}-symmetry surface with the resulting DMI vectors being in-plane and perpendicular to the bond directions of the nearest-neighbors. The resulting spin textures rotate around an axis that is normal to the propagation direction and the rotation direction is determined by the sign of the DMI vector, resulting in chiral spin textures. The $C_{3\text{v}}$-symmetry surface therefore conditions a skyrmion as shown in Fig. 5.2 (a), being exclusively of Néel character in all directions. The before described skyrmion lattice on the C_{3v} symmetry substrate Ir(111) displays such a case. Many other (partially) DMI-driven Néel type rotation systems where found such as spin helices [260, 261], chiral domain walls [262, 263] and the before described skyrmionic structures [35, 264, 265].

Also in ultrathin films with weak DMI, non-collinear spin textures of Néel type can be stabilized, in this case dominated by the competition of short- and long-range exchange interactions driving the textures. One example are spin helices in thin Fe films on the relatively light 3*d*-metal substrate Cu(111), featuring weak SOC and therefore weak DMI [247, 266]. Known heavy element containing systems featuring exchange-driven non-collinear structures are for example Mn/W(100) [250]and fcc-Rh/Fe/Ir(111) [267]. Nevertheless, in both cases residual contributions of DMI are assumed to be present, driving the present noncollinear state to a monodirectional Néel type rotation. In the case of hcp-Rh/Fe/Ir(111) a collinear ↑↑↓↓-spin structure due to higher-order exchange interactions is found [267], but DMI induces a slight spin canting in the ground state. A similar higher-order exchange-driven ↑↑↓↓-spin structure has been reported for Fe/Rh(111) [268].

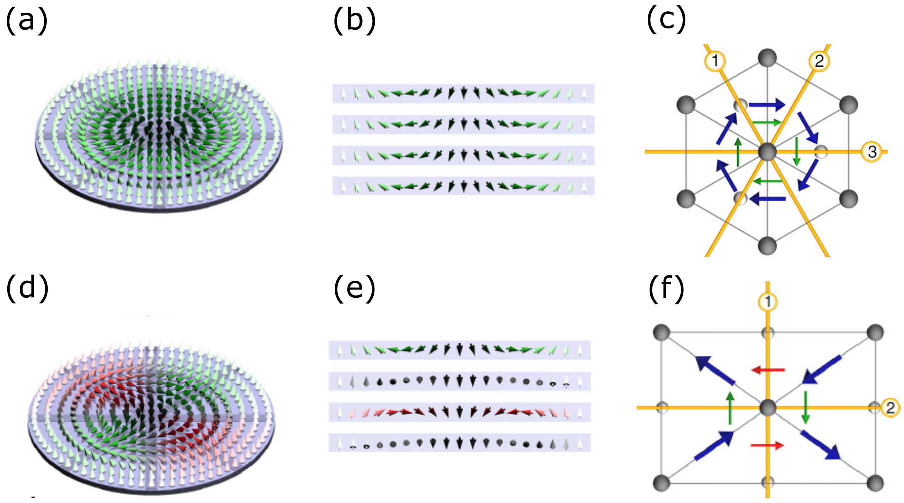

Figure 5.2: Skyrmionic spin structures and symmetry-dependent DMI vectors. (a) Spin texture of a Néel type skyrmion. (b) Cross section displaying the type of spin rotations present in (a). (c) DMI vectors in the case of a $C_{3\text{v}}$-symmetry surface. (d) Spin texture of an antiskyrmion. (e) Cross section displaying the type of spin rotations present in (d). (f) DMI vectors in the case of a $C_{2\text{v}}$-symmetry surface. Figure adapted from Ref. [51].

The other type of spin rotation, the so called Bloch type, where spins rotate around the axis of propagation, is not explainable in the picture of interface induced DMI for the above stated reasons. Rotations of this kind are only found in systems featuring reduced influence of DMI, i.e. thicker films beyond the monolayer limit. One example are domain walls featuring Bloch, Néel or even mixed wall character [269]. In these thicker films, interlayer exchange like the Ruderman-Kittel-Kasuya-Yosida (RKKY) interaction can favor a Bloch rotation, while in other cases only a Bloch component is introduced with magnetostatic interactions still favoring a Néel rotation [270], leading to a mixed Bloch-Néel state. Also Bloch type skyrmions have been routinely observed, for example in bulk MnSi [34], as well as $Fe_{0.5}Co_{0.5}Si$ [271]. So far, there is no evidence for Bloch type spin textures in ultrathin films.

One possible application of skyrmions is the above mentioned racetrack memory, utilizing skyrmions as information carriers (bits) in a magnetic nanoribbon [36, 41]. These proposed devices utilize the fact that, just as domain walls [272], skyrmions can be moved by an in-plane spin-polarized current, utilizing effects like spin-orbit-torque- and spin-transfer-torque [37, 38, 272–276]. Upon applying such a current, the skyrmions are subject to the skyrmion Hall effect [45, 46], similar to the well know Hall effect acting on charges, causing them to move to the side of the nanoribbon and eventually annihilate.

One proposed way to overcome this problem is to utilize so called antiskyrmions. Antiskyrmions are skyrmionic structures featuring both Bloch- and Néel rotations within a single unit as displayed in Fig. 5.2 (d). In the cross section of Fig. 5.2 (e) it is shown, that the type of spin rotation depends on the direction within the skyrmionic structure, in this case featuring the presence of both rotation types. The motivation behind the suggestion of antiskyrmions is that they feature different dynamics compared to skyrmions [277], e.g. a vanishing transverse Hall movement upon choosing the correct current direction [47, 48]. Antiskyrmions have been observed first in Heusler materials [49, 50]. They feature a break of cylindrical symmetry and a topological charge of $Q = 1$ in contrast to the topological charge of $Q = -1$ of regular skyrmions [51]. Another advantage is that antiskyrmions are relatively stable temperature wise [49].

The possible presence of antiskyrmions in ultrathin films, of relevance for the application in racetrack memories, has been treated in the theoretical work of Hoffmann et al. [51]. Since DMI in systems with C_{3v} symmetry is unidirectional along the azimuthal angle, antiskyrmions in this case have higher formation energy and are rendered unstable against skyrmions. Surfaces with lower symmetry, for example C_{2v} displayed in Fig. 5.2 (f), could offer a way of achieving DMI-driven skyrmions with both Bloch and Néel rotations. In the C_{2v} case the DMI vector directions differ in the high-symmetry directions, causing the spins to display opposite Néel chiralities along the two mirror symmetry axes (red and green arrows in the directions 1 and 2 in Fig. 5.2 (f). As the Moriya rules do not hold for low symmetry interfaces, an effective DMI appears along the nearest-neighbor directions, giving rise to Bloch features along these axes. In the work of Hoffmann et al. [51], the example of the spin structure in an Fe bilayer film on a bcc W(110) surface is calculated. Including Heisenberg interaction, DMI and anisotropy, this leads to an antiskyrmionic structure.

Motivated by these theoretical findings, in the manuscript of chapter 9 the spin texture in ultrathin Fe films on the $C_{2\mathrm{v}}$-symmetry surface of Ir(110) is investigated.

CHAPTER 6

Scanning Tunneling Microscopy for the Investigation of Surface Magnetism

This chapter serves as an introduction to spin-polarized STM, a method newly introduced at the University of Cologne. STM and STS are already well established experimental methods in the II. Institute of Physics and it should be noted that some limited spin-polarized measurements were conducted in our group before, using Cr bulk tips in a low-temperature system [278], but without an outer magnetic field being available. In the first part of this section, the basic concept of spin-polarized STM is presented and in the second part the technical features of the UNISOKU USM1300 system, newly set-up at the University of Cologne in 2018, are discussed.

In the picture of quantum mechanics, the propagation of a wave function through a potential barrier is called quantum mechanical tunneling effect. It was first described by Bardeen in 1960 [279]. On the basis of this effect, Binning and Rohrer developed the STM [280], which awarded them the Nobel prize in 1986. Ever since the invention, STM revolutionized the field of surface science and it is widely used in many aspects of research. The tunneling effect is triggered by bringing a metallic tip into the close vicinity of a conducting surface and applying a bias voltage between them. Due to the particle-wave behavior, electrons can tunnel through the vacuum barrier between tip and sample. The resulting tunneling current presents a strong distance dependence, thereby surfaces can be characterized on the atomic scale. Provided that tip and sample are magnetic, the concept of STM can be extended to spin-polarized STM (SP-STM). Here, the tunneling current is polarized in spin and information about the magnetic state of the sample can be obtained in real space with sub-nm resolution. The concept of SP-STM is discussed in following section.

6.1 Concept of Spin-Polarized Scanning Tunneling Microscopy

The following chapter loosely follows the description of SP-STM by Wortmann et al. [281] and the review article of Wiesendanger [282].

To understand the concept of SP-STM, first the situation of non-spin-polarized STM is considered. The current between a metallic tip and a conducting surface under an applied bias voltage in the formalism of Bardeen [279] is given by [283]

$$I = \frac{2\pi e}{\hbar} \sum_{\mu,\nu} f(E_\mu)[1 - f(E_\nu + eV)]|M_{\mu\nu}|^2 \delta(E_\mu - E_\nu), \tag{6.1}$$

where $f(E)$ is the Fermi function, $E_{\mu,\nu}$ are the energies of tip and sample states, V is the applied bias voltage and the δ-function describes the conservation of energy in the case of elastic tunneling. $M_{\mu\nu}$ is the tunneling matrix element, proportional to the tunneling transmission coefficient T of the tunneling process through the barrier. The tunneling matrix element can be expressed as:

$$M_{\mu\nu} = -\frac{\hbar^2}{2m} \int dS(\psi_\mu^* \nabla \psi_\nu - \psi_\nu \nabla \psi_\mu^*). \tag{6.2}$$

ψ_μ is the wave function of the tip states and ψ_ν the wave function of the sample states. The integral is evaluated over the surface S lying within the vacuum barrier region in between the two electrodes. Since the atomic configuration of the tip and therefore ψ_μ is generally not known, Tersoff and Hamann [283, 284] used a simple spherical geometry model for the tip apex, with an s-wave-like function $\psi_\mu = \frac{1}{R} e^{-\kappa R}$ with tip radius R and decay length κ. The approach also considers the limit of small bias voltages and low temperatures, leading to the tunneling current expression

$$I \propto n_\mathrm{s}(E_\mathrm{F}, \mathbf{r}_0) n_\mathrm{t}(E_\mathrm{F}) \cdot V e^{2\kappa R}, \tag{6.3}$$

where $n_\mathrm{s}(E_\mathrm{F}, \mathbf{r}_0)$ describes the local density of states (DOS) of the surface at the Fermi energy E_F and the center of the effective tip $\mathbf{r}_0$, and $n_\mathrm{t}(E_\mathrm{F})$ the local DOS of the tip at the Fermi energy. Metallic tips for example made of tungsten do not necessarily possess s-wave shape, but more likely d-wave shape [285–287] and STM measurements are usually conducted at a finite bias voltage. Therefore one can consider a more general expression for the current, assuming the bias voltage as a simple energy shift and an energy-dependent transmission coefficient $T(E, eV)$, containing the tip-dependent tunneling matrix elements M. This leads to the following expression for the current with all energies being relative to the Fermi energy E_F:

$$I \propto \int_0^{eV} n_\mathrm{t}(\pm eV \mp E) n_\mathrm{s}(E) T(E, eV) dE. \tag{6.4}$$

A particular case of quantum mechanical tunneling is the spin-dependent/spin-polarized tunneling. The effect relies on the conservation of spin in the tunneling process. It was first described for a ferromagnet-oxide-superconductor tunnel junction by Tedrow and Merservey in 1971 [288, 289] and for tunneling through an insulating barrier between two ferromagnetic electrodes by Julliere in 1975 [290]. The tunneling in these compounds is dependent on the spin states of the two electrodes. Spin-polarized tunneling can be introduced to the situation in the STM picture by replacing the tip and sample wave functions by spinors with

$$\psi_\mu^{\mathrm{t}} = \begin{pmatrix} \psi_{\mu\uparrow}^{\mathrm{t}} \\ 0 \end{pmatrix} \text{ or } \psi_\mu^{\mathrm{t}} = \begin{pmatrix} 0 \\ \psi_{\mu\downarrow}^{\mathrm{t}} \end{pmatrix}, \tag{6.5}$$

which describes the bilinear spin state ↑ , ↓ of a ferromagnetic tip and

$$\psi_\nu^{\mathrm{s}} = \begin{pmatrix} \psi_{\nu\uparrow}^{\mathrm{s}} \\ \psi_{\nu\downarrow}^{\mathrm{s}} \end{pmatrix} \tag{6.6}$$

in the case of the sample. The fact, that the quantization axes of tip and sample are not necessarily aligned causes the spin-mixed character of the sample wave function. Assuming the simple picture of an *s*-wave-like tip as described above, Wortmann et al. [281] derive an expression for the total current at the tip position $\mathbf{r}_0$ with the applied bias voltage V, as a combination of a non-spin-polarized current component $I_0(\mathbf{r}_0,V)$ and the spin-polarized current component $I_{\mathrm{sp}}(\mathbf{r}_0,V,\theta)$:

$$I(\mathbf{r}_0,V,\theta) = I_0(\mathbf{r}_0,V) + I_{\mathrm{sp}}(\mathbf{r}_0,V,\theta) = \frac{4\pi^3 C^2 \hbar^3 e}{\kappa^2 m^2}[n_{\mathrm{t}}\tilde{n}_{\mathrm{s}}(\mathbf{r}_0,V) + \mathbf{m}_{\mathrm{t}}\tilde{\mathbf{m}}_{\mathrm{s}}(\mathbf{r}_0,V)]. \tag{6.7}$$

$\mathbf{m}_{\mathrm{t}}$ is the vector of the spin-polarized local DOS of the tip and $\tilde{\mathbf{m}}_{\mathrm{s}}$ the vector of the energy-integrated spin-polarized local DOS of the sample:

$$\tilde{\mathbf{m}}_{\mathrm{s}}(\mathbf{r}_0,V) = \int_0^{eV} \mathbf{m}_{\mathrm{s}}(\mathbf{r}_0,E)dE. \tag{6.8}$$

In the non-spin-polarized part, n_{t} is the local DOS of the tip and $\tilde{n}_{\mathrm{s}}$ the energy-integrated local DOS of the sample:

$$\tilde{n}_{\mathrm{s}}(\mathbf{r}_0,V) = \int_0^{eV} n_{\mathrm{s}}(\mathbf{r}_0,E)dE. \tag{6.9}$$

Taking the derivative of equation 6.7 eliminates the integration and leads to the differential conductance term:

$$dI/dV(\mathbf{r}_0,V) \propto [n_{\mathrm{t}}n_{\mathrm{s}}(\mathbf{r}_0,E_{\mathrm{F}}+eV) + \mathbf{m}_{\mathrm{t}}\mathbf{m}_{\mathrm{s}}(\mathbf{r}_0,E_{\mathrm{F}}+eV)] = [1 + P_{\mathrm{t}}P_{\mathrm{s}}(\mathbf{r}_0,E_{\mathrm{F}}+eV)\cdot\cos(\theta)]. \tag{6.10}$$

$P_{\mathrm{t,s}} = \frac{m_{\mathrm{t,s}}}{n_{\mathrm{t,s}}}$ is the polarization of tip and sample respectively, with $n_{\mathrm{t,s}}$ being the non-spin-polarized

DOS and $m_{t,s} = m^{\uparrow}_{t,s} - m^{\downarrow}_{t,s}$ the spin-polarized DOS at the Fermi energy in the case of a bilinear spin system. θ describes the angle between the tip and sample magnetization axes.

From the cosine function it is clear that the spin-polarized conductance becomes large when the magnetization of tip and sample are aligned and becomes zero for a 90° angle. This is the basic principle of SP-STM and is illustrated for the case of a simple Stoner model of ferromagnetism in Fig. 6.1, showing that tunneling between tip and sample majority states of same polarization [Fig. 6.1 (a)], gives a larger spin-polarized signal I_{SP} than tunneling between oppositely polarized majority states [Fig. 6.1 (b)]. Utilizing this difference in spin-polarized signal strength, SP-STM enables to detect spatial changes of the surface magnetization on the atomic scale.

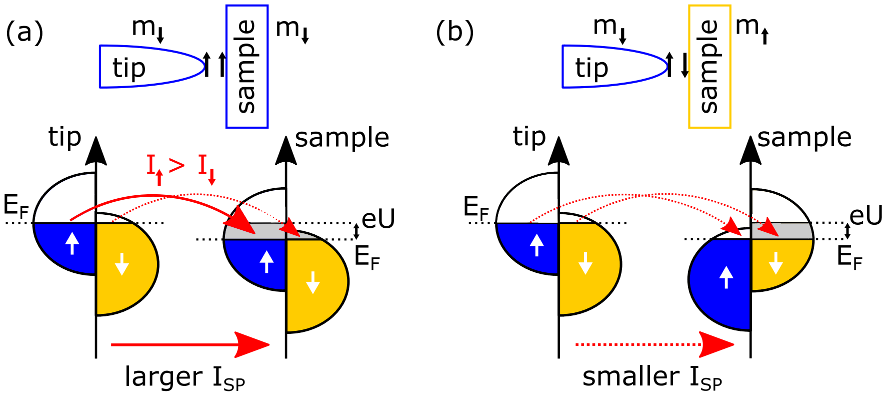

Figure 6.1: Stoner model of ferromagnetism describing the principle of spin-polarized tunneling. (a) Both tip and sample majority polarization directions are parallel. In this case the occupied majority (minority) states of the tip tunnel into unoccupied majority (minority) states of the sample, leading to a large tunneling current. (b) Tip and sample majority polarization directions are antiparallel. The occupied majority (minority) states of the tip tunnel into unoccupied minority (majority) states of the sample, causing a small tunneling current I_{SP}. $m_{\uparrow,\downarrow}$ denotes the magnetization direction of tip and sample. Figure partially adapted from Ref. [291] and Ref. [282].

Regarding different modes of operation, SP-STM has first been applied in constant current mode [292–295], utilizing bulk ferromagnetic tips. This mode is problematic though, as in constant current mode, the feedback loop of the STM varies the distance between tip and sample to keep the current on a constant level. This can lead to a mixing of topographic and spin-polarized information, making interpretation of the results difficult. Also the integration of the current signal in constant current mode is problematic, since depending on the integration range, for some energies the spin-polarization can change sign, leading to a reduced total spin-polarized signal upon integration. The integration becomes especially important for larger bias voltages.

One way to to achieve magnetic resolution independent of the topography, is the spin-resolved differential conductance dI/dV mode. The dI/dV signal, as evident from equation 6.10, is directly proportional to the spin-polarized DOS of the sample at the energy $E_F + eV$, different to the current itself being proportional to the energy-integrated DOS. The differential conductance can be measured utilizing a lock-in amplifier, modulating the bias voltage and detecting the derivative dI/dV from the resulting current modulation [296]. The mode is especially useful in case of tunneling into a strongly energy-dependent spin-polarized surface state [297, 298]. It should be noted, that even though the integration problem is sorted out, the polarization alignment of tip and sample can still be strongly energy-dependent, so that for a certain detected spin-polarized signal, only the magnetization alignment at that selected energy (bias voltage) can be assessed.

Regarding the tips for SP-STM, ferromagnetic bulk tips were used first [294]. Such tips [illustrated in Fig. 6.2 (a)], made for example of Fe, have the disadvantage of sizable magnetic stray fields that can possibly influence and perturb the magnetic structure of the surface. Another disadvantage is the high saturation magnetization, making the change of magnetization axis by an applied field very difficult. As an alternative, antiferromagnetic bulk tips can be used, for example made of Cr [294, 299], or MnNi alloys [300]. The expected antiferromagnetic configuration is illustrated in Fig. 6.2 (b). In an ideal antiferromagnetic tip the total magnetic moment is nearly compensated and only the apex atom determines the tip magnetization axis, therefore the resulting stray field is negligible. Another solution is to utilize a nonmagnetic tip and cover it by a thin film of magnetic material in situ under UHV conditions [298, 301], as displayed in Fig. 6.2 (c). Generally, the magnetization direction of a covering film is determined by local surface- and interface anisotropies, but can be forced into a certain direction by an applied outer magnetic field [33, 302], as shown in Fig. 6.2 (c). Here, the stray fields are given by the thickness of magnetic material and may be reduced in comparison to ferromagnetic bulk tips. Like in the case of bulk tips, the coating with an antiferromagnetic film like Cr can be feasible [303, 304]. Realistic STM tips unfortunately do not have the shapes given by the illustrations of Fig. 6.2 (a)-(c). Instead of a single apex, a typical tip can contain a collection of apices [Fig. 6.2 (d)] and the one closest to the surface determines the magnetic behavior. Thanks to the small size of these apices the total magnetic moment is relatively small and it has been shown that such a nano apex can feature superparamagnetic behavior [305], enabling to rotate the tip magnetization by an applied outer field, while still being able to conduct nonmagnetic measurements with the same tip when no field is applied.

The method of SP-STM is applied in the manuscript of chapter 9 for the investigation of surface magnetism.

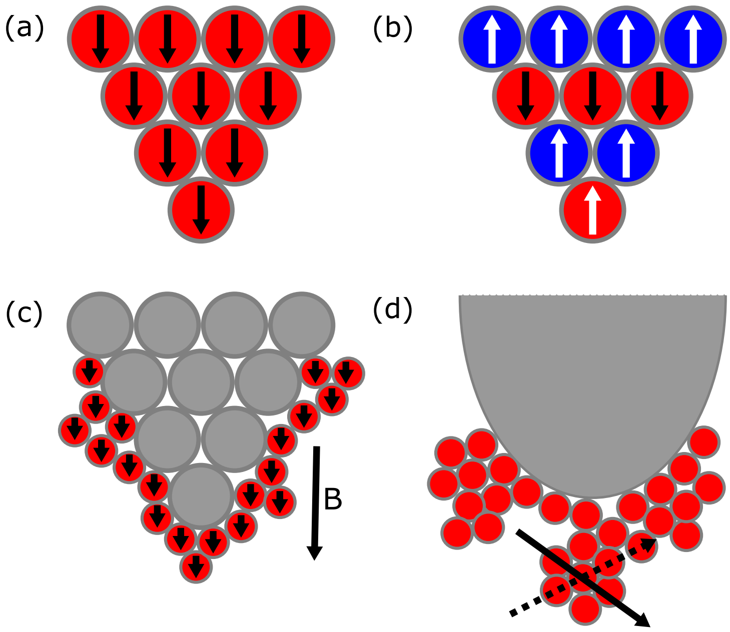

Figure 6.2: Different types of magnetic STM tips. (a) Ferromagnetic bulk tip, (b) Antiferromagnetic bulk tip, (c) Nonmagnetic tip covered by a magnetic film. The black arrow marks an outer magnetic field. (d) Nonmagnetic tip covered by a magnetic film featuring several apices representing sometimes superparamagnetic nanoclusters. Figure partially adapted from Ref. [282].

6.2 The UNISOKU USM1300 System

To further extend the range of surface science investigation methods at the University of Cologne, the UNISOKU USM1300 system was introduced in 2018, designated as MSTM in our group. It is a low-temperature UHV apparatus, enabling to conduct high-resolution STM and STS measurements at temperatures down to 0.4 K, utilizing a ^{4}He bath cryostat and an embedded ^{3}He cycle. It features a vector magnetic field of 9 T normal to the surface plane and 2 T in plane. In total, a field can be applied in any direction with a magnitude of 2 T. Main parts of the system are a load-lock chamber for sample transfer, a preparation chamber for sample synthesis, an exchange chamber and the cryostat hosting the STM itself, as well as the vector magnet. In the following a description of the different parts and features of the system is given, as well as examples of technical challenges that had to be sorted out during the setup process.

Sample Holders

Two types of sample holders are utilized in the system. The first type is made for electron beam (e-beam) heating and is the one used for the experiments in this thesis. The concept of the e-beam sample holders is shown in Fig. 6.3. Fig. 6.3 (a) displays the original configuration of the sample holders as supplied by UNISOKU. At the top of the sample holder, square hat-shaped

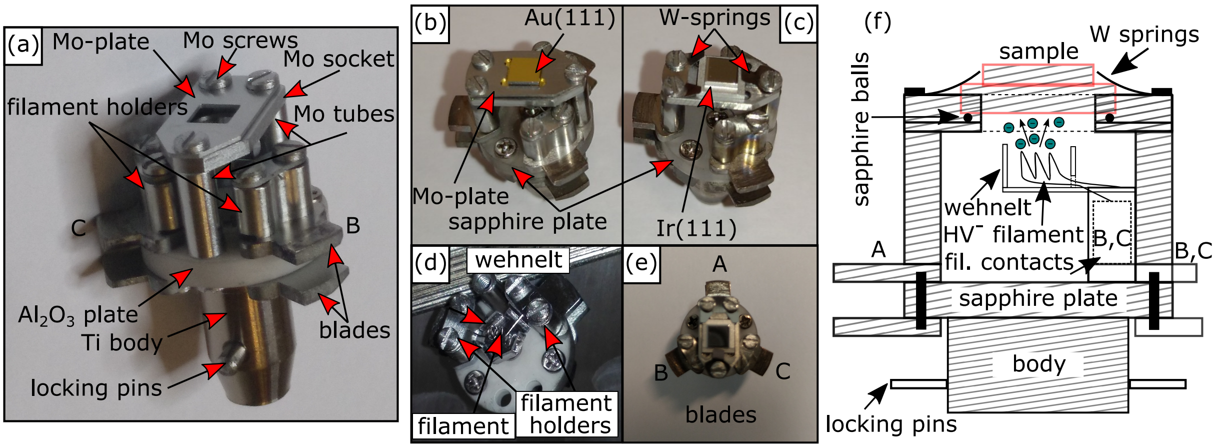

Figure 6.3: Layout of the e-beam sample holder. (a) Original configuration supplied by UNISOKU. (b) Mo plate featuring an enlarged cutout fixing an Au(111) crystal. (c) W springs fixing an Ir(111) crystal. In (b) and (c) the Al_2O_3 plate visible in (a) has been replaced by a sapphire plate. (d) Partially disassembled sample holder. Filament and Wehnelt are visible. (e) Contact blades for filament (B,C) and sample contact (A). (f) Drawing of the e-beam sample holder and heating principle.

crystal samples can be placed in a Mo socket. The samples are originally supposed to feature a base-width of 4×4 mm and a top-width of 2.5×2.5 mm, with a total thickness of 1.5 mm, and are then fixed by a Mo plate placed on top. To utilize larger crystals of base size 4.5×4.5 mm and top size 3×3 mm, both the cutouts of the Mo socket and the Mo top plate have been enlarged by us. The arrangement with the crystal being fixed by a Mo plate [Fig. 6.3 (b)], providing balanced pressure onto the sample, is fine for soft crystals requiring relatively low annealing temperatures during sample synthesis, like in case of the Au(111) crystal shown in (b). For higher annealing temperatures in the case of for example Ir(111), the Mo plate offers to much thermal conductivity and therefore thermal load to the sample holder. This causes sample holder screws to become loose very quickly and also causes excessive degassing of parts. Therefore two more changes were made: The Mo top plate was replaced by W springs pressing onto the crystal to minimize the amount of thermal contact and also to spring-load the top Mo screws, thereby avoiding loosening. Furthermore, the crystal was placed on three sapphire balls further decoupling it from the Mo socket. The modified configuration is shown in Fig. 6.3 (c) for the case of the mentioned Ir(111) crystal. The position of the sapphire balls can be seen in Fig. 6.3 (f).

As marked in Fig. 6.3 (a), below the part in which the sample is fixed, two double tubes hold the filament necessary for the e-beam heating process. The filament itself is visible in the partially disassembled sample holder in Fig. 6.3 (d). It is placed in a Ta Wehnelt, itself also fixed to one of the filament holders. Regarding the electrical contacts for the filament and the crystal, the sample holder features 3×2 blades [Fig. 6.3 (a) and (e)] that are the connection points in the manipulator and STM stage. The top row is marked A,B and C in Fig. 6.3 (e). Blade A contacts the sample and blades B and C are connected to the filament below the sample. The second row of blades is connected to the first row (A,B,C). The principle of heating is illustrated in Fig. 6.2 (f):

The sample resting on the sapphire balls (black) and fixed by W springs, is connected to blade A (ground) during the heating process. Below the sample, the filament and Wehnelt combination is connected to the blades B and C. Upon letting a current of up to 3 A flow from blade B to C, the filament starts to glow and emits electrons (green). By applying negative high voltage (HV^-) to the filament, electrons will move to the grounded sample and heat it to up to 1800 K. The electrons are focused towards the sample by the Wehnelt, which lies on the same HV potential as the filament.

Despite the modifications described above regarding the fixing of the samples, as a consequence of heating a significant amount of thermal power is transferred to the sample holder. On the lower side, it features a Ti body with two locking pins [Fig. 6.3 (a)]. The body and the pins display the point where the sample holders can be grabbed by transfer rods, as described later in this chapter. Ti is a much less heat resistant material than the Mo (and W) parts at the top. To restrict the amount of heat transfer, a white Al_2O_3 plate as originally provided by UNISOKU is visible in (a), decoupling the lower body of the sample holder thermally from the top part, as well as electrically decoupling the three blades and therefore sample and filament. It turned out that these plates tend to get covered by material like metal upon heating, as well as transmitting to much heat. For that reason they were replaced by sapphire plates as visible in Fig. 6.3 (b) and (c).

More detailed technical drawings of the improved sample holder parts can be found in Appendix B.

The second type of sample holders used in the system is the direct-current sample holder, applied to heat materials like semiconducting silicon wavers. The main difference compared to the e-beam sample holder is the absence of a filament. Here the sample is heated by letting a current flow directly from blade B to C while passing the sample and heating it up due to electrical resistance. The direct current sample holders are not used in this work and therefore not further described here.

Tip carriers

The tip carriers used in the system consist of a Cu body with a hole on the top and a threat on the backside [Fig. 6.4]. The hole at the top enables to fix wires of 0.5 mm diameter by two titanium screws from the site. Optimal tip length (part sticking out) is 3 mm. With the thread, the tip carriers can be screwed into the scanner piezo in the STM, as well as into several storage points. Also here the same kind of locking pins as on the sample holders for grabbing with transfer rods can be found.

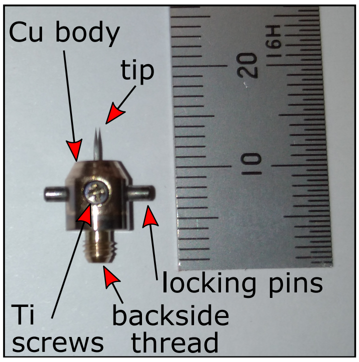

Figure 6.4: Tip carriers featuring a thread to fix them into the STM and other storage points.

Load-Lock

The Load-Lock (LL) is a fastly-pumped UHV chamber for sample transfer into- and out-of the UHV system. As shown in Fig. 6.5, part of the LL are a turbo molecular pump for evacuation, with the pressure being measured by an ion pressure gauge. The pump is parted from the LL by a pneumatic valve and a leak valve for venting the LL chamber is present. Samples and tips can be inserted from the outside into the LL through the quick-access door and can be stored in a garage module. After evacuating the LL to $p < 1 \cdot 10^{-7}$ mbar, the gate valve connecting the LL with the preparation chamber can be opened. By grabbing the sample or tip carriers with the transfer rod, they can be moved into the preparation chamber.

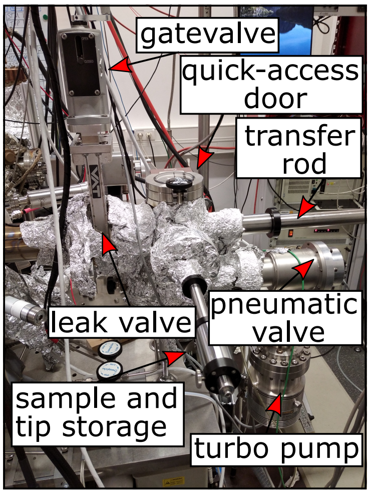

Figure 6.5: The Load-Lock chamber modules.

Preparation Chamber

The preparation chamber (prc) contains tools allowing sample and tip preparation. It features a 4-axis manipulator, resting on top of the prc. It consists of a Cu body, with a sample stage at the end [Fig. 6.6 (a)]. Further up there are garage slots to store samples and tips. The sample stage is shown in Fig. 6.6 (b). It contains three contacts to connect the blades A, B and C of the sample holders. Two connections are for the filament and one to ground the sample. Additionally, the manipulator temperature can be measured by a sensor. The sample stage can be tilted from vertical to horizontal by grabbing the turning knob with the prc transfer rod. In Fig. 6.6 (c) a sample holder locked into the sample stage is shown. The sample holder blades fit into the marked slots. It is then rotated clockwise so that the blades move under the fixing springs. A similar locking mechanism is used at every position the sample can be put in (garages, STM etc.). In the sample stage it is possible to conduct heating up to 1800 K with the e-beam sample holders, as well as heating with direct-current sample holders. The glowing sample can be seen on the front side of the heating stage [Fig. 6.6 (d)] and the sample temperature can be measured by aligning a pyrometer to the surface of the sample. The manipulator is movable in x,y and z direction plus a rotation angle θ and can be cooled by liquid N_2 and liquid He, enabling to prepare samples at 77 K and 4 K.

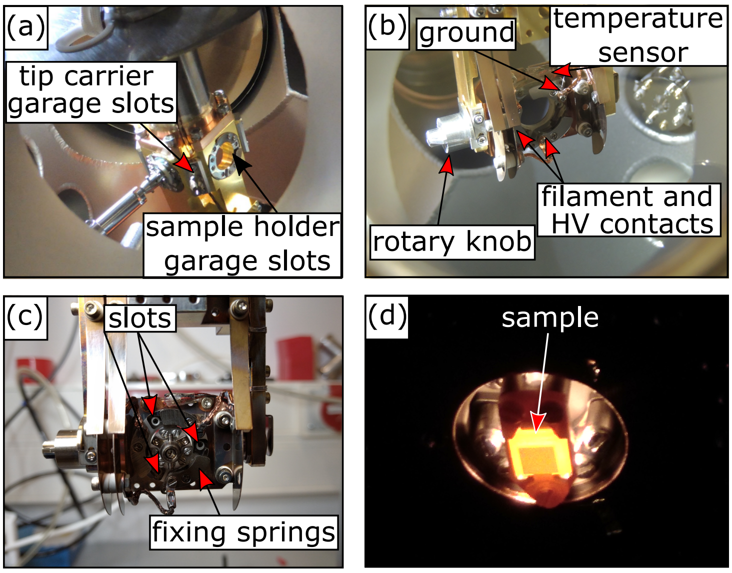

Figure 6.6: The manipulator in the prc. (a) Garage slots. (b) Sample stage layout. (c) Sample holder fixed into the sample stage. (d) Front view of a sample holder during e-beam heating.

A schematic top view layout of the prc is shown in Fig. 6.7. Attached are transferable quadruple- and triple-pocket e-beam evaporators, as well as quadruple- and double-pocket Knudsen cells. Gas dosing valves with a gas tube pointing to the sample stage are present, as well as a transfer rod to grab samples and tips to move them to the exchange chamber. For cleaning sample surfaces, an ion gun is used and there is a tip heater to anneal and clean STM tips. To calibrate evaporators and deposition rates, a quartz microbalance is available and a mass spectrometer for residual gas analysis is connected to the vacuum space. For surface investigation right after sample preparation, a low-energy electron diffraction (LEED) apparatus is present. The chamber is pumped by a turbo molecular pump parted by a pneumatic valve and an ion pump below the system (not shown). The base pressure of the prc is $p = 2 \cdot 10^{-10}$ mbar, measured by an ion pressure gauge. A gate valve identical to the one between the LL and the prc parts the latter from the exchange chamber.

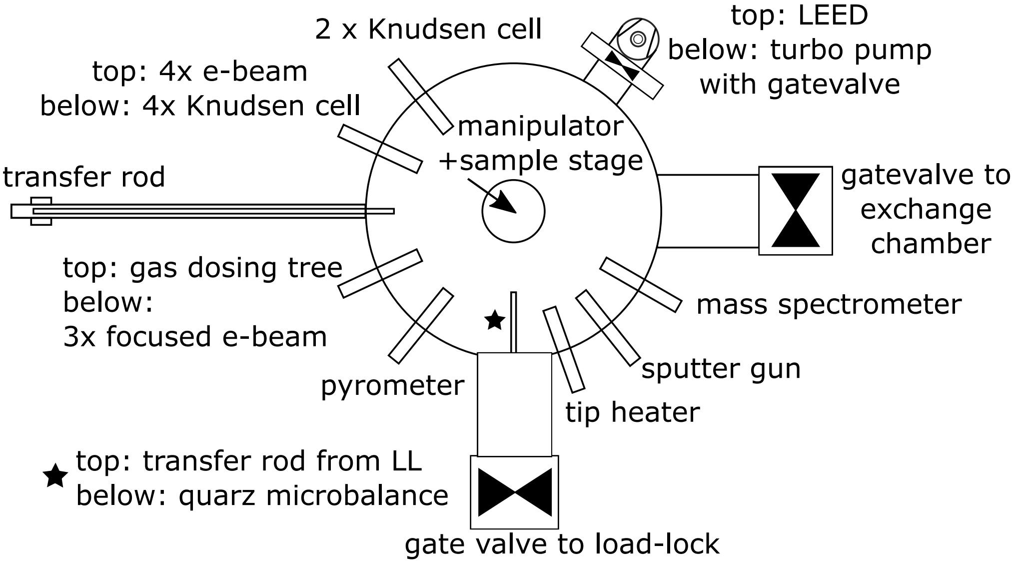

Figure 6.7: Schematic top view layout of the preparation chamber.

The Exchange Chamber

Connected to the prc is the exchange chamber (exc), located directly above the cryostat with the STM insert. A schematic top view layout can be seen in Fig. 6.8. The exc is separated from the prc and the STM insert by gate valves. A movable cleaving stage is used to cleave samples in situ. It can be cooled by liquid N_2 and liquid He for low-temperature cleaving. A vacuum suitcase is available, enabling to transfer samples from other labs to the MSTM system, without exposure to air. The exc is usually pumped by an ion pump (same as in the prc) and base pressure is $p < 2 \cdot 10^{-10}$ mbar. Additionally a turbo molecular pump is present if needed. Samples and STM tips prepared in the prc, as well as the He4 and He3 shields of the STM insert (described below), can be parked in the movable exc storage module. The STM transfer rod resting on top of the exc chamber is used to transfer tips and sample down into the STM. It is much longer than the transfer rods of the prc and the LL, since the distance down into the STM is much longer.

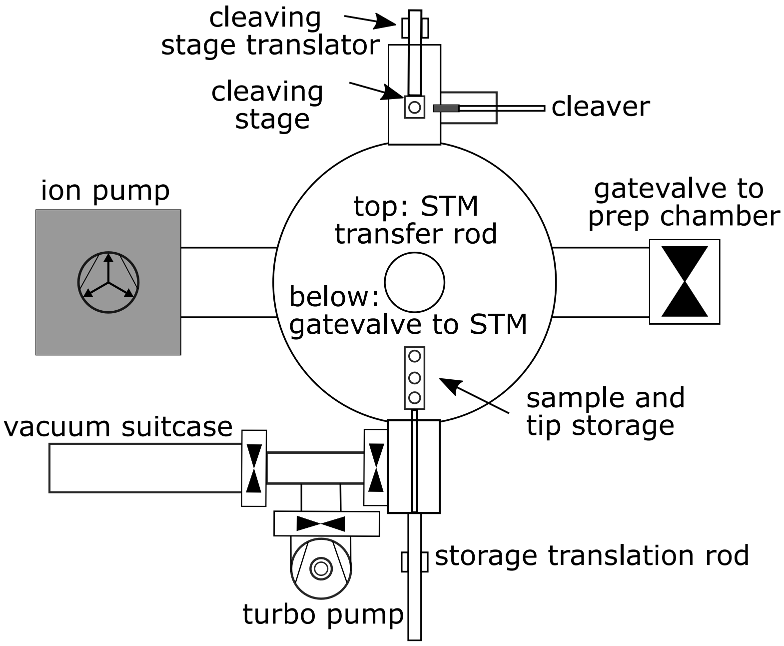

Figure 6.8: Schematic top view layout of the exchange chamber.

The STM Insert, ^{4}He Cryostat and ^{3}He Cycle

Below the exc, the cryostat and the STM insert are located. The STM insert is also a UHV space and is parted from the exc by a gate valve. It hosts the STM and is itself placed in a ^{4}He cryostat. The schematic layout of insert and cryostat is displayed in Fig. 6.9. The cryostat is filled with up to 100 L of liquid ^{4}He (T = 4.2 K). The lower part hosting the STM is surrounded by a magnet consisting of superconducting coils resting inside the He^4. Currents up to 100 A can be applied, resulting in magnetic fields up to 9 T normal to the sample surface (z-direction) and 2 T along the two directions parallel to the surface plane (x- and y-directions). A field can be applied in any direction with a magnitude of 2 T. The STM hangs at the end of the insert in UHV and is enclosed by a Cu cup [Fig. 6.10 (a) and (b)]. Sealing of the cup is achieved by indium gaskets. The space outside the UHV insert is called isolation vacuum space (IVC). It is closed around the STM by another indium sealed cup [Fig. 6.10 (c)]. Under vacuum, the IVC space acts as an insulation barrier, decoupling the liquid ^{4}He temperature from acting upon the STM. When filled with He gas, it couples the STM thermally to the ^{4}He cryostat, making the STM reach the temperature of 4.2 K in this scenario.

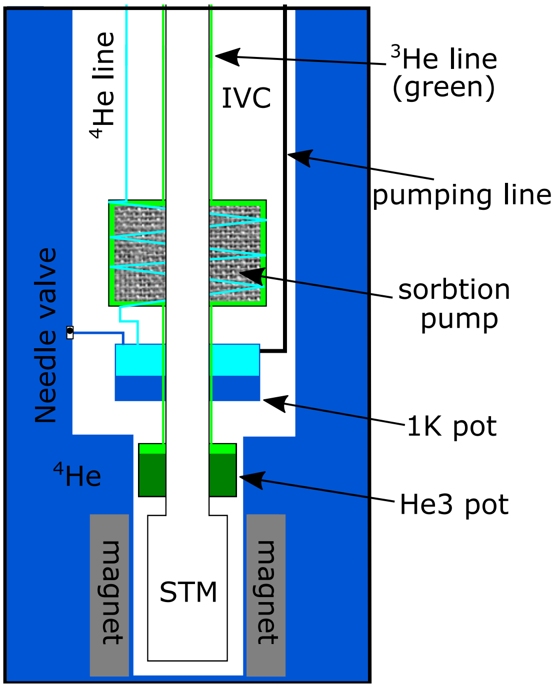

Figure 6.9: Layout of cryostat and insert. Figure adapted from Ref. [306].

^{4}He temperature is not is not the lowest that can be reached at the STM. When looking at the vapor pressure curve of ^{3}He and ^{4}He [Figure 6.11], one can see that the temperature of these liquids depends on the vapor pressure in the vicinity. In the pressure range of around 0.01 Torr, the ^{4}He temperature drops from the normal 4.2 K to the 1 K range under ideal conditions. The so called 1K pot marked in Fig. 6.9 utilizes this effect. Liquid ^{4}He from the outside space is directed through an inlet port, controlled by a needle valve, into the 1K pot. There is a cooling line surrounding the sorption pump and another line is connected to an outside rough pump. By letting liquid ^{4}He flow to the 1K pot upon opening of the needle valve and by pumping on it using the pumping line, one can achieve a pressure below 10 mbar, making the 1K pot and subsequently the sorption pump reach 1.7 K. In this case the before mentioned IVC needs to be in a pumped state, since otherwise the liquid ^{4}He in the outer space would warm the 1K pot and the insert back up to 4.2 K.

Located in between the IVC and the insert is the ^{3}He gas space. It is connected to a reservoir on the outside containing the ^{3}He gas. Placed in this space is the sorption pump, featuring a body of charcoal. It is possible to heat the sorption pump, which is important for the supercooling process to reach temperatures down to 0.4 K, as advertised in the beginning of the chapter. The slightly enlarged space close to the STM is called He3 pot. When looking at Fig. 6.11, one can see that ^{3}He has the trait of being able to reach even lower temperatures than the ^{4}He at low vapor pressures.

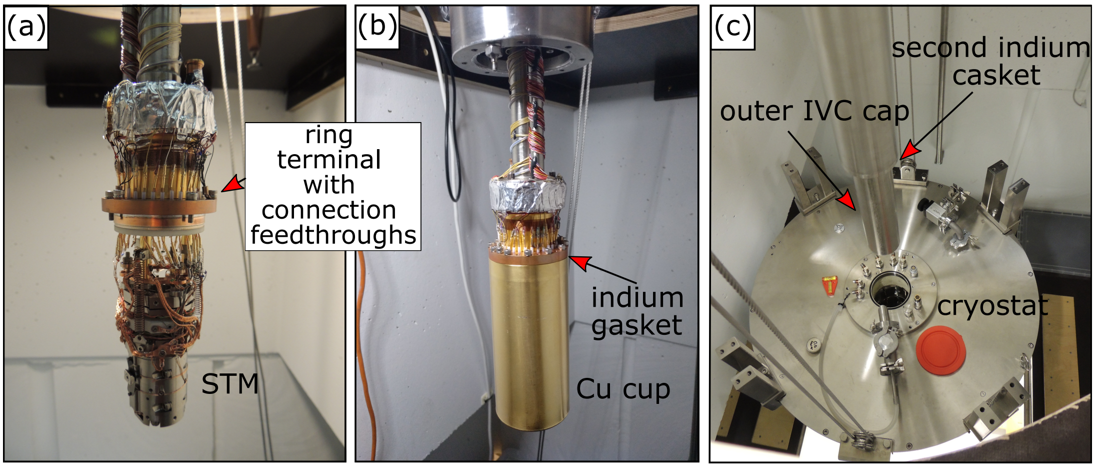

Figure 6.10: The STM at the end of the insert tube. (a) Ring terminal connection feedthrough and STM. (b) Cu cup closing the UHV space around the STM. (c) A second cup closing the IVC space. The cryostat is visible below.

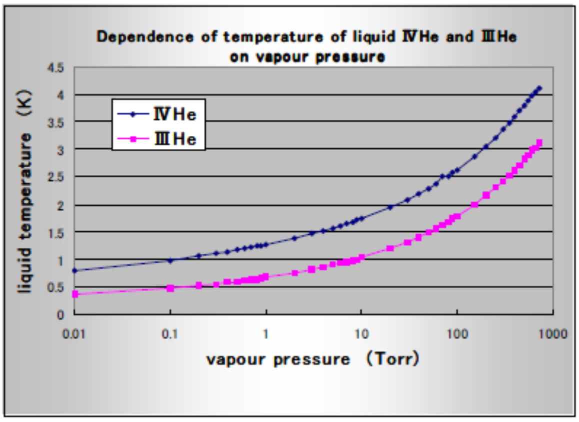

Figure 6.11: Dependence of the ^{3}He and ^{4}He temperature on vapor pressure. Figure reprinted from Ref. [306].

The cooling cycle to 0.4 K works as follows:

1. First, one cools the STM down to 4.2 K. This is achieved by filling the before described outer space with liquid ^{4}He and using the He gas filled IVC for thermal transfer.

2. When the STM reaches a temperature of 4.2 K, the IVC is pumped and the needle valve, controlling the flow of liquid ^{4}He to the 1K pot and the sorption pump, is opened. The needle valve is adjusted, so that the pressure in the 1K pot settles just below 10 mbar, while pumping on it using the outside pumping line. The 1K pot and the sorption pump are cooled in this process, reaching a temperature of 1.7 K and resulting in all the ^{3}He being pumped to the sorption pump.

3. In order to establish a thermal bridge between 1K pot and He3 pot, the sorption pump is heated from 1.7 K to 50 K. ^{3}He gas absorbed in the sorption pump evaporates and is cooled by the 1K pot thereby cooling also the He3 pot and STM. After thermal equilibrium is obtained, the ^{3}He starts to condensate at the 1.7 K cold He3 pot. This process takes up to 1 hour to be completed.

4. In the fourth step, the heating of the sorption pump is turned off and the temperature of the liquid ^{3}He condensed in the He3 pot slowly starts to drop. The cold sorption pump keeps the vapor pressure in the vicinity of the ^{3}He still condensed in the He3 pot low, enabling to reach the temperature in the range of 0.4 K as visible in Fig. 6.11. The typical holding time is up to 48 hours until all ^{3}He has evaporated from the He3 pot and has moved to the sorption pump. To repeat the cycle, the sorption pump is again heated to 50 K to condense all the ^{3}He in the He3 pot once more.

Thermal shielding of the STM is essential to maintain temperatures below 4 K. Therefore the STM is shielded from thermal radiation coming from the exc and warm parts of the UHV insert above by two plugs called the He3 and He4 shields [Fig. 6.12, shields screwed into the exc storage module]. The He3 shield is placed just above the STM and below the He3 pot after sample and tip were inserted into the STM. The He4 pot offers further protection and is inserted at the height of the 1K pot.

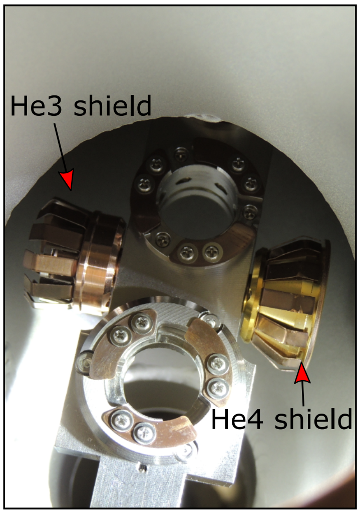

Figure 6.12: The He3 and He4 shields screwed into the exc storage module.

The Transfer Rod Locking Mechanism on the Example of the Tip Carriers

All parts of the system that are transferable (sample holders, tip carriers, He3 and He4 shields) utilize the same mechanism to grab them with the transfer rods of the system. The transfer rods feature a chuck head at the end, shown in Fig. 6.13 (a). Each chuck hat has two slots in the side wall. At the end of the slots there is a pocket slightly larger than the slot itself. This is the locking position of the locking pins on the sample holders, tip carriers etc.. [Fig. 6.13 (b)]. When moving the chuck head onto a tip carrier to unscrew it for example from the STM scanner, one rotates clockwise until the locking pins fit/slide into the slots. The initial clockwise rotation impedes that parts like the tip carrier are unscrewed before they are properly grabbed by the transfer rod. Once the locking pins are in the chuck head slots, one rotates counter clockwise until the pins are in the locking position. Going further will start to unscrew the tip carrier until it is loose and can be taken out. Fixing the tip carrier into a position works by reverse application of all the steps. Both processes are depicted in Figure 6.13 (c) (removing the tip carrier) and (d) (fixing the tip carrier).

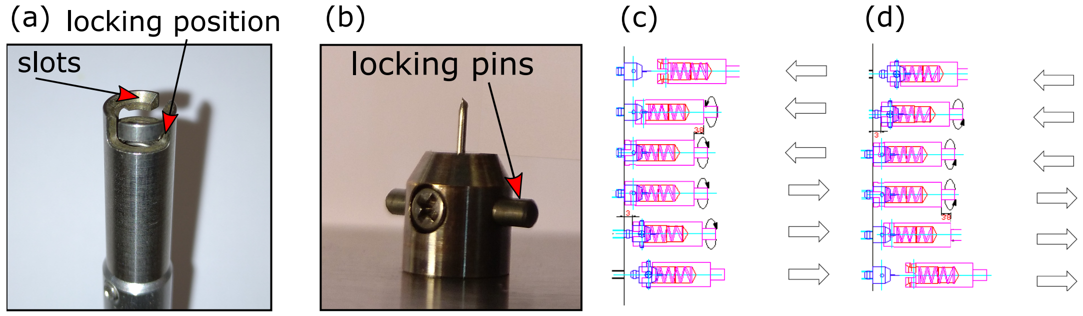

Figure 6.13: Grabbing mechanism of transferable parts. (a) Chuck head at the end of the transfer rod. (b) Locking pins on the tip carrier. (c) Procedure of grabbing a tip carrier. (d) Procedure of fixing a tip carrier. Figure (c) and (d) reprinted from Ref. [306].

The Pan Slider Scanning Tunneling Microscope

The STM used in this system is the so called "Pan slider" type (Fig. 6.14). This type of STM was first proposed by Shuheng Pan and shows great performance at low temperatures [307]. The tube piezo scanner holding the tip is fixed to a sapphire prism, which is pressed by shear piezo stacks, called inertial piezo slider. The whole mechanism is surrounded partially by a macor body and a spring plate as shown in the figure. Upon application of periodic HV pulses to the shear piezos, a coarse motion in z-direction is induced, moving the tip closer to the sample or further away. The movement is divided into an initial sliding phase, when the piezos move quickly while the prism stays in position and a riding phase, when the piezos move slowly and the prism is moved. This process is also known as slip-stick motion. At RT, each 120 V pulse causes a step of about 5 μm. The total working distance of the approach stage is 5 mm in z-direction. Different to the situation in Fig. 6.14, in our case the sample is not in a fixed position. It is part of a so called x-y stage, enabling to move the sample in x-y direction by ±0.5 mm. Like the z-coarse motion it utilizes a shear piezo movement. Attached to the tube-type piezo holding the tip are 5 electrodes (+X, +Y, -Y, -Y and Z,). These electrodes bend the tip piezo and enable a scanning motion. The maximum scan range of the scan piezo is about 2.3 μm.

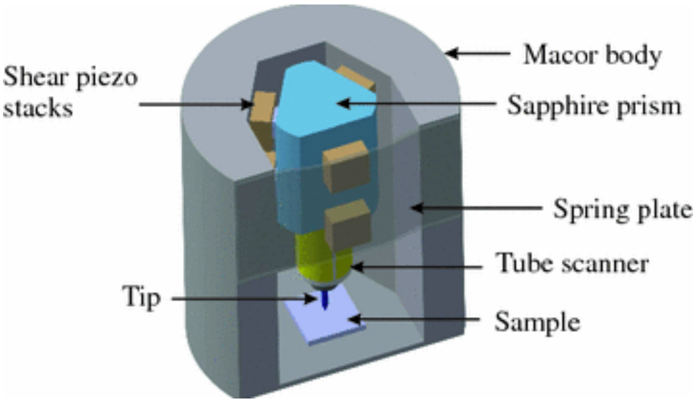

Figure 6.14: Basic principle of the Pan slider STM. Figure reprinted with permission from Ref. [307] © 2015 Springer-Verlag Berlin Heidelberg.

CHAPTER 7

Manuscript 1: Electronic Structure and Charge Density Wave Order in Monolayer NbS_2

This chapter consists of the above-named manuscript and its supplement, in preparation for submission to a publishing journal.

The experiments were proposed by T. Knispel, J. Fischer, T. Wehling and T. Michely. Sample growth and experiments were conducted at the low temperature magnetic STM system (MSTM) in our group. Sample growth and LEED, STM and STS experiments were carried out by T. Knispel under the guidance of J. Fischer and advice from T. Michely. Data analysis was performed by T. Knispel.

J. Berges, A. Schobert, E. G. C. P. van Loon, W. Jolie and T. Wehling made a significant contribution to the discussion of the experimental results.

T. Knispel wrote the manuscript and finalized it in close collaboration with J. Fischer and T. Michely.

Electronic structure and charge density wave order in monolayer NbS_2

Timo Knispel,[1] Jeison Fischer,[1] Jan Berges,[2] Arne Schobert,[2] Erik G. C. P. van Loon,[2,3] Wouter Jolie,[1] Tim Wehling,[2] and Thomas Michely[1]

[1] *II. Physikalisches Institut, Universität zu Köln,*
Zülpicher Straße 77, 50937 Köln, Germany

[2] *Institut für Theoretische Physik, Bremen Center for Computational Materials Science,*
and MAPEX Center for Materials and Processes,
Universität Bremen, Otto-Hahn-Allee 1 28359 Bremen, Germany

[3] *Department of Physics, Lund University,*
Professorsgatan 1, 223 63 Lund, Sweden

(Dated: March 30, 2022)

Abstract

Charge density waves are present in many transition metal dichalcogenides and their mechanisms and driving forces are subject to an ongoing discussion. In this work we investigated quasi-freestanding monolayer H-NbS_2 grown in situ on graphene/Ir(111) by high resolution scanning tunneling microscopy and spectroscopy at low temperatures. While no charge density wave is reported for bulk 2H-NbS_2, in the monolayer limit we find a 3×3 modulation pattern and unambiguously link it to a charge density wave phase. We find an inversion of the charge density wave contrast in dI/dV maps towards both sides of a gap-like intensity minimum close to the Fermi energy, in agreement with the picture of a weakly coupling charge density wave driven by Fermi surface nesting. The electronic structure in the occupied and unoccupied states is mapped by scanning tunneling spectroscopy point spectra, also investigating features close to the Fermi energy. Furthermore, quasi-particle interference is observed at island edges and defects, enabling us to extract the dispersion of the hole-like band pocket around the Γ-point. Finally we address the absence of superconductivity in the monolayer.

I. INTRODUCTION

Transition metal dichalcogenides (TMDCs) are layered materials of the form MX_2, with M being a transition metal atom and X a chalcogen atom [1, 2]. Many of these materials feature an interplay of interesting electronic phenomena like Mott insulating phases, superconductivity and charge density waves (CDWs) [3–5]. The mechanism and collective behavior of these electronic phenomena is however not fully understood.

A well established CDW mechanism is Fermi surface nesting in the classical 1D Peierls picture [6], valid for a 1D metallic atom chain developing a periodic lattice distortion. Due to the electronic response of the system, such a distortion is accompanied by an energy gap emerging at the Fermi energy and charge modulation with its periodicity given by the so called nesting wave vector. For many TMDC materials instead of only Fermi surface nesting, the effect is accompanied by a stronger, wave-vector-dependent electron-phonon coupling, which appears as the force driving the CDW [7–9]. These mechanisms can affect the band structure on a broader range [5, 10, 11], not limited to the Fermi energy like in the case of a classical Peierls transition.

One TMDC that stands out is the compound 2H-NbS_2, which does not feature a CDW ground state in the bulk [12, 13], however the presence of defects on the surface has been reported to lead to a locally pinned incommensurate CDW [14]. The absence of CDW order is explained by anharmonic suppression, but a softening of phonon modes towards a CDW is present [15–17]. On the other hand, 2H-NbS_2 has been found to be superconducting in the bulk with a critical temperature of $T_\mathrm{c} \approx 6\,\mathrm{K}$ [12, 18, 19] prevailing down to $4-6\,\mathrm{nm}$ thickness [20, 21].

In the case of $NbSe_2$, CDW order and superconductivity coexist from the bulk down to the monolayer limit, for example in H-$NbSe_2$ monolayers MBE grown on bilayer Gr/6H-SiC(0001) [22]. In this system, the monolayer CDW phase features a critical temperature between 25 K and 45 K, both in bulk and monolayer. A small gap at the Fermi energy of $2\Delta = 8\,\mathrm{meV}$ has been correlated with the amplitude of the CDW, which is taken as a hallmark for Fermi surface nesting as the driving force. On the other hand in theoretical works, similar to the bulk case [8, 23–25], the absence of Fermi surface nesting is discussed and stronger wave-vector-dependent electron-phonon coupling has been assumed to be the dominating driving force of the CDW [26, 27]. This is supported by the fact that for exfoliated monolayer samples of $NbSe_2$ on sapphire, an enhanced T_c of about 145 K was found for the CDW phase [28, 29], pointing towards a stronger interaction mechanism than Fermi surface nesting. This enhancement of T_c has again been questioned and the topic remains under discussion [30].

The case of H-NbS_2 is different, most discussion is from the theoretical point of view addressing the absence of CDW order in bulk and predicting the ground state of the monolayer. Van Loon et al. [31] discard the simple nesting scenario, but instead argue that a strain induced competition between long-range Coulomb and electron-phonon interaction leaves the system at the edge between a state of charge or spin fluctuations. Regarding the spin order, a tendency towards a spin density wave instability caused by Fermi surface nesting [32] and switching of magnetic states caused by strain [33, 34] has been predicted theoretically before. Bianco et al. [17] found an enhancement of phonon mode softening in monolayer H-NbS_2 as compared to the bulk, but also report that even small anharmonic effects like compression or dilatation can allow or inhibit the CDW order.

From the point of view of experiments little is know for the monolayer. The case of high interacting substrates shows no indications for a CDW as shown for H-NbS_2 monolayers on Au(111) [35], however, other TMDCs also have their known monolayer CDW suppressed due to hybridization occurring between the TMDC and Au(111) as substrate [36, 37].

Despite a previous observation of a 3×3 modulation pattern very similar to the CDW pattern in monolayer H-$NbSe_2$ on bilayer Gr/6H-SiC(0001) [40], little is known about it and experimental evidence of the possible electronic mechanisms is still lacking. The superconducting behavior reported for 2H-bulk samples has been shown to vanish in samples thinner than 6 nm attributed to oxidation [20], leaving that question unsolved for the monolayer. Bulk van der Waals superlattices of alternating Ba_3NbS_5/NbS_2 [38] and $SnS_{1.7}/NbS_2$ [39] have been found to possess superconductivity with $T_\mathrm{c} = 1.6\,\mathrm{K}$ and $T_\mathrm{c} = 2.8\,\mathrm{K}$ correspondingly, but no sign of a CDW is provided and the van der Waals superlattice situation is of only limited comparability to a (quasi-) freestanding monolayer situation.

In this work, we provide a comprehensive characterization of the H-NbS$_2$ monolayer low-temperature electronic properties. We utilize in situ MBE growth of H-NbS$_2$ monolayers on a weakly interacting Gr/Ir(111) substrate to investigate the electronic footprints of the 3×3 modulation pattern by high resolution scanning tunneling microscopy (STM) and scanning tunneling spectroscopy (STS) at low temperatures, thereby linking it to a CDW phase. By STS, we investigate the electronic structure in the occupied and the unoccupied states to determine the exact position of the CDW gap and the possible driving force being Fermi surface nesting. We clarify the lack of a superconducting state down to 0.4 K, highlighting the competing behavior between the CDW and superconductivity in this system.

II. EXPERIMENTAL METHODS

Sample preparation was accomplished in an UHV preparation system with a base pressure of $p < 2 \times 10^{-10}$ mbar. Ir(111) was cleaned using cycles of 1 kV Ar^{+}-sputtering and subsequent flash annealing to 1520 K. Graphene (Gr) was grown by ethylene exposure to saturation, subsequent flash annealing to 1470 K and a final exposure to 800 L ethylene at 1370 K. The quality of the closed single crystal Gr monolayer was checked by low energy electron diffraction (LEED) and STM.

Monolayer H-NbS$_2$ was grown on Gr/Ir(111) by reactive molecular beam epitaxy (MBE). The substrate was exposed to an Nb flux of 5.8×10^{15} atoms/m^{2}s from an e-beam evaporator in an elemental sulfur (S) background pressure of $p = 1 \times 10^{-8}$ mbar from a pyrite filled Knudsen cell. The growth was conducted at 300 K for 660 s, then the sample was annealed to 800 K, similar to the growth of other TMDCs on Gr/Ir(111) [41]. In order to maximize the monolayer coverage, the island seeds were extended to final size by additional growth at 800 K for 660 s.

After synthesis, the H-NbS$_2$ monolayer was checked using LEED. The sample was subsequently transferred *in situ* to the connected UHV bath cryostat STM chamber for investigation. The temperature T_s of STM or STS investigation is specified in each figure and was either 0.4 K using a He^3 cycle, 1.7 K when pumping on He^4, 4 K using He^4 cooling without pumping, or even higher than 4 K by using an internal heater. Dependence of the STS features on magnetic field was checked by a superconducting magnet creating fields of up to 9 T normal to the sample surface. Both, constant height and constant current modes were used to measure the STM topography and

STS dI/dV maps, while STS dI/dV point spectra were recorded only at constant height. Constant current STM topographs and constant current dI/dV maps were recorded with sample bias V_s and tunneling current I_t specified in each figure. Constant height STS dI/dV point spectra and dI/dV maps were recorded with stabilization bias V_stab and stabilization current I_stab using a lock-in amplifier with a modulation frequency f_mod and modulation voltage V_mod and are also specified in the captions. In case that for a constant height dI/dV map the sample bias during measurement does not coincide with V_stab, e.g. because a set of dI/dV maps is taken at the same height defined by V_stab and I_stab but different voltages, the sample bias V_s is specified additionally. When needed, a voltage divider was applied to improve resolution. To ensure a reproducible and flat tip density of states (DOS) for the STS measurements, Au-covered W tips were used and calibrated beforehand using the surface state of Au(111) [42, 43].

III. RESULTS

Structure of NbS_2 monolayers on Gr/Ir(111)

Fig. 1 (a) displays a large-scale STM topograph of monolayer NbS_2 on Gr/Ir(111). The coalesced islands cover about 73 % of the surface area. They conform without disturbance to the Gr sheet also at locations where Gr is deformed due to its overgrowth of Ir(111) substrate steps, which run from the upper left to the lower right. The height profile in Fig. 1 (b) taken along the black line of Fig. 1 (a) displays an apparent height of 0.64 nm for the monolayer NbS_2 islands. For a tunneling bias between -1 V and 1 V the apparent height varies slightly and is in the range of 0.53-0.64 nm. Our measured apparent heights match half the c-axis lattice parameter of 1.195 nm for bulk 2H-NbS_2 [12]. The measured heights are also in agreement with the apparent STM height of 0.578 nm obtained for a specific set of tunneling parameters for monolayer NbS_2 on Gr/6H-SiC(0001) [40].

In the atomically resolved STM topograph of Fig. 1 (c) the moiré of Gr with Ir(111) can be recognized being superimposed on the NbS_2 monolayer (yellow rhomboid indicates the moiré unit cell). The lack of an own moiré between the NbS_2 monolayer and Gr indicates a very weak interaction between the two materials. The inset of Fig. 1 (c) highlights the unit cell and primitive lattice translations $\vec{a}_1$ and $\vec{a}_2$ of the two dimensional NbS_2 lattice. The measured in-plane lattice periodicity of the NbS_2 monolayer is 0.32(2) nm, in good agreement with the bulk value of 0.3324 nm [12] and the one for monolayer NbS_2 on Gr/6H-SiC(0001) of 0.334 nm [40]. STM does not provide information on the coordination of the Nb atoms. In NbS_2 bulk [12] and in chemical vapor deposition grown thin NbS_2 films down to the monolayer thickness [44] the Nb atoms are

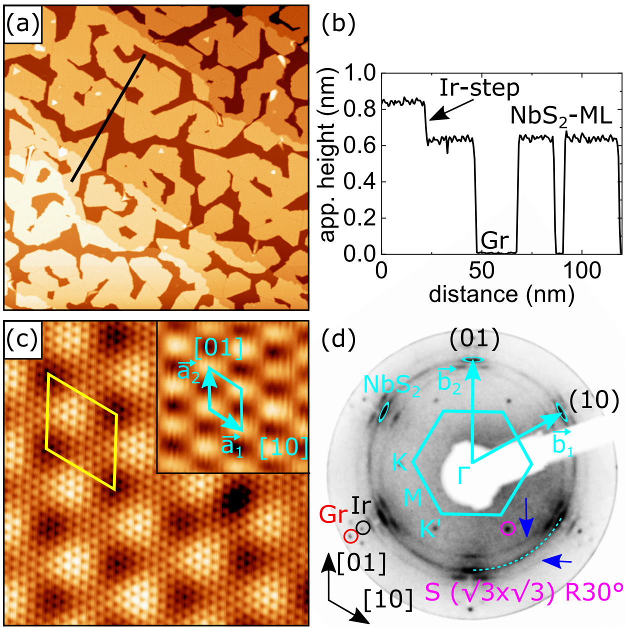

FIG. 1. Structure of the NbS_2/Gr/Ir(111) sample: (a) Large-scale constant current STM topograph of monolayer NbS_2 on Gr/Ir(111). (b) Height profile marked by a black line in (a). (c) Atomically resolved constant current STM topograph of monolayer NbS_2. The moiré unit cell is indicated by a yellow rhomboid. The unit cell, primitive lattice vectors and 2D lattice directions of NbS_2 are indicated in turquoise in the inset. (d) 100 eV microchannel plate LEED pattern. First order reflections corresponding to NbS_2 are marked in turquoise, to Gr in red, to Ir in black, and to S intercalation in pink. Two faint moiré satellite rings are highlighted by blue arrows (see text). Additionally the NbS_2 Brillouin zone (turquoise), Miller indices (black), and real space lattice directions (black) are given. Image information: (a) size 250 nm × 250 nm, $V_\mathrm{s} = 1\,\mathrm{V}$, $I_\mathrm{t} = 0.1\,\mathrm{nA}$, $T_\mathrm{s} = 1.7\,\mathrm{K}$; (c) size 10 nm × 10 nm, $V_\mathrm{s} = 100\,\mathrm{mV}$, $I_t = 0.7\,\mathrm{nA}$, $T_\mathrm{s} = 1.7\,\mathrm{K}$.

only found in trigonal-prismatic coordination (H-phase). Therefore we here assume the monolayer on Gr/Ir(111) to be also present in the H-phase.

The 100 eV LEED pattern of a NbS_2/Gr/Ir(111) sample in Fig. 1 (d) displays first order NbS_2 intensity as superposition of (i) prominent elongated spots (several encircled turquoise) reasonably aligned with Gr (one first order reflection encircled red) and the Ir substrate (one first order reflection encircled black) and (ii) a diffraction ring due to randomly oriented islands (dashed turquoise segment). This indicates that most islands are aligned with small angular scatter to Gr/Ir(111) substrate, while some display random orientation. Additionally, faint off-centered rings are visible (two highlighted by blue arrows). These rings belong to NbS_2, but are each shifted by one moiré periodicity of Gr. S intercalation under Gr gives rise to a $(\sqrt{3} \times \sqrt{3})\mathrm{R}30°$ structure with respect to Ir(111) and corresponding reflections, of which one first order reflection is encircled in pink. Real space lattice directions relating to Fig. 1 (c) are marked in the lower left. The lattice constant, determined by the length of the reciprocal vectors of the $\mathrm{NbS_2}$ lattice in LEED, yields 0.331(3) nm in good agreement with our STM measurements and the literature data.

The 3×3 CDW in monolayer $\mathrm{NbS_2}$

The fast Fourier transform (FFT) of the $-15\,\mathrm{meV}$ constant height dI/dV map shown in Fig. 2 (a) is presented as Fig. 2 (b). The red encircled spots at 1/3 and 2/3 of the distance between the Γ-point and the first order $\mathrm{NbS_2}$ lattice spots (encircled turquoise) are indicative of a 3×3 superstructure. It is obvious that the three equivalent wave vectors of the superstructure are oriented along the $\overline{\Gamma\mathrm{M}}$-directions. For better visualization of the 3×3 superstructure in real space, the moiré spots (an example spot is encircled yellow) are bandstop filtered as shown in the inset of in Fig. 2 (b).

Upon back transformation of the bandstop processed FFT, the 3×3 superstructure (highlighted by red circles and a rhomboid) becomes obvious in Fig. 2 (c). The sequence Fig. 2 (c), (d), and (e) are from the same set of dI/dV maps taken without tip change, but with sample bias voltages $V_\mathrm{s} = -15\,\mathrm{mV}$, $V_\mathrm{s} = 7.5\,\mathrm{mV}$, and $V_\mathrm{s} = 40\,\mathrm{mV}$, respectively. It is apparent that the 3×3 superstructure contrast vanishes in (d) and regains intensity in (e). The intensity ratio $I_{3\times3}/I_\mathrm{atom}$ of the first order 3×3 superstructure spots and the $\mathrm{NbS_2}$ lattice spots is shown as a function of bias voltage $\mathrm{V_s}$ in Fig. 2 (f). The plot displays a clear minimum at 7.5 mV, where the intensity ratio is lower by a factor of 20 compared to the maximum at about $-15\,\mathrm{mV}$. As indicated, the full width at half maximum (FWHM) is about 14 meV. Considering that a dI/dV map represents the local density of states (LDOS) at the energy associated to the voltage of measurement, it is evident that at an energy of 7.5 meV above the Fermi level the LDOS associated to the superstructure vanishes.

Additional information is obtained by only back transforming the first order 3×3 reflections as shown in the insets of Fig. 2 (c) and (e). A pattern of red lines is superimposed to the inset of Fig. 2 (c) such that the line crossings are placed on maxima of the superstructure intensity. Using the atom encircled white at the upper left of Fig. 2 (c) and (e) as a marker, the line pattern is superimposed at the precise same location to the inset of Fig. 2 (e). It is obvious that now the superstructure minima are located at the line crossings, i.e the superstructure intensity is phase-shifted on the two sides of the intensity ratio $I_{3\times3}/I_\mathrm{atom}$ minimum.

Taken together, the 3×3 superstructure, the $I_{3\times3}/I_\mathrm{atom}$ intensity ratio minimum reminiscent of a charge density wave gap, and the phase-shifted superstructure intensity adjacent to the energy of the minimum, as frequently observed on both sides of a CDW gap [11, 45, 46], our observations provide sound evidence for the presence of a CDW in monolayer $\mathrm{NbS_2}$. The 3×3 real space periodicity implies a superposition of three equivalent CDW wave vectors $q_\mathrm{CDW} = 2/3\ \overline{\Gamma\mathrm{M}}$.

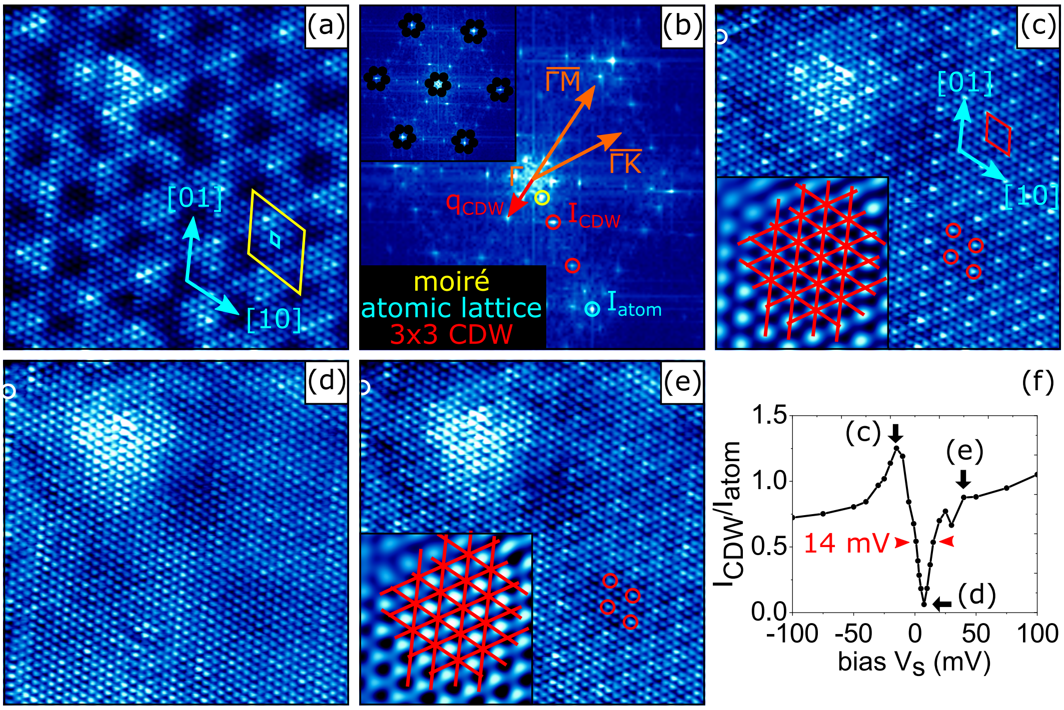

FIG. 2. 3×3 charge density wave in the NbS_2 monolayer: (a) Constant height dI/dV map. The moiré of Gr and Ir(111) is marked by a yellow rhomboid. (b) is the FFT of (a). Spots corresponding to the NbS_2 lattice, the 3×3 CDW and the moiré of Gr and Ir(111) are marked in turquoise, red and yellow correspondingly, as well as the reciprocal lattice directions in orange. The inset illustrates the application of bandstop filtering to remove the moiré in the backtransformed image. (c), (d), and (e) are bandstop filtered constant height dI/dV maps taken at $V_s = -15\,\mathrm{mV}$, $V_s = 7.5\,\mathrm{mV}$, and $V_s = 40\,\mathrm{mV}$, respectively. Red circles in (c) and (d) and a rhomboid in (c) mark the 3×3 CDW. The crystallographic lattice directions and unit cell of NbS_2 are indicated turquoise in (c). In the insets of (c) and (e) only first order 3×3 spots were backtransformed. The red line pattern is located at the exact same position in relation to the atom marked in the top left by a white circle. (f) Intensity ratio $I_{3\times3}/I_{\mathrm{atom}}$ of the first order 3×3 CDW spots and the NbS_2 lattice spots visible in the FFTs as shown in (b). The data points for (c), (d) and (e) are indicated. Image information: (a) size $12\,\mathrm{nm} \times 12\,\mathrm{nm}$, $V_s = -15\,\mathrm{mV}$, $V_{\mathrm{mod}} = 5\,\mathrm{mV}$, $f_{\mathrm{mod}} = 1890\,\mathrm{Hz}$, $T_s = 4\,\mathrm{K}$; (c) size $12\,\mathrm{nm} \times 12\,\mathrm{nm}$, $V_{\mathrm{mod}} = 5\,\mathrm{mV}$, $f_{\mathrm{mod}} = 1890\,\mathrm{Hz}$, $T_s = 4\,\mathrm{K}$, FFT filtered; (d) size $12\,\mathrm{nm} \times 12\,\mathrm{nm}$, $V_{\mathrm{mod}} = 3\,\mathrm{mV}$, $f_{\mathrm{mod}} = 1890\,\mathrm{Hz}$, $T_s = 4\,\mathrm{K}$, FFT filtered; (e) size $12\,\mathrm{nm} \times 12\,\mathrm{nm}$, $V_{\mathrm{mod}} = 8\,\mathrm{mV}$, $f_{\mathrm{mod}} = 1890\,\mathrm{Hz}$, $T_s = 4\,\mathrm{K}$, FFT filtered. All constant height dI/dV maps were stabilized at $V_{\mathrm{stab}} = 300\,\mathrm{mV}$ and $I_{\mathrm{stab}} = 5\,\mathrm{nA}$.

The temperature dependence of the 3×3 CDW is addressed in Fig. 3. Fig. 3 (a) to (c) is a sequence of constant current dI/dV maps measured at sample temperatures of 4 K in (a), 30 K in (b) and 40 K in (c). It is obvious that the 3×3 CDW superstructure corrugation diminishes with increasing temperature and is marginal at 40 K. Interestingly, although by eye at 40 K no CDW is visible in the dI/dV map anymore, the FFT inset of Fig. 3 (c) displays in one direction a residual

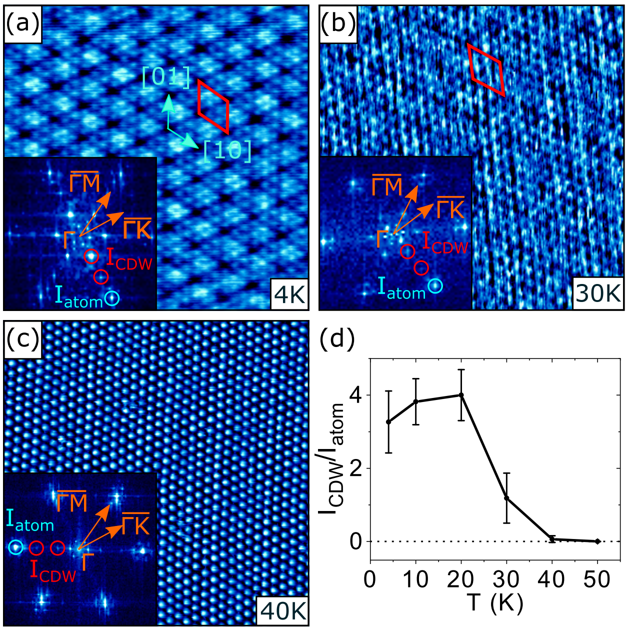

FIG. 3. Temperature dependence of the 3×3 CDW in NbS$_2$: (a) Constant current dI/dV map at 4 K. The 3×3 CDW modulation is indicated by a red rhomboid, the crystallographic lattice directions of NbS$_2$ in turquoise. (b) Constant current dI/dV map at 30 K. (c) constant current dI/dV map at 40 K. The insets are the FFTs of the dI/dV maps. Reflections belonging to the 3×3 modulation are marked in red, a reflection belonging to the atomic lattice of NbS$_2$ is indicated in turquoise and the reciprocal space directions are shown as orange arrows. Image information for (a), (b) and (c): image size 8.75 nm × 8.75 nm, $V_\mathrm{s} = 100\,\mathrm{mV}$, $I_\mathrm{t} = 0.7\,\mathrm{nA}$, $V_\mathrm{mod} = 10\,\mathrm{mV}$, $f_\mathrm{mod} = 1873\,\mathrm{Hz}$.

intensity $I_{3\times3}$ highlighted by red circles around the spots. A quantitative analysis confirming our qualitative inference is presented in Fig. 3 (d), where $I_{3\times3}/I_\mathrm{atom}$ is plotted as a function of temperature. Based on the data, we estimate a CDW transition temperature T_CDW in the range between 40 K and 50 K.

Local density states of the NbS$_2$ monolayer

To gain further insight into the electronic structure, STS point spectra were measured on NbS$_2$, shown in Fig. 4. Fig. 4 (a) displays a large-range constant height STS spectrum which can be compared to the density functional theory (DFT) band structure shown in Fig. 4 (b). For the comparison it has to be noted that (i) van Hove singularities appear pronounced in dI/dV spectra due to the large LDOS associated to them, and (ii) states with large parallel momentum $k_{||}$ are hard to detect in dI/dV spectra, since a large $k_{||}$ is associated with a large decay constant κ, i.e. a rapid decay of the wave functions into vacuum [47, 48].

The pronounced peak at $-1.25\,\mathrm{V}$ in Fig. 4 (a) is attributed to the two hole-like S p_z-type bands [49] centered at the Γ-point in Fig. 4 (b), which have their maximum at about the energy corresponding to the peak voltage. The third S p_z-type band with its maximum located further away from the Γ-point at about $-0.75\,\mathrm{eV}$ is hardly visible in the dI/dV spectrum because of its larger $k_{||}$. It presumably is connected to the intensity above the pronounced $-1.25\,\mathrm{V}$ peak. The broad and intense maximum with its peak at about $+0.85\,\mathrm{V}$ in Fig. 4 (a) is associated with the band maximum of the Nb d_{z^2}-type hole-like band [49] at the Γ-point in Fig. 4 (b), though located at slightly lower energy compared to the calculation. The steep rise in the dI/dV spectrum at voltages above about $+2.2\,\mathrm{V}$ is associated with empty Nb d-type bands and S p-type bands above $2\,\mathrm{eV}$ in

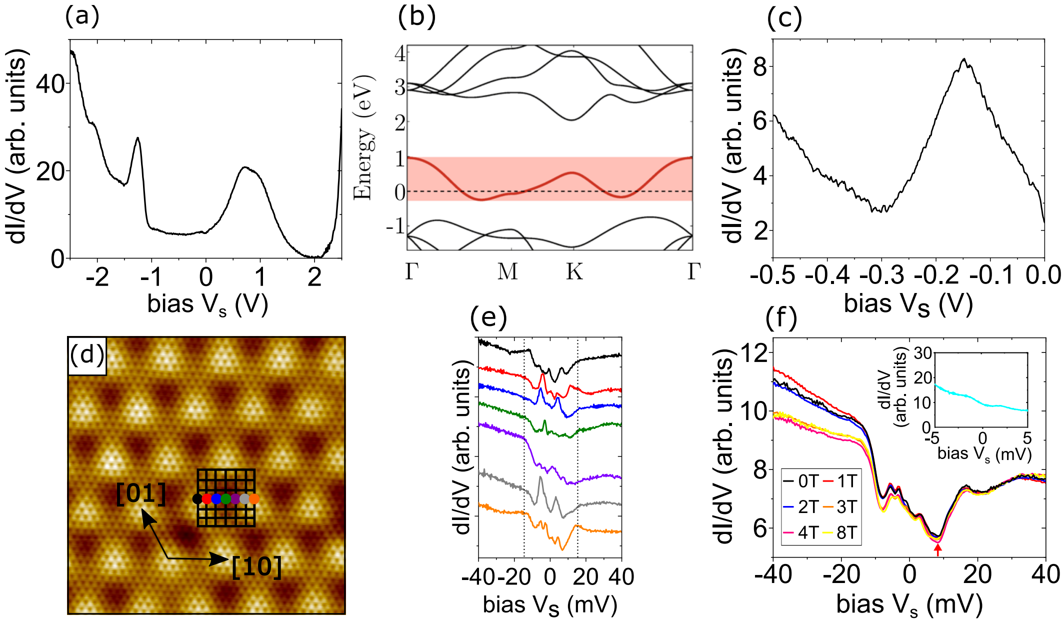

FIG. 4. Constant height STS point spectra on $\mathrm{NbS_2}$: (a) Large-range dI/dV spectrum from $-2.5\,\mathrm{V}$ to $+2.5\,\mathrm{V}$. (b) Calculated band structure of freestanding $\mathrm{NbS_2}$ [31]. (c) dI/dV spectrum of boxed voltage range in (a) with tip very close to sample. (d) Constant current STM image of $\mathrm{NbS_2}$ with a grid of measurement points indicated. (e) High resolution dI/dV spectra close to the Fermi level measured at the points color-coded in (d). Thin dashed lines at $-15\,\mathrm{mV}$ and $15\,\mathrm{mV}$ bound central intensity depression range. (f) Average of 49 dI/dV spectra defined by the grid in (d) taken at the indicated magnetic fields normal to the sample surface. The position of the minimum CDW intensity in Fig. 2 (f) is marked by a red arrow. Inset: High resolution STS point spectrum recorded at 0.4 K and 0 T. Image information: (d) size $12\,\mathrm{nm} \times 12\,\mathrm{nm}$, $V_\mathrm{s} = 100\,\mathrm{mV}$, $I_\mathrm{t} = 0.7\,\mathrm{nA}$, $T_\mathrm{s} = 1.7\,\mathrm{K}$. point spectra parameters: (a) $V_\mathrm{stab} = 2.5\,\mathrm{V}$, $I_\mathrm{stab} = 1.0\,\mathrm{nA}$, $V_\mathrm{mod} = 15\,\mathrm{mV}$, $f_\mathrm{mod} = 797\,\mathrm{Hz}$, $T_\mathrm{s} = 1.7\,\mathrm{K}$; (c) $V_\mathrm{stab} = -0.5\,\mathrm{V}$, $I_\mathrm{stab} = 0.5\,\mathrm{nA}$, $V_\mathrm{mod} = 5\,\mathrm{mV}$, $f_\mathrm{mod} = 1873\,\mathrm{Hz}$, $T_\mathrm{s} = 0.4\,\mathrm{K}$; (e) and (f) $V_\mathrm{stab} = 40\,\mathrm{mV}$, $I_\mathrm{stab} = 0.7\,\mathrm{nA}$, $V_\mathrm{mod} = 0.5\,\mathrm{mV}$, $f_\mathrm{mod} = 797\,\mathrm{Hz}$, $T_\mathrm{s} = 1.7\,\mathrm{K}$. Inset in (f): $V_\mathrm{stab} = 5\,\mathrm{mV}$, $I_\mathrm{stab} = 0.5\,\mathrm{nA}$, $V_\mathrm{mod} = 0.1\,\mathrm{mV}$, $f_\mathrm{mod} = 797\,\mathrm{Hz}$, $T_\mathrm{s} = 0.4\,\mathrm{K}$

the calculated band structure. Fig. 4 (c) displays an STS spectrum for the voltage range from $-0.5\,\mathrm{V}$ to $0\,\mathrm{V}$ [boxed in Fig. 4 (a)]. It is stabilized at $-0.5\,\mathrm{V}$, i.e. at an energy with a low density of states as seen in Fig. 4 (a). To pick up the stabilization current of $I_\mathrm{t} = 0.5\,\mathrm{nA}$, the tip moves close to the surface and thus becomes sensitive to less pronounced features in the LDOS. The peak at $-0.15\,\mathrm{V}$ in the resulting spectrum can be interpreted as the van Hove singularity associated with the minima of the in-plane Nb $d_{\mathrm{xy,x^2-y^2}}$-type band [49] below the Fermi level (actually a toriodial minimum surrounding Γ).

The local DOS close to the Fermi energy is addressed in Fig. 4 (d), (e) and (f). Fig. 4 (d) is a constant current topograph with a black grid superimposed which indicates the locations of spectra measured in Fig. 4 (e) and (f). Fig. 4 (e) displays a set of high resolution constant height dI/dV spectra measured at the color equivalent points marked in Fig. 4 (d). In all spectra at $-15\,\mathrm{mV}$ and $+15\,\mathrm{mV}$ (thin dashed lines) the dI/dV intensity starts to slope down and in this voltage range generally a reduced dI/dV intensity is found. However, the individual spectra vary greatly and within the range of reduced intensity often clear peaks or double peaks can be distinguished. They are typically centered around $-5\,\mathrm{mV}$ and $3\,\mathrm{mV}$. Fig. 4 (f) shows the average of 49 dI/dV spectra in the absence of a magnetic field (black), taken at the grid crossings indicted in Fig. 4 (d) and including the individual point spectra of Fig. 4 (e). In this average a double peak at $-5.5\,\mathrm{mV}$ and $-3.1\,\mathrm{mV}$ and a single peak at $3.0\,\mathrm{mV}$ can be clearly discerned. Moreover two dI/dV intensity minima at $-8.0\,\mathrm{mV}$ and $8.2\,\mathrm{eV}$ are present, of which the latter is the total minimum. The location of the total minimum (red arrow) coincides with the minimum of the intensity ratio $I_{3\times3}/I_\mathrm{atom}$ in Fig. 2 (f). Applying a magnetic field of up to $8\,\mathrm{T}$ normal to the surface does not modify the spectra in the range of interest and the described features appear to be independent on magnetic fields. Somewhat lower dI/dV intensity at negative voltages and fields of $3\,\mathrm{T}$, $4\,\mathrm{T}$ and $8\,\mathrm{T}$ can be attributed to drift. The complex dI/dV intensity structure close to zero bias will be discussed in detail in the discussion section.

To check for the presence of superconductivity, a high resolution STS point spectrum was recorded at $0.4\,\mathrm{K}$ in the range of $\pm 5\,\mathrm{mV}$ using a voltage divider to increase resolution. The turquoise spectrum in the inset of Fig. 4 (f) does not show any drop in the dI/dV signal as would be expected for the case of a superconducting gap. Therefore we conclude that there is no indication for the presence of superconductivity in monolayer $\mathrm{NbS_2}$ down to $0.4\,\mathrm{K}$.

Band structure of NbS_2 near Γ from quasi-particle scattering

Besides the CDW superstructure, another electronic feature cannot be overlooked in NbS_2 monolayer islands. The 100 mV dI/dV map in Fig. 5 (a) displays standing wave patterns at the NbS_2 island edges originating from quasi-particle interference (QPI) of electron waves. Zooming into the island, Fig. 5 (b) shows a constant current dI/dV map recorded at 30 mV. At this bias voltage close to the Fermi energy damping of the QPI is weak and the interference pattern is spread out

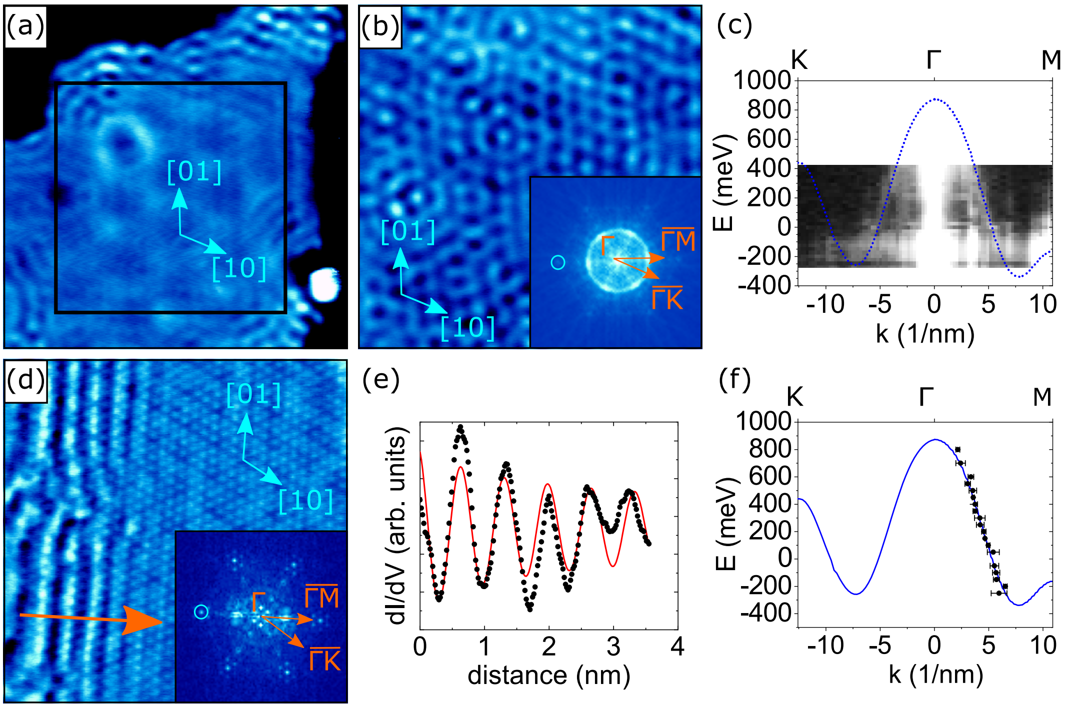

FIG. 5. Quasi-particle interference on NbS_2: (a) Constant current dI/dV map. Crystallographic directions are marked in turquoise. (b) Constant current dI/dV map in the area inside the black square shown in (a). Inset displays the FFT of the dI/dV map. An atomic lattice reflection is marked turquoise, the reciprocal space directions marked orange. (c) FFT intensity of the dI/dV signal at every 25 mV energy step was profiled along $\overline{\Gamma M}$ and $\overline{\Gamma K}$. Data extracted from a 200 × 200 grid of constant height STS point spectra in an area of 9 nm×9 nm on NbS_2. Superimposed as a dashed-blue line is a DFT calculation of the freestanding NbS_2 band structure [31]. (d) Constant current dI/dV map with the standing wave pattern due to island edge scattering. Direction of the wave vector indicated by an orange arrow. Inset is analogue to (b). (e) Line profile along the orange arrow in (d) (black dots) and fitted by a Bessel function (red line) [50]. (f) $E(k)$ dispersion relation extracted from the Bessel function fits and compared to the calculated band structure of freestanding NbS_2 (blue line) [31]. Image information: (a) size 13 nm × 13 nm, $V_s = 200\,\text{mV}$, $I_t = 1.0\,\text{nA}$, $V_{\text{mod}} = 20\,\text{mV}$, $f_{\text{mod}} = 797\,\text{Hz}$, $T_s = 0.4\,\text{K}$; (b) size 9 nm × 9 nm, $V_s = 30\,\text{mV}$, $I_t = 0.8\,\text{nA}$, $V_{\text{mod}} = 7\,\text{mV}$, $f_{\text{mod}} = 1890\,\text{Hz}$, $T_s = 0.4\,\text{K}$; (c) size 10 nm × 10 nm, $V_s = 150\,\text{mV}$, $I_t = 0.3\,\text{nA}$, $V_{\text{mod}} = 20\,\text{mV}$, $f_{\text{mod}} = 1890\,\text{Hz}$, $T_s = 1.7\,\text{K}$.

over the whole island. The FFT inset exhibits a ring-like feature, which shows enhanced intensity in the $\overline{\Gamma\mathrm{M}}$ direction. QPI at a given energy is thus close to isotropic in wave vector, but anisotropic in scattering intensity. The QPI pattern is used to extract the dispersion [50–52] of the hole-like metallic *d*-band discussed in Fig. 4 (b), which crosses the Fermi energy.

In Fig. 5 (c) the FFT intensity profiles along the high-symmetry directions in k-space are plotted as function of energy at increasing energies $E = eV_\mathrm{s}$ in steps of 25 meV. The data is extracted from a 200×200 grid of constant height STS point spectra in an area of 9 nm×9 nm on $\mathrm{NbS_2}$. The result shows a dispersing feature in both high symmetry directions. The DFT dispersion of the hole-like *d*-band centered at the Γ-point is superimposed to the data as dashed-blue line in the plot [31]. The bright cut-off towards larger *k*-values agrees reasonably with the calculation.

Using a larger data set extending over a wider energy range, the band dispersion is also determined by analysis of the real space periodicity of the standing waves at $\mathrm{NbS_2}$ island edges. Following the approach of Crommie et al. [50], the standing wave pattern resulting from backscattering at a straight island edge is fitted after proper background subtraction through $dI/dV_{\mathrm{V_s}} = L_0[1 - J_0(2kx + \phi)]$. Here J_0 is the zeroth order Bessel function, $L_0 = m^*/(\pi\hbar^2)$ with m^* being the effective mass, ϕ is a phase constant, x the distance from the step edge and k is the wave vector related to the electron energy $E = eV_\mathrm{s}$. Fig. 5 (e) exemplifies our approach for a profile (black dots) taken along the orange arrow in the 150 mV dI/dV map shown in Fig. 5 (d). The fit is shown as thin red line and yields the *k*-vector for $E = 150$ meV. Fig. 5 (f) represents as a result of our analysis the dispersion in the energy range from -250 meV to 800 meV (black dots), which compares favorably with the DFT calculated dispersion [31] shown as blue line. Note that this analysis was only possible in $\overline{\Gamma\mathrm{M}}$-direction, as straight steps normal to the $\overline{\Gamma\mathrm{K}}$-direction (armchair direction) are rare and, if present, display only small amplitude interference patterns.

IV. DISCUSSION

As shown in Fig. 2, the intensity of the CDW modulation in $\mathrm{NbS_2}$ features a gap-like minimum at 7.5 mV. We attributed this loss of intensity to a small gap opening in the band structure. The small gap indicates that this is the case of a weak coupling CDW, in agreement with a periodic distortion in the classic Peierls picture with Fermi surface nesting [5, 6]. A similar interpretation has been reported in literature for $\mathrm{NbSe_2}$ monolayers [22]. Strikingly, the position of the gap in energy does not perfectly fit the Peierls picture, in which case one would expect a gap directly at the Fermi energy. The finding of a slightly displaced CDW gap may be attributed to doping effects causing a change in charge carrier concentration and shift of the gap to higher binding energy [46, 53], or anharmonic longitudinal-transverse phonon mode coupling [11]. However, both effects are not expected to take place within the simple Peierls picture with Fermi surface nesting. Nevertheless, the deviation from the Fermi energy in our case is small, so that the weakly interacting nature of the CDW can not be discarded.

Due to the opening of an energy gap at the Fermi energy, Van Hove singularities are expected to be present in the local density of states at the edges of the gap. Recording dI/dV maps at bias voltages close to these singularities then images alternating regions of charge accumulation and depletion in real space due to the charge density redistribution, and inversion of the CDW contrast is expected upon switching the bias polarity. On the one hand, this is observed in many cases of CDWs [11, 45, 46, 54], but also in the case of high T_c superconductivity [55], where the superconducting gap at the Fermi energy causes the contrast in STM to behave similar to the CDW case. On the other hand, the absence of contrast inversion is discussed for CDW phases featuring strong lattice distortions [56]. The close to full contrast inversion of the CDW modulation we find in the dI/dV maps in Fig. 2 above and below the energy gap indeed is a footprint of a CDW driven by Fermi surface nesting.

The electronic structure of $\mathrm{NbS_2}$ monolayers [Fig. 4 (a), (c)] resembles the band structure calculated for freestanding $\mathrm{NbS_2}$ monolayers [31], showing that the substrate of Gr/Ir(111) has a negligible impact on the general electronic structure of $\mathrm{NbS_2}$. This is also supported by the fact, that the calculated dispersion of the d-band crossing the Fermi energy is reproduced by the result extracted from standing waves at the edges of the islands (Fig. 5). The band structure seemingly being unaltered except for the small gap close to the Fermi energy is again in agreement with the assumption of a weakly interacting CDW mechanism, given the absence of gaping in a broader energy range characteristic of wave-vector-dependent electron-phonon coupling [5, 10, 11].

High resolution STS point spectra measured on $\mathrm{NbS_2}$ [Fig. 4 (f)], show a double gap feature close to the Fermi energy, with the large outer gap having the points of maximum slope at $\approx \pm 10\,\mathrm{mV}$. These points are characteristic for an inelastic tunneling process with electron-phonon scattering, similarly observed for STS measurements on bulk 2H-$\mathrm{NbS_2}$ [14] and attributed to bulk Nb phonon modes at around $\pm$ 10 mV [15, 57, 58]. Inside the large gap, a smaller gap of $\approx 7\,\mathrm{mV}$ width is visible. The magnitude of the energy gap is similar to the case of monolayer $\mathrm{NbSe_2}$ [22], but might be perturbed by the described phonon gap from inelastic tunneling. It features the total minimum of the dI/dV signal at 8.2 mV, slightly above the Fermi energy and in reasonable agreement with the energy position of the minimum CDW intensity in Fig. 2 (f) (7.5 mV). This result identifies the small gap present in the differential conductance spectra as a CDW feature. On this basis we can relate the gap size to the critical temperature for a weak coupling CDW at zero temperature within the classic Peierls picture. We implement the BCS-like relation $2\Delta(0) = 3.52 k_\mathrm{B} T_0$ [59] and extract that the determined width of the energy gap $2\Delta(0) \approx 7\,\mathrm{mV}$ yields a transition temperature $T_0 \approx 23\,\mathrm{K}$. This is smaller than the temperature of $\approx 40\,\mathrm{K}$ at which the CDW intensity vanishes in our experiments (Fig. 3), but in the same order of magnitude taking into account possible influence of the described inelastic tunneling process on the gap shape, further justifying the assumption of a weakly interacting CDW. Other features in the spectra like the double peak structure at $-5.5\,\mathrm{mV}$ and $-3.1\,\mathrm{mV}$ are of unknown origin and yet to explain, since as visible in the plot of single spectra in Fig. 4 (d), we were unable to correlate their appearance to any locations on the sample, even though they seem to be more pronounced in the atop regions of the moiré of Gr and Ir(111) compared to the valley regions. Correlation to defects within or under the $\mathrm{NbS_2}$ layer was not possible, since the layer is seemingly perfect and generally no defects are visible as show in Fig. 1. As one can see in Fig. S1 in the supporting information, the features are more prominent towards the edge of the $\mathrm{NbS_2}$ island and are possibly related to the influence the edges have on the electronic structure. This is supported by the finding of standing waves from QPI spreading quite far from the edges to the center of the islands (compare Fig. 5), showing that the edges have a sizable influence on the low energy electronic structure far away from the edges. In this case the islands can be seen as a quantum-well confinement system [60, 61].

One more important point is the absence of superconductivity in our H-$\mathrm{NbS_2}$ monolayer islands. High resolution STS taken at 0.4 K and 0 T [inset of Fig. 4 (f)] revealed the absence of a gap feature in the range of $\pm 5\,\mathrm{mV}$ and the double gap features in the range of $\pm 40\,\mathrm{mV}$ do not show any reaction to the applied vector magnetic field up to 8T, therefore the presence of superconductivity can be ruled out for our $\mathrm{NbS_2}$ islands. Also no signs for magnetic interactions are present. As discussed in section I, both bulk $\mathrm{NbSe_2}$ as well as bulk $\mathrm{NbS_2}$ feature superconductivity with coherence length of $\approx$7.5 nm [62, 63] and up to $\approx$60 nm [64] correspondingly, the coherence length of $\mathrm{NbS_2}$ being one order of magnitude larger. The monolayer coherence length of $\mathrm{NbSe_2}$ stays in the similar range of 10 nm [65] compared to the bulk, so a similar behavior could be expected for $\mathrm{NbS_2}$ monolayers. The finite size of our $\mathrm{NbS_2}$ monolayer islands connected by grain boundaries of about 20 nm×20 nm could therefore render superconductivity impossible. Also, as discussed before, the edges appear to have a sizable impact on the electronic structure and may also cause the absence of superconductivity. Even though our hypothesis for the absence of superconductivity is plausible, the lack of superconducting signal makes it difficult to provide a better assessment, the simple fact that the critical temperature may be lower than our lowest temperature cannot be excluded. This possibility is relevant when considering the fact, that already bulk 2H-NbS_2 features a lower critical temperature of $T_c \approx 6\,K$ [12, 18, 19] compared to the 7.2 K of bulk 2H-$NbSe_2$ [66]. For the monolayer H-$NbSe_2$ the T_c shrinks by 5.3 K and features a value of 1.9 K [22]. A similar reduction would drive the NbS_2 respective T_c to 0.7 K, which is above our lowest temperature, but may be inaccessible due the virtual temperature of the tunnel junction of about 0.9 K. Therefore the possibility of a T_c in the range of 0.5 K can not be excluded.

V. SUMMARY

In summary we present a comprehensive characterization of the electronic properties of quasi-freestanding H-NbS_2 monolayers grown in situ on Gr/Ir(111) by low-temperature STM and STS. We investigated electronic footprints and temperature dependence of the 3×3 modulation pattern found before in NbS_2 monolayers and unambiguously link the modulation to a charge density wave phenomenon. Our experimental data points towards a weak driving force, possibly in the picture of Fermi surface nesting. We demonstrate the possible influence of inelastic phonon scattering and the influence the island edges have on the electronic structure. The band structure in the occupied and unoccupied states is investigated by STS point spectra and STS maps of QPI interference, demonstrating agreement with the electronic structure of freestanding NbS_2 monolayers in theoretical descriptions. We do not find any sign of magnetic interactions or superconductivity, with the absence of the latter possibly being connected to the morphology of our NbS_2 monolayer islands.

ACKNOWLEDGMENTS

We acknowledge funding from Deutsche Forschungsgemeinschaft (DFG) through CRC 1238 (project number 277146847, subprojects A01, B06 and C01).

---

[1] J. Wilson and A. Yoffe, The transition metal dichalcogenides discussion and interpretation of the observed optical, electrical and structural properties, Advances in Physics **18**, 193 (1969).

[2] S. Manzeli, D. Ovchinnikov, D. Pasquier, O. V. Yazyev, and A. Kis, 2D transition metal dichalcogenides, Nature Reviews Materials **2**, 17033 (2017).

[3] B. Sipos, A. F. Kusmartseva, A. Akrap, H. Berger, L. Forró, and E. Tutiš, From Mott state to superconductivity in 1T-TaS$_2$, Nature Materials **7**, 960 (2008).

[4] S. Nagata, T. Aochi, T. Abe, S. Ebisu, T. Hagino, Y. Seki, and K. Tsutsumi, Superconductivity in the layered compound 2H-TaS$_2$, Journal of Physics and Chemistry of Solids **53**, 1259 (1992).

[5] K. Rossnagel, On the origin of charge-density waves in select layered transition-metal dichalcogenides, Journal of Physics: Condensed Matter **23**, 213001 (2011).

[6] R. E. Peierls, Quantum theory of solids (Clarendon Press, Oxford, 1955).

[7] M. D. Johannes and I. I. Mazin, Fermi surface nesting and the origin of charge density waves in metals, Physical Review B **77**, 165135 (2008).

[8] F. Weber, S. Rosenkranz, J.-P. Castellan, R. Osborn, R. Hott, R. Heid, K.-P. Bohnen, T. Egami, A. H. Said, and D. Reznik, Extended Phonon Collapse and the Origin of the Charge-Density Wave in $2H-$NbSe$_2$, Physical Review Letters **107**, 107403 (2011).

[9] J. Berges, E. G. C. P. van Loon, A. Schobert, M. Rösner, and T. O. Wehling, Ab initio phonon self-energies and fluctuation diagnostics of phonon anomalies: Lattice instabilities from Dirac pseudospin physics in transition metal dichalcogenides, Physical Review B **101**, 155107 (2020).

[10] P. Hofmann, M. M. Ugeda, A. Tamtögl, A. Ruckhofer, W. E. Ernst, G. Benedek, A. J. Martínez-Galera, A. Stróżecka, J. M. Gómez-Rodríguez, E. Rienks, M. F. Jensen, J. I. Pascual, and J. W. Wells, Strong-coupling charge density wave in a one-dimensional topological metal, Physical Review B **99**, 035438 (2019).

[11] C. van Efferen, J. Berges, J. Hall, E. van Loon, S. Kraus, A. Schobert, T. Wekking, F. Huttmann, E. Plaar, N. Rothenbach, K. Ollefs, L. M. Arruda, N. Brookes, G. Schönhoff, K. Kummer, H. Wende, T. Wehling, and T. Michely, A full gap above the Fermi level: the charge density wave of monolayer VS$_2$, Nature Communications **12**, 6837 (2021).

[12] W. G. Fisher and M. J. Sienko, Stoichiometry, structure, and physical properties of niobium disulfide, Inorganic Chemistry **19**, 39 (1980).

[13] I. Guillamón, H. Suderow, S. Vieira, L. Cario, P. Diener, and P. Rodière, Superconducting Density of States and Vortex Cores of 2H-NbS$_2$, Physical Review Letters **101**, 166407 (2008).

[14] C. Wen, Y. Xie, Y. Wu, S. Shen, P. Kong, H. Lian, J. Li, H. Xing, and S. Yan, Impurity-pinned incommensurate charge density wave and local phonon excitations in $2H-$ NbS$_2$, Physical Review B **101**, 241404 (2020).

[15] M. Leroux, M. Le Tacon, M. Calandra, L. Cario, M.-A. Méasson, P. Diener, E. Borrissenko, A. Bosak, and P. Rodière, Anharmonic suppression of charge density waves in $2H$-NbS$_2$, Physical Review B **86**, 155125 (2012).

[16] C. Heil, S. Poncé, H. Lambert, M. Schlipf, E. R. Margine, and F. Giustino, Origin of Superconductivity and Latent Charge Density Wave in NbS$_2$, Physical Review Letters **119**, 087003 (2017).

[17] R. Bianco, I. Errea, L. Monacelli, M. Calandra, and F. Mauri, Quantum Enhancement of Charge Density Wave in NbS$_2$ in the Two-Dimensional Limit, Nano Letters **19**, 3098 (2019).

[18] M. Van Maaren and G. Schaeffer, Superconductivity in group Va dichalcogenides, Physics Letters **20**, 131 (1966).

[19] C. Witteveen, K. Górnicka, J. Chang, M. Månsson, T. Klimczuk, and F. O. von Rohr, Polytypism and superconductivity in the NbS$_2$ system, Dalton Transactions **50**, 3216 (2021).

[20] R. Yan, G. Khalsa, B. T. Schaefer, A. Jarjour, S. Rouvimov, K. C. Nowack, H. G. Xing, and D. Jena, Thickness dependence of superconductivity in ultrathin NbS$_2$, Applied Physics Express **12**, 023008 (2019).

[21] Z. Wang, C.-Y. Cheon, M. Tripathi, G. M. Marega, Y. Zhao, H. G. Ji, M. Macha, A. Radenovic, and A. Kis, Superconducting 2D NbS$_2$ Grown Epitaxially by Chemical Vapor Deposition, ACS Nano **15**, 18403 (2021).

[22] M. M. Ugeda, A. J. Bradley, Y. Zhang, S. Onishi, Y. Chen, W. Ruan, C. Ojeda-Aristizabal, H. Ryu, M. T. Edmonds, H.-Z. Tsai, A. Riss, S.-K. Mo, D. Lee, A. Zettl, Z. Hussain, Z.-X. Shen, and M. F. Crommie, Characterization of collective ground states in single-layer NbSe$_2$, Nature Physics **12**, 92 (2016).

[23] F. Flicker and J. van Wezel, Charge order from orbital-dependent coupling evidenced by NbSe$_2$, Nature Communications **6**, 7034 (2015).

[24] M. Leroux, I. Errea, M. Le Tacon, S.-M. Souliou, G. Garbarino, L. Cario, A. Bosak, F. Mauri, M. Calandra, and P. Rodière, Strong anharmonicity induces quantum melting of charge density wave in $2H-$NbSe$_2$ under pressure, Physical Review B **92**, 140303 (2015).

[25] F. Weber, R. Hott, R. Heid, L. L. Lev, M. Caputo, T. Schmitt, and V. N. Strocov, Three-dimensional Fermi surface of $2H-$NbS$_2$: Implications for the mechanism of charge density waves, Physical Review B **97**, 235122 (2018).

[26] J. Á. Silva-Guillén, P. Ordejón, F. Guinea, and E. Canadell, Electronic structure of $2H$-NbSe$_2$ single-layers in the CDW state, 2D Materials **3**, 035028 (2016).

[27] F. Zheng and J. Feng, Electron-phonon coupling and the coexistence of superconductivity and charge-density wave in monolayer NbSe$_2$, Physical Review B **99**, 161119 (2019).

[28] X. Xi, L. Zhao, Z. Wang, H. Berger, L. Forró, J. Shan, and K. F. Mak, Strongly enhanced charge-density-wave order in monolayer NbSe$_2$, Nature Nanotechnology **10**, 765 (2015).

[29] D. Lin, S. Li, J. Wen, H. Berger, L. Forró, H. Zhou, S. Jia, T. Taniguchi, K. Watanabe, X. Xi, and M. S. Bahramy, Patterns and driving forces of dimensionality-dependent charge density waves in

2H-type transition metal dichalcogenides, Nature Communications **11**, 2406 (2020).

[30] R. Bianco, L. Monacelli, M. Calandra, F. Mauri, and I. Errea, Weak Dimensionality Dependence and Dominant Role of Ionic Fluctuations in the Charge-Density-Wave Transition of $NbSe_2$, Physical Review Letters **125**, 106101 (2020).

[31] E. G. C. P. van Loon, M. Rösner, G. Schönhoff, M. I. Katsnelson, and T. O. Wehling, Competing Coulomb and electron–phonon interactions in NbS_2, npj Quantum Materials **3**, 32 (2018).

[32] F. Güller, V. L. Vildosola, and A. M. Llois, Spin density wave instabilities in the NbS_2 monolayer, Physical Review B **93**, 094434 (2016).

[33] Y. Zhou, Z. Wang, P. Yang, X. Zu, L. Yang, X. Sun, and F. Gao, Tensile Strain Switched Ferromagnetism in Layered NbS_2 and $NbSe_2$, ACS Nano **6**, 9727 (2012).

[34] Y. Xu, X. Liu, and W. Guo, Tensile strain induced switching of magnetic states in $NbSe_2$ and NbS_2 single layers, Nanoscale **6**, 12929 (2014).

[35] R.-M. Stan, S. K. Mahatha, M. Bianchi, C. E. Sanders, D. Curcio, P. Hofmann, and J. A. Miwa, Epitaxial single-layer NbS_2 on Au(111): Synthesis, structure, and electronic properties, Phys. Rev. Materials **3**, 044003 (2019).

[36] C. E. Sanders, M. Dendzik, A. S. Ngankeu, A. Eich, A. Bruix, M. Bianchi, J. A. Miwa, B. Hammer, A. A. Khajetoorians, and P. Hofmann, Crystalline and electronic structure of single-layer TaS_2, Physical Review B **94**, 081404 (2016).

[37] H. M. Lefcochilos-Fogelquist, O. R. Albertini, and A. Y. Liu, Substrate-induced suppression of charge density wave phase in monolayer 1H-TaS_2 on Au(111), Physical Review B **99**, 174113 (2019).

[38] A. Devarakonda, H. Inoue, S. Fang, C. Ozsoy-Keskinbora, T. Suzuki, M. Kriener, E. K. L. Fu, D. C. Bell, and J. G. Checkelsky, Clean 2D superconductivity in a bulk van der Waals superlattice, Science **370**, 231 (2020).

[39] W. Bai, P. Li, S. Ju, C. Xiao, H. Shi, S. Wang, S. Qin, Z. Sun, and Y. Xie, Monolayer Behavior of NbS_2 in Natural van der Waals Heterostructures, The Journal of Physical Chemistry Letters **9**, 6421 (2018).

[40] H. Lin, W. Huang, K. Zhao, C. Lian, W. Duan, X. Chen, and S.-H. Ji, Growth of atomically thick transition metal sulfide films on graphene/6H-SiC(0001) by molecular beam epitaxy, Nano Research **11**, 4722 (2018).

[41] J. Hall, B. Pielić, C. Murray, W. Jolie, T. Wekking, C. Busse, M. Kralj, and T. Michely, Molecular beam epitaxy of quasi-freestanding transition metal disulphide monolayers on van der Waals substrates: a growth study, 2D Materials **5**, 025005 (2018).

[42] W. J. Kaiser and R. C. Jaklevic, Spectroscopy of electronic states of metals with a scanning tunneling microscope, IBM Journal of Research and Development **30**, 411 (1986).

[43] R. C. J. M. P. Everson, L. C. Davis and W. Shen, Effects of surface features upon the Au(111) surface state local density of states studied with scanning tunneling spectroscopy, Journal of Vacuum Science & Technology B **9**, 891 (1991).

[44] X. Wang, J. Lin, Y. Zhu, C. Luo, K. Suenaga, C. Cai, and L. Xie, Chemical vapor deposition of trigonal prismatic NbS_2 monolayers and 3R-polytype few-layers, Nanoscale **9**, 16607 (2017).

[45] J. Hall, N. Ehlen, J. Berges, E. van Loon, C. van Efferen, C. Murray, M. Rösner, J. Li, B. V. Senkovskiy, M. Hell, M. Rolf, T. Heider, M. C. Asensio, J. Avila, L. Plucinski, T. Wehling, A. Grüneis, and T. Michely, Environmental Control of Charge Density Wave Order in Monolayer 2H-TaS_2, ACS Nano **13**, 10210 (2019).

[46] M. Spera, A. Scarfato, A. Pásztor, E. Giannini, D. R. Bowler, and C. Renner, Insight into the Charge Density Wave Gap from Contrast Inversion in Topographic STM Images, Physical Review Letters **125**, 267603 (2020).

[47] R. Feenstra, J. A. Stroscio, and A. Fein, Tunneling spectroscopy of the Si(111)2 × 1 surface, Surface Science **181**, 295 (1987).

[48] J. Tersoff and D. R. Hamann, Theory and Application for the Scanning Tunneling Microscope, Physical Review Letters **50**, 1998 (1983).

[49] C. Heil, M. Schlipf, and F. Giustino, Quasiparticle GW band structures and Fermi surfaces of bulk and monolayer NbS_2, Phys. Rev. B **98**, 075120 (2018).

[50] M. F. Crommie, C. P. Lutz, and D. M. Eigler, Imaging standing waves in a two-dimensional electron gas, Nature **363**, 524 (1993).

[51] Y. Hasegawa and P. Avouris, Direct observation of standing wave formation at surface steps using scanning tunneling spectroscopy, Physical Review Letters **71**, 1071 (1993).

[52] G. Hörmandinger, Imaging of the Cu(111) surface state in scanning tunneling microscopy, Physical Review B **49**, 13897 (1994).

[53] M. Spera, A. Scarfato, E. Giannini, and C. Renner, Energy-dependent spatial texturing of charge order in 1T-Cu_xTiSe_2, Physical Review B **99**, 155133 (2019).

[54] D. Stoltz, M. Bielmann, M. Bovet, L. Schlapbach, and H. Berger, Tunneling evidence for spatial location of the charge-density-wave induced band splitting in $1T-$$TaSe_2$, Physical Review B **76**, 073410 (2007).

[55] H. L. Edwards, D. J. Derro, A. L. Barr, J. T. Markert, and A. L. de Lozanne, Spatially Varying Energy Gap in the CuO Chains of $YBa_2Cu_3O_{7-x}$ Detected by Scanning Tunneling Spectroscopy, Physical Review Letters **75**, 1387 (1995).

[56] J. Dai, E. Calleja, J. Alldredge, X. Zhu, L. Li, W. Lu, Y. Sun, T. Wolf, H. Berger, and K. McElroy, Microscopic evidence for strong periodic lattice distortion in two-dimensional charge-density wave systems, Physical Review B **89**, 165140 (2014).

[57] Y. Nishio, M. Shirai, N. Suzuki, and K. Motizuki, Role of Electron-Lattice Interaction in Layered Transition Metal Dichalcogenide $2H-NbS_2$. I. Phonon Anomaly and Superconductivity, Journal of the Physical Society of Japan **63**, 156 (1994).

[58] M. Leroux, L. Cario, A. Bosak, and P. Rodière, Traces of charge density waves in NbS_2, Physical Review B **97**, 195140 (2018).

[59] G. Grüner, Density Waves In Solids (1st ed.) (Taylor & Francis, 1994).

[60] M. F. Crommie, C. P. Lutz, and D. M. Eigler, Confinement of Electrons to Quantum Corrals on a Metal Surface, Science **262**, 218 (1993).

[61] M. Crommie, C. Lutz, D. Eigler, and E. Heller, Quantum interference in 2D atomic-scale structures, Surface Science **361-362**, 864 (1996).

[62] P. de Trey, S. Gygax, and J.-P. Jan, Anisotropy of the Ginzburg-Landau parameter κ in $NbSe_2$, Journal of Low Temperature Physics **11**, 421 (1973).

[63] A. Nader and P. Monceau, Critical field of 2H-$NbSe_2$ down to 50mK, SpringerPlus **3**, 16 (2014).

[64] K. Onabe, M. Naito, and S. Tanaka, Anisotropy of Upper Critical Field in Superconducting 2H-NbS_2, Journal of the Physical Society of Japan **45**, 50 (1978).

[65] C. Rubio-Verdú, A. M. García-García, H. Ryu, D.-J. Choi, J. Zaldívar, S. Tang, B. Fan, Z.-X. Shen, S.-K. Mo, J. I. Pascual, and M. M. Ugeda, Visualization of Multifractal Superconductivity in a Two-Dimensional Transition Metal Dichalcogenide in the Weak-Disorder Regime, Nano Letters **20**, 5111 (2020).

[66] E. Revolinsky, E. Lautenschlager, and C. Armitage, Layer structure superconductor, Solid State Communications **1**, 59 (1963).

7.1 Supporting Information

Supporting Information

POSITION-DEPENDENT STS POINT SPECTRA AT THE EDGE AND IN THE CENTER OF A NbS_2 ISLAND

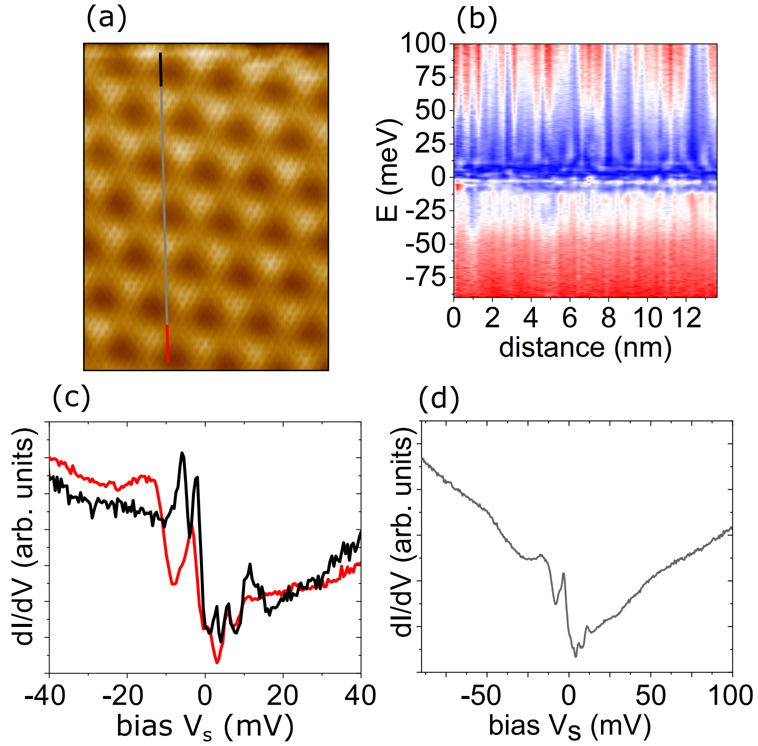

FIG. S1. Constant height STS point spectra recorded on NbS_2 along a line. (a) Constant height STM image of an NbS_2 island (size 10 nm × 15 nm, $V_s = 100\,\mathrm{mV}$, $I_t = 1.0\,\mathrm{nA}$). (b) Color plot of 75 constant height STS spectra measured along the line in (a) from the edge of the island [black in (a)] towards the middle [red in (a)]. The dI/dV signal in each spectrum has been normalized between 0 and 1. Large dI/dV signal is shown in red, small dI/dV signal is shown in blue. (c) Average of the first (last) 7 STS spectra close to the edge (center) of the island. The positions are marked in black and red accordingly in (a). (d) Average of the complete set of 75 spectra. STS parameters: $V_{\mathrm{stab}} = 100\,\mathrm{mV}$, $I_{\mathrm{stab}} = 1.0\,\mathrm{nA}$, $V_{\mathrm{mod}} = 0.5\,\mathrm{mV}$, $f_{\mathrm{mod}} = 497\,\mathrm{Hz}$, $T_s = 0.4\,\mathrm{K}$.

CHAPTER 8

Manuscript 2: Post-Growth Intercalation at the Interface of Graphene and Monolayer NbS_2

This chapter consists of the above-named manuscript and its supplement, in preparation for submission to a publishing journal.

The experiments were proposed by T. Knispel, D. Mohrenstecher, J. Fischer and T. Michely based on the Master thesis of C. Speckmann. Sample growth and experiments were conducted at the low temperature magnetic STM system (MSTM) and a variable temperature STM system (TUMAII) in our group. Sample growth and LEED, STM and STS experiments were carried out by T. Knispel and D. Mohrenstecher under the guidance of J. Fischer and advice from T. Michely. Data analysis was performed by T. Knispel and D. Mohrenstecher.

Y. Falke, A. Grüneis and N. Atodiresei made a significant contribution to the discussion of the experimental results.

T. Knispel wrote the manuscript and finalized it in close collaboration with J. Fischer and T. Michely.

Some of the results in this chapter can be found in the Master thesis of D. Mohrenstecher.

Post-growth intercalation at the interface of graphene and monolayer NbS_2

Timo Knispel,[1] Daniela Mohrenstecher,[1] Carsten Speckmann,[1,2] Yannic Falke,[1]
Alexander Grüneis,[1] Nicolae Atodiresei,[3] Jeison Fischer,[1] and Thomas Michely[1]

[1]*II. Physikalisches Institut, Universität zu Köln,*
Zülpicher Straße 77, 50937 Köln, Germany
[2]*Physics of Nanostructured Materials, Universität Wien,*
Boltzmanngasse 5, 1090 Wien, Austria
[3]*Peter Grünberg Institut und Institute for Advanced Simulation,*
Forschungszentrum Jülich, Wilhelm-Johnen-Straße, 52428 Jülich, Germany

(Dated: March 30, 2022)

Abstract

Intercalation of a foreign species into the van der Waals gap of two layers of the same layered material is a well known tool to design the properties of layered bulk crystals and thin films. Here, intercalation into the van der Waals gap of a vertical stack consisting out of two monolayers of different two-dimensional materials is demonstrated. The concept is exemplified experimentally for a heterostack consisting of a monolayer NbS_2 and graphene. Intercalation of the van der Waals gap is either accomplished by post-growth annealing of the heterostack in the absence of a stabilizing S background or through Nb deposition onto the preformed heterostack at an elevated temperature below the destabilization of NbS_2. The latter method can also be applied to intercalate species chemically distinct from the constituents of the heterostack as is demonstrated for Fe intercalation at the interface of NbS_2 and graphene. Scanning tunneling microscopy and -spectroscopy are used to follow the intercalation process, to uncover its details, and to determine the structure of the new compound material formed.

I. INTRODUCTION

Intercalation is the insertion of atoms (or molecules) into the space between individual layers of a layered material [1–3]. The atoms within a layer of such a material are strongly bound to each other, whereas the interaction between the layers is much weaker and often dominated by van der Waals (vdW) interactions. Intercalation of species into the vdW gap between the layers has been proven to be a strong lever to change the properties of layered bulk crystals. To give two examples in recent research: upon intercalation of alkali atoms black phosphorus becomes superconducting [4], or by switching the antiferromagnetic order in Fe-intercalated NbS_2 with current pulses, information can be written to the material [5]. Besides of fundamental interest in phase transformations and property changes, reversible intercalation is the fundamental principle for the operation of Li ion batteries in both, the cathode (in early days TiS_2 [6]) and the anode (typically graphite [7]).

When thinning down a layered material to few or single layers it becomes a two-dimensional (2D) material. 2D materials have become an area of intense research in the last decade because of their unique properties distinct from their bulk counterpart, often related to poor electronic screening in turn giving rise to strong electronic correlations [8–10]. Consequently, intercalation has recently demonstrated the same power of inducing phase transition and property changes when applied to thin flakes and few layer 2D materials [11–14]. Also for a monolayer 2D materials intercalation is applicable: when placed on a substrate, again a vdW gap may arise. Intercalation into this gap has been shown the ability to not only modify the properties of the monolayer, but also to decouple the layer further to a quasi-freestanding state [15–18].

Currently the flexibility to create new properties by stacking single 2D layers of different composition, e.g, different semiconducting transition metal dichalcogenides (TMDCs) [19, 20], has moved into the focus of research. It is obvious that post-growth insertion of atoms or molecules into the vdW gaps of such heterostacks of monolayer 2D materials through intercalation provides a new strong tool for the property design of such 2D layer stacks. Indeed, with a strong focus on Li intercalation for energy storage, calculations and theoretical literature on the intercalation of heterostacks appear to flourish [21–27], while there are just a few experimental publications on the topic reporting electrochemical Li intercalation of MoS_2/Gr/h-BN, MoS_2/h-BN and h-BN/Gr heterostacks [28–30].

The research documented with the present manuscript provides a different pathway for intercalation of heterostacks and for elements other than Li. Instead of using electrochemical methods, the intercalating species is provided from the vapor phase or by thermal decomposition under ultra-high vacuum conditions. Intercalation into the interface of a heterostack is first investigated for the special case where the intercalating species is chemically identical to one of the atomic species of the 2D layers constituting the gap [12, 31]. This case of self-intercalation is demonstrated here for Nb intercalation into a NbS_2/Gr vertical heterostructure. The methods developed can also be applied to species being chemically dissimilar to the constituents of the heterostack, as exemplified for Fe intercalation of NbS_2/Gr. Thereby the possibilities for tuning the properties of heterostacks are vastly enlarged.

Since NbS_2 is of specific interest in the present manuscript, we briefly summarize its properties. Bulk NbS_2 is metallic and the Nb atoms display trigonal-prismatic coordination to S with either rhombohedral 3R-NbS_2 or hexagonal 2H-NbS_2 layer stacking [31, 32]. Bulk 2H-NbS_2 is a superconductor below $T_c \approx 6\,\mathrm{K}$ [32–34] and down to 4-6 nm thickness [35, 36]. No superconducting behavior is reported so far for monolayer NbS_2. Bulk 2H-NbS_2 displays no charge density wave (CDW) [32, 37, 38], while for the monolayer conflicting results are reported: on Gr a 3×3 − superstructure indicative of a CDW [39] is observed, while superstructures are absent in the NbS_2 monolayer on Au(111) [40].

Self-intercalation of Nb at the octahedral sites of the vdW gap in bulk NbS_2 has been reported by Jellinek as early as 1960 [31] and recently been shown to provide an excellent catalyst for the hydrogen evolution reaction [41]. Also metal rich compounds featuring NiAs structure with the stoichiometry NbS have been investigated [42]. Cr, Mn, V, Co, Fe and Ni intercalation compounds of 2H-NbS_2 with composition $M_{1/3}$H-NbS_2 are all magnetically ordered [43–46], making these elements of interest for intercalation of a heterostack involving an NbS_2 layer.

II. EXPERIMENTAL METHODS

Sample preparation was accomplished in two different molecular beam epitaxy (MBE) systems, both with a base pressure of $p < 2 \times 10^{-10}\,\mathrm{mbar}$ and equipped with or connected to a scanning tunneling microscope (STM). Ir(111) was prepared by cycles of keV Ar^+ sputtering and flash annealing to 1520 K. Subsequently, Gr was grown by room temperature ethylene exposure of Ir(111) to saturation, subsequent flash annealing to 1470 K, and finally followed by exposure to ≈ 800 L of ethylene at 1370 K. As confirmed by STM and low energy electron diffraction (LEED), this recipe results in a closed single crystal Gr monolayer on Ir(111) [47].

Monolayer H-$\mathrm{NbS_2}$ was prepared by exposing Gr/Ir(111) to a Nb flux of $\approx 6 \times 10^{15}\,\mathrm{atoms/m^2s}$ from an e-beam evaporator in a background pressure of $\approx 8 \times 10^{-9}\,\mathrm{mbar}$ elemental S, supplied by a pyrite filled Knudsen cell about 10 cm distant from the sample. Growth was conducted for about 510 s at room temperature, followed by annealing to 820 K for 360 s with the pyrite filled Knudsen cell turned off. Since the S pressure drops only slowly and as during heating also S adsorbed during the growth step desorbs from the environment of the sample holder, the S partial pressure during annealing is smaller than $8 \times 10^{-9}\,\mathrm{mbar}$, but non-zero. This growth procedure results in an ordered monolayer island coverage [48] of about 0.35 ML.

Intercalation at the interface of Gr with H-$\mathrm{NbS_2}$ was achieved by additional annealing of H-$\mathrm{NbS_2}$, as well as by deposition of elemental Nb and Fe onto the H-$\mathrm{NbS_2}$ sample at different temperatures, partly followed by annealing steps. The details are given where the respective data is discussed.

After synthesis, the samples were investigated in situ by STM, either at 300 K directly in the MBE system or at 1.7 K after transfer into a bath cryostat with STM. In both systems the constant current mode was utilized to measure the sample topography. STS was conducted within the bath cryostat at constant height. To ensure a reproducible and flat tip density of states (DOS), Au covered W-tips calibrated using the surface state of Au(111) [49, 50] were used for STS. Constant current STM topographs were recorded with sample bias V_s and tunneling current I_t specified in each figure. Constant height STS dI/dV point spectra were recorded with stabilization bias V_stab and stabilization current I_stab using a lock-in amplifier with a modulation frequency f_mod and modulation voltage V_mod, also specified in the captions.

III. CONCEPTS FOR INTERCALATION OF A HETEROSTACK

Our course of action to achieve (self)-intercalated TMDC/Gr monolayer heterostacks is depicted in Fig. 1. Fig. 1 (a) displays the H-NbS_2 monolayer we grow on Gr/Ir(111) as described in Section II. It consists of a Nb layer (blue), sandwiched in between two layers of S (yellow). The bonding within the sandwich layer is of covalent nature. In between the NbS_2 and the Gr substrate, a vdW gap is present. The first way to intercalate material into the gap is to heat up the sample to a temperature T_d that causes the NbS_2 to partially dissolve [Fig. 1 (b)]. While the freed S escapes (either into vacuum or to Ir(111), Nb from the monolayer moves into the vdW gap between the monolayer of NbS_2 and the Gr substrate. The resulting compound is expected to possess an increased height $d' = d + \Delta d$ in STM, compared to the height d of the pristine monolayer. Upon partly dissociating the NbS_2 monolayer, causing the Nb to move into the vdW gap, the total sample coverage decreases.

The second way to intercalate the NbS_2/Gr heterostack is deposition of additional material from the vapor phase onto the sample and subsequent heating [Fig. 1 (c)], with the material being provided by the same e-beam evaporator used to grow the NbS_2 monolayer as described in Section II. When arriving on the surface, the deposited material moves into the vdW gap between the NbS_2 monolayer and the Gr substrate, creating a similar situation as depicted in Fig. 1 (b), with an increase in height of the compound. This method is used for intercalation by deposition of elemental Nb, as well as of elemental Fe.

IV. SELF-INTERCALATION OF THE MONOLAYER NbS_2/Gr HETEROSTACK BY NbS_2 DISSOCIATION

This section describes self-intercalation of monolayer H-NbS_2/Gr heterostacks by heating to above the dissociation temperature T_d of H-NbS_2.

Fig. 2 (a) displays the topography of the pristine NbS_2 monolayer islands. The NbS_2 was grown as described in Section II, involving an annealing step to 820 K. The islands cover about 0.34 ML of the surface, are continuous also in areas where the substrate Gr layer is deformed due to overgrowth of monoatomic Ir steps, and are of irregular shape. A height profile along the black line is shown below the topograph. All islands feature an apparent height of $d = 0.63$ nm, indicating phase purity. The height fits reasonably well to the height of 0.578 nm found for monolayer H-NbS_2 on Gr/6H-SiC(0001) [39] and to half of the c-axis lattice constant 1.195 nm of bulk 2H-NbS_2 [32]. It should be

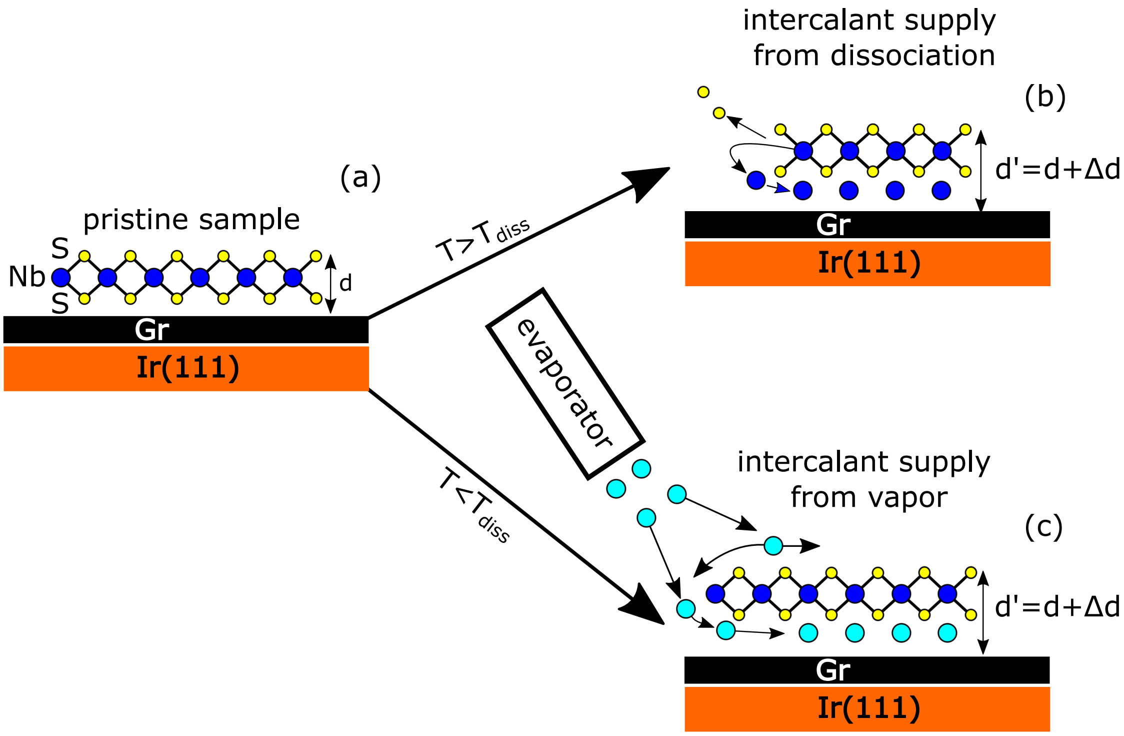

FIG. 1. Concept of intercalation for the heterostack H-NbS_2/Gr on Ir(111). (a) Structure of the H-NbS_2 monolayer on Gr/Ir(111). (b) Self-intercalation of NbS_2/Gr by heating and dissociation. (c) Intercalation of the NbS_2/Gr heterostack with Nb or other elements supplied from the vapor.

noted that the apparent heights measured by STM in this work generally vary by about ±0.02 nm depending on the tunneling condition. Heights stated in the following therefore are always an average value regarding the variation. Whether the NbS_2 islands are grown in the H-phase (Nb atoms in trigonal-prismatic coordination) or in the T-phase (Nb atoms in octahedral coordination) cannot be determined by STM. Since bulk NbS_2 [32] and monolayer NbS_2 on Au(111) [40] grow in the H-phase, it is reasonable to assume that this holds for NbS_2 on Gr as well.

Upon annealing the sample to 920 K for 360 s [Fig. 2 (b)], the total coverage decreases to about 0.29 ML. Within the pristine NbS_2 monolayer islands, higher triangular shaped areas emerge. In these areas, height profiles give an increased apparent height of $d' = 1.00\,\mathrm{nm}$. These areas are designated as Nb $\sqrt{3} \times \sqrt{3}$ – phase for reasons discussed below.

After annealing the same sample to 1020 K for 360 s [Fig. 2 (c)], all islands display a uniform height again. The height profile along the black line, shown below the STM topograph, gives an apparent height of $d' = 1.00\,\mathrm{nm}$, consistent with the assumption that all islands transformed entirely to the Nb $\sqrt{3} \times \sqrt{3}$ – phase. The total coverage after this annealing step decreased further to 0.17 ML, about half the initial coverage. Since no other significant changes of the morphology

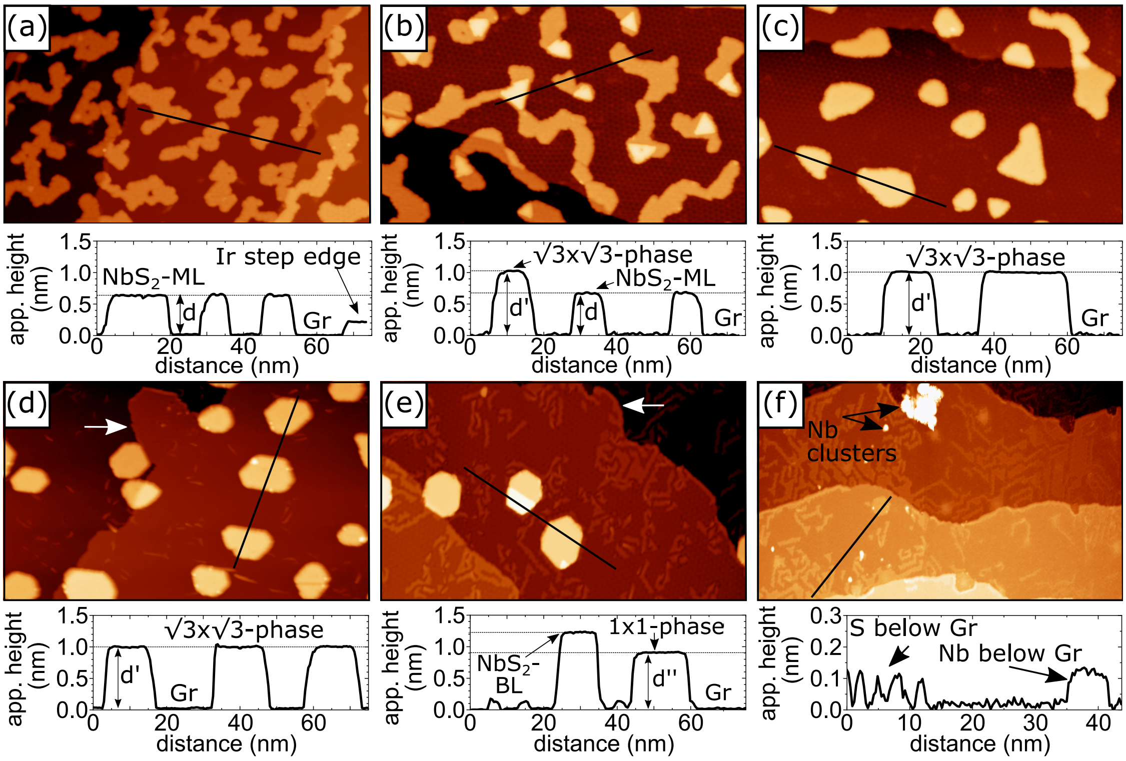

FIG. 2. STM topographs of pristine NbS_2 monolayer islands annealed up to 1220 K without supplying additional S. Height profiles along the black line in the STM topographs are shown below the topographs. (a) Pristine NbS_2 grown including annealing to 820 K for 360 s (compare Section II). (b) After additional annealing to 920 K for 360 s. (c) After additional annealing to 1020 K for 360 s. (d) After additional annealing to 1120 K for 360 s. (e) After additional annealing to 1220 K for 360 s. (f) After additional annealing to 1320 K for 360 s. Image information: (a) size 150 nm×90 nm, V_s =1.0 V, I_t = 0.23 nA; (b) size 150 nm×90 nm, V_s = 0.95 V, I_t = 0.34 nA; (c) size 150 nm×90 nm, V_s = 1.0 V, I_t = 0.26 nA; (d) size 150 nm×90 nm, V_s = 0.92 V, I_t = 0.33 nA; (e) size 150 nm×90 nm, V_s = 1.0 V, I_t = 0.32 nA; (f) size 120 nm×72 nm, V_s = 2.2 V, I_t = 0.06 nA.

are visible, we tentatively attribute the substantial reduction in island area and the height increase of the islands to $d' = 1.00$ nm, to NbS_2 dissociation. We note that the height $d' = 1.00$ nm is inconsistent with bilayer NbS_2, which should have an apparent height of ≈ 1.2 nm.

At first glance, annealing the sample to 1120 K for 360 s as shown in Fig. 2 (d), does not change the situation much. As evident from the height profile below the STM topograph, all islands still display a height $d' = 1.00$ nm characteristic for the Nb $\sqrt{3} \times \sqrt{3}$ – phase. The islands appear mostly hexagonal after this annealing step. However, the NbS_2 island coverage further decreases to 0.12 ML and new features appear as highlighted by the white arrow. It marks an island attached to an Ir step edge of similar height as the Ir step height. We attribute these islands to be Nb that penetrated the Gr sheet and intercalated between Gr and Ir(111). Indeed, Nb directly deposited on Ir(111) after annealing displays pseudomorphic islands on the terrace and attaches to steps of Ir, featuring approximately the Ir step height (data not shown).

After annealing to 1120 K it was also possible to laterally shift the monolayer NbS_2 islands by the STM tip (see Fig. S1 (a) in the supporting information). The Gr, initially underneath the islands, displayed neither structural nor height changes. Thereby it is ruled out that the height increase to $d' = 1.00\,\mathrm{nm}$ is caused by changes in the Gr height level, e.g. by intercalation of S or Nb in between Gr and the Ir(111) substrate underneath the islands.

Subsequent annealing to 1220 K (360 s) with the result shown in Fig. 2 (e), causes substantial changes of the morphology as now again two different height levels are present, of which none coincides with the aforementioned ones. As obvious from the height profile shown below the STM topograph, a height of $d'' = 0.91\,\mathrm{nm}$ is found, which is slightly, but unambiguously lower than the apparent height of the Nb $\sqrt{3} \times \sqrt{3} -$ phase. We designate areas with this height level as Nb $1 \times 1 -$ phase for reasons that become evident below. Moreover, a second height level of 1.23 nm is apparent, which is close to the height of unannealed bilayer islands (data not shown). The total NbS_2 island coverage is reduced further to 0.10 ML, with 0.03 ML in bilayers. Besides bulges in the Ir step edges (white arrow) that were already interpreted as Nb intercalated below Gr, also stripes and patches with an apparent height of about 0.1 nm with respect to the Gr base level are prominent now. In LEED $(\sqrt{3} \times \sqrt{3})\mathrm{R}30^\circ$ spots with respect to Ir(111) are present (compare Fig. S2 in the supporting information). S is well known to form a $(\sqrt{3} \times \sqrt{3})\mathrm{R}30^\circ$ superstructure on Ir(111) and in between Ir(111) and Gr [51]. Thus it is unambiguous that these stripes and patches are due to S intercalation between Gr and Ir(111). In lower concentration these stripes are already present at lower annealing temperature [compare Fig. 2 (d)]. S intercalation between Gr and Ir(111) is similarly also observed for growth of other TMDCs [48, 52].

The final annealing step to 1330 K leads to the entire decomposition of NbS_2 and no more NbS_2 islands are visible. Large metallic Nb clusters are present in the STM topograph, as well as large patches of intercalated S and islands of intercalated Nb highlighted through the height profile below the STM topograph.

To justify our designation of the 0.63 nm, 1.00 nm, and 0.91 nm high islands as pristine NbS_2, Nb $\sqrt{3}\times\sqrt{3}-$phase, and Nb $1\times1-$phase, we present atomically resolved STM images of the structures in Fig. 3 (a), (c) and (e). From the STM image of an area on a pristine NbS_2 monolayer island in Fig. 3 (a), one obtains a lattice parameter of 0.32(2) nm, in good agreement with values found for the NbS_2 monolayers on bilayer Gr/6H-SiC(0001) (0.334 nm) [39] and bulk 2H-NbS_2 (0.3324 nm) [32].

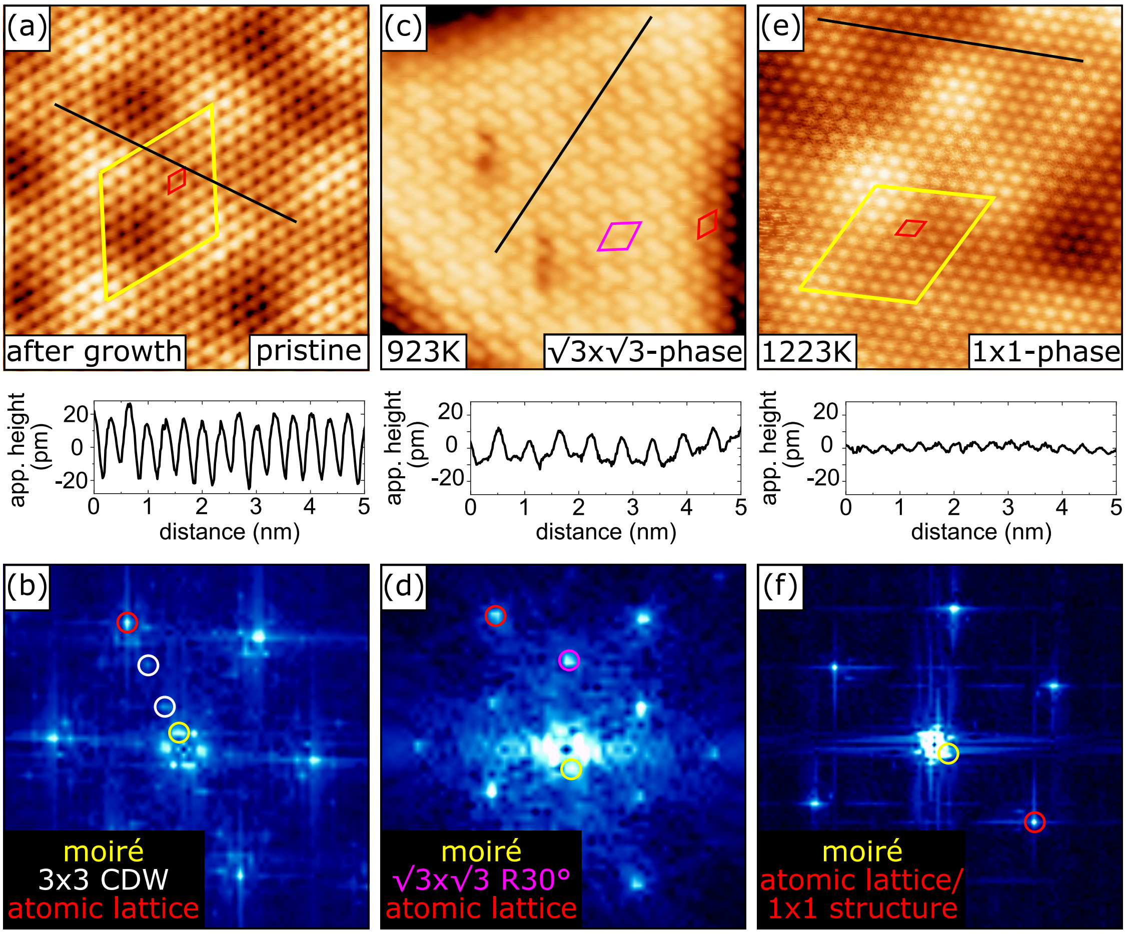

FIG. 3. STM topographs with atomic resolution of (a) the pristine monolayer NbS_2, (c) the Nb $\sqrt{3} \times \sqrt{3} -$ phase, and (e) the Nb $1 \times 1 -$ phase taken at 1.7 K, together with corresponding fast Fourier transforms (FFTs) in (b), (d) and (f). In the STM topographs the unit cell of NbS_2 is marked by a red rhomboid, the moiré of Gr and Ir(111), superimposed to the NbS_2 lattice, is marked by a yellow rhomboid, and the unit cell of the $(\sqrt{3} \times \sqrt{3})$R30° superstructure by a pink rhomboid. The atomic corrugation is shown by height profiles along the black lines below the topographs. Image information: (a) size $7\,\mathrm{nm} \times 7\,\mathrm{nm}$, $V_\mathrm{s} = 50\,\mathrm{mV}$, $I_\mathrm{t} = 0.5\,\mathrm{nA}$, $T_\mathrm{s} = 1.7\,\mathrm{K}$; (c) size $7\,\mathrm{nm} \times 7\,\mathrm{nm}$, $V_\mathrm{s} = 100\,\mathrm{mV}$, $I_\mathrm{t} = 0.80\,\mathrm{nA}$, $T_\mathrm{s} = 1.7\,\mathrm{K}$; (e) size $7\,\mathrm{nm} \times 7\,\mathrm{nm}$, $V_\mathrm{s} = 100\,\mathrm{mV}$, $I_\mathrm{t} = 0.70\,\mathrm{nA}$, $T_\mathrm{s} = 1.7\,\mathrm{K}$.

The atomic corrugation is in the order of 35 pm as apparent from the height profile along the black line shown below the topograph. The moiré of Gr and Ir(111) is superimposed to the NbS_2 monolayer (yellow rhomboid). In the fast Fourier transform (FFT) of the topograph in Fig. 3 (b), both the moiré reflections, as well as the first order reflections of the NbS_2 atomic lattice are indicated. Additionally a 3×3 periodicity is visible, marked by white circles at 1/3 and 2/3 of the distance between the center and the first order reflections. This feature, also found on monolayer NbS_2 on Gr/6H-SiC(0001) [39], is due to a CDW in monolayer NbS_2 [53]. It is not visible in the STM topograph, because the moiré and atomic patterns dominate.

An atomically resolved area of an NbS_2 island in the Nb $\sqrt{3} \times \sqrt{3}$ – phase is shown in Fig. 3 (c). It displays a clear $(\sqrt{3} \times \sqrt{3})$R30° superstructure with respect to the NbS_2 lattice, which is also apparent in the FFT of Fig. 3 (d). The superstructure results from a height modulation in the order of 15 pm. Apparently, the atomic positions are unchanged. The FFT of Fig. 3 (d) displays no more spots of the CDW. At the island edges and at defects the $(\sqrt{3} \times \sqrt{3})$R30° superstructure fades away, while the atomic periodicity is still present. Surprisingly, in LEED no spots of a $(\sqrt{3} \times \sqrt{3})$R30° superstructure with respect to NbS_2 are visible, although first order reflections of the NbS_2 islands being aligned with the Gr lattice are present (see Fig. S2 in the supporting information).

In Fig. 3 (e) an atomically resolved image of an island area in the Nb 1×1 – phase is displayed and Fig. 3 (c) shows the corresponding FFT. Also the Nb 1×1 – phase displays the eponymous structure atomically resolved, with the same lattice parameter as found for pristine monolayer NbS_2. It is distinct from pristine NbS_2 because: (i) it differs in height (0.91 nm vs. 0.63 nm); (ii) the 3×3 CDW is absent [Fig. 3(f)]; (iii) the atomic corrugation is only in the order of 5 pm, reduced by about a factor 7 compared to the pristine NbS_2; and (iv) the moiré contrast is considerably weaker.

Pristine NbS_2, the Nb $\sqrt{3} \times \sqrt{3}$ – phase, and the Nb 1×1 – phase differ not only in apparent height and structure, but also in electronic structure as visible in Fig. 4. All STS point spectra, were measured with Au covered STM tips providing a flat DOS and highly reproducible spectra. It is obvious that the three spectra of the three phases are grossly different. The spectrum of pristine NbS_2 agrees well with features deduced from the density functional theory (DFT) calculated band structure by van Loon et al. [54], as discussed in Ref. [53]. Interpretation of the disparities in the spectra of the three phases is beyond the scope of this manuscript and just emphasizes their substantial difference.

Taken together we interpret our results as follows: Upon annealing to 1020 K NbS_2 monolayer islands partly dissociate by loss of S. The released Nb intercalates between the NbS_2 islands and Gr forming a $(\sqrt{3} \times \sqrt{3})$R30° superstructure with respect to NbS_2. This assumption is consistent with (i) the increased height; (ii) the reduction of NbS_2 island coverage; (iii) the absence of a modified height of the Gr underneath the islands when they are removed by the STM tip; (iv) the observed $(\sqrt{3} \times \sqrt{3})$R30° superstructure; (v) the absence of $(\sqrt{3} \times \sqrt{3})$R30° superstructure diffraction spots in LEED; (vi) the continuous merge of the $(\sqrt{3} \times \sqrt{3})$R30° superstructure into the 1×1 structure at island edges; (vii) the reduced corrugation of the $(\sqrt{3} \times \sqrt{3})$R30° superstructure (15 pm) compared

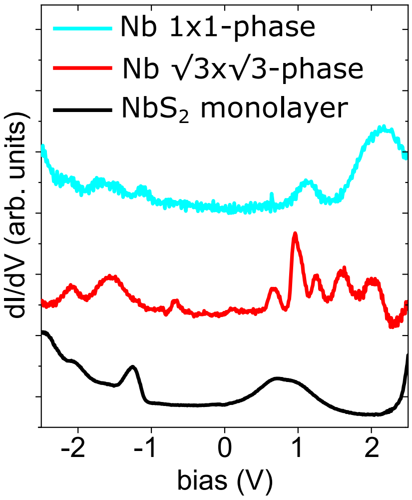

FIG. 4. (a) Constant height STS point spectra of pristine NbS_2 (black), the Nb $\sqrt{3} \times \sqrt{3}$ – phase (red), and the Nb 1×1 – phase (turquoise). Point spectra parameters: black: $V_{\mathrm{stab}} = 2.5\,\mathrm{V}$, $I_{\mathrm{stab}} = 1.0\,\mathrm{nA}$, $V_{\mathrm{mod}} = 15\,\mathrm{mV}$, $f_{\mathrm{mod}} = 797\,\mathrm{Hz}$, $T_{\mathrm{s}} = 1.7\,\mathrm{K}$; red: $V_{\mathrm{stab}} = 3\,\mathrm{V}$, $I_{\mathrm{stab}} = 0.8\,\mathrm{nA}$, $V_{\mathrm{mod}} = 10\,\mathrm{mV}$, $f_{\mathrm{mod}} = 797\,\mathrm{Hz}$, $T_{\mathrm{s}} = 1.7\,\mathrm{K}$; turquoise: $V_{\mathrm{stab}} = 2.5\,\mathrm{V}$, $I_{\mathrm{stab}} = 0.7\,\mathrm{nA}$, $V_{\mathrm{mod}} = 10\,\mathrm{mV}$, $f_{\mathrm{mod}} = 811\,\mathrm{Hz}$, $T_{\mathrm{s}} = 1.7\,\mathrm{K}$.

to the pristine NbS_2 (35 pm); (viii) the very different electronic structure from point spectra of the Nb $\sqrt{3} \times \sqrt{3}$ – phase compared to pristine NbS_2.

One could argue that the released Nb is not intercalated between Gr and the NbS_2 monolayer, but rests on top of the NbS_2 islands. In this case the absence of LEED spots (v) would be hardly understandable, while in the case of intercalation electron diffraction is diminished by two layers of sulfur and one layer of Nb above. Also one would expect a strong corrugation of the Nb $\sqrt{3} \times \sqrt{3}$ – phase due to the adsorbed Nb adatoms, while the corrugation is indeed lower (vii) and the $(\sqrt{3} \times \sqrt{3})\mathrm{R}30°$ structure smoothly merges into a 1×1 pattern at edges (vi).

For the formation of a $(\sqrt{3} \times \sqrt{3})\mathrm{R}30°$ Nb intercalation structure, 1/3 or 2/3 of the concentration of Nb in NbS2 is needed in the most simple scenario. This would result in $Nb_{4/3}S_2$ or $Nb_{5/3}S_2$ connected to a shrinkage of the pristine NbS_2 islands by 1/6 or 1/3 in areal coverage. The observed shrinkage in area by about a factor of 2 (from 34 % ML to 17 % ML) is consistent with this scenario, but may indicate that some Nb is already lost to the interface between Ir(111) and Gr [compare Fig. 2 (d)]. More complex scenarios involving rearrangement of the atomic positions and a composition Nb_2S_2 can also not be ruled out, as there is no clear evidence for Nb loss to under Gr at 1020 K.

Upon annealing to 1220 K the Nb 1×1 – phase forms, which is interpreted to result from additional NbS_2 dissociation giving rise to a full intercalation layer with a 1×1 structure underneath

NbS_2. The resulting global stoichiometry of the observed islands is then Nb_2S_2. This interpretation is consistent with (i) a height distinct from the pristine NbS_2 monolayer; (ii) the additional decrease of NbS_2 island coverage; (iii) the electronic structure being distinct from the pristine NbS_2 islands that also display a 1×1 structure; (iv) the continuous evolution of the Nb $1 \times 1-$phase out of the Nb $\sqrt{3} \times \sqrt{3}-$phase and their similarity in height and (v) the lowered corrugation compared to the pristine NbS_2 monolayers. The next section will provide additional evidence for our preliminary interpretation.

V. SELF-INTERCALATION OF THE NbS$_2$/Gr HETEROSTACK BY Nb DEPOSITION

In the last section it was demonstrated that pristine NbS_2 monolayer islands on Gr transform upon additional annealing to successively higher temperature into self-intercalated islands on Gr in the Nb $\sqrt{3} \times \sqrt{3}$ – phase (1020 K and 1120 K) and eventually in the Nb 1×1 – phase (1220 K). We argued that self-intercalation is triggered by a Nb excess resulting from gradual decomposition of NbS_2 monolayer islands due to annealing. If this rational is correct, one could expect self-intercalation to take place already at temperatures below T_d, if Nb is supplied from a different source.

To test this idea we fabricated pristine NbS_2 monolayer islands [compare Fig. 5 (a)]. Subsequently an amount Nb identical to what was used during growth is supplied at 820 K, that is the temperature of the annealing step during growth at which dissociation should be absent. As apparent in Fig. 5 (b), the pristine NbS_2 monolayer islands transformed by deposition into the Nb 1×1 – phase: the island height increased to 0.91 nm and the atomic resolution inset displays a 1×1 structure. Additionally small clusters of large height are present at the island edges. The island coverage only marginally decreased from 0.33 ML to 0.29 ML, while the formation of the Nb $1 \times 1-$phase by plain annealing in the absence of Nb supply required a temperature of 1220 K and involved a coverage decrease from 0.34 ML to 0.10 ML (compare Section IV). The sample remains in the Nb 1×1 – phase upon additional annealing to 1020 K with a marginal coverage drop to 0.26 ML as shown in Fig. 5 (c). Moreover, the clusters at the island edges largely disappeared. We finally note that islands in the Nb 1×1 – phase are especially easy to move with the STM, such that the topography is already hard to scan at room temperature without moving islands.

The interpretation is straightforward. Nb supplied in the absence of S vapor cannot react to NbS_2 and is thus intercalated at the interface of pristine NbS_2 and Gr. As the Nb supply is not limited, the maximum density of intercalation, i.e. the Nb 1×1 – phase, is realized. The

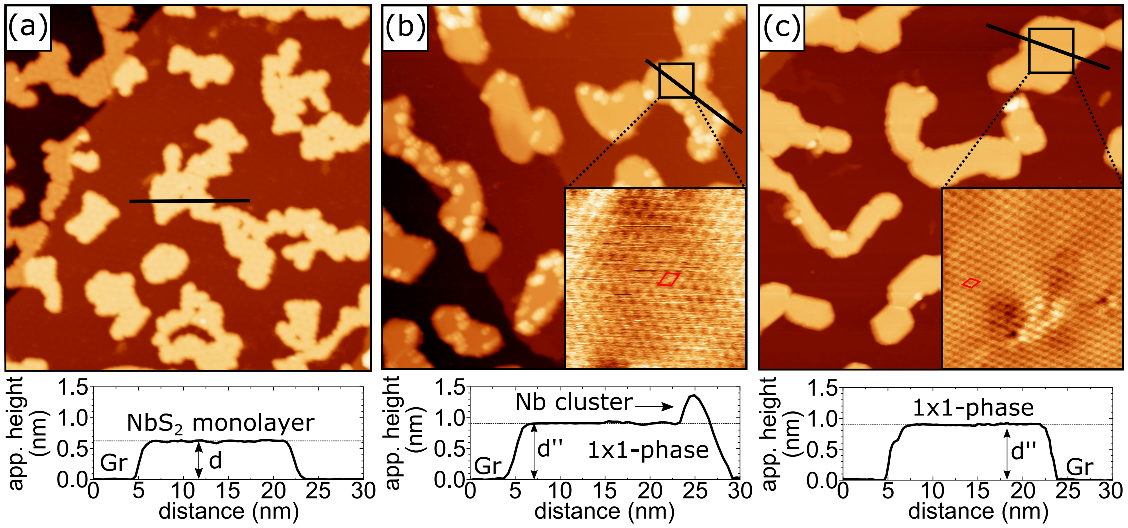

FIG. 5. Self-intercalation by supply of elemental Nb to the NbS$_2$/Gr heterostack. (a) Pristine NbS$_2$ grown including annealing to 820 K for 360 s (compare Section II). (b) Sample after additional Nb deposition at 820 K of same amount as used to create NbS$_2$ in (a). Inset: atomic resolution topograph of the boxed area. (c) Sample after additional annealing to 1023 K for 360 s. Inset: atomic resolution STM topograph of the boxed area. Height profiles are taken along the black lines in the topographs. Image information: (a) size 100 nm × 100 nm, $V_\mathrm{s} = 1.0\,\mathrm{V}$, $I_\mathrm{t} = 0.23\,\mathrm{nA}$; (b) size 100 nm × 100 nm, $V_\mathrm{s} = 1.0\,\mathrm{V}$, $I_\mathrm{t} = 0.3\,\mathrm{nA}$; Inset: 5 nm × 5 nm, $V_\mathrm{s} = 0.1\,\mathrm{V}$, $I_\mathrm{t} = 5\,\mathrm{nA}$; (c) size 100 nm × 100 nm, $V_\mathrm{s} = 1.2\,\mathrm{V}$, $I_\mathrm{t} = 0.3\,\mathrm{nA}$; Inset: 7.5 nm × 7.5 nm, $V_\mathrm{s} = 0.1\,\mathrm{V}$, $I_\mathrm{t} = 5\,\mathrm{nA}$.

almost constant coverage indicates that deposited Nb rather than dissociated Nb is used for the Nb $1 \times 1 -$ phase formation. The presence of Nb clusters at the island edges in Fig. 5 (b) could be due to a slight excess of Nb beyond what is needed for the Nb $1 \times 1 -$ phase. The excess could result from a deposited surplus or from minor (slow) NbS$_2$ dissociation already at 820 K, which would be consistent with the slight coverage decrease from 0.33 ML to 0.29 ML.

The disappearance of the Nb clusters after annealing to 1020 K is consistent with Nb already escaping under Gr, while the marginal coverage decrease points to a larger thermal stability of the Nb $1 \times 1 -$ phase compared to pristine NbS$_2$ – the Nb sink provided by the vdW gap between NbS$_2$ islands and Gr is already closed. We note that if compared to Fig. 5 (b) only half the amount of Nb is deposited during annealing at 820 K, Nb clusters are largely absent and both Nb $1 \times 1 -$ phase and Nb $\sqrt{3} \times \sqrt{3} -$ phase islands are observed, as expected (data not shown).

We also conducted experiments, where the additional Nb is deposited at room temperature rather than at 820 K. In these experiments the metallic Nb clusters formed upon deposition gradually decay during annealing and pristine NbS$_2$ islands are transformed to self-intercalated islands.

Under these conditions the Nb 1×1 – phase , but also Nb $\sqrt{3} \times \sqrt{3}$ – phase islands form. Apparently the dissociation of preformed Nb clusters at the annealing temperature provides a less accessible source of Nb (clusters need to decay) than the single deposited atoms, whereby the Nb is not entirely concerted to the intercalation layer. These experiments are discussed in detail in the Supporting Information with Figs. S3 and S4.

VI. INTERCALATION OF THE NbS_2/Gr HETEROSTACK BY Fe DEPOSITION

Since for bulk NbS_2 not only Nb, but also metals like Cr, Mn, V, Fe and Ni are readily intercalated [43–46], it is tempting to speculate that also intercalation of such elements is possible at the interface of an NbS_2 monolayer and Gr.

The validity of this speculation is explored for elemental Fe. The methodology applied is Fe supply to pristine NbS_2 islands at elevated temperatures below the dissociation threshold of NbS_2, as for the Nb case (compare Fig. 5). Using again NbS_2 monolayer islands as starting point [Fig. 6 (a)], elemental Fe is deposited at 820 K, resulting in the morphology represented by the topograph in Fig. 6 (b). A considerable reduction in coverage from 0.34 ML in Fig. 6 (a) to 0.22 ML in Fig. 6 (b) is apparent. Clusters with a height above 2 nm are attached to the edges of most islands. A height profile taken along the black line in the topograph displays two different island heights. The lower height is $d' = 0.95$ nm, closely resembling the value found for the self-intercalated monolayer islands in sections IV and V. The upper height is 1.22 nm, roughly double the height of the NbS_2 monolayer. The upper height level is the dominant one in the islands observed, covering an area fraction of 0.12, while the lower one covers 0.10 of the surface area.

As shown in Fig. 6 (c), upon further annealing to 1020 K the islands become more compact and the clusters at the island edges either disappear or shrink. The island covered area drops further to 0.15 ML. As obvious from the profile below the topograph, the island heights remain unchanged (0.95 nm and 1.22 nm), though the lower level becomes rare. Moreover, a third height level of 1.84 nm is present on the sample (area fraction 0.05).

To gain additional insight, atomic resolution STM topographs where recorded. Fig. 7 (a) features an island with the two dominant height levels. As obvious from the boxed areas in Fig. 7 (a) represented as atomically resolved differentiated zooms in Figs. 7 (b) and (c), both islands heights display a $\sqrt{3} \times \sqrt{3}$ R30° superstructure with respect to the pristine NbS_2 lattice. The same conclusion holds for these height levels after annealing to 1020 K (compare Fig. S5). The corrugations of the two $\sqrt{3} \times \sqrt{3}$ R30° superstructures are 20 pm for the lower and 6 pm for the

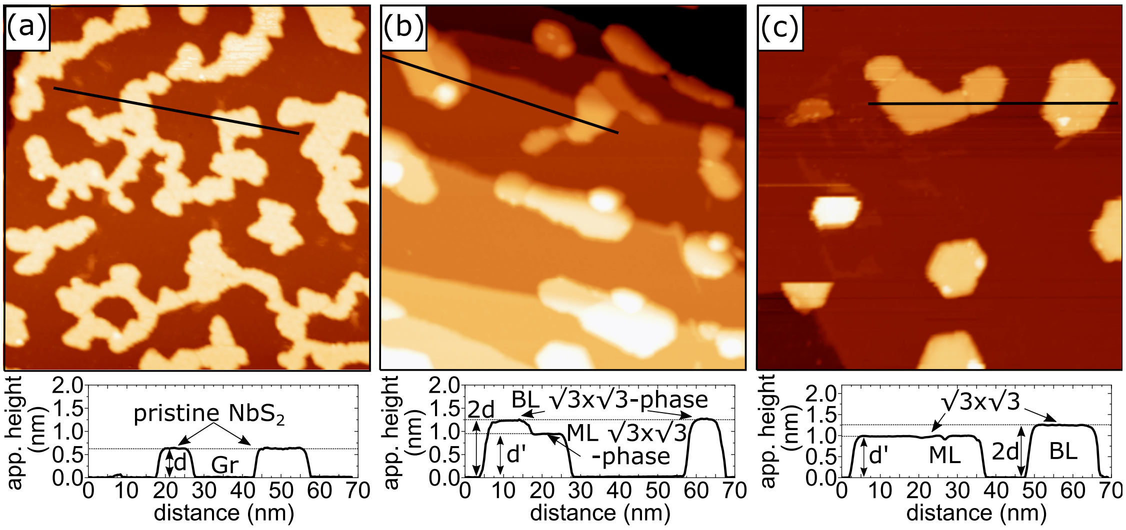

FIG. 6. Fe intercalation of NbS_2 monolayer islands. (a) Pristine NbS_2 sample grown including annealing to 820 K for 360 s (compare Section II). (b) Sample after Fe deposition at 820 K. The deposited amount of Fe is identical to the deposited amount of Nb during NbS_2 growth. (c) Sample after annealing to 1020 K. Height profiles are along the black lines in the topographs. Image information: (a) size 100 nm × 100 nm, $V_s = 1.0\,V$, $I_t = 0.3\,nA$; (b) size 100 nm × 100 nm, $V_s = 2.0\,V$, $I_t = 0.05\,nA$; (c) size 100 nm × 100 nm, $V_s = 2.0\,V$, $I_t = 0.2\,nA$.

upper level. LEED of the sample does not show a $\sqrt{3} \times \sqrt{3}$ R30° superstructure. Finally, we note that after annealing to 1020 K islands adhere so weakly to the substrate, such that they can be scratched away easily by the STM tip [compare Fig. S1 (b) in the supporting information]. The Gr layer underneath the island locations is undamaged and displays the same height as the surrounding Gr, ruling out Fe intercalation between Ir(111) and Gr underneath the islands.

We interpret the lower height level to result from Fe intercalation of pristine NbS_2 monolayer islands (ML Fe $\sqrt{3} \times \sqrt{3}$ − phase). Arguments for this assignment are (i) the increased height with a similar value as for the self-intercalation case; (ii) the absence of a modified height of the Gr underneath the islands when they are removed by the STM tip; (iv) the observed $(\sqrt{3} \times \sqrt{3})$R30° superstructure after annealing to a temperature where Nb self-intercalation is absent; (v) the absence of $(\sqrt{3} \times \sqrt{3})$R30° superstructure diffraction spots in LEED which makes Fe intercalation rather than Fe adsorption plausible; (vi) the low corrugation of 20 pm of the $(\sqrt{3} \times \sqrt{3})$R30° superstructure making again Fe intercalation more plausible than Fe adsorption. Overall the ML Fe $\sqrt{3} \times \sqrt{3}$ − phase is very similar to the Nb $\sqrt{3} \times \sqrt{3}$ − phase, with the only difference that the former is created by Nb deposition while the later by Fe deposition.

However the similarities with the Nb case cease, when considering the upper height level which

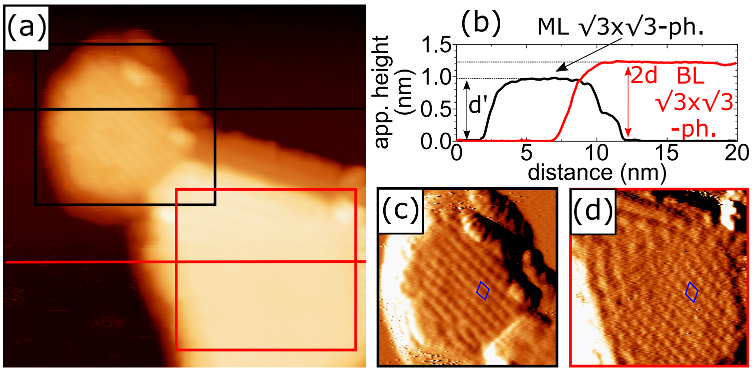

FIG. 7. Island of NbS_2 after Fe deposition at 820 K. (a) Constant current STM image of an Island. (b) Two height profiles taken along the black (red) lines in (a). (c) Differentiated constant current STM image of the area marked by a black box in (a). (d) Differentiated constant current STM image of the area marked by a red box in (a). In (c) and (d) the found $\sqrt{3} \times \sqrt{3}$ R30° superstructures are marked by blue rhomboids. Image information: (a) size 20 nm × 20 nm, $V_s = 0.5$ V, $I_t = 0.7$ nA; (b) size 10 nm × 10 nm, $V_s = 0.5$ V, $I_t = 0.7$ nA; (c) size 10 nm × 10 nm, $V_s = 0.5$ V, $I_t = 0.7$ nA.

is absent for the Nb case. It is interpreted to result from Fe intercalation into the van der Waals gap of NbS_2 bilayer islands (BL Fe $\sqrt{3} \times \sqrt{3} -$ phase). The idea is that Fe deposition triggers the reorganization of the NbS_2 monolayer islands to bilayers, in order to be able to intercalate Fe into the vdW gap between two NbS_2 layers rather than the vdW gap between an NbS_2 layer and Gr. This implies that the latter is energetically unfavorable compared to the former. Consistent with this speculation, the fraction of islands displaying the ML Fe $\sqrt{3} \times \sqrt{3} -$ phase decreases from $\approx 50\%$ to $\approx 3\%$ (with a corresponding increase of the BL Fe $\sqrt{3} \times \sqrt{3} -$ phase) by annealing from 820 K to 1020 K. Inspecting Fig. 6 (b) and Fig. 7 (a) reveals that nearly all island that display the ML Fe $\sqrt{3} \times \sqrt{3} -$ phase also display the BL Fe $\sqrt{3} \times \sqrt{3} -$ phase, while such phase coexistence in an island is absent after annealing to 1020 K. It seems the STM topographs taken at 820 K are snapshots during the transformation of the phases.

Consistent with our interpretation of the BL Fe $\sqrt{3} \times \sqrt{3} -$ phase is the strong reduction in coverage from 0.34 ML to 0.22 ML after Fe deposition at 820 K and further to 0.15 ML after annealing to 1020 K, which we attribute to NbS_2 bilayer and NbS_2 trilayer formation. When Nb is deposited instead of Fe, the decrease is much smaller with the corresponding numbers being 0.33 ML, 0.29 ML and 0.26 ML. The 1.22 nm height of the BL Fe $\sqrt{3} \times \sqrt{3} -$ phase is close to the expected geometrical height of a NbS_2 bilayer, which is identical to the 1.195 nm c-axis lattice parameter of bulk 2H-NbS_2 [32]. The occasional island of 1.84 nm height after annealing to 1020 K corresponds most likely to NbS_2 trilayers.

The absence of $(\sqrt{3} \times \sqrt{3})\mathrm{R}30^\circ$ spots with respect to the $\mathrm{NbS_2}$ reflections in LEED even after annealing to 1020 K, when the BL Fe $\sqrt{3} \times \sqrt{3}-$phase is almost exclusively present, and the very low corrugation of only 6 pm make again Fe intercalation much more plausible than Fe adsorption on the top layer. One could argue that BL Fe $\sqrt{3} \times \sqrt{3}-$phase has the intercalated Fe still in the vdW gap between the lower $\mathrm{NbS_2}$ layer and Gr rather than in the vdW gap between the two $\mathrm{NbS_2}$ layers. However, since $\mathrm{NbS_2}$ layers interact only weakly with each other, the apparent STM height of the top $\mathrm{NbS_2}$ layer with respect to the bottom $\mathrm{NbS_2}$ layer, even if this layer has some Fe underneath, must be very close to the geometrical height of 0.60 nm. This is because the two levels are chemically nearly identical. Since we measure a difference of $1.22\,\mathrm{nm} - 0.95\,\mathrm{nm} = 0.27\,\mathrm{nm}$, this scenario is unlikely. The height difference of 0.27 nm differs by more than a factor of two from the expectation. In contrast the apparent STM height of 1.22 nm for the BL Fe $\sqrt{3}\times\sqrt{3}-$phase matches very well not only with the 1.195 c-axis parameter of pristine bulk $\mathrm{NbS_2}$, but even better with the 1.22 nm c-axis parameter of $\mathrm{Fe_{1/3}NbS_2}$ [43]. This structure displays a $(\sqrt{3}\times\sqrt{3})\mathrm{R}30^\circ$ superstructure arrangement of the Fe atoms with respect to the $\mathrm{NbS_2}$ layers [43].

Up to now the origin of the large clusters at the edges of the $\mathrm{NbS_2}$ islands in Figs. 6 (b) has not yet been discussed. As much more Fe has been deposited (ratio Fe:Nb is 1:1) than what is needed for the formation of $(\sqrt{3} \times \sqrt{3})\mathrm{R}30^\circ$ superstructure induced by Fe, the clusters are speculated to consist of metallic Fe. Upon annealing the sample to 1020 K their number and size decreases [Figs. 6 (c)], since the excess Fe escapes to the Ir(111) substrate where it forms pseudomorphic monolayer islands [55].

VII. DISCUSSION

While the previous sections provided straightforward evidence for intercalation at the heterostack interface $\mathrm{NbS_2}$/Gr, detailed structures were not yet discussed and no link to literature was provided. We begin the discussion with the least ambiguous case of Fe intercalation before analyzing in more detail Nb self-intercalation.

Intercalation of Fe into $\mathrm{NbS_2}$ bulk crystals invariably results in magnetically ordered intercalation compounds $\mathrm{Fe_{1/3}NbS_2}$, where the Fe atoms are located in octahedral sites between layers arranged in H-stacking and give rise to a $\sqrt{3}\times\sqrt{3}\,\mathrm{R}30^\circ$ superstructure [43, 56]. We identify the BL Fe $\sqrt{3} \times \sqrt{3}-$phase with the bulk situation and visualize it in Fig. 8 (a). As discussed in the last section, the BL Fe $\sqrt{3} \times \sqrt{3}-$phase has no Fe in the hetero-interface $\mathrm{NbS_2}$/Gr, but only between the two $\mathrm{NbS_2}$ layers, where the intercalated Fe atoms occupy one third of the octahedral sites as

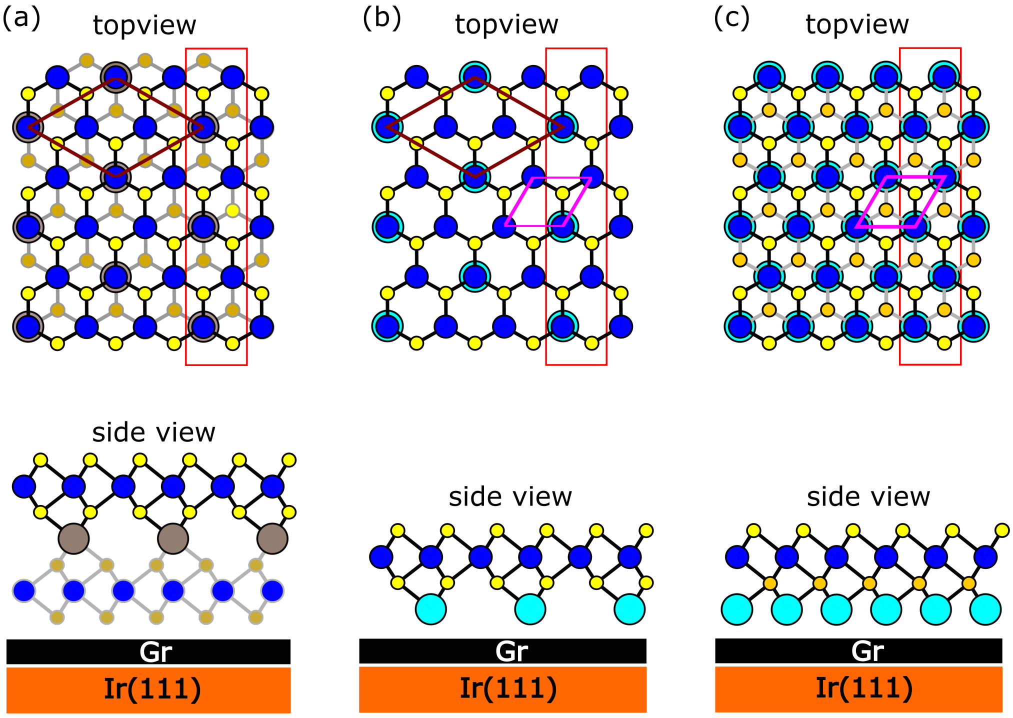

FIG. 8. Top and side view ball models for intercalation of NbS_2/Gr on Ir(111). (a) Bilayer NbS_2 with every third octahedral site between the two NbS_2 layers occupied by an Fe atom. Model for BL Fe $\sqrt{3}\times\sqrt{3}-$phase. (b) Monolayer NbS_2 with every third interstitial site occupied. Model for ML Fe $\sqrt{3}\times\sqrt{3}-$ phase and Nb $\sqrt{3}\times\sqrt{3}-$ phase. (c) Bilayer of NbS (or Nb_2S_2) in the NiAs-structure. Model for the Nb $1\times 1-$ phase. See text. Nb atoms: blue balls; S atoms: yellow or orange balls; intercalated Nb or Fe atoms: brown and turquoise balls correspondingly. The side views contain the atoms within the red boxes in the top views.

depicted in Fig. 8 (a). The structural assignment of the BL Fe $\sqrt{3}\times\sqrt{3}-$ phase is consistent with all experimental observations discussed in the last section and appears very likely in view of the existing literature for Fe-intercalated NbS_2 bulk crystals.

For the ML Fe $\sqrt{3}\times\sqrt{3}-$ phase we identified the deposited Fe to be located at the NbS_2/Gr interface. It is plausible that the Fe atoms occupy again the locations directly underneath the Nb atom positions, the locations that would be octahedral sites if also the lower layer would consist of NbS_2 (interstitial sites). As depicted in the corresponding sketch of Fig. 8 (b), again one third occupation of these sites is assumed, which results in the observed $\sqrt{3}\times\sqrt{3}\,\mathrm{R}30^\circ$ superstructure. Though on the basis of the present data it can not be ruled out that the concentration of Fe is higher in the ML Fe $\sqrt{3}\times\sqrt{3}-$ phase, this unlikely scenario would imply a substantial release of intercalated Fe during the annealing induced transformation of the ML Fe $\sqrt{3}\times\sqrt{3}-$ phase to the BL Fe $\sqrt{3}\times\sqrt{3}-$ phase.

Although we were able to realize Fe intercalation into the heterostack NbS_2/Gr, the ML Fe $\sqrt{3} \times \sqrt{3} -$ phase could not be realized phase-pure, presumably due to its metastability compared to the BL Fe $\sqrt{3} \times \sqrt{3} -$ phase. However, by tuning the temperature of Fe deposition to slightly lower values (and possibly also Fe flux and amount), it is not unlikely to make samples with pure ML Fe $\sqrt{3} \times \sqrt{3} -$ phase possible.

Next we consider Nb self-intercalation. For bulk NbS_2 crystals, self-intercalation with the composition $Nb_{1+x}S_2$ for the rhombohedral 3R-NbS_2 and hexagonal 2H-NbS_2 have been synthesized [31, 42]. The stability range of 2H-$Nb_{1+x}S_2$ is $0.3 \leq x \leq 0.43$ and the 2H-phase is the only crystal structure that is observed for thin films in that case [41]. There, again the intercalated atoms are found in octahedral sites similar to the ball model of Fig. 8 (a). From the similarity of the ML Fe $\sqrt{3} \times \sqrt{3} -$ phase and the Nb $\sqrt{3} \times \sqrt{3} -$ phase (apparent height, $\sqrt{3} \times \sqrt{3}\,\mathrm{R}30^\circ$ superstructure), we tentatively conclude that the Nb $\sqrt{3} \times \sqrt{3} -$ phase has the same structure as the ML Fe $\sqrt{3} \times \sqrt{3} -$ phase , shown in Fig. 8 (b).

The observed decrease of the island area would not only allow a composition $Nb_{4/3}S_2$ as suggested here, but also $Nb_{5/3}S_2$ and Nb_2S_2. The composition $Nb_{5/3}S_2$ would also be compatible with the observed $\sqrt{3} \times \sqrt{3}\,\mathrm{R}30^\circ$ superstructure that could be formed for this composition through a regular arrangement of missing interstitial atoms. However, such a composition has never been observed for self-intercalated bulk crystals or thin films of NbS_2 and appears thus less probable.

For bulk crystals in the composition $Nb_{2-y}S_2$ with stability range $0.0 \leq y \leq 0.3$ the NiAs-structure was reported, where depending on the temperature of formation slight deviations of the atomic positions from the ideal NiAs-structure were observed [31, 42]. Because of the lack of a superstructure, for the Nb $1 \times 1 -$ phase we assumed a composition Nb_2S_2. Considering the reported literature data for this composition, instead of H-NbS_2 with a full intercalation layer in interstitial sites [as depicted in Fig. 8 (b), but with all interstitial sites occupied], we assume the Nb $1 \times 1 -$ phase to be a double layer of Nb_2S_2 (NbS) in the NiAs-structure as depicted in Fig. 8 (c). This structure can also be considered as T-NbS_2 with an additional intercalation layer in the vdW gap between T-NbS_2 and Gr.

If contrary to our assignment the Nb $1 \times 1 -$ phase would be just the Nb $\sqrt{3} \times \sqrt{3} -$ phase , but with all interstitial sites filled instead of just one third of them, one would expect a more or less continuous transition between the two structures rather than a sharp phase boundary. However, as obvious from Fig. 9, if the Nb $1 \times 1 -$ phase and the Nb $\sqrt{3} \times \sqrt{3} -$ phase coexist in one island, the two phases are separated by a clear phase boundary, contradicting this scenario.

A scenario that we cannot rule out is that the Nb $\sqrt{3} \times \sqrt{3} -$ phase is, instead of our current

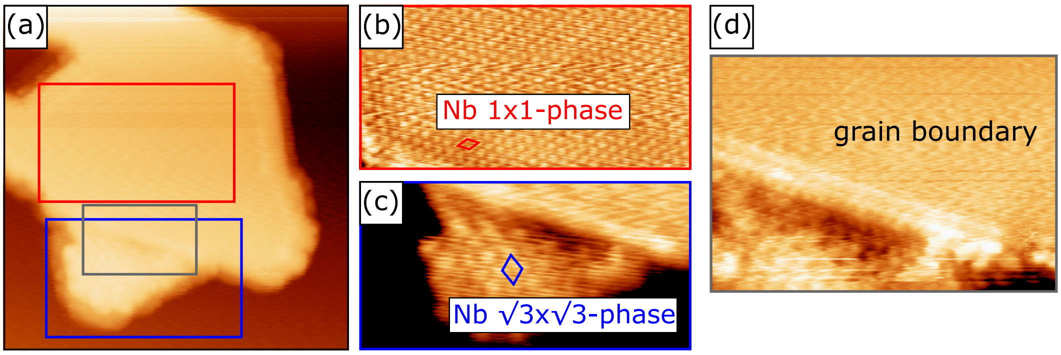

FIG. 9. Phase boundary between Nb $\sqrt{3} \times \sqrt{3}$ – phase and Nb 1×1 – phase after Nb deposition at 820 K. (a) Constant current STM image of a Nb-intercalated NbS_2 monolayer island. (b) Atomically resolved STM topograph of the red boxed area marked in (a). A 1×1 structure with respect to the pristine NbS_2 lattice is visible, marked by a red rhomboid. (c) Atomically resolved STM topograph of the blue boxed area in (a). A $\sqrt{3} \times \sqrt{3}\,R30°$ superstructure with respect to the pristine NbS_2 lattice is visible, marked by a blue rhomboid. (d) Zoom of gray boxed area in (a) highlighting the phase boundary. Image information: (a) size 20 nm × 20 nm, $V_s = 0.51$ V, $I_t = 0.12$ nA; (b) size 10 nm × 5 nm, $V_s = 0.31$ V, $I_t = 18$ nA; (c) size 10 nm × 5 nm, $V_s = 0.51$ V, $I_t = 0.12$ nA; (d) size 8.6 nm × 5.9 nm, $V_s = 0.32$ V, $I_t = 9.1$ nA;

assignment represented by Fig. 8 (b), a double layer of a NiAs-type structure as depicted in Fig. 8 (c), but involving for instance trimerization of the Nb atoms in one of the Nb layers to create the $\sqrt{3} \times \sqrt{3}\,R30°$ superstructure. This scenario would attribute the large decrease of island area (from 0.34 ML to 0.17 ML) upon transformation of pristine NbS_2 monolayer islands to the Nb $\sqrt{3} \times \sqrt{3}$ – phase by annealing (compare Fig. 2) entirely to intercalation, rather than to a combination of intercalation and Nb losses to the Ir(111) substrate. Finally we note, that in bulk all structures considered here display lattice parameters that agree within a margin of much less than 5 %. Thereby, on the level of STM crystallography, the measurement of the in-plane lattice parameter could not be used as a tool to distinguish different structures.

Admittedly, although the structural assignments presented here are reasonable, they are not definitive due to unproven assumptions involved. A sound assignment of the intercalation structures will require additional experiments involving for instance x-ray photoelectron spectroscopy and diffraction experiments. Nevertheless these structural ambiguities do not affect the main conclusion of the present work.

VIII. SUMMARY

Ordered intercalation into the vdW gap of two dissimilar monolayers of 2D materials may be accomplished by deposition of the species needed for intercalation or just by partial dissociation of one of the materials. This was demonstrated for the self-intercalation of Nb and the intercalation of Fe into the $\mathrm{NbS_2}$/Gr heterostack.

By Nb self-intercalation, pristine $\mathrm{NbS_2}$ islands on Gr transformed into two ordered intercalation phases with apparent heights of 1.00 nm and 0.91 nm, both being distinctly different from the pristine $\mathrm{NbS_2}$ monolayer with 0.63 nm and the pristine bilayer with 1.21 nm height (see height profile in Fig. S6 in the supporting information). These intercalation phases display a $\sqrt{3} \times \sqrt{3}\,\mathrm{R}30^\circ$ superstructure and a 1×1 structure referred to the $\mathrm{NbS_2}$ lattice, respectively. The Nb $\sqrt{3} \times \sqrt{3}-$phase was prepared phase-pure by annealing to 1020 K in the absence of a S background pressure, while the Nb $1 \times 1-$phase can be prepared phase-pure by additional annealing to 1220 K, or by Nb deposition onto a sample with pristine $\mathrm{NbS_2}$. The Nb $\sqrt{3} \times \sqrt{3}-$ phase was tentatively attributed to the occupation of one third of the interstitial sites in the vdW gap of the $\mathrm{NbS_2}$/Gr heterostack, while the Nb $1 \times 1-$ phase was attributed to an intercalation induced rearrangement into a double layer of NbS, which can be considered to result from a reorganization of the pristine $\mathrm{NbS_2}$ monolayer.

By Fe deposition onto pristine $\mathrm{NbS_2}$ islands at 820 K, two coexisting phases with characteristic apparent heights of 0.95 nm and 1.22 nm are formed, that both exhibit a $\sqrt{3} \times \sqrt{3}\,\mathrm{R}30^\circ$ superstructure with respect to $\mathrm{NbS_2}$. The phases are interpreted to result from the occupation of one third of the interstitial sites in the vdW gap of the $\mathrm{NbS_2}$/Gr heterostack (ML Fe $\sqrt{3} \times \sqrt{3}-$ phase) and from occupation of one third of the octahedral sites in the vdW gap of the $\mathrm{NbS_2}$ bilayer (BL Fe $\sqrt{3} \times \sqrt{3}-$ phase), respectively. The BL Fe $\sqrt{3} \times \sqrt{3}-$ phase appears to be energetically favorable and can be prepared almost pure by additional annealing to 1020 K. Whether the ML Fe $\sqrt{3} \times \sqrt{3}-$phase can be prepared phase-pure remains to be explored, but it is likely that tuning the temperature of intercalation will enable to enlarge the fraction of ML Fe $\sqrt{3} \times \sqrt{3}-$phase formed.

While the intercalation of Nb and Fe into the $\mathrm{NbS_2}$/Gr vdW gap could be established undoubtedly, the structure assignments made are not unambiguous and call for additional chemical, structural, and theoretical investigations using e.g. x-ray photoelectron diffraction and spectroscopy or DFT. Since Fe-intercalated $\mathrm{NbS_2}$ bulk crystals order antiferromagnetically with indications for substantial spin-orbit coupling, it is likely that also ML Fe $\sqrt{3} \times \sqrt{3}-$ and BL Fe $\sqrt{3} \times \sqrt{3}-$phase display interesting magnetic properties. Such an investigation would also be timely, since in literature already for monolayer NbS_2 a tendency to form spin order was discussed [54, 57–59]. Investigations through spin-polarized STM or x-ray magnetic circular dichroism will provide more understanding of this issue.

Possibly the most important consequence of the present work is the insight, that new 2D material heterostacks can be created by using simple methods like thermal annealing or physical vapor deposition at suitable temperature. This insight provides a new handle to tailor properties and create new functions of 2D layer heterostacks.

ACKNOWLEDGMENTS

We acknowledge funding from Deutsche Forschungsgemeinschaft (DFG) through CRC 1238 (project number 277146847, subprojects A01, B06 and C01).

[1] E. A. Marseglia, Transition Metal Dichalcogenides and Their Intercalates, International Reviews in Physical Chemistry **3**, 177 (1983).

[2] D. Guerard and A. Herold, Intercalation of lithium into graphite and other carbons, Carbon **13**, 337 (1975).

[3] M. S. Dresselhaus and G. Dresselhaus, Intercalation compounds of graphite, Advances in Physics **51**, 1 (2002).

[4] R. Zhang, J. Waters, A. K. Geim, and I. V. Grigorieva, Intercalant-independent transition temperature in superconducting black phosphorus, Nature Communications **8**, 15036 (2017).

[5] N. L. Nair, E. Maniv, C. John, S. Doyle, J. Orenstein, and J. G. Analytis, Electrical switching in a magnetically intercalated transition metal dichalcogenide, Nature Materials **19**, 153 (2020).

[6] M. S. Whittingham, Electrical Energy Storage and Intercalation Chemistry, Science **192**, 1126 (1976).

[7] J. Asenbauer, T. Eisenmann, M. Kuenzel, A. Kazzazi, Z. Chen, and D. Bresser, The success story of graphite as a lithium-ion anode material - fundamentals, remaining challenges, and recent developments including silicon (oxide) composites, Sustainable Energy Fuels **4**, 5387 (2020).

[8] M. Chhowalla, H. S. Shin, G. Eda, L.-J. Li, K. P. Loh, and H. Zhang, The chemistry of two-dimensional layered transition metal dichalcogenide nanosheets, Nature Chemistry **5**, 263 (2013).

[9] S. Z. Butler, S. M. Hollen, L. Cao, Y. Cui, J. A. Gupta, H. R. Gutiérrez, T. F. Heinz, S. S. Hong, J. Huang, A. F. Ismach, E. Johnston-Halperin, M. Kuno, V. V. Plashnitsa, R. D. Robinson, R. S. Ruoff, S. Salahuddin, J. Shan, L. Shi, M. G. Spencer, M. Terrones, W. Windl, and J. E. Goldberger, Progress, Challenges, and Opportunities in Two-Dimensional Materials Beyond Graphene, ACS Nano **7**, 2898 (2013).

[10] K. S. Novoselov, A. Mishchenko, A. Carvalho, and A. H. C. Neto, 2D materials and van der Waals heterostructures, Science **353**, aac9439 (2016).

[11] Y. Yu, F. Yang, X. F. Lu, Y. J. Yan, Y.-H. Cho, L. Ma, X. Niu, S. Kim, Y.-W. Son, D. Feng, S. Li, S.-W. Cheong, X. H. Chen, and Y. Zhang, Gate-tunable phase transitions in thin flakes of 1T-TaS$_2$, Nature Nanotechnology **10**, 270 (2015).

[12] X. Zhao, P. Song, C. Wang, A. C. Riis-Jensen, W. Fu, Y. Deng, D. Wan, L. Kang, S. Ning, J. Dan, T. Venkatesan, Z. Liu, W. Zhou, K. S. Thygesen, X. Luo, S. J. Pennycook, and K. P. Loh, Engineering covalently bonded 2D layered materials by self-intercalation, Nature **581**, 171 (2020).

[13] M. Rajapakse, B. Karki, U. O. Abu, S. Pishgar, M. R. K. Musa, S. M. S. Riyadh, M. Yu, G. Sumanasekera, and J. B. Jasinski, Intercalation as a versatile tool for fabrication, property tuning, and phase transitions in 2D materials, npj 2D Materials and Applications **5**, 30 (2021).

[14] J. Zhou, Z. Lin, H. Ren, X. Duan, I. Shakir, Y. Huang, and X. Duan, Layered Intercalation Materials, Advanced Materials **33**, 2004557 (2021).

[15] C. Riedl, C. Coletti, T. Iwasaki, A. A. Zakharov, and U. Starke, Quasi-Free-Standing Epitaxial

Graphene on SiC Obtained by Hydrogen Intercalation, Physical Review Letters **103**, 246804 (2009).

[16] E. Grånäs, J. Knudsen, U. A. Schröder, T. Gerber, C. Busse, M. A. Arman, K. Schulte, J. N. Andersen, and T. Michely, Oxygen Intercalation under Graphene on Ir(111): Energetics, Kinetics, and the Role of Graphene Edges, ACS Nano **6**, 9951 (2012).

[17] M. Petrović, I. Šrut Rakić, S. Runte, C. Busse, J. T. Sadowski, P. Lazić, I. Pletikosić, Z.-H. Pan, M. Milun, P. Pervan, N. Atodiresei, R. Brako, D. Šokčević, T. Valla, T. Michely, and M. Kralj, The mechanism of caesium intercalation of graphene, Nature Communications **4**, 2772 (2013).

[18] M. Bosnar, V. Caciuc, N. Atodiresei, I. Lončarić, and S. Blügel, Se intercalation between $PtSe_2$ and the Pt surface during synthesis of $PtSe_2$ by direct selenization of Pt(111), Physical Review B **102**, 115427 (2020).

[19] X. Zhou, X. Hu, S. Zhou, H. Song, Q. Zhang, L. Pi, L. Li, H. Li, J. Lü, and T. Zhai, Tunneling Diode Based on WSe_2/SnS_2 Heterostructure Incorporating High Detectivity and Responsivity, Advanced Materials **30**, 1703286 (2018).

[20] Z. Wang, D. A. Rhodes, K. Watanabe, T. Taniguchi, J. C. Hone, J. Shan, and K. F. Mak, Evidence of high-temperature exciton condensation in two-dimensional atomic double layers, Nature **574**, 76 (2019).

[21] S. N. Shirodkar and E. Kaxiras, Li intercalation at graphene/hexagonal boron nitride interfaces, Physical Review B **93**, 245438 (2016).

[22] D. T. Larson, I. Fampiou, G. Kim, and E. Kaxiras, Lithium Intercalation in Graphene-MoS_2 Heterostructures, Journal of Physical Chemistry C **122**, 24535 (2018).

[23] D.-X. Song, Y.-Z. Du, W.-G. Ma, and X. Zhang, High rate and capacity performances of functionalized MXene/graphene heterostructure anodes for magnesium-ion batteries, International Journal of Energy Research **45**, 3421 (2021).

[24] D.-X. Song, W.-G. Ma, and X. Zhang, Correlated migration of ions in a 2D heterostructure anode: guaranteeing a low barrier for a high site occupancy, Journal of Materials Chemistry A **8**, 17463 (2020).

[25] D.-X. Song, L. Xie, Y.-F. Zhang, Y. Lu, M. An, W.-G. Ma, and X. Zhang, Multilayer Ion Load and Diffusion on TMD/MXene Heterostructure Anodes for Alkali-Ion Batteries, ACS Applied Energy Materials **3**, 7699 (2020).

[26] Y. Shao, P. Gong, H. Pan, and X. Shi, H-/dT-MoS_2-on-MXene Heterostructures as Promising 2D Anode Materials for Lithium-Ion Batteries: Insights from First Principles, Advanced Theory and Simulations **2**, 1900045 (2019).

[27] J. Ma, J. Fu, M. Niu, and R. Quhe, MoO_2 and graphene heterostructure as promising flexible anodes for lithium-ion batteries, Carbon **147**, 357 (2019).

[28] D. K. Bediako, M. Rezaee, H. Yoo, D. T. Larson, S. Y. F. Zhao, T. Taniguchi, K. Watanabe, T. L. Brower-Thomas, E. Kaxiras, and P. Kim, Heterointerface effects in the electrointercalation of van der Waals heterostructures, Nature **558**, 425 (2018).

[29] S. Yazdani, J. V. Pondick, A. Kumar, M. Yarali, J. M. Woods, D. J. Hynek, D. Y. Qiu, and J. J.

Cha, Heterointerface Effects on Lithium-Induced Phase Transitions in Intercalated MoS_2, ACS Applied Materials & Interfaces **13**, 10603 (2021).

[30] S. Y. F. Zhao, G. A. Elbaz, D. K. Bediako, C. Yu, D. K. Efetov, Y. Guo, J. Ravichandran, K.-A. Min, S. Hong, T. Taniguchi, K. Watanabe, L. E. Brus, X. Roy, and P. Kim, Controlled Electrochemical Intercalation of Graphene/h-BN van der Waals Heterostructures, Nano Letters **18**, 460 (2018).

[31] F. Jellinek, G. Brauer, and H. Müller, Molybdenum and Niobium Sulphides, Nature **185**, 376 (1960).

[32] W. G. Fisher and M. J. Sienko, Stoichiometry, structure, and physical properties of niobium disulfide, Inorganic Chemistry **19**, 39 (1980).

[33] M. Van Maaren and G. Schaeffer, Superconductivity in group Va dichalcogenides, Physics Letters **20**, 131 (1966).

[34] C. Witteveen, K. Górnicka, J. Chang, M. Månsson, T. Klimczuk, and F. O. von Rohr, Polytypism and superconductivity in the NbS_2 system, Dalton Transactions **50**, 3216 (2021).

[35] R. Yan, G. Khalsa, B. T. Schaefer, A. Jarjour, S. Rouvimov, K. C. Nowack, H. G. Xing, and D. Jena, Thickness dependence of superconductivity in ultrathin NbS_2, Applied Physics Express **12**, 023008 (2019).

[36] Z. Wang, C.-Y. Cheon, M. Tripathi, G. M. Marega, Y. Zhao, H. G. Ji, M. Macha, A. Radenovic, and A. Kis, Superconducting 2D NbS_2 Grown Epitaxially by Chemical Vapor Deposition, ACS Nano **15**, 18403 (2021).

[37] I. Guillamón, H. Suderow, S. Vieira, L. Cario, P. Diener, and P. Rodière, Superconducting Density of States and Vortex Cores of 2H-NbS_2, Physical Review Letters **101**, 166407 (2008).

[38] M. Leroux, M. Le Tacon, M. Calandra, L. Cario, M.-A. Méasson, P. Diener, E. Borrissenko, A. Bosak, and P. Rodière, Anharmonic suppression of charge density waves in $2H$-NbS_2, Physical Review B **86**, 155125 (2012).

[39] H. Lin, W. Huang, K. Zhao, C. Lian, W. Duan, X. Chen, and S.-H. Ji, Growth of atomically thick transition metal sulfide films on graphene/6H-SiC(0001) by molecular beam epitaxy, Nano Research **11**, 4722 (2018).

[40] R.-M. Stan, S. K. Mahatha, M. Bianchi, C. E. Sanders, D. Curcio, P. Hofmann, and J. A. Miwa, Epitaxial single-layer NbS_2 on Au(111): Synthesis, structure, and electronic properties, Physical Review Materials **3**, 044003 (2019).

[41] J. Yang, A. R. Mohmad, Y. Wang, R. Fullon, X. Song, F. Zhao, I. Bozkurt, M. Augustin, E. J. G. Santos, H. S. Shin, W. Zhang, D. Voiry, H. Y. Jeong, and M. Chhowalla, Ultrahigh-current-density niobium disulfide catalysts for hydrogen evolution, Nature Materials **18**, 1309 (2019).

[42] F. Kadijk and F. Jellinek, The system niobium-sulfur, Journal of the Less Common Metals **19**, 421 (1969).

[43] B. Van Laar, H. Rietveld, and D. Ijdo, Magnetic and crystallographic structures of Me_xNbS_2 and Me_xTaS_2, Journal of Solid State Chemistry **3**, 154 (1971).

[44] S. S. P. Parkin and R. H. Friend, 3d transition-metal intercalates of the niobium and tantalum dichalco-

genides. I. Magnetic properties, Philosophical Magazine B **41**, 65 (1980).

[45] S. Mankovsky, S. Polesya, H. Ebert, and W. Bensch, Electronic and magnetic properties of $2H-\mathrm{NbS}_2$ intercalated by $3d$ transition metals, Physical Review B **94**, 184430 (2016).

[46] S. Polesya, S. Mankovsky, and H. Ebert, Electronic and magnetic properties of the 2H-NbS_2 intercalated by 3d transition metal atoms:, Zeitschrift für Naturforschung B **74**, 91 (2019).

[47] R. van Gastel, A. T. N'Diaye, D. Wall, J. Coraux, C. Busse, N. M. Buckanie, F.-J. Meyer zu Heringdorf, M. Horn von Hoegen, T. Michely, and B. Poelsema, Selecting a single orientation for millimeter sized graphene sheets, Applied Physics Letters **95**, 121901 (2009).

[48] J. Hall, B. Pielić, C. Murray, W. Jolie, T. Wekking, C. Busse, M. Kralj, and T. Michely, Molecular beam epitaxy of quasi-freestanding transition metal disulphide monolayers on van der Waals substrates: a growth study, 2D Materials **5**, 025005 (2018).

[49] W. J. Kaiser and R. C. Jaklevic, Spectroscopy of electronic states of metals with a scanning tunneling microscope, IBM Journal of Research and Development **30**, 411 (1986).

[50] R. C. J. M. P. Everson, L. C. Davis and W. Shen, Effects of surface features upon the Au(111) surface state local density of states studied with scanning tunneling spectroscopy, Journal of Vacuum Science &Technology B **9**, 891 (1991).

[51] B. Pielić, J. Hall, V. Despoja, I. r. Rakić, M. Petrović, A. Sohani, C. Busse, T. Michely, and M. Kralj, Sulfur Structures on Bare and Graphene-Covered Ir(111), The Journal of Physical Chemistry C **124**, 6659 (2020).

[52] J.Hall, Controlling Growth and Electronic Properties of Transition Metal Disulphide Layers via Molecular Beam Epitaxy, Dissertation, University of Cologne (2019).

[53] T. Knispel, Structure, Electronic Correlations and Magnetism in 2D Layers and 2D Layer Stacks on Iridium Substrates, Dissertation, University of Cologne (2021).

[54] E. G. C. P. van Loon, M. Rösner, G. Schönhoff, M. I. Katsnelson, and T. O. Wehling, Competing Coulomb and electron–phonon interactions in NbS_2, npj Quantum Materials **3**, 32 (2018).

[55] J. Brede, J. Sławińska, M. Abadia, C. Rogero, J. E. Ortega, I. Piquero-Zulaica, J. Lobo-Checa, A. Arnau, and J. I. Cerdá, Tuning the Graphene on Ir(111) adsorption regime by Fe/Ir surface-alloying, 2D Materials **4**, 015016 (2016).

[56] R. H. Friend, A. R. Beal, and A. D. Yoffe, Electrical and magnetic properties of some first row transition metal intercalates of niobium disulphide, The Philosophical Magazine: A Journal of Theoretical Experimental and Applied Physics **35**, 1269 (1977).

[57] F. Güller, V. L. Vildosola, and A. M. Llois, Spin density wave instabilities in the NbS_2 monolayer, Physical Review B **93**, 094434 (2016).

[58] Y. Xu, X. Liu, and W. Guo, Tensile strain induced switching of magnetic states in NbSe_2 and NbS_2 single layers, Nanoscale **6**, 12929 (2014).

[59] Y. Zhou, Z. Wang, P. Yang, X. Zu, L. Yang, X. Sun, and F. Gao, Tensile Strain Switched Ferromagnetism in Layered NbS_2 and NbSe_2, ACS Nano **6**, 9727 (2012).

8.1 Supporting Information

Supporting information

INTERCALATED NbS_2 REMOVED BY THE STM TIP

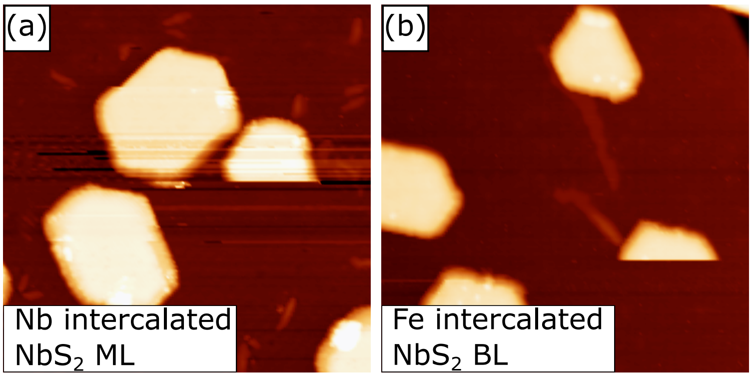

FIG. S1. Intercalated NbS_2 islands removed by the STM tip. (a) Nb intercalated NbS_2 monolayer islands after annealing the pristine NbS_2 sample to 1120 K. (b) Fe intercalated NbS_2 bilayer islands after Fe deposition at 820 K and subsequent annealing to 1020 K. Image information: (a) size 60 nm×60 nm, V_s =1.0 V, I_t = 0.29 nA; (b) size 60 nm×60 nm, V_s = 1.9 V, I_t = 0.19 nA.

LEED OF PRISTINE NbS_2 MONOLAYERS ANNEALED TO DIFFERENT TEMPERATURES

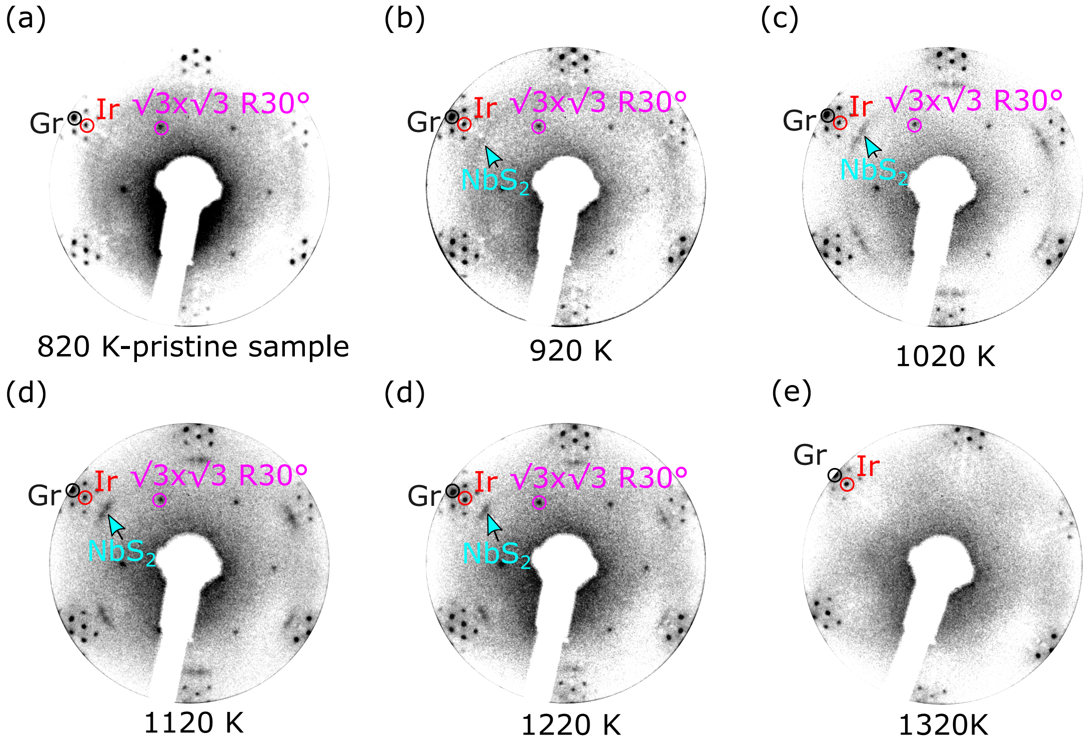

FIG. S2. Inverted LEED images at 100 eV of pristine NbS_2 islands annealed up to 1320 K. First order reflections of Gr, Ir, and NbS_2 are marked black, red, and turquoise, respectively. Reflections of a $\sqrt{3} \times \sqrt{3}$ R30° superstructure with respect to Ir due to S intercalated between Ir(111) and Gr are marked pink. In LEED no sign of hetero-intercalation is visible. It should give rise to a $\sqrt{3} \times \sqrt{3}$ R30° superstructure with respect to the NbS_2.

TRANSFORMATION OF PRISTINE NbS_2 ISLANDS TO Nb $\sqrt{3}\times\sqrt{3}$ – PHASE AND Nb 1×1 – PHASE ISLANDS BY ROOM TEMPERATURE Nb DEPOSITION AND SUBSEQUENT ANNEALING

Hetero-self-intercalation between pristine NbS_2 monolayer islands [Fig. S3 (a)] and Gr can also be accomplished by room temperature Nb deposition in the absence of S vapor [Fig. S3 (b)] and subsequent annealing [Figs. S3 (c) and (d)]. Upon room temperature deposition, Nb forms clusters templated by the moiré of Gr with Ir(111) in the space between the pristine NbS_2 islands [Fig. S3 (b)]. Small irregular clusters are formed on top of the NbS_2 islands. As seen in the topograph of Fig. S3 (c), annealing to 820 K causes the Nb clusters on the Gr terrace to largely disappear.

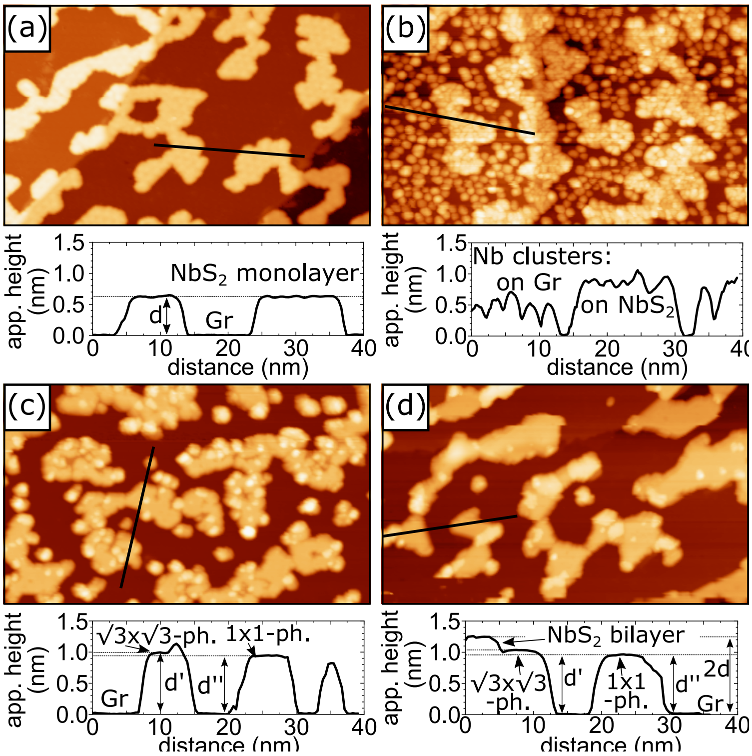

FIG. S3. STM topographs visualizing the transformation of pristine NbS_2 islands to Nb $\sqrt{3}\times\sqrt{3}-$phase and Nb 1×1 – phase islands by room temperature Nb deposition and subsequent annealing. (a) Pristine NbS_2 grown including annealing to 820 K for 360 s. (b) Same amount of elemental Nb as used during NbS_2 growth deposited at room temperature in the absence of additional S vapor. (c) Annealing of (b) in the absence of additional S vapor to 820 K for 360 s. (d) Annealing of (c) in the absence of additional S vapor to 1020 K for 360 s. The STM height profiles are taken along the black lines in the topographs. Image information: (a) size 100 nm × 60 nm, $V_s = 1$ V, $I_t = 0.23$ nA; (b) size 100 nm × 60 nm, $V_s = 3.4$ V, $I_t = 0.041$ nA; (c) size 100 nm × 60 nm, $V_s = 2.5$ V, $I_t = 0.05$ nA; (d) size 100 nm × 60 nm, $V_s = 2.1$ V, $I_t = 0.17$ nA.

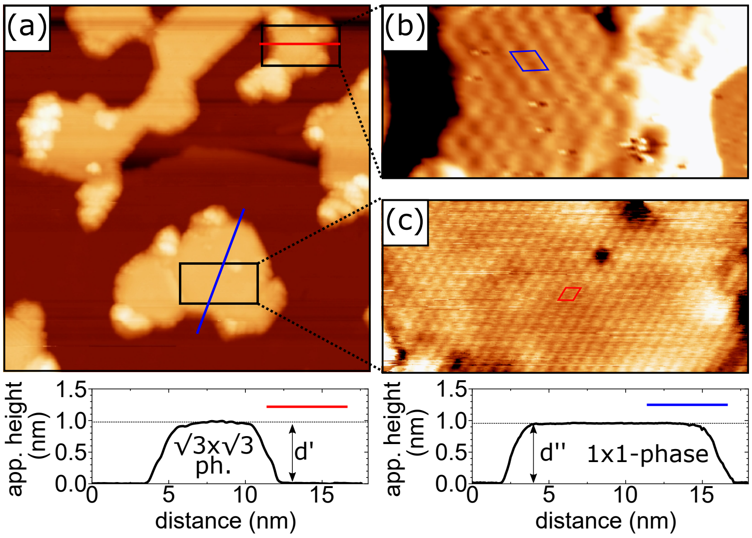

FIG. S4. Coexistence of Nb $\sqrt{3}\times\sqrt{3}-$phase and Nb $1\times1-$phase after room temperature Nb deposition onto the sample with pristine NbS_2 islands and additional annealing to 1020 K. (a) Larger magnification STM topograph after annealing to 1020 K from same experiment as visualized already in Fig. S3. (b) STM topograph from boxed area indicated in (a) featuring the $\sqrt{3}\times\sqrt{3}$ R30° superstructure. Unit cell indicated by a blue rhomboid. Topograph is differentiated to enhance contrast and make Nb $\sqrt{3}\times\sqrt{3}-$phase visible. (c) STM topograph from boxed area indicated in (a) featuring the 1×1 structure. Unit cell indicated by red rhomboid. Height profiles are taken along red and blue lines in (a). Image information: (a) size $50\,\mathrm{nm}\times50\,\mathrm{nm}$, $V_s = 0.97\,\mathrm{V}$, $I_t = 0.13\,\mathrm{nA}$; (b) size $10\,\mathrm{nm}\times4.7\,\mathrm{nm}$, $V_s = 0.97\,\mathrm{V}$, $I_t = 0.13\,\mathrm{nA}$; (c) size $10\,\mathrm{nm}\times4.7\,\mathrm{nm}$, $V_s = 2.5\,\mathrm{V}$, $I_t = 0.05\,\mathrm{nA}$.

Also the NbS_2 islands are cleared to a good extend. Clusters are found still in great number at the NbS_2 islands edges. The height profile provides evidence that the pristine NbS_2 islands transformed partly into the Nb $\sqrt{3}\times\sqrt{3}-$phase and partly into the Nb $1\times1-$phase. Additional annealing to 1020 K reduces the number of clusters. Besides islands in the Nb $1\times1-$phase and the Nb $\sqrt{3}\times\sqrt{3}-$phase, in small island patches a new height level of 1.24 nm is apparent (compare also STM height profile). We attribute this height level to NbS_2 bilayer islands. There are indications that these bilayer islands show signs of Nb intercalation in the van der Waals gap between the two NbS_2 layers. However, the analysis of the structure of the bilayers is beyond the scope of the present manuscript.

Fig. S4 (a) displays an STM topograph of the experiment already visualized by Fig. S3 (d). Zooms into the boxed areas shown in Figs. S4 (b) and (c) display the Nb $\sqrt{3}\times\sqrt{3}-$phase and the Nb $1\times1-$phase in atomic resolution with their corresponding unit cells marked by a blue/red rhomboid correspondingly. The apparent island heights, measured through the height profiles shown below the STM topographs, are consistent with the atomic structure measured.

STRUCTURES OF NbS_2 ISLANDS AFTER Fe DEPOSITION AT 820 K AND ADDITIONAL ANNEALING TO 1020 K

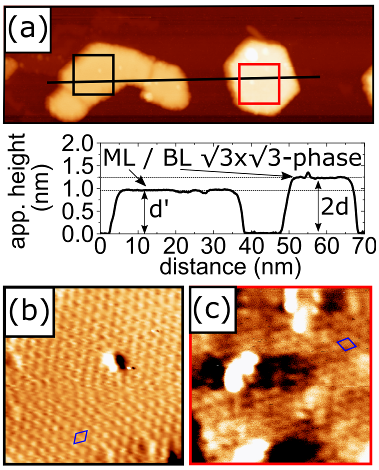

FIG. S5. Structures of NbS_2 islands after Fe deposition at 820 K and subsequent annealing to 1020 K. (a) STM topograph with one NbS_2 island in the ML Fe $\sqrt{3} \times \sqrt{3}$ – phase (left) and one island in the BL Fe $\sqrt{3} \times \sqrt{3}$ – phase (right). Height profile is taken along the black line in the topograph. (b), (c) Differentiated STM topographs of boxed areas in (a). $\sqrt{3} \times \sqrt{3}$ R30° superstructure unit cell is indicated by blue a rhomboid. Image information: (a) size 100 nm × 32 nm, $V_s = 0.51$ V, $I_t = 0.2$ nA; (b) size 10 nm × 10 nm, $V_s = 0.51$ V, $I_t = 0.2$ nA; (c) size 10 nm × 10 nm, $V_s = 0.22$ V, $I_t = 0.64$ nA.

As already mentioned in the main manuscript, also after annealing to 1020 K, both islands with ML Fe $\sqrt{3} \times \sqrt{3}$ – phase [left in Fig. S5 (a)] and with BL Fe $\sqrt{3} \times \sqrt{3}$ – phase [right in Fig. S5 (a)], display a $\sqrt{3} \times \sqrt{3}$ R30° superstructure as shown in Figs. S5 (b) and (c).

33 NbS$_2$ BILAYER ISLANDS AFTER GROWTH

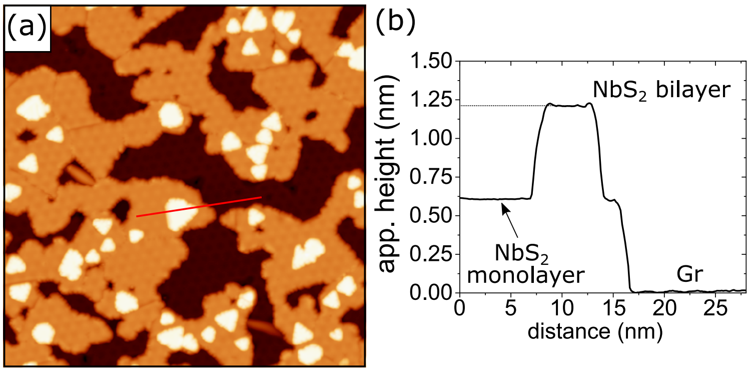

FIG. S6. Height comparison of NbS$_2$ monolayer and bilayer after growth on Gr/Ir(111) including annealing to 820 K for 360 s. (a) STM topograph of a sample area featuring both monolayer- and bilayer islands. (b) Height profile measured along the red line in (a). Image information: size 75 nm × 75 nm, $V_s = 1.0$ V, $I_t = 0.1$ nA, $T_s = 0.4$ K

CHAPTER 9

Manuscript 3: Bloch Spin Helix in an Ultrathin Fe Film on Ir(110)

This chapter consists of the above-named manuscript, in preparation for submission to a publishing journal.

The experiments were proposed by T. Knispel, S. Blügel, T. Michely and J. Fischer. Sample growth and experiments were conducted at the low temperature magnetic STM system (MSTM) in our group. Sample growth and STM and STS experiments were carried out by T. Knispel and J. Fischer under the advice from T. Michely. Data analysis was performed by T. Knispel and J. Fischer.

V. Tseplyaev , M. Hoffmann and S. Blügel made a significant contribution to the discussion of the experimental results and performed theoretical calculations included in the manuscript.

T. Knispel wrote the manuscript and finalized it in close collaboration with J. Fischer and T. Michely.

Bloch spin helix in an ultrathin Fe film on Ir(110)

Timo Knispel,[1] Vasily Tseplyaev,[2] Markus Hoffmann,[2]
Stefan Blügel,[2] Thomas Michely,[1] and Jeison Fischer[1]

[1] *II. Physikalisches Institut, Universität zu Köln,*
Zülpicher Straße 77, 50937 Köln, Germany
[2] *Peter Grünberg Institut und Institute for Advanced Simulation,*
Forschungszentrum Jülich, Wilhelm-Johnen-Straße, 52428 Jülich, Germany

(Dated: March 28, 2022)

Abstract

We employed spin-polarized scanning tunneling microscopy and spectroscopy to study the spin texture of ultrathin films of Fe on Ir(110). Our results reveal a magnetic stripe phase with a period of 1.27 nm along the close-packed $[\bar{1}10]$-direction within the Fe film. The spin texture behind the stripe pattern is an incommensurate spin helix. Based on detailed field-dependent measurements with a vector magnet, we conclude that the spin helix is of Bloch-type, where the rotation axis of the helix is parallel to the propagation direction. The rotational sense is degenerate as left and right rotations are found in different Fe islands. These results contradict the assumption of a spin helix being driven by an interface in-plane DMI vector. Combined with theoretical insights, we discuss our findings in terms of an exchange-driven spin texture.

Introduction

Non-collinear spin textures, helical or skyrmionic, are currently in the spotlight for their potential use for new applications in spintronics [1–3]. This perspective leads to a large interest in understanding the magnetic interactions that stabilize these novel spin textures [4–6]. When helical spin order was imaged for the first time in a thin crystal of $\mathrm{Fe_{0.5}Co_{0.5}Si}$ by Uchida et al. [7] or in a Mn monolayer on W(110) by Bode et al. [4], the chiral spin order was explained by invoking the Dzyaloshinskii-Moriya interaction (DMI), which had been at the sidelines until then. The nanoskyrmion square lattice discovered in a Fe monolayer on Ir(111) by Heinze et. al forced the inclusion of four-spin higher-order exchange interaction terms to explain the observations [6]. The addition of these magnetic interactions to the established repertoire expanded the view on spin texture formation. Subsequently, additional magnetic interactions beyond conventional Heisenberg exchange were introduced to the field [8] and found to act in reality [9]. Obviously, the interplay between the observation of novel spin textures and the proposition of new magnetic interactions drives the development of this active research field.

The stabilization of non-collinear spin textures is often ascribed to a competition of the Heisenberg exchange interaction which aligns neighboring spins, with the asymmetric DMI, which cants neighboring spins. Two ingredients are necessary to establish DMI, spin-orbit coupling (SOC), which connects the lattice with the spin symmetry, and broken inversion symmetry [10, 11]. While SOC is acting for materials of elements with large Z, broken inversion symmetry is present in chiral bulk crystals [7] or at surfaces and interfaces [4]. The DMI Hamiltonian between two neighboring atomic spins is $H_{\mathrm{DMI}} = -\vec{D}_{ij}.(\vec{S}_i \times \vec{S}_j)$, where $\vec{D}_{ij}$ is the DM vector being in magnitude to first order proportional to the strength of SOC and $(\vec{S}_i \times \vec{S}_j)$ is the vector chirality between atomic spins. For interface or surface DMI, according to the Moriya rules [11] valid for high-symmetry surfaces, the DM vector is in-plane and perpendicular to the bond direction connecting nearest neighbors.

This orientation of the DM vector implies that either left- or right-rotation of the spins around an axis normal to the propagation direction is possible. That is, only either right- or left-rotating Néel-type spin chiralities are consistent with the action of the DMI. Bloch-type spin chiralities, where the spins rotate around the axis of propagation are inconsistent with the DMI being a decisive factor for spin texture formation. In fact, evidence for unique chirality Néel type rotation was found in several DMI-driven spin textures, such as spin helices [12, 13], skyrmions [6, 14], or chiral domain walls [15, 16].

Since it was established that the DMI was an essential ingredient for non-collinear spin textures, Bloch type rotation appeared to be inaccessible in ultrathin films. In *thicker* films beyond the monolayer limit, where magnetostatic interactions are relevant, depending on the domain wall orientation Bloch, Néel, or mixed wall character has been observed [17]. Here, anisotropic DMI may favor Néel-type rotation in certain directions, while otherwise magnetostatic energy is reduced for a Bloch-type rotation. Interlayer exchange interaction may also influence a Bloch component in a multilayer system, where magnetostatic interactions lead to Néel [18]. The competition of magnetostatic and RKKY results in an intermediate Bloch-Néel domain wall texture.

In the case of weak DMI non-collinear spin textures can also be stabilized exclusively by isotropic exchange interactions, that could give rise to Bloch type rotation. Such a system, Fe/Cu(111), was first investigated by Phark et al. [19, 20]. For Fe/Cu(111), the DMI is small due to the light 3d transition metals with small SOC. In this system, the competition of short- and long-range exchange interactions is the driving force for the spin texture. Some systems containing heavy elements have also been described to be stabilized by exchange interaction, such as the Mn/W(100) [21] and Rh-fcc/Fe/Ir(111) [22]. Nevertheless, for all these cases a single Néel-type rotation was assumed, due to a residual contribution of interfacial DMI. In fact, evidence for a Bloch-type spin texture in ultrathin films is still lacking.

In this paper, we report on the observation of a spin texture with Bloch-type chirality in an ultrathin film of Fe on Ir(110). This finding is in fact surprising, as one would expect a sizable interfacial DMI to be present, originating from the strong spin–orbit coupling in Ir. The interfacial DMI should compete against the exchange interaction, defining a Néel type spin texture. This expectation is not met. Our experimental observation is a spin helix with a short period of a few atomic distances. The observation of a Bloch-type spin helix forces us to assume the spin texture to be the result of strong, complex, and competing exchange interactions within the Fe film. The DMI is not able to lift the degeneracy of spin chirality and we observe a coexistence of left- and right-rotating Bloch-type spin helices.

Experimental details

The measurements were performed in an ultra-high vacuum (UHV) chamber (base pressure < 3×10^{-10} mbar) equipped with a scanning tunneling microscope (STM) operating at 1.7 K and superconducting magnets producing a magnetic field of up to 9 T normal and 2 T parallel to the sample surface. Ir(110) was cleaned by cycles of 1 kV Ar-sputtering and annealing at 1500 K. After cool-down, the sample displays the thermodynamically stable {331}-nanofacet reconstruction [23, 24]. In order to establish a clean Ir(110)-(1×1) surface we applied a two-step procedure. First, during cooling oxygen exposure to saturation lifted the nanofacet reconstruction and induced oxygen covered Ir(110)-(1×1), as was first shown by Chan et al. [25]. Second, following the approach of Heinz et al. [26] to prepare *clean* unreconstructed Ir(001), chemisorbed oxygen was titrated through exposure to 1×10^{-7} mbar hydrogen at 633 K until clean Ir(110)-(1×1) resulted. 0.6 ML to 1.4 ML Fe was deposited by e-beam evaporation onto clean Ir(110)-(1×1) at 633 K. Here ML denotes monolayer and one monolayer corresponds to the surface atomic density of Ir(110)-(1×1), which is 1.09×10^{-19} atoms/m^2.

Experimental results

Figure 1(a) shows an overview constant current STM image with Fe islands (orange in color scale) grown on bare Ir(110)-(1×1) (turquoise). The close-packed atomic rows of bare Ir(110)-(1×1) lines are parallel to the $[\bar{1}10]$-direction. A detailed view of bare Ir(110) is shown in the atomically resolved STM image in Fig. 1(b). The surface unit cell is represented by a rectangle [compare also Fig. 1(d)]. Its short sides are parallel to the $[\bar{1}10]$-direction and the long sides are aligned with the [001]-direction. Their length is 0.27 nm and 0.38 nm, respectively.

As apparent from Fig. 1(a), Fe deposition leads to the formation of large Fe islands with roughly 10 nm of lateral size as well as smaller ones. The larger islands are pseudomorphic and of bilayer height as is discernible from the alignment between the rows on top of the Fe islands and the Ir surface, see Fig. 1(c) and Fig. 1(d), and the line profile of Fig. 1(e). The apparent height of the Fe islands is measured to be 0.27 nm.

To study the spin texture of the bilayer Fe islands, we performed spin-polarized STM measurements. In order to obtain magnetic contrast, we used Fe-coated-W tips. This type of tip is usually magnetically soft and can be tuned in any direction with moderate external magnetic field. In some cases the response is superparamagnetic [27].

Figure 2(a) shows a constant current STM image of a bilayer Fe island on Ir(110). The image is

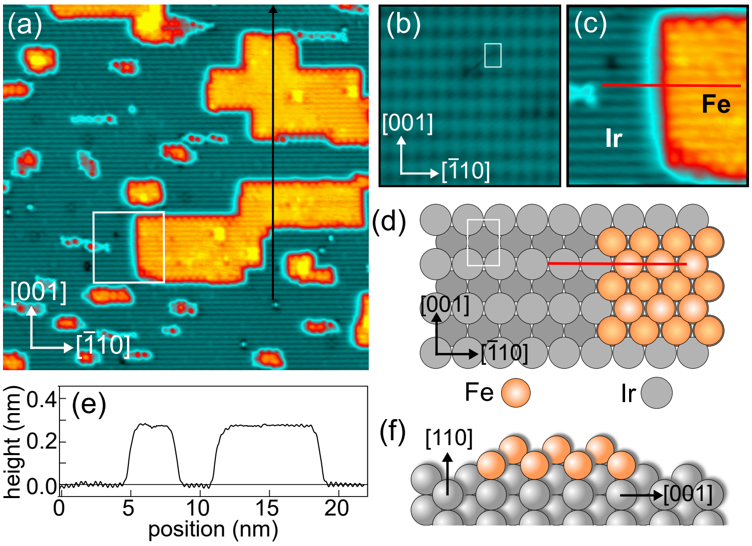

FIG. 1. (a) Constant current STM image of submonolayer Fe on Ir(110). (b) Atomically resolved Ir(110)-(1 × 1) lattice. The surface unit cell is indicated by a rectangle. (c) Zoomed area indicated by a white square in (a). The red line highlights the in-phase behavior of the atomic rows in the Fe island and the substrate, consistent with pseudomorphic bilayer. (d) Top view ball model showing the surface Ir atoms (grey) and the Fe atoms (orange), the rectangular surface unit cell, and the in-phase behavior of atomic rows of Fe and Ir (red line) (e) STM height profile along black line in (a). The apparent height of the islands is consistent with the bilayer character of the Fe growth. (f) Side view ball model of the Fe islands on Ir(110). Image information: (a) size 28 nm × 28 nm, $V_\mathrm{s} = 100\,\mathrm{mV}$, $I_\mathrm{t} = 1\,\mathrm{nA}$, $T_\mathrm{s} = 1.7\,\mathrm{K}$; (b) size 3 nm × 3 nm, $V_\mathrm{s} = 50\,\mathrm{mV}$, $I_\mathrm{t} = 30\,\mathrm{nA}$, $T_\mathrm{s} = 1.7\,\mathrm{K}$.

taken under an external magnetic field of 1 T normal to the sample surface. The STM image reveals a periodic stripe contrast parallel to the [001]-direction on the surface of the bilayer Fe island. As the magnetic field assures an out-of-plane direction of the tip magnetization, the bright and dark modulation pattern characterizes an out-of-plane sample magnetization parallel and antiparallel to the tip magnetization. Figure 2(b) shows a line profile averaged within the rectangle of Fig. 2(a). This profile reveals an almost sinusoidal variation of the apparent height with a periodicity of 1.27 nm. Figure 2(c) displays an STM topograph with simultaneous atomic and spin resolution of bilayer Fe. Bright spots correspond to Fe atom positions. For better visualization a ball model is superimposed in the lower part of the STM image. Here, the bilayer Fe shows the same lattice structure as Ir(110) [see Fig. 1(b)], as expected for pseudomorphic growth. The long-range brightness oscillation in Fig. 2(c) corresponds to the magnetic stripe pattern. The brightness oscillation is visualized by a black sinusoidal line. The periodicity λ divided by the nearest neighbor distance d_NN yields 4.69, *i.e.* the spin periodicity appears to be incommensurate with respect to the un-

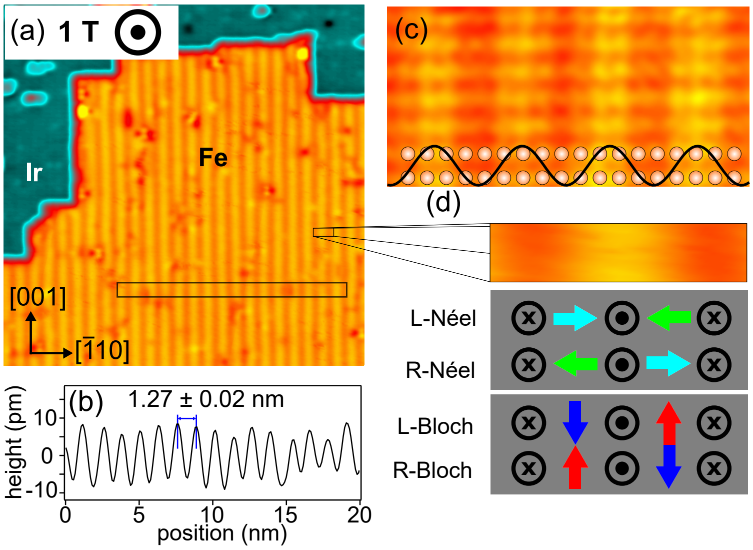

FIG. 2. (a) Constant current STM image of a bilayer Fe island on Ir(110) in an external out-of-plane magnetic field of 1 T. A magnetic modulation pattern parallel to the [001]-direction and with wave-vector aligned to the [$\bar{1}$10]-direction is visible. Bright and dark stripes represent local magnetization parallel and antiparallel to the out-of-plane tip magnetization. (b) Line profile averaged over lines within the rectangle in (a). The modulation pattern has a periodicity of 1.27 nm. (c) Atomically- and spin-resolved STM image of bilayer Fe at an external out-of-plane field of 1 T. Atomic positions are superimposed in the lower part of the image. The height modulation is schematically represented by a sinusoidal curve. The height maxima show no correlation with the atomic positions, indicating an incommensurate magnetic texture. (d) A slice of the out-of-plane modulation pattern is compared to artist's top views of spin helices. The sequence of directions indicated by the arrows denotes the sequence of spin orientations for a left-rotating (L-Néel) and a right-rotating (R-Néel) Néel spin helix as well as for a left-rotating (L-Bloch) and a right-rotating (R-Bloch) Bloch spin helix. Image information: (a) size 28 nm × 28 nm, $V_s = 100\,\text{mV}$, $I_t = 1\,\text{nA}$, $T_s = 1.7\,\text{K}$; (c) size 5 nm × 2.5 nm, $V_s = 50\,\text{mV}$, $I_t = 1\,\text{nA}$, $T_s = 1.7\,\text{K}$.

derlying Fe lattice. Further evidence is shown in Fig. 2(c), as the spin contrast maxima do not match to a specific position in the atomic lattice. In Fig. 2(d), a slice of the stripe pattern of (a) is compared with potential spin textures that could give rise to the observed magnetic contrast. The slice shows dark-bright-dark contrast due to an out-of-plane down-up-down spin alignment. However, with a tip only magnetized out-of-plane, in-plane components are inaccessible. Possible in-plane spin alignments in between the down-up and up-down spins lead to four possible spin textures, as indicated in Fig. 2(d).

Next, we simply look for the in-plane components of the magnetization to scrutinize the origin of the spin texture on the surface of bilayer Fe. In spin-polarized STM this is possible thanks to the dependence of the differential conductance (dI/dV) on the scalar product of sample ($\vec{m}_\text{S}$)

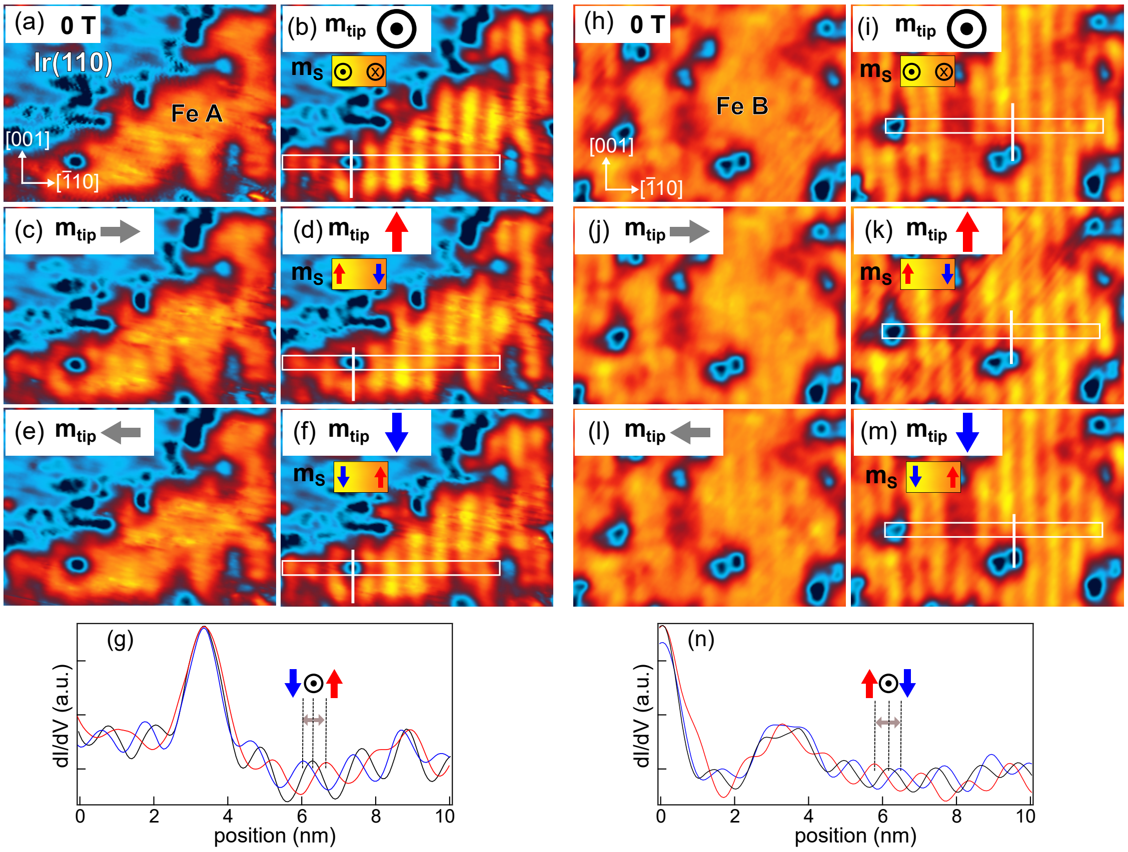

FIG. 3. Spin-polarized differential conductance (dI/dV) maps and profiles recorded on two different bilayer Fe islands represented by (a)-(g) and (h)-(n), tip magnetization orientation $\vec{m}_{\mathrm{tip}}$ is given in each sub-figure. (a) Zero field dI/dV map displays no magnetic contrast. (b),(d),(f) dI/dV maps show magnetic stripe modulation within the bilayer Fe region. For (b) the tip magnetization is out-of-plane and for (d),(f) it is in-plane, parallel to the stripes along the [001]- and the [00$\bar{1}$]-direction, respectively. The inset represents the color code of the local sample magnetization ($\vec{m}_{\mathrm{S}}$) within each figure. (c),(e) The stripe contrast vanishes for tip magnetization along the [$\bar{1}$10]- and the [1$\bar{1}$0]-direction, respectively. The vertical white lines in (b),(d) and (f) mark a defect position and are used as a guide to the eye for identification of shifts of the modulation pattern due to the changed direction of tip magnetization. (g) Averaged differential conductance line profiles taken within the rectangles in (b),(d),(f). The color code of the profiles matches with the color code used in the dI/dV maps for tip magnetization. Black: out-of-plane, red: parallel, and blue: antiparallel to the in-plane [001]-direction. The red curve is shifted forward by 0.31 nm with respect to the black curve, into the [$\bar{1}$10]-direction, while the blue curve is shifted backwards by 0.24 nm with respect to the black curve. (h)-(m) Identical measurements for a second Fe island with the same general behavior as in (a)-(f), except for the pattern shifts. (n) Averaged differential conductance line profiles taken within the rectangles in (i),(k),(m). Now the red curve is shifted backwards by 0.31 nm and the blue curve is shifted forward by 0.28 nm with respect to the black curve. Image information: size 11 nm × 15 nm, $V_{\mathrm{s}} = 100\,\mathrm{mV}$, $I_{\mathrm{t}} = 2.0\,\mathrm{nA}$, $V_{\mathrm{mod}} = 10\,\mathrm{mV}$, $f_{\mathrm{mod}} = 6670\,\mathrm{Hz}$, $T_{\mathrm{s}} = 1.7\,\mathrm{K}$.

and tip ($\vec{m}_{\text{tip}}$) magnetization, as in $dI/dV \propto \vec{m}_{\text{S}} \cdot \vec{m}_{\text{tip}}$ [28]. In this case, in-plane components of the sample are detected by rotating the tip magnetization from out-of-plane to in-plane with the help of the vector magnetic field. Since the spin texture of the sample ($\vec{m}_{\text{S}}$) is not affected by an external out-of-plane field of up to 9 T (not shown here), this allows us to measure different local magnetization orientations at the same position by realigning the tip magnetization ($\vec{m}_{\text{tip}}$) with the vectorial magnetic field [6, 12]. Differential conductance maps are recorded of the same area for different in-plane directions of $\vec{m}_{\text{tip}}$ to obtain the full spin texture.

Figures 3(a)-(f) show differential conductance maps of a bilayer Fe island on Ir(110). At 0 T, no magnetic contrast is observed, see (a). This is due to the negligible remanent magnetization of the tip, indicating it to be superparamagnetic. The color code is chosen such that the bilayer Fe island is orange, while the Ir(110) substrate and defects are blue and black. Next, in Figs. 3(b)-(f), dI/dV maps for five orientations of tip magnetization are shown: out-of-plane along the [110]-direction in (b); in-plane along the [$\bar{1}$10]-direction in (c), along the [001]-direction in (d), along the [1$\bar{1}$0]-direction in (e), and finally along the [00$\bar{1}$]-direction in (f). The map in Fig. 3(b) displays a clear out-of-plane magnetic stripe pattern contrast on the Fe bilayer as described in Fig. 2(a), while the contrast of the Ir surface and the defects are unchanged. The stripe contrast indicates sample magnetization parallel (bright) or antiparallel (dark) to the out-of-plane tip magnetization, as specified by the insets defining the relation of contrast and $\vec{m}_{\text{S}}$. In Figs. 3(c) and (e), the stripe pattern contrast is almost completely suppressed, which is attributed to the absence of in-plane components along the [$\bar{1}$10]- and [1$\bar{1}$0]-directions. In the dI/dV maps of Figs. 3(d) and (f), when the tip magnetization is aligned along [001]- and the [00$\bar{1}$]-direction, the magnetic contrast is recovered. The modulation contrast arises now from the in-plane spins of the magnetic texture. In Figs. 3(d) and (f) the vertical white line pinned to a defect makes obvious that the modulation pattern is exactly inverted for these opposing in-plane tip magnetization orientations. The outcome is that the sample carries out-of-plane components that are surrounded by in-plane components pointing in opposite directions along the [001]-direction. The observation of opposite in-plane components along {001}, coexisting with opposite out-of-plane components, characterizes a Bloch type spin helix. Our observation is inconsistent with collinear spin textures, like spin-density waves or multiple-row-wise antiferromagnetism [8, 9].

The dI/dV line profile analysis presented in Fig. 3(g) makes obvious that the sample magnetization $\vec{m}_{\text{S}}$ rotates counterclock-wise, *i.e.* the spin helix is a left-rotating Bloch spin helix. The black line profile is the result of an average over the scan lines indicated within Fig. 3(b) by the white rectangle. When turning the tip magnetization from the out-of-plane [110]-direction [compare

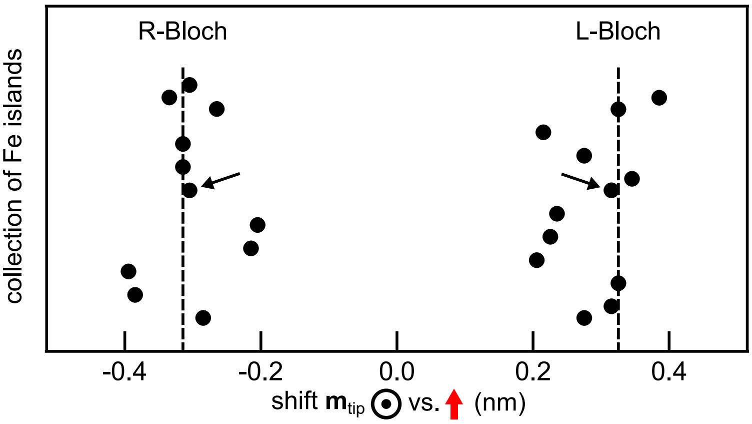

FIG. 4. Rotational senses of Bloch spin helices in bilayer Fe islands. Each data point represents a different island. The shifts are obtained as discussed in the text for Fig. 3(g) and (n), of which the values are indicated by arrows. Positive (negative) shifts represents L-Bloch (R-Bloch) spin helices. The dashed lines mark the $\lambda/4$ (0.32 nm) positions, corresponding to the full rotation from the out-of-plane to the in-plane direction.

Fig. 3(b)] into the in-plane [001]-direction [compare Fig. 3(d)] the bright wave pattern crests move forward into the $[\bar{1}10]$-direction, as obvious from the comparison of the black and the red profile in Fig. 3(g). When turning into the in-plane $[00\bar{1}]$-direction [compare Fig. 3(f)] the wave crests move backwards with respect to the $[\bar{1}10]$-direction, as obvious from the comparison of the black and the blue profile in Fig. 3(g). The total shift between the wave crests of the blue and red profiles is 0.55 nm, within the limits of error in agreement with $\lambda/2 = 1/2 \times 1.27\,\mathrm{nm} = 0.63\,\mathrm{nm}$. Taking the directions of wave pattern shifts and their magnitude together, they imply a counterclock-wise or left-rotating Bloch spin helix as depicted in Fig. 2(d). Note that the spin helix rotation is counterclock-wise or left-rotating, irrespective of whether its propagation direction is viewed along the $[\bar{1}10]$-direction or the opposite $[1\bar{1}0]$-direction.

A similar analysis for a second Fe bilayer island exemplified in Fig. 3(h) to (n) makes plain that in this island the spin texture displays a *clock-wise or right-rotating* Bloch spin helix. The total shift of the wave crests between the blue and the red profile in Fig. 3(n) is 0.59 nm, in even better agreement with the expectation of $\lambda/2$.

We performed similar experiments as shown in Fig. 3 for additional 21 different bilayer Fe islands and plot the shifts of the wave crest patterns obtained in Fig. 4. Our analysis finds 12 left- and 11 right-rotating spin helices consistent with the absence of an energetic preference of one over the other. A unique rotational sense for spin helices in bilayer Fe on Ir(110) can be ruled out on the basis of our results.

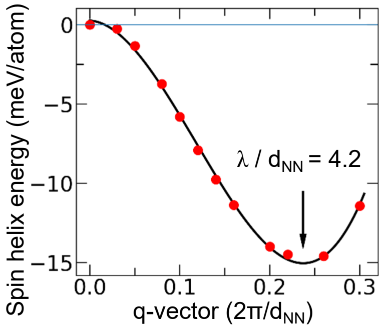

FIG. 5. Calculated formation energy of a spin helix (circles) as a function of wave vector q along the $[1\bar{1}0]$-direction for the system BL-Fe/Ir(110). SOC is not included.

Theory results and discussion

The results shown in Fig. 3 and in Fig. 4 demonstrate that bilayer Fe islands on Ir(110) exhibit Bloch spin helices which are degenerate between left- and right-rotation. Such Bloch spin helices have not been observed before on the surface of an ultrathin film.

In order to gain insight into the driving force of the spin helix, we study the non-collinear magnetism of 2 layers of Fe on Ir(110) based on density functional theory. The magnetic structure has been determined in the local density approximation [29], using the full-potential linearized augmented plane wave (FLAPW) method in film geometry as implemented in the FLEUR code [30]. The system was modeled by two pseudomorphic Fe monolayers on a 7-layer Ir(110) slab with the experimental Ir lattice constant (0.384 nm) for the lateral interatomic distances, the distance between the Fe-Fe layers was reduced by $-4.8\,\%$, in accordance with surface relaxation.

Figure 5 shows the formation energy of the spin helix as a function of the q-vector along the $[\bar{1}10]$-direction (propagation direction of the spin helix). The calculations are performed without including SOC. The energy minimum corresponds to the q-vector of the spin helix in this system with the corresponding ratio $\frac{\lambda}{d_{\text{NN}}} = 4.2$, which is in fair agreement with the experimental observation (4.69). This remarkable result indicates that SOC (and therefore DMI) does not play a role in the formation of the spin helix in bilayers of Fe on Ir(110). The energy gain per Fe atom in the spin helix state as compared to the FM state ($q = 0$) is of the order of 15 meV (depth of the minimum in Fig. 5). This value gives the stability of the magnetic state, which is way above the available external field energy, in agreement with the lack of phase transition up to an external field of 9 T.

If we take Fig. 5 as evidence that DMI is not present or has negligible contribution as compared to exchange interaction, another consequence might be discussed. In a system that is not stabilized by DMI, chirality is not expected and a degeneracy between right- and left-rotation spin helices is anticipated. This results from the spatially symmetric nature of the exchange interaction. Here, again, a firm agreement with our experimental results is obtained, as shown in Fig. 4, the Bloch spin helices are fully degenerate.

It is important to note that additional calculations showed that when including SOC (not shown), DMI contribution is quite significant and the system tends to feature a Néel type spin helix with an energy gain of 2.5 meV/atom for the left-rotation. This result is expected as interfacial DMI always favors Néel type rotation. However, Bloch spin helices would remain degenerate even in the presence of DMI.

In conclusion, our study reveals that Bloch spin helix is also conceivable for ultrathin films. We provide unambiguous experimental data evidencing that a Bloch spin helix is present in bilayer Fe on Ir(110). This opens the way for alternative venues to apply non-collinear spin states for potential applications. Remarkably, in contrast to previous experimental studies on non-collinear magnetism in magnetic films supported on 5d metals, the magnitude of the DMI is not only too small to drive the spin helix formation, but also not capable of lifting the degeneracy between left- and right rotation in Bloch spin helices. This points to a different mechanism that goes beyond the established knowledge in the field.

ACKNOWLEDGMENTS

We acknowledge funding from Deutsche Forschungsgemeinschaft (DFG) through CRC 1238 (project number 277146847, subprojects A01, B06 and C01).

---

[1] N. Nagaosa and Y. Tokura, Topological properties and dynamics of magnetic skyrmions, Nature Nanotechnology **8**, 899 (2013).

[2] A. Fert, N. Reyren, and V. Cros, Magnetic skyrmions: advances in physics and potential applications, Nature Reviews Materials **2**, 17031 (2017).

[3] W. Jiang, G. Chen, K. Liu, J. Zang, S. G. te Velthuis, and A. Hoffmann, Skyrmions in magnetic multilayers, Physics Reports **704**, 1 (2017), skyrmions in Magnetic Multilayers.

[4] M. Bode, M. Heide, K. Von Bergmann, P. Ferriani, S. Heinze, G. Bihlmayer, A. Kubetzka, O. Pietzsch, S. Blügel, and R. Wiesendanger, Chiral magnetic order at surfaces driven by inversion asymmetry, Nature **447**, 190 (2007).

[5] S. Mühlbauer, B. Binz, F. Jonietz, C. Pfleiderer, A. Rosch, A. Neubauer, R. Georgii, and P. Boni, Skyrmion Lattice in a Chiral Magnet, Science **323**, 915 (2009).

[6] S. Heinze, K. Von Bergmann, M. Menzel, J. Brede, A. Kubetzka, R. Wiesendanger, G. Bihlmayer, and S. Blügel, Spontaneous atomic-scale magnetic skyrmion lattice in two dimensions, Nature Physics **7**, 713 (2011).

[7] M. Uchida, Y. Onose, Y. Matsui, and Y. Tokura, Real-space observation of helical spin order, Science **311**, 359 (2006).

[8] A. Al-Zubi, G. Bihlmayer, and S. Blügel, Modeling magnetism of hexagonal Fe monolayers on 4d substrates, Physica Status Solidi (B) Basic Research **248**, 2242 (2011).

[9] A. Krönlein, M. Schmitt, M. Hoffmann, J. Kemmer, N. Seubert, M. Vogt, J. Küspert, M. Böhme, B. Alonazi, J. Kügel, H. A. Albrithen, M. Bode, G. Bihlmayer, and S. Blügel, Magnetic Ground State Stabilized by Three-Site Interactions: Fe/Rh (111), Physical Review Letters **120**, 207202 (2018).

[10] I. Dzyaloshinskii, A thermodynamic theory of “weak” ferromagnetism of antiferromagnetics, Journal of Physics and Chemistry of Solids **4**, 241 (1958).

[11] T. Moriya, Anisotropic superexchange interaction and weak ferromagnetism, Physical Review **120**, 91 (1960).

[12] S. Meckler, N. Mikuszeit, A. Preßler, E. Y. Vedmedenko, O. Pietzsch, and R. Wiesendanger, Real-Space Observation of a Right-Rotating Inhomogeneous Cycloidal Spin Spiral by Spin-Polarized Scanning Tunneling Microscopy in a Triple Axes Vector Magnet, Physical Review Letters **103**, 157201 (2009).

[13] P.-J. Hsu, A. Finco, L. Schmidt, A. Kubetzka, K. von Bergmann, and R. Wiesendanger, Guiding Spin Spirals by Local Uniaxial Strain Relief, Physical Review Letters **116**, 017201 (2016).

[14] R. Lo Conte, A. K. Nandy, G. Chen, A. L. Fernandes Cauduro, A. Maity, C. Ophus, Z. Chen, A. T. N’Diaye, K. Liu, A. K. Schmid, and R. Wiesendanger, Tuning the Properties of Zero-Field Room Temperature Ferromagnetic Skyrmions by Interlayer Exchange Coupling, Nano Letters **20**, 4739 (2020).

[15] G. Chen, J. Zhu, A. Quesada, J. Li, A. T. N’Diaye, Y. Huo, T. P. Ma, Y. Chen, H. Y. Kwon, C. Won, Z. Q. Qiu, A. K. Schmid, and Y. Z. Wu, Novel Chiral Magnetic Domain Wall Structure

in Fe/Ni/Cu(001) Films, Physical Review Letters **110**, 177204 (2013).

[16] F. Ajejas, A. Gudín, R. Guerrero, A. Anadón Barcelona, J. M. Diez, L. De Melo Costa, P. Olleros, M. A. Niño, S. Pizzini, J. Vogel, M. Valvidares, P. Gargiani, M. Cabero, M. Varela, J. Camarero, R. Miranda, and P. Perna, Unraveling Dzyaloshinskii-Moriya Interaction and Chiral Nature of Graphene/Cobalt Interface, Nano Letters **18**, 5364 (2018).

[17] G. Chen, A. T. N'Diaye, S. P. Kang, H. Y. Kwon, C. Won, Y. Wu, Z. Q. Qiu, and A. K. Schmid, Unlocking Bloch-type chirality in ultrathin magnets through uniaxial strain, Nature Communications **6**, 6598 (2015).

[18] M. J. Meijer, J. Lucassen, O. Kurnosikov, H. J. Swagten, B. Koopmans, R. Lavrijsen, F. Kloodt-Twesten, R. Frömter, and R. A. Duine, Magnetic Chirality Controlled by the Interlayer Exchange Interaction, Physical Review Letters **124**, 207203 (2020).

[19] S. H. Phark, J. A. Fischer, M. Corbetta, D. Sander, K. Nakamura, and J. Kirschner, Reduced-dimensionality-induced helimagnetism in iron nanoislands, Nature Communications **5**, 5183 (2014).

[20] J. A. Fischer, L. M. Sandratskii, S.-h. Phark, D. Sander, and S. Parkin, Atomic structure governed diversity of exchange-driven spin helices in Fe nanoislands: Experiment and theory, Physical Review B **96**, 140407 (2017).

[21] P. Ferriani, K. von Bergmann, E. Y. Vedmedenko, S. Heinze, M. Bode, M. Heide, G. Bihlmayer, S. Blügel, and R. Wiesendanger, Atomic-Scale Spin Spiral with a Unique Rotational Sense: Mn Monolayer on W(001), Physical Review Letters **101**, 027201 (2008).

[22] N. Romming, H. Pralow, A. Kubetzka, M. Hoffmann, S. von Malottki, S. Meyer, B. Dupé, R. Wiesendanger, K. von Bergmann, and S. Heinze, Competition of Dzyaloshinskii-Moriya and Higher-Order Exchange Interactions in Rh/Fe Atomic Bilayers on Ir(111), Physical Review Letters **120**, 207201 (2018).

[23] R. Koch, M. Borbonus, O. Haase, and K. H. Rieder, New aspects on the Ir(110) reconstruction: Surface stabilization on mesoscopic scale via (331) facets, Physical Review Letters **67**, 3416 (1991).

[24] A. Ney, J. J. Schulz, M. Sturmat, and R. Koch, Stress-driven self-assembly on Ir(110): Stripes, droplets, and missing-row-type reconstructions, Surface Science **519**, 192 (2002).

[25] C. M. Chan, S. L. Cunningham, K. L. Luke, W. H. Weinberg, and S. P. Withrow, Determination of the atomic arrangement of the unreconstructed Ir(110) surface by low-energy electron diffraction, Surface Science **78**, 15 (1978).

[26] K. Heinz, G. Schmidt, L. Hammer, and K. Müller, Dynamics of the reconstruction process Ir(100) 1×1→1×5, Physical Review B **32**, 6214 (1985).

[27] S. H. Phark, J. A. Fischer, M. Corbetta, D. Sander, and J. Kirschner, Superparamagnetic response of Fe-coated W tips in spin-polarized scanning tunneling microscopy, Applied Physics Letters **103**, 13 (2013).

[28] D. Wortmann, S. Heinze, P. Kurz, G. Bihlmayer, and S. Blügel, Resolving Complex Atomic-Scale Spin Structures by Spin-Polarized Scanning Tunneling Microscopy, Physical Review Letters **86**, 4132 (2001).

[29] S. H. Vosko, L. Wilk, and M. Nusair, Accurate spin-dependent electron liquid correlation energies for local spin density calculations: a critical analysis, Canadian Journal of Physics **58**, 1200 (1980).

[30] `http://www.flapw.de.`

CHAPTER 10

Summary and Discussion

10.1 Electronic Structure and Charge Density Wave Order in Monolayer NbS_2

For a long time it is known that on the one hand, different to other H-phase bulk TMDCs of group V, 2H-NbS_2 presents no long-range CDW [17,19,20], however, it is superconducting with a critical temperature $T_c \approx 6\,K$ [7,17,18]. On the other hand, quasi-freestanding H-NbS_2 monolayers on Gr/6H-SiC(0001) show a 3×3 superstructure in STM [21], reminiscent of a CDW as found in monolayer H-$NbSe_2$ on the same substrate [128], but the origin of this superstructure and its electronic footprints remain elusive. Even less is known about the superconducting state of quasi-freestanding monolayer NbS_2 – the thinnest NbS_2 samples found to be superconducting are $4-6$ nm thick [144,155]. This is in contrast with the $NbSe_2$ monolayer case, which is known to feature superconductivity below $T_c = 1.9\,K$ [128].

To address the uncertainty regarding electronic correlation effects in monolayer NbS_2, in the first manuscript of this thesis (chapter 7), the electronic structure of quasi-freestanding H-NbS_2 monolayers grown in situ on Gr/Ir(111) was investigated by high-resolution low-temperature STM and STS. The growth process yields flat monolayer islands of H-NbS_2, which confirm without traces of disturbance to the Gr sheet and also in some cases overgrow Ir(111) substrate steps. In differential conductance dI/dV maps recorded on NbS_2 islands, the 3×3 superstructure reported before in Ref. [21] is found. The intensity of the superstructure features a gap-like minimum close to the Fermi energy, and by adjusting the bias voltage a contrast phase shift is found on both sides of the gap. Both the intensity minimum and the phase shift provide evidence that the found superstructure is indeed a CDW. It disappears at close to 40 K. By recording large-range STS point spectra and by analyzing quasi-particle interference patterns at the edges of NbS_2 islands, the electronic structure in the occupied and unoccupied states is found to reproduce DFT band structure calculations of freestanding H-NbS_2 monolayers, showing that the Gr/Ir(111) substrate has negligible influence and that the CDW does not affect the band structure on a larger energy scale. In high-resolution STS point spectra, the local density of states close to the Fermi energy is addressed. A double gap is found, with the wider one attributed to an inelastic scattering process with Nb phonon modes upon tunneling, similar to what was reported for bulk 2H-NbS_2 [148]. Inside the wide gap a smaller one is found, marking the total minimum in the dI/dV signal centered at an energy matching the intensity minimum of the 3×3 superstructure very close to the Fermi energy. With a width of $\approx 7\,\mathrm{mV}$ it is also of similar size and therefore attributed to be a CDW gap feature. Assuming a BCS-like relation for a weakly-interacting CDW in the picture of a classical Peierls transition, a 7 mV gap yields a transition temperature of $\approx 22\,\mathrm{K}$, in the same order of magnitude as the temperature at which the CDW disappears in the experiments ($\approx 40\,\mathrm{K}$). Overall the results, including a small CDW gap close to the Fermi energy, moderate transition temperature of $\approx 40\,\mathrm{K}$, and an unaffected band structure on the broader energy range, indicate that the CDW in monolayer H-NbS_2 can be understood as weakly-interacting in the picture of a Peierls transition being driven by electronic Fermi surface nesting. A similar interpretation was attained for the CDW in H-$NbSe_2$ monolayers on Gr/6H-SiC [128].

Unsolved remains the origin of additional, position dependent features in dI/dV spectra close to the Fermi energy, like a double peak on the negative energy side. This feature was found to be most pronounced at the edges of islands, indicating that these have a significant influence on the electronic structure of the islands. This is supported by the fact that at low energies, the standing waves arising from quasi-particle scattering extend far into the center of the islands.

In the experiments no sign of superconductivity could be found down to 0.4 K. Its absence might be explainable with regard to limited island sizes. The islands at best feature a finite size of $\approx 20\,\mathrm{nm}\times 20\,\mathrm{nm}$ and do not display a continuous film, since at the connection points of many islands grain boundaries could be found. The typical superconducting coherence length in bulk NbS_2 is of up to about $\approx 60\,\mathrm{nm}$ [308], significantly larger than the size of the monolayers and therefore might be the limiting factor, if one assumes that the coherence length remains in the same order of magnitude in the monolayer limit, as is the case for $NbSe_2$ [309–311]. Another possibility is that the critical temperature of superconductivity could be too low to be experimentally accessible in the system in which the experiments were conducted.

Looking forward, the finding that the 3×3 superstructure indeed is a CDW calls for theoretical contributions regarding the possible driving force in the system. The evidence from experiments that the CDW is caused by a weak driving force like Fermi surface nesting could be confirmed that way. The surface morphology could be improved so that the growth of larger continuous films could be achieved, possibly enabling the monolayer to become superconducting. Lastly angle-resolved photoemission spectroscopy experiments, missing so far in literature for the monolayer limit of NbS_2, could be a useful tool to confirm the STS results regarding the electronic band structure.

10.2 Post-Growth Intercalation at the Interface of Graphene and Monolayer NbS_2

Post-growth intercalation of foreign species into the vdW gap of layered materials is a formidable tool to design and alter the properties of layered bulk crystals [23–25] including TMDCs [22], thereby offering many possibilities of technological application like energy storage in the case of Li intercalation [53, 184, 185] and information storage in the case of Fe intercalation introducing magnetic interactions [26]. Furthermore, intercalation can also be applied to 2D monolayer materials [27–30]. An important field of research are heterostacks of different 2D monolayer TMDCs [31, 32], but experimental work regarding intercalation of such heterostacks are mostly limited to electrochemical Li intercalation [242–244].

To extend the possibilities regarding the intercalation and property tuning of 2D monolayer heterostacks, in the second manuscript (chapter 8) the post-growth intercalation at the interface between NbS_2 monolayers and a single sheet of Gr on Ir(111) was demonstrated. Nb intercalation was achieved by both partial dissociation of NbS_2 upon heating the pristine heterostack, as well as deposition of additional Nb from the vapor phase at an elevated temperature below dissociation. Two ordered intercalated phases of similarly increased apparent height compared to the NbS_2 monolayer arise, the Nb $\sqrt{3} \times \sqrt{3} -$ phase and Nb $1 \times 1 -$ phase. For the Nb $\sqrt{3} \times \sqrt{3} -$ phase two structural possibilities are discussed. On the one hand, it could be the result of intercalation by 1/3 of the amount of Nb present in the pristine monolayer NbS_2, with the intercalated species in octahedral sites. The resulting compound features a $\sqrt{3} \times \sqrt{3}$ R30° superstructure due to every third site below the NbS_2 monolayer being occupied by the intercalated Nb. On the other hand, the observed decrease in island area upon intercalation by decomposition possibly points towards a double layer NiAs structure of stoichiometry Nb_2S_2 [201]. This NiAs structure in our case could be considered as a single T-NbS_2 sheet with an additional metal layer in the vdW gap between T-NbS_2 and Gr. The $\sqrt{3} \times \sqrt{3}$ R30° superstructure could be explained by a trimerization of Nb atoms in one of the Nb layers as similarly reported by Kadijk et al. [201]. The Nb $1 \times 1 -$ phase is then attributed to a high-temperature NiAs structural phase without any trimerization. The fact that the transition between the Nb $\sqrt{3} \times \sqrt{3} -$ phase and Nb $1 \times 1 -$ phase is non-continuous with grain boundaries between the phases, is in disagreement with the assumption of both featuring a NiAs structure. Independent of the possible NiAs structure formation the attempted insertion of Nb in between the pristine H-NbS_2 monolayer and Gr can in any case be considered successful. Intercalation of Nb was shown to have a profound effect on the electronic structure of the pristine H-NbS_2 monolayer, since the STS point spectra recorded on both the Nb $\sqrt{3} \times \sqrt{3} -$ phase and Nb $1 \times 1 -$ phase differ significantly from the ones recorded on pristine H-NbS_2 and the 3×3 CDW treated in chapter 7 disappears.

Fe intercalation was achieved by deposition from the vapor phase at elevated temperature. Two phases of increased apparent height emerge, a ML Fe $\sqrt{3} \times \sqrt{3} -$ phase featuring similar height as the Nb $\sqrt{3}\times\sqrt{3}$ – phase and a BL Fe $\sqrt{3}\times\sqrt{3}$ – phase of similar height as pristine NbS_2 bilayers, both featuring a $\sqrt{3}\times\sqrt{3}$ R30° superstructure. The ML Fe $\sqrt{3}\times\sqrt{3}$ – phase was identified as a NbS_2 monolayers being intercalated by Fe in 1/3 of the sites as described for one of the possible Nb $\sqrt{3}\times\sqrt{3}$ – phase structures. The BL Fe $\sqrt{3}\times\sqrt{3}$ – phase was attributed to NbS_2 bilayers, formed in the process of deposition. They were assumed to be intercalated by Fe with 1/3 of the octahedral sites occupied in the vdW gap between the NbS_2 layers, similar to the situation reported for Fe-intercalated bulk 2H-NbS_2 [190, 192]. The BL Fe $\sqrt{3}\times\sqrt{3}$ – phase dominates after deposition at elevated temperature.

The structures identified upon insertion of Nb and Fe into the vdW gap between the NbS_2 monolayers and the Gr sheet can not be unambiguously proven by our measurements, as STM does not access structures in sublayers. Experiments like x-ray photoelectron spectroscopy, as well as structural calculations could bring light into the binding situation of the intercalated material. The insertion of magnetic material opens up the possibility to study TMDCs in the monolayer limit being in contact with a magnetic material. Especially NbS_2 is interesting in this regard, as a tendency for spin order was predicted for the monolayer [142, 152–154]. Plenty of experimental methods exist to investigate magnetism in such compounds with x-ray magnetic circular dichroism and SP-STM being two prominent examples. The possible rise of magnetic phenomena induced by the intercalated Fe could be compared to compounds intercalated by other magnetic materials such as Cr. The intercalation of chemically dissimilar species offers a sheer endless playground.

10.3 Bloch Spin Helix in an Ultrathin Fe Film on Ir(110)

Non-collinear spin textures are a fascinating phenomenon originating from the interplay of magnetic interactions at the interface of a ultrathin film and a substrate [33]. One specific case are skyrmions [34–36], of interest for the application in spintronics like the realization of the so called "racetrack memory" [40–42]. In that regard, in order to overcome some problematic properties of skyrmions like the skyrmion Hall effect [45, 46], antiskyrmions could feature a promising alternative [47, 48, 277]. Antiskyrmions have been reported in Heusler materials [49, 50], but not in ultrathin films compatible with reduced-size tendencies in technology. In 2017, Hoffmann et al. [51] presented a theoretical work investigating the presence of antiskyrmions in ultrathin films on C_{2v}-symmetry substrates, like W(110). This fuels the interest into these kind of substrates and in the manuscript of chapter 9, the spin texture in an ultrathin Fe film grown in situ on Ir(110) was investigated by SP-STM.

By oxygen dosing and hydrogen titration, the unreconstructed Ir(110) (1×1) surface was achieved (see Appendix A). Subsequently, Fe was deposited onto the surface, leading to pseudomorphic Fe bilayer islands of $\approx$ 10 nm size. Using Fe-coated W tips in a vector magnetic field, spin-resolved STM images were obtained. Here, the dependence of the tunneling current on the magnetization alignment of tip and sample (see chapter 6), allowed the identification of an incommensurate magnetic stripe pattern of λ = 1.27 nm pitch parallel to the [001]-direction. By reorienting a soft magnetization tip with the vector field, the spin texture of the stripe pattern was fully mapped allowing identification of a Bloch spin helix with degenerate rotational sense. No magnetic phase transitions were identified as the spin helix is unchanged up to 9 T.

To gain insight into the driving forces of the spin helix, DFT calculations were conducted. Using a reduced Fe-Fe distance of $-4.8\,\%$ in the bilayer from surface relaxations, calculating the spin helix formation energy without SOC yields a spin helix of q-vector $\lambda/d_{\mathrm{NN}} = 4.2$ in reasonable agreement with the experimental value of 4.69. The stability of the spin helix up to 9 T is corroborated by the calculated energy gain of the Fe atom spins by remaining in their canted state. The fact that a spin helix of similar pitch as in the experiments is possible without SOC, results in the interpretation that the spin helix is not driven by DMI. Instead, including the result of degenerate rotational sense and Bloch type being unfavorable in the case of sizable DMI, exchange interactions are assumed to be the dominating driving force. The finding is in contrast to previous studies of magnetic films on 5*d* metal substrates and points to a mechanism beyond what is know in this field.

Looking forward, different continuative experiments are imaginable. The magnetic interactions present on Fe/Ir(110) could be manipulated for example by adding an easily polarizable Pd film on top of the Fe bilayers as shown for Pd/Fe/Ir(111) [259], thereby possibly softening the exchange interactions and increasing the influence of DMI. Interesting in our case would be the layer-dependent influence of the added Pd on the upper and lower Fe plane subsequently and what the resulting magnetic texture would be. Furthermore the addition of hydrogen was shown to tune exchange interactions and DMI in Fe bilayers on Ir(111) [312], offering another possible pathway to influence the spin texture in Fe bilayers on Ir(110). Also the presence of a Gr layer on top of Fe/Ir(110) (see Appendix A) is of interest for spintronic applications [313], due to the spin-polarizability of Gr [314]. Extending the range of materials, different $C_{2\mathrm{v}}$-symmetry substrates like Rh(110) could replace Ir(110) and other magnetic materials like Cr could be deposited.

APPENDIX A

Scientific Appendix

A.1 Manipulating NbS_2/Gr/Ir(111) via Substrate Doping

The properties of atomically thin TMDCs are known to be strongly dependent on their environment [60, 315–317]. One way of influencing the environment is a change of substrate (compare section 3.3), with one example being the absence of a CDW in NbS_2 on Au(111) [151], while it is present in NbS_2 on Gr (see [21] and manuscript in chapter 7). Another example is the change induced in the CDW phase properties of TaS_2 monolayers on Gr/Ir(111) by Li doping [107]. Due to the reduced screening efficiency of 2D layers [4], they are prone to electronic effects like gating for example by utilizing a Gr substrate and altering its charge carrier concentration [318, 319]. One specific way of altering the charge carrier concentration of Gr is intercalation of foreign species like Eu and O [320–323], causing n-doping of up to 1.43 eV in the case of Eu [321] and p-doping of up to 0.64 eV in the case of O [322]. In the following the growth of NbS_2 on Eu and O intercalated Gr/Ir(111) is demonstrated and the influence of the substrate manipulation on the CDW phase is discussed.

NbS_2 on Eu Intercalated Gr/Ir(111)

To create Eu intercalated Gr/Ir(111), first a closed layer of highly oriented Gr was grown by TPG and CVD analogue to the procedure described in the manuscripts of chapter 7 and 8. The resulting LEED image in Fig. A.1 (a) features first order reflections belonging to the hexagonal Gr lattice (red), to the Ir(111) lattice (black) and satellite reflections corresponding to the moiré of Gr and Ir(111) (yellow). Afterwards, 6 monolayer-equivalents of Eu were evaporated from a Knudsen cell over the course of 360 s, while the sample was hold at 750 K. The deposition rate was calibrated by using a quartz microbalance. The most dense intercalation structure of Eu under Gr is described to be a $\sqrt{3} \times \sqrt{3}$ R30° superstructure with respect to Ir and residual non-intercalated Eu is known to evaporate back into the vacuum [321]. In the resulting LEED image shown in Fig. A.1 (b), in addition to the reflections visible in (a), a reflection corresponding to a Eu $\sqrt{3} \times \sqrt{3}$ R30° superstructure with respect to Ir is present (pink), indicating that the intercalation was indeed successful, creating Gr/Eu/Ir(111). Only very faint satellite reflections surrounding the Gr reflections, attributed to the moiré of Gr and Ir(111), are visible, showing that it is partially lifted as a result of the intercalation. Fig. A.1 (c) features a constant current STM image with atomic resolution of the intercalated sample. As marked by a yellow rhomboid, the moiré of Gr and Ir(111) persists after intercalation. In the inset on the top right (close-up atomic resolution), two patterns are evident. The atomic lattice of Gr is marked by a red rhomboid and an additional $\sqrt{3} \times \sqrt{3}$ R30° structure is marked pink. The found superstructure is in agreement to the most dense Eu intercalation structure described in literature [321].

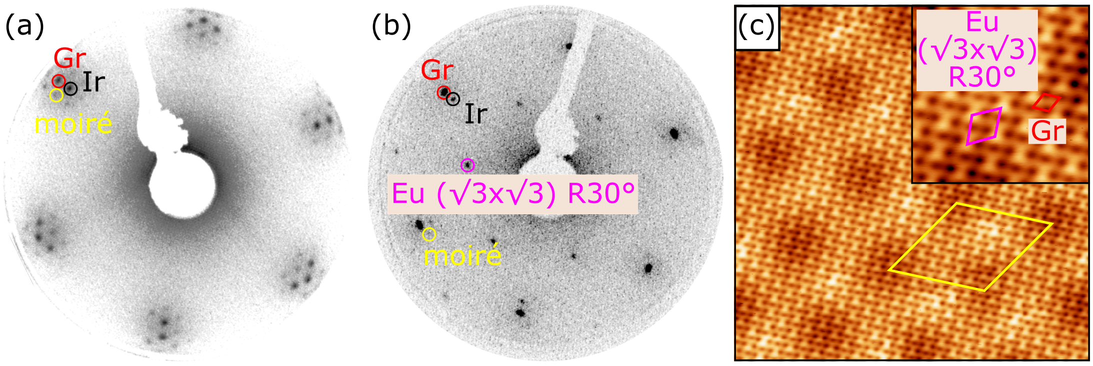

Figure A.1: Eu intercalation of Gr/Ir(111). (a) 76 eV inverted contrast LEED image of the pristine Gr/Ir(111) sample. An example first order reflection of Gr is marked by a red circle, of Ir by a black circle and of the moiré of Gr/Ir(111) by a yellow circle. (b) 81 eV inverted contrast LEED image after intercalation. First order reflection of an emerging Eu $\sqrt{3} \times \sqrt{3}$ R30° superstructure with respect to Ir is marked by a pink circle, moiré traces of Gr/Ir(111) are marked by a yellow circle. (c) Constant current STM image. The moiré superstructure of Gr/Ir(111) is indicated by a yellow rhomboid. Inset: Eu $\sqrt{3} \times \sqrt{3}$ R30° superstructure with respect to Ir marked by a pink rhomboid, atomic lattice of Gr marked by a red rhomboid. Image information: (c) size 10 nm×10 nm, V_s = 500 mV, I_t = 0.5 nA, T_s = 1.7 K. Inset: size 3 nm × 3 nm, V_s = 500 mV, I_t = 0.5 nA, T_s = 1.7 K.

As a next step NbS_2 monolayers were grown on top of the Gr/Eu/Ir(111) substrate. The growth procedure is described in detail in the manuscript of chapter 7 and contains Nb deposition at an elevated temperature of about 800 K in a S background. The resulting surface morphology can be seen in Fig. A.2 (a). Next to the NbS_2 monolayer islands on Gr/Eu/Ir(111) marked by the white arrow, another structure of larger apparent height is visible. The origin of this structure can be explained when looking at the atomic resolution STM image of the intercalated Gr after the growth of NbS_2 [Fig. A.2 (b)]. Different to the situation before the growth (Fig. A.1), the intercalation appears to be irregular, with order only being present in a few places showing a (2×2) superstructure with respect to Ir (see inset). The $p(2 \times 2)$ intercalation structure of Eu under Gr with respect to the Ir lattice is the less dense one compared to the $\sqrt{3} \times \sqrt{3}$ R30° superstructure [321] observed before the growth of NbS_2. This means that some Eu was probably removed from below the Gr, reacting with S present during the NbS_2 growth and creating the higher structures visible in Fig. A.2 (a), possibly consisting of EuS. Regarding the areas without a (2×2) superstructure still showing variable height, it could be speculated that S from the environment moved below the Gr, also reacting with residual Eu below. The EuS appears to rest on top of the NbS_2 islands as evident in Fig. A.2 (c) and the corresponding height profile along the white line, shown in Fig. A.2 (d). In the profile, the structure features an apparent height of about 1.2 nm, while the NbS_2 below features an apparent height of 0.47 nm. This value for NbS_2 is lower than what was found in the manuscripts of chapter 7 and 8 for NbS_2 monolayers on pristine Gr/Ir(111). One reason could be the fact, that the STM image in Fig. A.2 (c) was recorded at an unusually high bias voltage of 3 V, necessary due to the insulating nature of EuS [324]. The measured apparent height of the EuS structure of 1.2 nm corresponds to a bilayer of the material (lattice constant a_{Lit} = 0.596 nm [325]). It should be noted that STM, being dependent on the density of states of the sample, is not well suited to measure the height of an insulating structure resting on a metallic substrate. The structure of the presumed EuS on the atomic level is shown in the atomic resolution STM image in Fig. A.2 (e), measured in the area marked by a black box in Fig. A.2 (c). On the left side, a square lattice is marked black. The measured lattice constant of a = 0.60(1) nm fits well to the literature value of 0.596 nm [325] regarding the rock-salt lattice structure of EuS. On the right side of Fig. A.2 (e), a hexagonal lattice marked red is visible. It features a visibly lower apparent height and a corresponding lattice constant of about 0.60 nm. This structure does not correspond to the cubic rock-salt structure of EuS and may be a different phase. In Fig. A.2 (f) a LEED image of the sample is displayed. Next to the reflections of Gr (red) and NbS_2 (turquoise) (see manuscript of chapter 7 for a more detailed description), the (2×2) superstructure with respect to Ir, as found in the STM image in Fig. A.2 (b), is evident. Additionally, a faint ring-like reflection close to the center is visible. This feature in LEED results in a lattice constant of 0.64(4) nm which within the sizable error due to the faint and broad nature of the ring fits to the EuS lattice described above. The ring nature of the reflection hints that the EuS islands feature random orientation.

To investigate the electronic structure of the NbS_2 grown on the Eu intercalated Gr, constant current dI/dV maps were recorded on the NbS_2 islands, shown in Fig. A.3. Fig. A.3 (a) is a dI/dV map recorded at 10 K. The real space lattice directions of the NbS_2 lattice are indicated white. At the top of the image, close to the edge of the NbS_2 island, standing waves originating from quasi-particle interference are present (orange arrow). Just like in the case of NbS_2/Gr/Ir(111) (compare manuscript of chapter 7), the standing waves cause a ring-like intensity feature in the fast Fourier transformation (FFT) (inset) with an intensity maximum in $\overline{\Gamma M}$-direction. Analogue to chapter 7, the standing wave patterns are used to extract the dispersion of the hole-like metallic Nb d_z-type band crossing the Fermi energy by fitting a Bessel function to the line profiles taken as marked by the orange arrow in Fig. A.3 (a). The result is shown in Fig. A.3 (b) by red dots. For comparison, the band dispersion of NbS_2 on pristine Gr/Ir(111) from chapter 7 is added (black dots), as well as the calculated band structure of quasi-freestanding monolayer NbS_2 (blue line, [142]). It appears that the metallic band of NbS_2/Gr/Eu/Ir(111) is not significantly shifted compared to NbS_2/Gr/Ir(111) despite showing a slightly steeper dispersion. Another feature in the FFT inset of Fig. A.3 (a) (10 K) are reflections

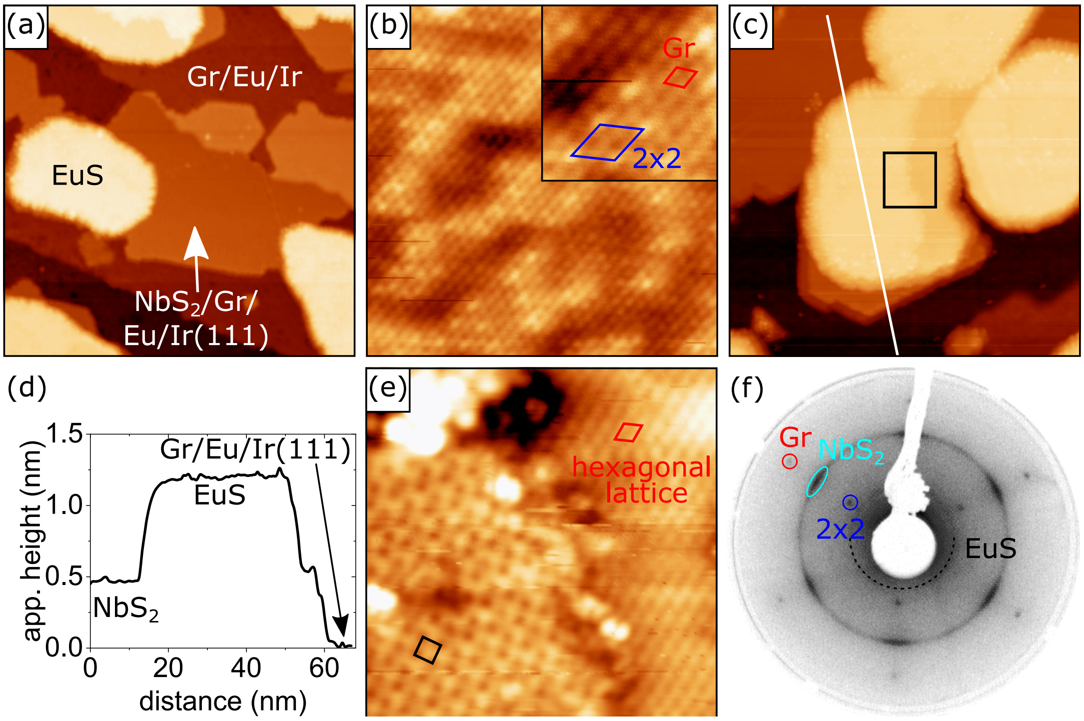

Figure A.2: Topography of the NbS$_2$/Gr/Eu/Ir/(111) sample. (a) Large-range constant current STM topograph showing areas of Gr/Eu/Ir(111), NbS$_2$ islands on Gr/Eu/Ir(111) islands and an additional structural feature attributed to EuS. (b) Atomic resolution of the Eu intercalated Gr after growth of NbS$_2$. The Gr lattice is indicated red, a 2 × 2 superstructure with respect to Ir is indicated blue. (c) Constant current STM topograph of an EuS island grown on top of NbS$_2$. (d) Height profile taken along the white line in (c). (e) Atomic resolution STM image of two present EuS phases, recorded in the area marked by a black box in (c). On the left side, a square lattice is marked black, on the right side a hexagonal lattice is marked red. (f) 95 eV inverted contrast LEED image. Example reflection of Gr marked red, of NbS$_2$ marked turquoise, of a (2 × 2) superstructure with respect to Ir marked blue and of a ring attributed to EuS marked by a dotted black half circle. Image information: (a) size 70 nm × 70 nm, V_s = 3 V, I_t = 0.4 nA, T_s = 20 K. (b) size 7.7 nm × 7.7 nm, V_s = 500 mV, I_t = 0.5 nA, T_s = 1.7 K. Inset: 2 nm × 2 nm. (c) size 70 nm × 70 nm, V_s = 3 V, I_t = 0.1 nA, T_s = 1.7 K. (e) size 12 nm × 12 nm, V_s = 3 V, I_t = 0.05 nA, T_s = 1.7 K.

(marked red) in between the center (Γ-point) and the reflections corresponding to the atomic lattice of NbS$_2$ (marked white). These reflections are similar to the CDW reflections found in the FFT of NbS$_2$/Gr/Ir(111) in chapter 7. Here, the CDW vector has a length of $q_{\mathrm{CDW}} = 0.69\overline{\Gamma \mathrm{M}}$, slightly larger then for the 3 × 3 CDW with wave vector $q_{\mathrm{CDW}} = 2/3\overline{\Gamma \mathrm{M}}$, making the CDW in NbS$_2$/Gr/Eu/Ir(111) slightly incommensurate. In the FFT inset of the dI/dV map in Fig. A.3 (c) recorded at 20 K, the CDW reflections are absent. This means, that the critical temperature T_c of the CDW is reduced compared to the pristine NbS$_2$/Gr/Ir(111) sample in chapter 7, where the CDW disappeared between 40 K and 50 K. The large-range constant height STS point spectra in Fig. A.3 (d) show that the electronic structure of NbS$_2$/Gr/Eu/Ir(111) (red) is very similar to the one of the pristine NbS$_2$/Gr/Ir(111) (black) already shown in chapter 7. Especially the peaks below -1 V, attributed to hole-like S p_z-type bands, lie on top of each other. The metallic Nb

d_{z^2}-type band showing a peak centered at around 0.80 V in the pristine case on the other hand appears broader in the intercalated case and is shifted to around 1.25 eV.

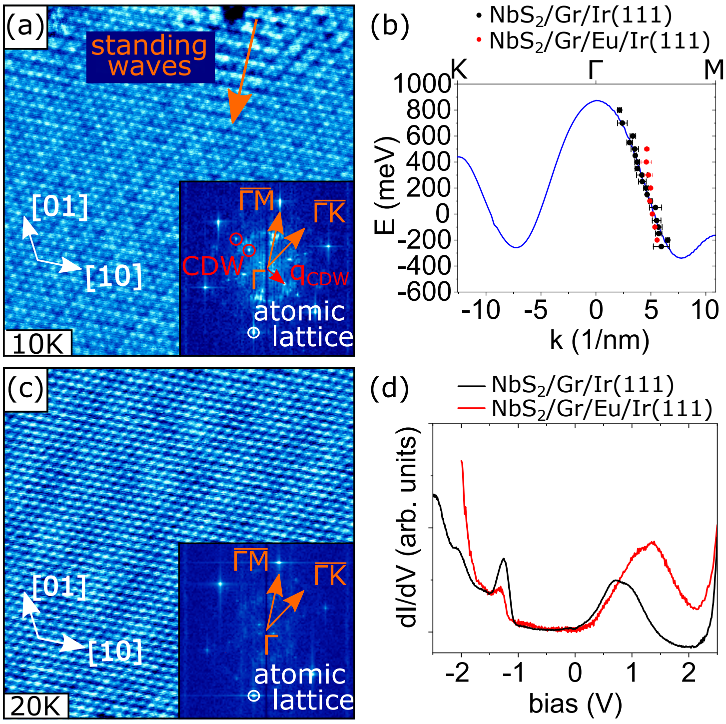

Figure A.3: Electronic structure of NbS_2/Gr/Eu/Ir(111). (a) Constant current dI/dV map on NbS_2/Gr/Eu/Ir(111) at 10 K. Standing waves arise at the edges. The real space lattice directions are indicated white. Inset: FFT of the dI/dV map. Reflections attributed to a CDW pattern are marked by red circles. The corresponding q-vector of the CDW is indicated by a red arrow. Reflections corresponding to the atomic lattice are marked by a white circle, the reciprocal lattice directions are indicated in orange. (b) Metallic band dispersion (red points) extracted by a Bessel function fit (see chapter 7) of the standing wave pattern as visible in (a), compared to the dispersion calculated for quasi-freestanding NbS_2 monolayers (blue line, [142]). The black points denote the metallic band dispersion found for the pristine NbS_2/Gr/Ir(111) sample as analyzed in chapter 7. (c) Constant current dI/dV map on NbS_2/Gr/Eu/Ir(111) at 20 K. The real space lattice directions are indicated white. Inset: FFT of the dI/dV map. The CDW reflections visible in the inset in (b) are absent. STS information: (a) size 11 nm × 11 nm, V_s = 100 mV, I_t = 0.7 nA, V_{mod} = 10 mV, f_{mod} = 1873 Hz, T_s = 10 K. (c) size 11 nm × 11 nm, V_s = 100 mV, I_t = 0.7 nA, V_{mod} = 10 mV, f_{mod} = 1873 Hz, T_s = 20 K. (d) Black: V_{stab} = 2.5 V, I_{stab} = 1.0 nA, V_{mod} = 15 mV, f_{mod} = 797 Hz, T_s = 0.4 K. Red: V_{stab} = 2.5 V, I_{stab} = 0.7 nA, V_{mod} = 10 mV, f_{mod} = 797 Hz, T_s = 1.7 K.

In case of significant n-doping effects by Eu intercalation, a rigid band shift to negative energies would be expected [320, 321, 323]. This is not evident from the metallic band dispersion extracted from the quasi-particle interference patterns, as well as the general band structure from STS point spectra. One explanation could be the missing $\sqrt{3} \times \sqrt{3}$ R30° superstructure below Gr after growth and the presence of EuS at the surface (Fig. A.2). This leads to the before mentioned interpretation that Eu left the Gr/Ir(111) interface. On the other hand due to the unordered intercalation pattern after growth of NbS_2, it was speculated above that S from the growth atmosphere actually moved below Gr, possibly reacting with residual Eu. Since O is known to cause p-doping [322], similar effects would result from S, being part of the same main group. The combination of both Eu and S below the Gr could result in cancellation of p- and n-doping, explaining the absence of a rigid band shift in our data. Also, the metallic nature of NbS_2 could give rise to sizable screening compensating the doping effect. Nevertheless, the fact that the CDW phase is influenced, with the result of a slightly incommensurate CDW with reduced T_c, shows that the intercalation has some effect on the electronic properties. The presence of EuS on top of a TMDC is interesting because of the ferromagnetic behavior EuS possesses [326]. Bringing EuS in contact with WSe_2 for example was shown to enhance valley splitting [327]. Regarding NbS_2, the presence of spin order was predicted when being in contact with magnetic species [152], leaving the EuS/NbS_2 structure a promising subject for investigation by SP-STM.

NbS_2 on O Intercalated Gr/Ir(111)

Additionally to the intercalation of Eu, the intercalation of O under Gr on Ir(111) was attempted. This time NbS_2 monolayers were grown on a full Gr layer on Ir(111) prior to intercalation. The growth recipe is again analogue to the procedure described in the manuscript of chapter 7. The resulting LEED picture of NbS_2 monolayers on Gr/Ir(111) is shown in Fig. A.4 (a), with first order reflections of Gr (red), Ir(111) (black), the moiré of both (yellow) and the NbS_2 (turquoise) marked. The slightly ring-like appearance of the NbS_2 reflection is also described in chapter 7. To achieve O intercalation, the sample was subsequently annealed ten times up to 843 K in an O pressure of $p = 5 \times 10^{-6}$ mbar for a total of 70 s (5-20 s each). Since the sample was placed in front of a gas dosing tube, the effective pressure was about 20 times higher. The annealing procedure causes the O to partly edge away the Gr and intercalate below, causing a $p(2 \times 2)$ superstructure with respect to Ir [28, 328]. After each of the ten steps, the sample was checked by LEED. After the described ten cycles, the LEED image shown in Fig. A.4 (b) emerged. Additionally to the reflections marked in Fig. A.4 (a), a 2×2 superstructure with respect to Ir is present and the moiré reflections are reduced in intensity, both in agreement with [28, 328]. The intercalation of NbS_2/Gr/Ir(111) by O, creating a NbS_2/Gr/O/Ir(111) stack, can therefore be regarded successful.

The sample was investigated by STM subsequently, with the topography shown in Fig. A.5. In the STM topograph of Fig. A.5 (a) monolayer NbS_2 islands on Gr/O/Ir(111) are visible. The islands feature clusters at the edges and in the Gr some holes resulting from the O edging process are evident. The structural features and the apparent heights of the sample are indicated in the height profile of Fig. A.5 (b), measured along the white line in Fig. A.5 (a). The reason for the clusters that are not present on pristine NbS_2/Gr/Ir(111) (compare chapter 7), is probably the O exposure at elevated temperatures, not only edging away Gr, but also partially dissolving NbS_2. In the atomic resolution STM image in Fig. A.5 (c), the Gr substrate is shown. Marked

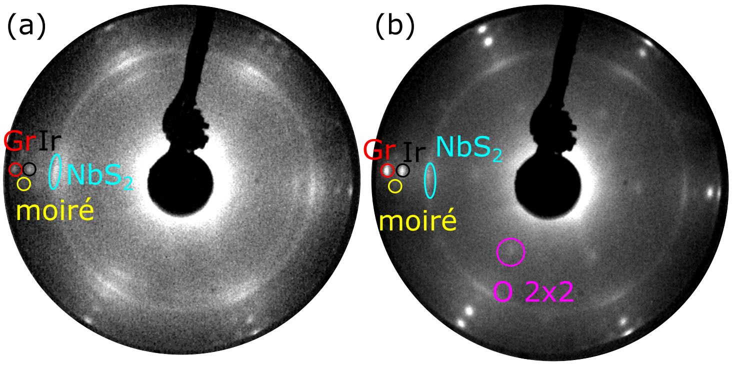

Figure A.4: O intercalation of NbS$_2$/Gr/Ir(111). (a) 65 eV LEED image of the pristine NbS$_2$/Gr/Ir(111) sample. An example first order reflection of Gr is marked by a red circle, of Ir by a black circle, of the moiré of Gr/Ir(111) by a yellow circle and of NbS$_2$ by a turquoise ellipse. (b) 65 eV LEED image after O intercalation. Additional reflections marked pink belonging to a 2 × 2 superstructure with respect to Ir caused by O intercalation emerge. The moiré spots marked yellow are reduced in intensity.

by the yellow rhomboid is the moiré of Gr/Ir(111), which is weakend by the intercalation but not absent. In the inset, additionally to the Gr lattice marked red, a 2 × 1 superstructure with respect to Ir is indicated by pink lines. The results of the STM investigation and the before shown LEED images are in agreement with the typical features of O intercalation [28, 328].

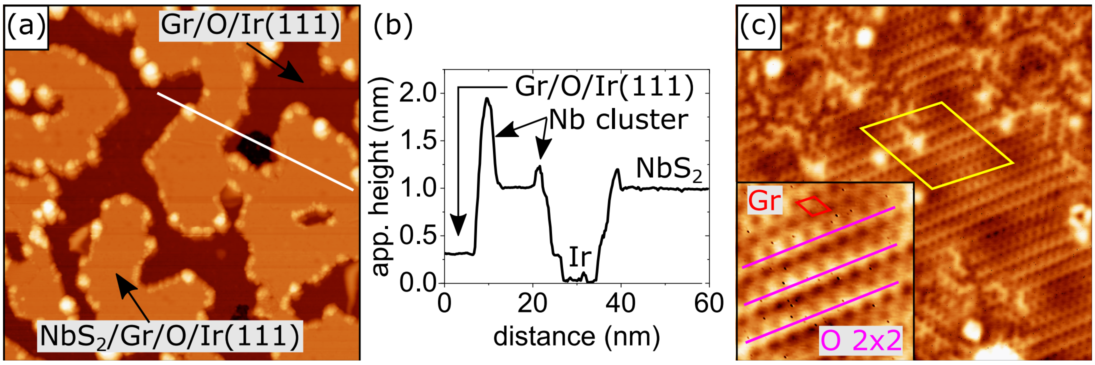

Figure A.5: NbS$_2$/Gr/Ir(111) intercalated by O. (a) Large-range constant current STM image. (b) Height profile along the white line in (a). (c) Atomic resolution STM image of Gr/Ir(111) intercalated by O. The moiré of Gr/Ir(111) is indicated by a yellow rhomboid. Inset: Close-up atomic resolution. The hexagonal Gr lattice is indicated by a red rhomboid, the O 2 × 1 superstructure by pink lines. Image information: (a) size 100 nm × 100 nm, V_s = 3 V, I_t = 0.5 nA, T_s = 1.7 K. (c) size 10 nm × 10 nm, V_s = 500 mV, I_t = 0.2 nA, T_s = 1.7 K. Inset: size 2.2 nm × 2.2 nm.

The Nb clusters at the edges of the NbS$_2$ islands make it very difficult to maintain a stable tip, nevertheless the electronic structure and especially the influence of O intercalation on the CDW phase was investigated by STS, with the results shown in Fig. A.6. Fig. A.6 (a) displays a constant current dI/dV map recorded on a NbS$_2$ island on Gr/O/Ir(111). Similar to the results in the manuscript of chapter 7 and on the Eu intercalated sample described above, standing waves from quasi-particle interference are present at the edges of the island, propagation along the orange arrow. Line profiles were taken at three bias voltages along the orange arrow and were fitted by a Bessel function to extract the $E-k$ dispersion of the hole-like metallic Nb d_{z^2}-type band crossing the Fermi energy. The result for NbS_2/Gr/O/Ir(111) is shown in Fig. A.6 (b) as pink dots. It is evident, that for these three energies, the k-values are very similar to the case of pristine NbS_2/Gr/Ir(111) (black dots), both fitting well to the calculated band dispersion of freestanding NbS_2 (blue line, [142]). This shows that just like in the case of the Eu intercalated sample, a rigid band shift due to doping is absent, possibly due to the metallic nature of NbS_2 and the before mentioned consequence of significant screening. Another feature that was present both in the Eu intercalated sample, as well as in the pristine sample (chapter 7), is a CDW, here in the case of NbS_2/Gr/O/Ir(111) marked by a red rhomboid in Fig. A.6 (a) and by red circles in the FFT inset of the dI/dV map in Fig. A.6 (c). While the CDW in the pristine case was commensurate featuring a wave vector of exactly $q_{\mathrm{CDW}} = 2/3\overline{\Gamma\mathrm{M}}$ and the CDW in the Eu intercalated case featuring a slightly incommensurate wave vector of $q_{\mathrm{CDW}} = 0.69\overline{\Gamma\mathrm{M}}$, here in the case of NbS_2/Gr/O/Ir(111) the CDW features a wave vector of $q_{\mathrm{CDW}} = 0.68\overline{\Gamma\mathrm{M}}$, being very close to the commensurate case. Regarding the general band structure, a large-range constant height STS point spectrum measured on NbS_2/Gr/O/Ir(111) is shown in Fig. A.6 (d) (red curve) and is compared to the pristine case (black curve). Similar to the result from the standing waves, no rigid shift of the features in one direction is visible. The rise due to the to the hole-like S p_z-type bands below -1 V is shifted to more negative energies, unexpected for p-doping in the case of O [322, 323]. On the other hand, the maximum of the metallic band crossing the Fermi energy and originating from Nb d_{z^2}-orbitals, is shifted to above 1 eV, in the direction expected for p-doping. On the small scale, in the STS spectrum in Fig. A.6 (e) a small gap close to the Fermi energy is present, partially attributed to the CDW phase in chapter 7. Also the peak feature within the gap just below the Fermi energy is reproduced.

In conclusion, both the intercalation of Eu and O under Gr does not cause significant doping effects in the band structure. The reason could be the metallic nature of the NbS_2 monolayer giving rise to sizable screening in both cases, or intermixing of Eu and S below graphene and formation of EuS on top of NbS_2 in the case of Eu intercalation. While the CDW phase is slightly influenced in the case of Eu intercalation, lowering the critical temperature T_c to between 10 K$-$20 K and causing a slightly incommensurate q_{CDW}, the CDW features in the case of the O intercalated sample are much closer to the pristine CDW phase.

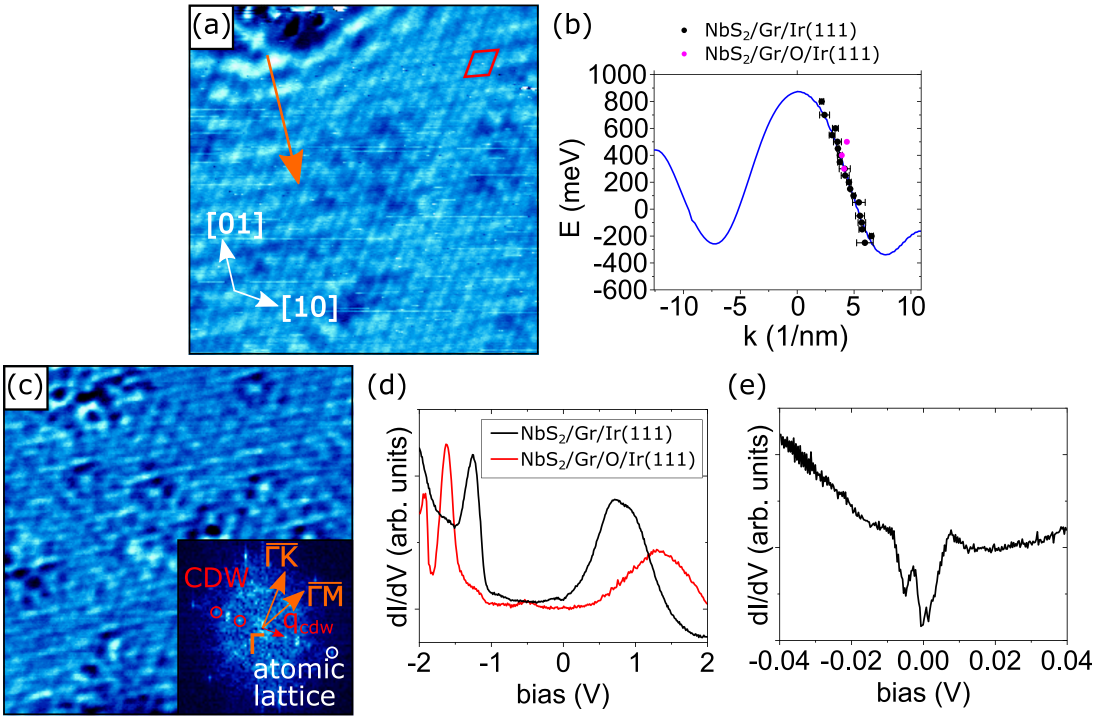

Figure A.6: Electronic structure of NbS_2/O/Ir(111). (a) Constant current dI/dV map. Standing wave propagation is marked by an orange arrow, the CDW is marked by a red rhomboid and the atomic lattice directions of NbS_2 are indicated white. (b) Band dispersion extracted from standing waves by a Bessel function fit similar to chapter 7, compared to the dispersion in the pristine sample and the calculated band dispersion of freestanding NbS_2 (blue line, [142]). (c) Another constant current dI/dV map. In the FFT inset, reflections corresponding to the CDW and the corresponding q-vector are indicated red. A reflection corresponding to the atomic lattice of NbS_2 is indicated white. (d) Large-range constant height STS point spectrum comparing the band structure of the pristine sample to the O intercalated one. (e) High-resolution constant height STS point spectrum. STS information: (a) size 9 nm × 9 nm, V_s = 300 mV, I_t = 0.5 nA, V_{mod} = 10 mV, f_{mod} = 1890 Hz, T_s = 1.7 K. (c) size 9 nm × 9 nm, V_s = −200 mV, I_t = 0.7 nA, V_{mod} = 10 mV, f_{mod} = 1890 Hz, T_s = 1.7 K. (d) Black: V_{stab} = 2.5 V, I_{stab} = 1.0 nA, V_{mod} = 15 mV, f_{mod} = 797 Hz, T_s = 0.4 K. Red: V_{stab} = 2.0 V, I_{stab} = 0.5 nA, V_{mod} = 10 mV, f_{mod} = 797 Hz, T_s = 1.7 K. (e) V_{stab} = 50 mV, I_{stab} = 0.5 nA, V_{mod} = 0.5 mV, f_{mod} = 797 Hz, T_s = 1.7 K.

A.2 The Ir(110) Surface

The fcc (110) surface of Ir used in this work as a substrate for Fe bilayer films (see manuscript in chapter 9), offers a challenge. As displayed in the STM pictures of Fig. A.7, the surface in its ground state features {331} nanofacets [329–333]. This faceted surface is not a suitable substrate for pseudomorphic growth of thin films, but possibilities exist to suppress the nanofacet formation and create a flat (1 × 1) surface.

One way of achieving a non-faceted surface is O exposure. Upon heating the sample to temperatures of 700 K−900 K, the reconstruction is lifted and by adsorbing more than 0.5 monolayer equivalents of O upon cooling, the unreconstructed surface is stabilized, leading to either a

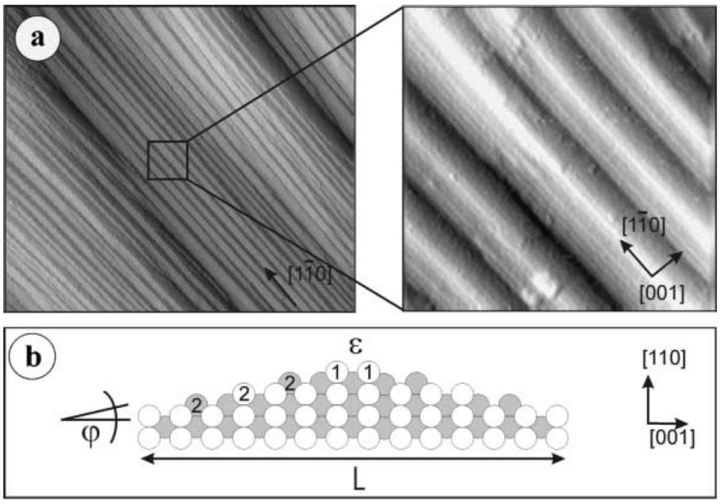

Figure A.7: The nanofaceted surface of Ir(110). Figure reprinted with permission from Ref. [330] © 2002 Elsevier.

$c(2 \times 2)$ or $p(2 \times 1)$ chemisorbed O overlayer on the Ir(110) (1×1) surface [334–336]. To get rid of the O overlayer, hydrogen titration at moderate temperatures, not causing renewed faceting, could feature a feasible procedure as demonstrated by Heinz et al. [337] for Ir(100). The application of O exposure and hydrogen titration to achieve the unreconstructed Ir(110) (1×1) surface as a template for the pseudomorphic growth of Fe bilayer islands (manuscript in chapter 9), is illustrated in the following.

Fig. A.8 (a) features a constant current STM topograph of the Ir(110) surface after Ar^+ sputtering and subsequent annealing to 1573 K. Similar to the surface shown in literature (Fig. A.7), the surface, featuring sizable corrugation as apparent in the height profile along the black line shown below the topograph, is dominated by {331} nanofacets. The facets shown in detail in the inset are oriented along the [$\bar{1}$10] direction. The corresponding LEED image is displayed in Fig. A.9 (a). The facets appear as line-like features in the [001] direction.

After heating the Ir(110) sample to 1173 K and cooling down in an O pressure of $p = 1 \times 10^{-8}$ mbar (local pressure in front of the gas dosing tube was higher by about a factor 20), the LEED image in Fig. A.9 (b) was recorded. As marked by the colored circles, the surface features two structures, one being the (1×1) pattern of the unreconstructed Ir(110) surface and the other one a $c(2 \times 2)$ superstructure of O on Ir(110) as reported in literature [334–336].

To get rid of the O at the sample surface, it was exposed to a hydrogen pressure of $p = 1 \times 10^{-7}$ mbar (local pressure in front of the gas dosing tube was again higher by about a factor 20), while being held at the moderate temperature of 623 K, a temperature that does not yet cause the reappearance of nanofacets, to cause the formation and desorption of water at the surface. Afterwards the sample is held at the elevated temperature for 300 s without gas dosing to get rid of residual hydrogen left at the surface. The resulting STM image in Fig. A.8 (b) shows

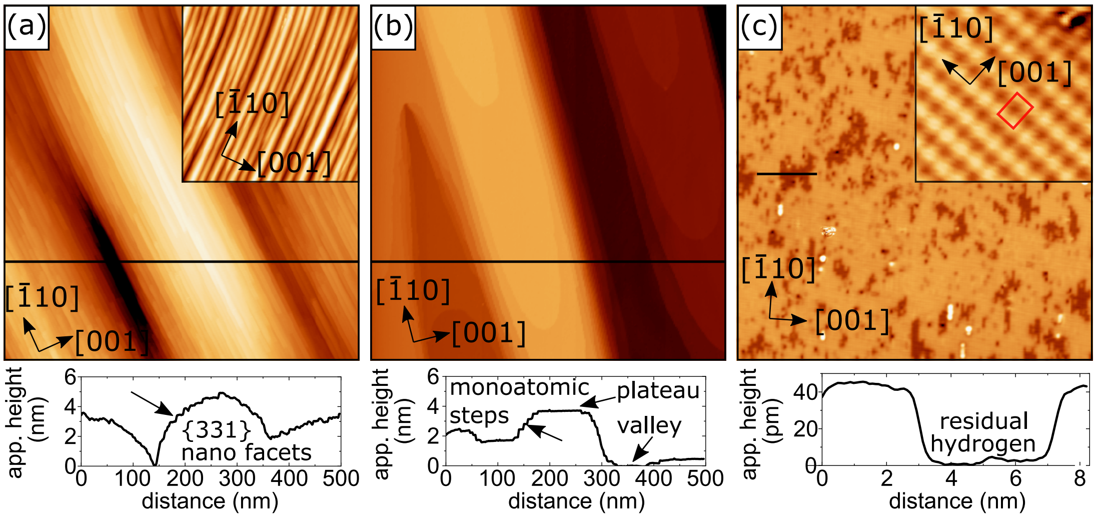

Figure A.8: Constant current STM topographs of the Ir(110) surface before and after the treatment procedure. (a) Nanofaceted surface after Ar^+ sputtering and subsequent annealing to 1573 K. Inset: nanofacets in detail. (b) Unreconstructed Ir(110) surface after O treatment and hydrogen titration. (c) STM image of a flat area. Inset: Atomic resolution STM image, the Ir(110) (1×1) unit cell is marked by a red rhomboid. High-symmetry directions are indicated in the STM images and the line profiles measured along the black lines in the images are displayed below. Image information: (a) size 500 nm × 500 nm, $V_\mathrm{s} = -2$ V, $I_\mathrm{t} = 0.36$ nA, T_s = RT; (b) size 500 nm × 500 nm, $V_\mathrm{s} = 1$ V, $I_\mathrm{t} = 1$ nA, $T_\mathrm{s} = 1.7$ K; (c) size 50 nm × 50 nm, $V_\mathrm{s} = 100$ mV, $I_\mathrm{t} = 1$ nA, $T_\mathrm{s} = 1.7$ K; Inset: size 2.5 nm × 2.5 nm $V_\mathrm{s} = -10$ mV, $I_\mathrm{t} = 30$ nA, $T_\mathrm{s} = 1.7$ K.

that the surface morphology changed significantly. While the overall corrugation remains the same (see height profile along the black line shown below the image), different to the situation displayed in Fig. A.8 (a), the nanofacets are gone and the surface features flat plateaus and valleys, with step edge bundles in between. Fig. A.8 (c) displays an STM image recorded on one of the plateaus. The dark areas possess an apparent height reduced by only 40 pm as apparent from the height profile along the black line shown below, rendering it unlikely to be a structural feature. One explanation could be the presence of residual hydrogen after the titration process, altering the local work function of the surface and creating the illusion of a height corrugation in STM. This is supported by the fact that the dark areas can be removed by scanning with a positive sample bias voltage and high current (not shown), a behavior reported in literature for hydrogen covered metallic surfaces [338]. In the inset, an atomic resolution image of the Ir(110) (1×1) surface is visible, with the rectangular unit cell possessing the $C_{2\mathrm{v}}$ surface symmetry discussed in chapter 5.2. The absence of the O $c(2\times2)$ superstructure that was visible in the LEED image after the O procedure [Fig. A.9 (b)], is evident in the STM image and also the corresponding LEED image in Fig. A.9 (c) only shows reflections corresponding to the (1×1) structure of Ir(110), showing that our procedure is suitable to achieve the clean unreconstructed Ir(110) surface. For further illustration, an atomic structural model is shown in Fig. A.10. The short side $n.n = 0.27$ nm of the marked unit cell [equivalent to the unit cell marked in the inset of Figure A.8 (c)] corresponds to the nearest-neighbor distance of Ir and is parallel to the closed

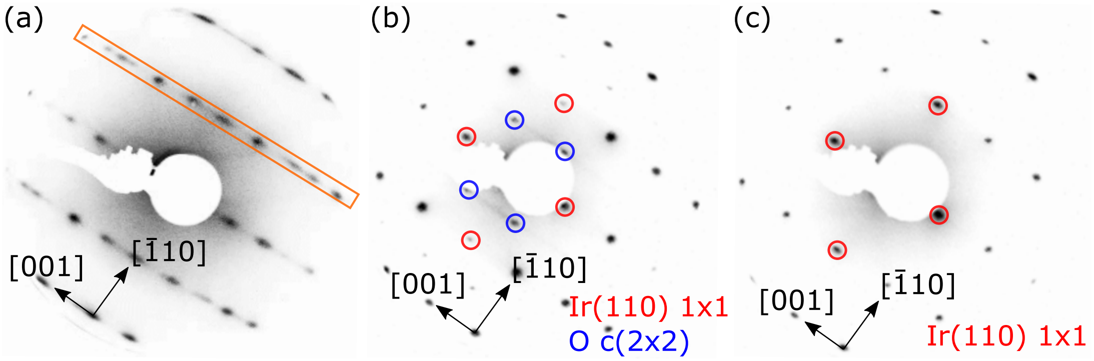

Figure A.9: Inverse contrast 194 eV LEED of the Ir(110) surface. (a) Nanofaceted surface after Ar^+ sputtering and subsequent annealing to 1573 K. One line-like reflection, characteristic for the faceted surface, is marked in orange. (b) Unreconstructed Ir(110) surface covered by O. Reflections belonging to the O-$c(2 \times 2)$ superstructure are marked in blue, reflections belonging to Ir(110) (1×1) lattice are marked in red. (c) Ir(110) surface after hydrogen titration. Reflections belonging to the Ir(110) (1×1) lattice structure are again marked in red.

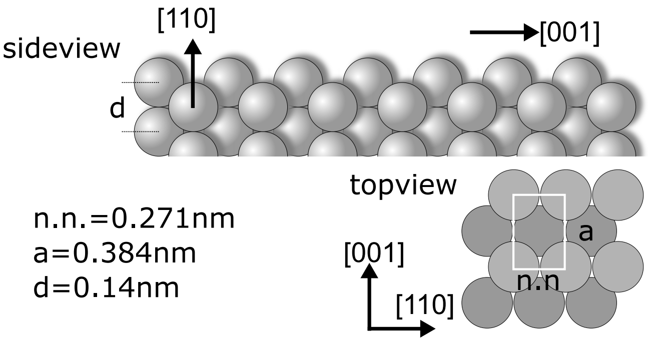

Figure A.10: Atomic structural model of the unreconstructed Ir(110) surface. Lattice constant of Ir adapted from Ref. [339]

packed atomic rows along the [$\bar{1}$10] direction, while the long side a = 0.38 nm corresponds to the lattice constant of Ir, aligned with the [001] direction. As visible in the side view, the distance d between two (110) layers is of 0.14 nm.

The unreconstructed Ir(110) surface is used in the manuscript of chapter 9 as a substrate for ultra thin pseudomorphic Fe films.

A.3 Monolayer Fe on Ir(110)

In the manuscript of chapter 9 the pseudomorphic growth of Fe bilayers on Ir(110) was demonstrated. For these samples, following O deposition, hydrogen was dosed onto the sample held at 623 K to get rid of O by the reaction of H and O and the sample was afterwards kept at this elevated temperature for 300 s to get rid of residual hydrogen (see section A.2). Growth of Fe on this sample at 623 K resulted in Fe bilayer formation (chapter 9). However, when the annealing after hydrogen dosing is omitted, the Ir surface shown in Fig. A.11 (a) is visible in STM. Similar to what is discussed for Fig. A.8 (c) in section A.2, also here regions of higher and lower apparent height can be found (corrugation on the pm scale, see height profile below the STM image). Different to Fig. A.8 (c), the regions of lower apparent height dominate. Since these have been attributed to residual hydrogen on the surface it can be concluded that, due to the omitted annealing to get rid of residual hydrogen, larger portions of the Ir surface are covered by hydrogen. When Fe is deposited onto the surface featuring residual H at RT instead of 623 K, the topography visible in Fig. A.11 emerges. Fig. A.11 (b) is a constant current STM images of Fe on the Ir(110) surface. The height profile along the black line shown in Fig. A.11 (c) shows that the Fe features an apparent height close to the layer-layer distance of Ir(110) of about 0.14 nm (compare section A.2), showing that Fe monolayers are present at the surface. In the inset of (b) rows of Fe are marked blue and the Ir(110) unit cell is marked black. The Fe rows follow the periodicity of the Ir(110) lattice in the [001] direction, showing that the growth is pseudomorphic. In Fig. A.11 (d), the row-like configuration is illustrated by an atomic structural model.

Similar to chapter 9, the surface was investigated by spin polarized STM, but no magnetic contrast could be found. The different growth mode of Fe can be attributed to the presence of hydrogen at the surface, favoring monolayer growth over bilayer growth.

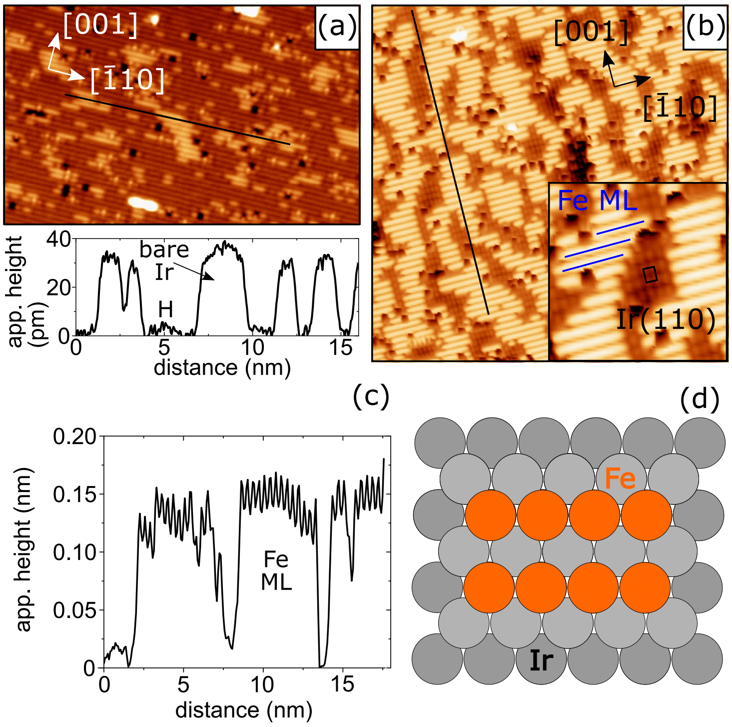

Figure A.11: Constant current STM images of Fe monolayers on hydrogen covered Ir(110). (a) Hydrogen covered Ir(110) surface. (b) Fe monolayers on Ir(110). Inset: atomic resolution, Fe rows are indicated blue, the Ir(110) unit cell is indicated black. (c) Height profile along the black line in (b). (d) Atomic structural model of the Fe rows on Ir(110). Image information: (a) size 25 nm × 25 nm, V_s = 50 mV, I_t = 30 nA, T_s = 0.4 K; (b) size 20 nm × 20 nm, V_s = 100 mV, I_t = 1 nA, T_s = 0.4 K; Inset: size 5 nm × 5 nm V_s = 100 mV, I_t = 1 nA, T_s = 0.4 K.

A.4 Gr/Ir(110) as a Substrate for the Growth of Transition Metal Dichalcogenides

As recently shown in the work of Kraus et al. [340], also the growth of Gr on top of Ir(110) suppresses the nanofacet formation on the Ir(110) surface. The Gr layer on the C_{2v} symmetry substrate features a wave pattern on the nm scale and has been shown to possess a corresponding modulation in its electronic properties. One application is the growth of uniaxial 2D layers, demonstrated for organometallic wires and the templated adsorption of aromatic molecules in [340]. In the following, the growth of NbS_2 on Gr/Ir(110) is demonstrated as an alternative to NbS_2/Gr/Ir(111) discussed in the manuscripts of chapter 7 and 8.

The procedure to obtain a full single crystal Gr layer on the unreconstructed Ir(110) surface is demonstrated in detail in the work of Kraus et al. [340]. In short, after using cycles of noble gas sputtering and brief annealing to 1500 K for cleaning, a closed single domain Gr layer is grown by ethylene exposure at 1500 K. On the Gr/Ir(110), monolayer NbS_2 was grown by exposing the sample to a Nb flux of 2.6×10^{15} atoms/m^{2}s from an e-beam evaporator, in an elemental S background of $p = 5 \times 10^{-9}$ mbar originating from a pyrite filled Knudsen cell. The growth was conducted at 150 K for 1800 s, then the sample was annealed to 823 K in a S background pressure of $p = 7.5 \times 10^{-9}$ mbar for the same duration, similar to the growth of other TMDCs on Gr/Ir(111) [180] and the procedure described for the growth of NbS_2 monolayers on Gr/Ir(111) (chapter 7 and 8). The growth procedure results in the LEED image shown in Fig. A.12 (a). Similar to the structure shown by Kraus et al. [340], the rectangular unit cell of Ir(110) results in reflections marked in black, while the hexagonal Gr reflections are indicated red. Additionally a ring feature marked turquoise is present, being the result of NbS_2 with random orientation, in agreement with the results in chapter 7. The NbS_2 monolayer islands grown on the sample with a coverage of about 0.44 ML are visible in the STM topograph of Fig. A.12 (b). The NbS_2 is assumed to be present in the H-phase (see chapter 3, chapter 7 and chapter 8). In the height profile shown below the topograph, an apparent height of the NbS_2 monolayers of about 0.57 nm is evident, in the same range as the heights found for NbS_2 monolayers on Gr/Ir(111) in the manuscripts of chapters 7 and 8. Fig. A.12 (c) is an STM image recorded on top of a NbS_2 monolayer island. The line profile along the black line shown below features a modulation of 3 nm periodicity in agreement with the long periodicity of the moiré of Gr/Ir(110) [340]. In the atomic resolution inset the hexagonal unit cell of NbS_2 is marked by a red rhomboid. The lattice constant extracted from STM is 0.33(3) nm, in good agreement with the results for NbS_2/Gr/Ir(111) in the before mentioned chapters. One special topographic feature is visible in Fig. A.12 (d). The Gr substrates features line-like features and a varying apparent height in some areas. Since the sample has been heated in S background, the lines could originate from S intercalation. In the height profile along the black line shown below the STM image, the height of the lines results as about 0.15 nm. The mentioned variation in apparent height is marked by black arrows and is of about 0.14 nm. This height is in agreement with the step height of Ir(110) described in section A.2. This behavior was not present in pristine Gr/Ir(110) and also not in NbS_2/Gr/Ir(111). One interpretation is that the sulfur intercalation visible as the the line-like features strongly interacts with the Ir(110) substrate causing it to deform. The structure does not seem to be present in large portions of the sample, since it does not cause reflections in the LEED image of Fig. A.12. The quality of the LEED image is limited though rendering the attribution of additional features non-trivial.

In Fig. A.13 (a) the Gr in the presumably S intercalated area is shown in detail. As evident from the height profiles shown on the right, the Gr features a modulation of 0.58(5) nm along the direction marked by the black line. This is reasonably close to double the lattice constant of Ir being 0.27 nm. In the direction of the red line, the visible periodicity is of 1.3(2) nm. The found periodicities can not stem from the moiré of Gr and Ir(110) found by Kraus et al. [340] being of about 1 nm/3 nm in the high-symmetry directions. The periodicity of 0.58(5) nm could point to some kind of $(2\times?)$ superstructure with respect to Ir, possibly originating from S intercalation. Also in areas not showing the line-like features attributed to S intercalation [Fig. A.13 (b)] the Gr sometimes features modulation pattern in disagreement with the moiré superstructures found in [340]. In the shown case there appears to be a domain boundary to an area featuring S lines as shown in (a). The periodicity along the blue line is of 1.1(1) nm and the one along the pink line of 3.1(5) nm, both in agreement with the moiré in Ref. [340], but is not featuring a 90° angle between the two moiré directions, possibly being the sign of a different phase of Gr/Ir(110) not described so far. To solve this question, further investigations would be necessary.

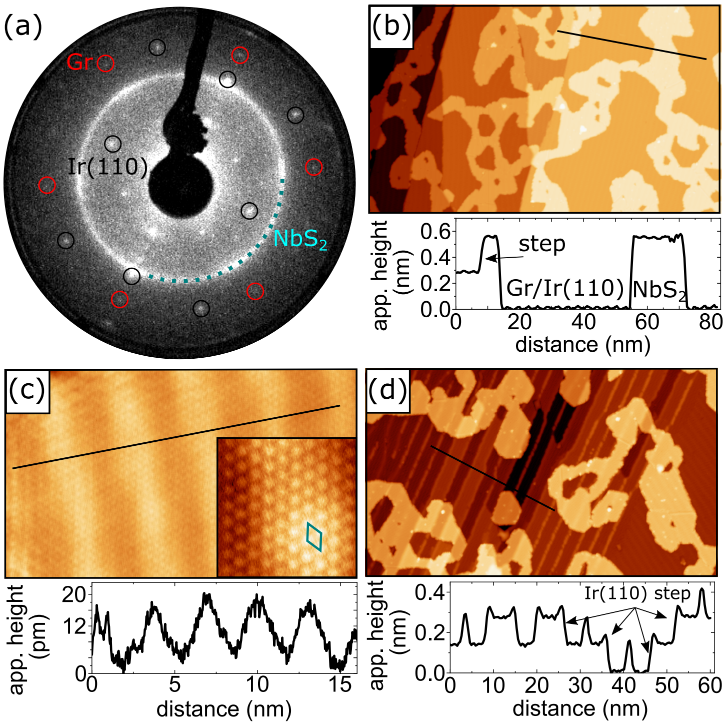

Figure A.12: Structure of NbS_2 monolayers on Gr/Ir(110). (a) 98 eV LEED. Reflections belonging to Ir(110) are marked black, reflections of Gr are marked red, and a ring-like reflection of NbS_2 is marked turquoise. (b) Large scale constant current STM topograph. A height profile measured along the black line showing the apparent height of the NbS_2 monolayers and the Ir(110) step height, is shown below the topograph. (c) STM image of the moiré superstructure of Gr/Ir(110) superimposed to NbS_2. The height profile measured along the black line shows the long moiré periodicity of about 3 nm. Inset: Atomic resolution STM image of the NbS_2 lattice. The unit cell of NbS_2 is marked by a turquoise rhomboid. (d) Large-range STM topograph of an area featuring uniaxial S intercalation of Gr. The height profile measured along the black line shown below the STM topograph shows the periodicity of S intercalation chains and the apparent height of Ir(110) steps presumably caused by the S. Image information: (b) size 200 nm × 200 nm, V_s = 2 V, I_t = 0.05 nA, T_s = 1.7 K; (c) size 160 nm × 160 nm, V_s = 175 mV, I_t = 0.5 nA, T_s = 1.7 K; Inset: size 7 nm × 7 nm V_s = 175 mV, I_t = 0.5 nA, T_s = 1.7 K; (d) size 150 nm × 150 nm, V_s = 2 V, I_t = 0.05 nA, T_s = 1.7 K.

Similar to the measurements conducted in the manuscript of chapter 7, the electronic structure of NbS_2/Gr/Ir(110) was investigated by constant current dI/dV maps as well as constant height STS point spectra. The result is shown in Fig. A.14. Fig. A.14 (a) is a constant current dI/dV map of an NbS_2 island on Gr/Ir(110). Similar to the result of chapter 7, standings waves from quasi-particle interference are present at the edges of the islands, propagating in $\overline{\Gamma M}$-direction

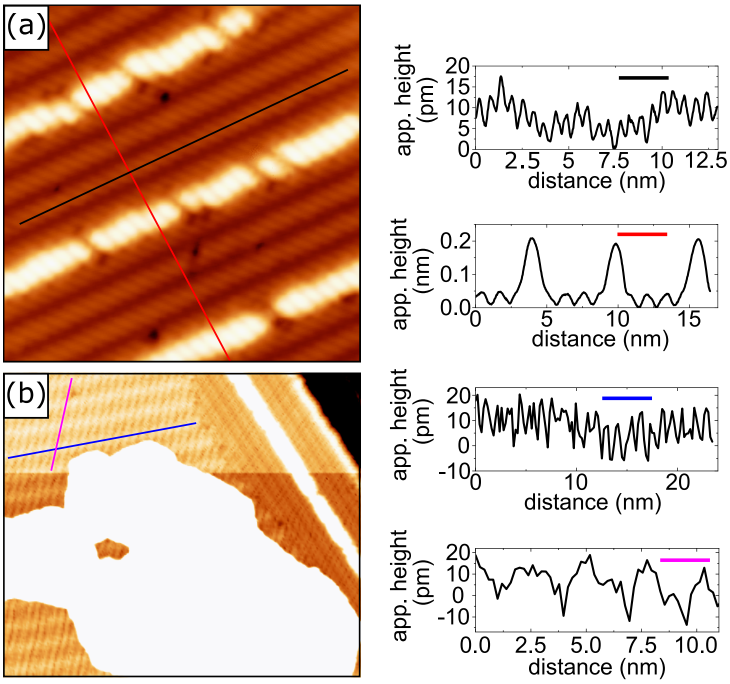

Figure A.13: Constant current STM images of different modulation patterns in Gr. (a) Gr partially intercalated by S. (b) Unknown Gr phase in an unintercalated area. The contrasted is adjusted so that NbS_2 appears white. Height profiles along the colored lines in (a) and (b) are shown on the right site. Image information: (a) size 15 nm × 15 nm, V_s = 200 mV, I_t = 0.1 nA, T_s = 1.7 K; (b) size 44 nm × 37 nm, V_s = 2 V, I_t = 0.5 nA, T_s = 1.7 K.

as marked by the orange arrow. Analogue to the analysis in the manuscript of chapter 7, line profiles taken along the orange arrow in (a) were fitted by a Bessel function to extract the wave vectors of the standing waves for different bias voltages/energies to gain access to the metallic band dispersion. The result is shown as red dots in Fig. A.14 (b). Compared to the dispersion of the standing waves in NbS_2/Gr/Ir(111) (black points) and the calculated band dispersion in freestanding NbS_2 monolayers (blue line [142]), the dispersion is a little steeper, but the wave vectors are of the same magnitude. Fig. A.14 (c) displays another constant current dI/dV map of a NbS_2 island. In the corresponding FFT inset, weak reflections between the Γ-point and the atomic lattice reflections in two high-symmetry directions are visible. The exact q vector results in $q = 0.7\overline{\Gamma\mathrm{M}}$, similar to the found 3×3 CDW superlattice of $q = 2/3\overline{\Gamma\mathrm{M}}$ in the manuscript of chapter 7 and therefore very likely of the same origin, even though the intensity in NbS_2/Gr/Ir(110) generally appears to be lower and the superlattice is not visible in the real space dI/dV map. The slight deviation from the value of $q = 2/3\overline{\Gamma\mathrm{M}}$ could be a sign of incommensurability, but the amount of data available at this point is very limited. The presence of a very similar CDW, although being of weaker intensity and the similar wave length of the standing waves points towards the fact that the electronic structure of the NbS_2 monolayers on Gr/Ir(110) is not significantly changed compared to NbS_2/Gr/Ir(111). This is confirmed by the comparison of constant height STS point spectra recorded on NbS_2 on the two different substrates [Fig. A.14 (e)]. The spectrum recorded on NbS$_2$/Gr/Ir(110) closely resembles the features of the NbS$_2$/Gr/Ir(111) spectrum, which themselves were nicely comparable with the features of the calculated band structure of quasi-freestanding NbS$_2$ (compare chapter 7 and chapter 3).

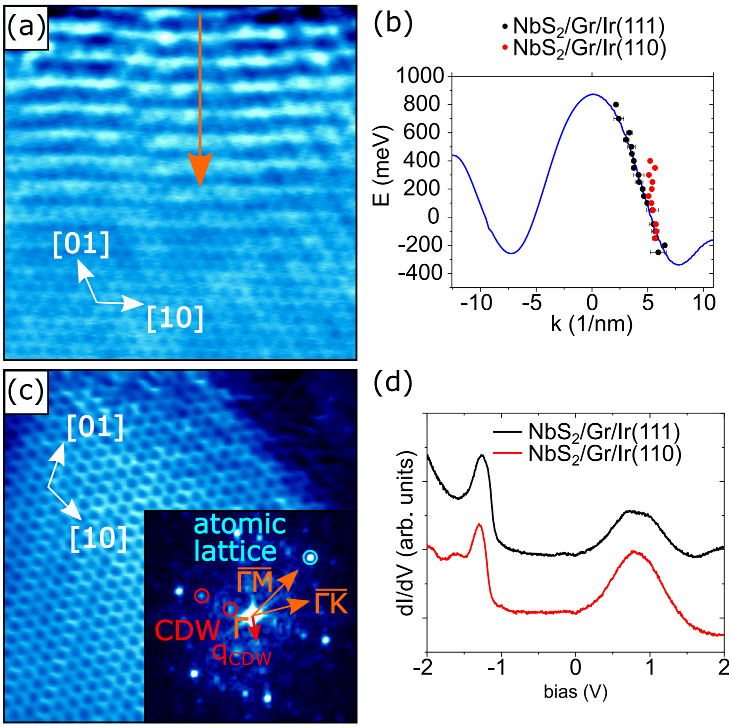

Figure A.14: Electronic structure of NbS$_2$/Gr/Ir(110). (a) Constant current dI/dV map showing standing waves propagating in $\overline{\Gamma M}$ direction, indicated by an orange arrow. (b) Band dispersion extracted from Bessel function fit of standing wave line profiles taken along the orange arrow in (a) (red dots) compared to the dispersion of the standing waves in NbS$_2$/Gr/Ir(111) (black dots) and the calculated band dispersion in freestanding NbS$_2$ monolayers (blue line [142]). (c) Another constant current dI/dV map. Inset: FFT featuring reflections (red circles) in between the center and the atomic lattice reflections, attributed to a CDW superlattice. The corresponding q-vector of the CDW is indicated by a red arrow. (d) Large-range constant height STS point spectrum of NbS$_2$/Gr/Ir(110) (red) compared to a spectrum recorded on NbS$_2$/Gr/Ir(111) (black). STS information: (a) size 15 nm × 15 nm, V_s = 100 mV, I_t = 0.5 nA, V_{mod} = 20 mV, f_{mod} = 1890 Hz, T_s = 1.7 K; (c) size 8 nm × 8 nm, V_s = 200 mV, I_t = 0.15 nA, V_{mod} = 20 mV, f_{mod} = 1890 Hz, T_s = 1.7 K; (d) V_{stab} = 2.0 V, I_{stab} = 1.0 nA (red), I_{stab} = 0.7 nA (black), V_{mod} = 15 mV, f_{mod} = 797 Hz, T_s = 1.7 K.

A.5 Fe Intercalation of Gr/Ir(110)

As described in the manuscript of chapter 9 and section A.3, Fe grows pseudomorphic on the unreconstructed Ir(110) surface. It is known from literature is that magnetic materials in contact with Gr can induce and influence spin polarization in the latter [314]. The contact of Gr with a ferromagnetic layer is generally of interest for spintronic applications [313]. Regarding Fe, its intercalation below Gr on Ir(111) is described in [341]. Regarding Gr/Ir(110), recently described by Kraus et al. [340], the intercalation of Fe would be interesting regarding the magnetic states of Fe on Ir(110), possibly changing the spin spiral state described in the manuscript of chapter 9, but also because of the influence the Fe could have on Gr itself.

The intercalation of Fe below Gr/Ir(110) was attempted by deposition at elevated temperatures of 823 K onto the sample. Surprisingly, Fe only intercalated the Gr in the case of NbS_2 islands being present presumably caused by defects induced by the NbS_2 islands and in the following the shown sample, featuring Fe intercalated below Gr, also features NbS_2/Gr/Ir(110) as described in section A.4.

Fig. A.15 (a) shows a constant current STM image of Fe islands below Gr on Ir(110). The moiré of Gr/Ir(110) described in detail in Ref. [340] is also visible on top of the Fe islands, showing that the Fe is actually located below the Gr and that the growth is pseudomorphic, since the moiré is offset by one Ir atomic row length on the Fe island (see inset), resulting from the A-B stacking of Fe layers on Ir(110) (compare section A.3). The height profile displayed in Fig. A.15 taken along the black line in Fig. A.15 (a) shows that the Fe islands have an apparent height of about 0.13 nm, in good agreement with the step height of Ir(110) (as described in section A.2, step height of Fe layers in section A.3 and manuscript in chapter 9) and therefore can be considered a monolayer.

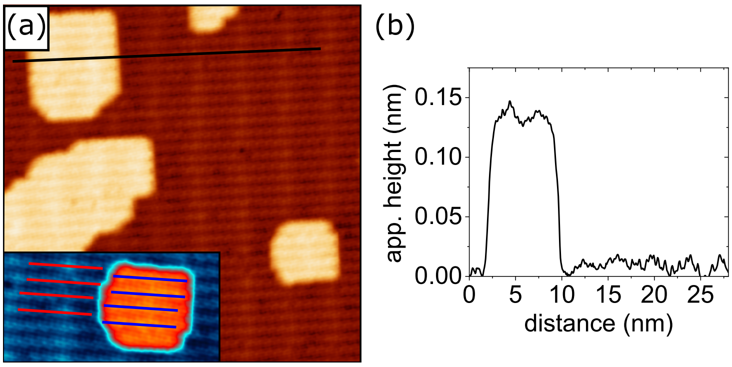

Figure A.15: Fe intercalated under Gr/Ir(110). (a) Constant current STM image of pseudomorphic Fe monolayer islands under Gr. (b) Height profile measured along the black line in (a). Image information: (a) size 30 nm × 30 nm, V_s = 5 mV, I_t = 1 nA, T_s = 1.7 K. Inset: size 13.6 nm × 7 nm

A.6 Hetero-Self-Intercalation of Bilayer NbS_2 on Gr/Ir(111)

In the manuscript of chapter 8, the heterostack intercalation of NbS_2 monolayers on Gr by Nb upon heating was described. When heating the NbS_2 monolayers to above 820 K, they partially dissolve and Nb from the pristine phase of NbS_2 moves below, causing a stack of NbS_2/Nb/Gr/Ir(111).

A similar phenomenon takes place when heating up a sample also featuring NbS_2 bilayers. Fig. A.16 (a) displays a STM image of such a sample. As apparent from the height profile along the black line, both monolayers and bilayers are present with apparent heights of 0.57 nm and 1.17 nm correspondingly, in good agreement with the results presented in the manuscript of chapter 8. The total NbS_2 coverage including the bilayers is of about 69 %. The sample was annealed to 873 K (above the temperature of 820 K used to prepare the pristine sample) for 15 min without providing additional S. From chapter 8 it is known that this process causes a partial dissociation of the pristine NbS_2 and the subsequent intercalation of Nb below NbS_2. The result is visible in the STM image of Fig. A.16 (b). Similar to chapter 8, the total coverage of the sample is decreased (to 43 %), and additional phases of different apparent heights emerge, indicating that the pristine NbS_2 is indeed intercalated. One example of a phase with increased apparent height is the 0.89 nm high phase indicated as SI (self-intercalation) in the height profile taken along the black line in the STM image. This apparent height is in good agreement with the Nb $\sqrt{3} \times \sqrt{3}$ – phase and the Nb 1×1 – phase of chapter 8, attributed to intercalated monolayer NbS_2. Fig. A.16 (c) shows an area of the sample with several different intercalation structures. The bias-dependent apparent heights, marked by color equivalent points in Fig. A.16 (c), are displayed in Fig. A.16 (d). Different to the results of chapter 8, besides the NbS_2 monolayers and bilayers not only one additional height (monolayer $\sqrt{3} \times \sqrt{3}$ R30° – phase, red) is present, but several different ones close to the apparent height of the bilayer are evident. This is probably the result of the NbS_2 bilayers present in Fig. A.16 (a), absent in the samples shown in chapter 8. The new phases, featuring close to double-monolayer or bilayer height are described as the bilayer $\sqrt{3} \times \sqrt{3}$ R30° type I – phase and the bilayer $\sqrt{3} \times \sqrt{3}$ R30° type II – phase. The reason for the designation is that just as the intercalated monolayer $\sqrt{3} \times \sqrt{3}$ – phase, these bilayer phases feature a $\sqrt{3} \times \sqrt{3}$ R30° superstructure with respect to the pristine NbS_2 lattice. The bilayer superstructures are visible in Fig. A.17. Fig. A.17 (a) displays a large-range constant current STM topograph showing a sample area with different intercalation phases present. In the high-resolution STM image of Fig. A.17 (b), recorded on a bilayer $\sqrt{3} \times \sqrt{3}$ R30° type I – phase island in Fig. A.17 (a) (orange dot), a $\sqrt{3} \times \sqrt{3}$ R30° superstructure with respect to the pristine NbS_2 lattice is marked by a black rhomboid. The same superstructure is found in the bilayer $\sqrt{3} \times \sqrt{3}$ R30° type II – phase [blue point in (a)] in Fig. A.17 (c). The superstructure present in both phases is an indication, that both phases are bilayers intercalated by for example 1/3 the amount of Nb present in the pristine NbS_2-as discussed for Fe intercalation in

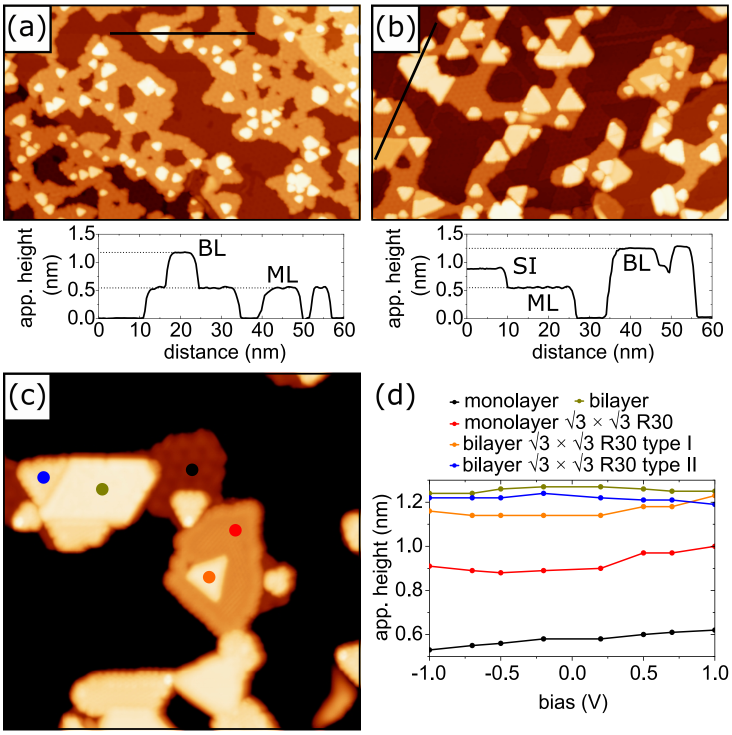

Figure A.16: Constant current STM topographs of different NbS_2 phases on Gr/Ir(111). (a) Pristine NbS_2 monolayers (ML) and bilayers (BL). (b) Monolayer NbS_2, bilayer NbS_2 and self-intercalated NbS_2 (SI). (c) Sample area featuring different intercalation phases. (d) Bias-dependent apparent heights of the different phases marked by color equivalent dots in (c). Image information: (a) size 150 nm × 90 nm, $V_s = 2\,\mathrm{V}$, $I_t = 0.1\,\mathrm{nA}$, $T_s = 1.7\,\mathrm{K}$; (b) size 150 nm × 90 nm, $V_s = -1\,\mathrm{V}$, $I_t = 0.1\,\mathrm{nA}$, $T_s = 1.7\,\mathrm{K}$; (c) size 50 nm × 50 nm, $V_s = 1\,\mathrm{V}$, $I_t = 0.5\,\mathrm{nA}$, $T_s = 1.7\,\mathrm{K}$.

chapter 8, causing the found superstructures. It should be noted, that in the manuscript the formation of an NiAs structure of stoichiometry NbS was discussed with trimerization being responsible for the $\sqrt{3} \times \sqrt{3}$ R30° superstructure, being a possible alternative to 1/3 intercalation also here. The corrugation in the two phases, measured along orange/blue lines in Fig. A.17 (b) and (c), is displayed in Fig. A.17 (d). Obviously the corrugation is much lower in the bilayer $\sqrt{3} \times \sqrt{3}$ R30° type II – phase compared to type I. Assuming 1/3 intercalation and leaving out the possibility of NbS formation, the difference regarding the corrugation could be that in one case (bilayer $\sqrt{3} \times \sqrt{3}$ R30° type I), the intercalated Nb is placed in between the two NbS_2 layers, while it is placed below both NbS_2 layers in the other case (bilayer $\sqrt{3} \times \sqrt{3}$ R30° type II). The more layers are place above the superstructure, the weaker the corrugation is expected to appear in STM. Of course the difference could also be that in one case 1/3 of all lattice sites in the vdW gap are occupied by Nb and in the other case NbS of NiAs structure is formed, with trimerization as described in chapter 8 causing the $\sqrt{3} \times \sqrt{3}$ R30° superstructure.

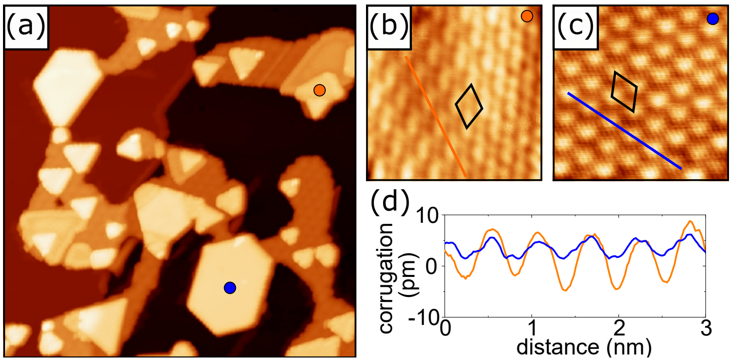

Figure A.17: Different phases of hetero-self-intercalated NbS$_2$ bilayers on Gr/Ir(111). (a) Large-range constant current STM topograph of a sample area featuring intercalated bilayer NbS$_2$. (b), (c) High-resolution STM images recorded at the color equivalent points in (a). Orange: bilayer $\sqrt{3} \times \sqrt{3}$ R30° type I – phase, blue: bilayer $\sqrt{3} \times \sqrt{3}$ R30° type II – phase. The $\sqrt{3} \times \sqrt{3}$ R30° superstructures are marked by black rhomboids. (d) Apparent corrugation of the superstructures in both phases measured along the color equivalent lines in (b) and (c). Image information: (a) size 80 nm × 80 nm, $V_s = -5002$ mV, $I_t = 0.2$ nA, $T_s = 1.7$ K, (b) size 4 nm × 4 nm, $V_s = -200$ mV, $I_t = 0.5$ nA, $T_s = 1.7$ K, (c) size 4 nm × 4 nm, $V_s = -200$ mV, $I_t = 0.5$ nA, $T_s = 1.7$ K.

In Fig. A.18 large-range constant height STS point spectra measured on all pristine and Nb-intercalated phases, also including the phases treated in chapter 8, are displayed. A spectrum recorded on a pristine NbS$_2$ monolayer is shown in black at the bottom for reference. Two black lines indicate prominent peaks of the NbS$_2$ monolayer, one at -1.27 V belonging to S p_z-type bands and one at 0.73 V belonging to the Nb d_{z^2}-type band crossing the Fermi energy (compare chapter 7). For the two spectra belonging to the intercalated monolayer phases (Nb $\sqrt{3} \times \sqrt{3}$ – and Nb 1×1 – phases in chapter 8), the negative bias features are shifted to lower energies. In case of the monolayer $\sqrt{3} \times \sqrt{3}$ – phase, the positive bias peak features oscillations and also extends to higher energies. Similar oscillations can be observed in the bilayer $\sqrt{3} \times \sqrt{3}$ type I spectrum. Nevertheless, here the shift of features on the negative energy side to even more negative energies in the monolayer $\sqrt{3} \times \sqrt{3}$ – phase can not be reproduced. For the bilayer $\sqrt{3} \times \sqrt{3}$ R30° type II – phase it is obvious that on the positive bias site the feature present in the pristine monolayer is not present, but some features close to the Fermi energy on the negative side are there. This is dissimilar to all the other phases. Finally, the pristine non-intercalated NbS$_2$ bilayer has a feature almost at the same energy as the NbS$_2$ monolayer on the negative side but an additional one is present beside it just above -1 V. This peak can be attributed to a S p-bands being present closer to the Fermi energy (compare DFT calculated band structure of NbS$_2$ bilayers in Ref. [342]). In summary, all the phases feature a unique electronic structure that allows to differentiate them.

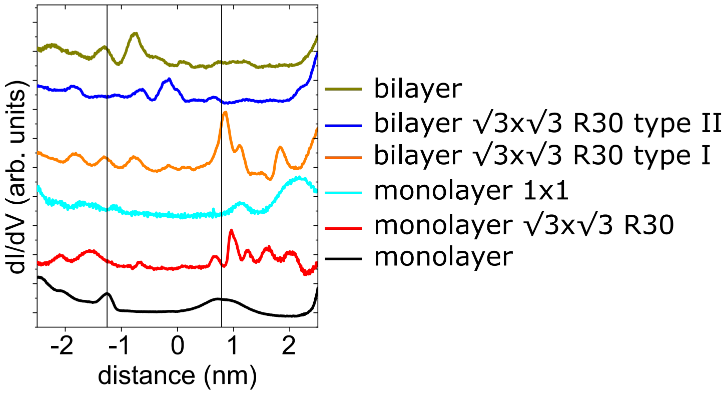

Figure A.18: Large-range constant height STS point spectra of the different pristine and intercalated phases. STS parameters: black: $V_{\mathrm{stab}} = 2.5\,\mathrm{V}$, $I_{\mathrm{stab}} = 1.0\,\mathrm{nA}$, $V_{\mathrm{mod}} = 15\,\mathrm{mV}$, $f_{\mathrm{mod}} = 797\,\mathrm{Hz}$, $T_{\mathrm{s}} = 1.7\,\mathrm{K}$; red: $V_{\mathrm{stab}} = 3\,\mathrm{V}$, $I_{\mathrm{stab}} = 0.8\,\mathrm{nA}$, $V_{\mathrm{mod}} = 10\,\mathrm{mV}$, $f_{\mathrm{mod}} = 797\,\mathrm{Hz}$, $T_{\mathrm{s}} = 1.7\,\mathrm{K}$; turquoise: $V_{\mathrm{stab}} = 2.5\,\mathrm{V}$, $I_{\mathrm{stab}} = 0.7\,\mathrm{nA}$, $V_{\mathrm{mod}} = 10\,\mathrm{mV}$, $f_{\mathrm{mod}} = 811\,\mathrm{Hz}$, $T_{\mathrm{s}} = 1.7\,\mathrm{K}$; orange: $V_{\mathrm{stab}} = 2.5\,\mathrm{V}$, $I_{\mathrm{stab}} = 0.7\,\mathrm{nA}$, $V_{\mathrm{mod}} = 10\,\mathrm{mV}$, $f_{\mathrm{mod}} = 811\,\mathrm{Hz}$, $T_{\mathrm{s}} = 1.7\,\mathrm{K}$; blue: $V_{\mathrm{stab}} = 2.5\,\mathrm{V}$, $I_{\mathrm{stab}} = -0.5\,\mathrm{nA}$, $V_{\mathrm{mod}} = 10\,\mathrm{mV}$, $f_{\mathrm{mod}} = 797\,\mathrm{Hz}$, $T_{\mathrm{s}} = 1.7\,\mathrm{K}$; khaki: $V_{\mathrm{stab}} = 3\,\mathrm{V}$, $I_{\mathrm{stab}} = 0.8\,\mathrm{nA}$, $V_{\mathrm{mod}} = 10\,\mathrm{mV}$, $f_{\mathrm{mod}} = 797\,\mathrm{Hz}$, $T_{\mathrm{s}} = 1.7\,\mathrm{K}$.

APPENDIX B

Technical Appendix

Improved e-beam Sample Holder parts

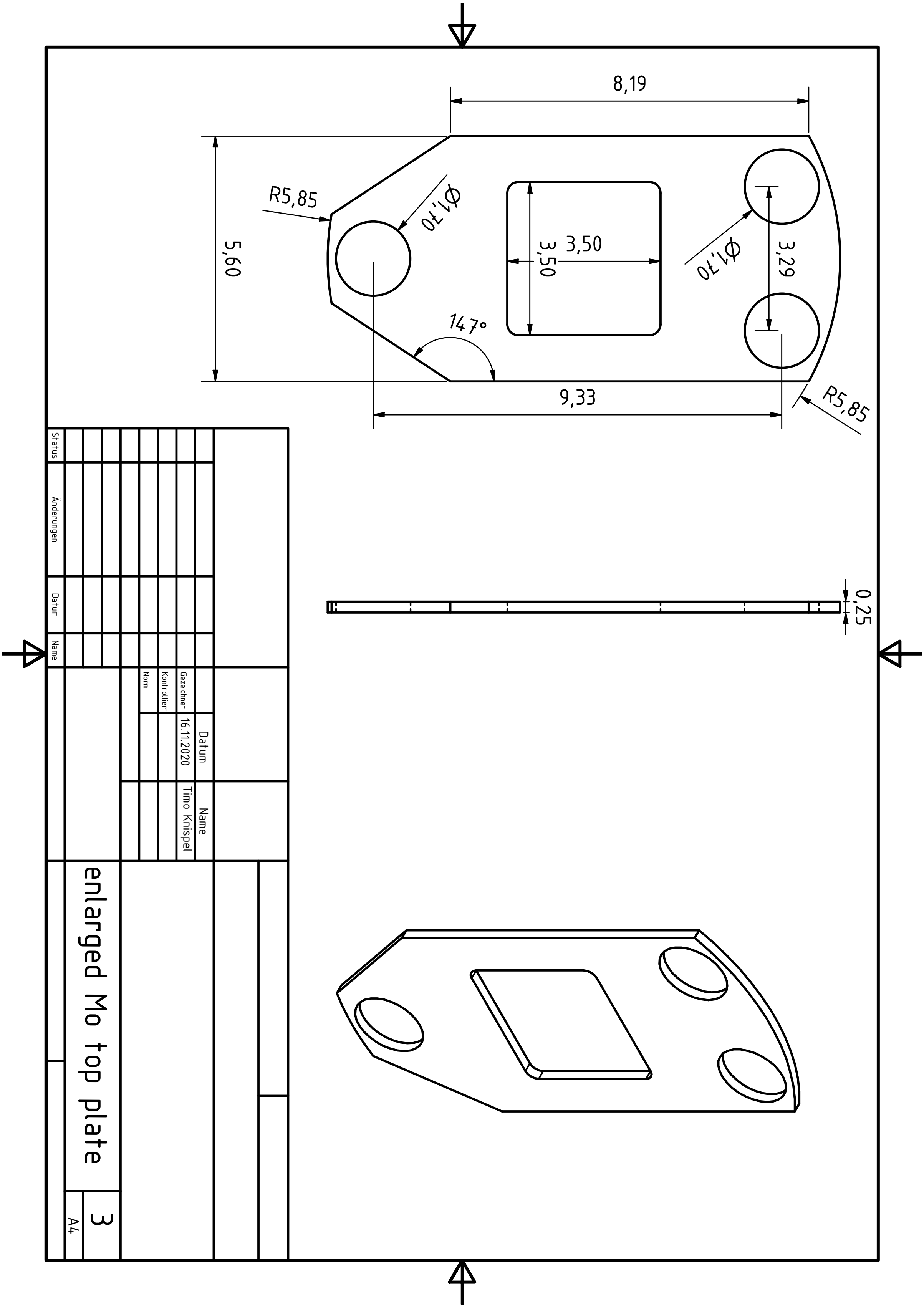

Figure B.1: Enlarged Mo top plate to fix larger crystals.

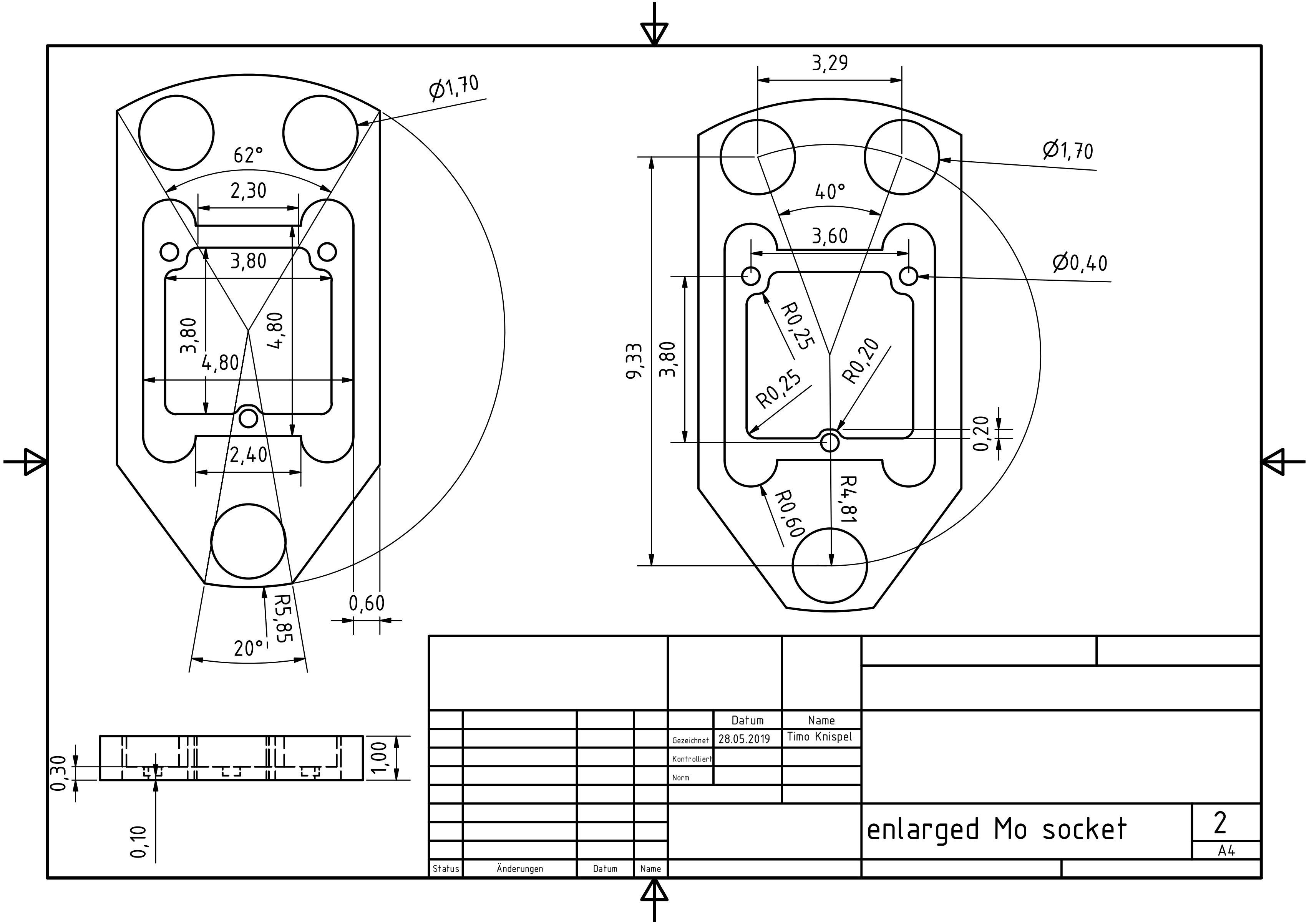

Figure B.2: Enlarged Mo socket to fit larger crystals on three sapphire balls.

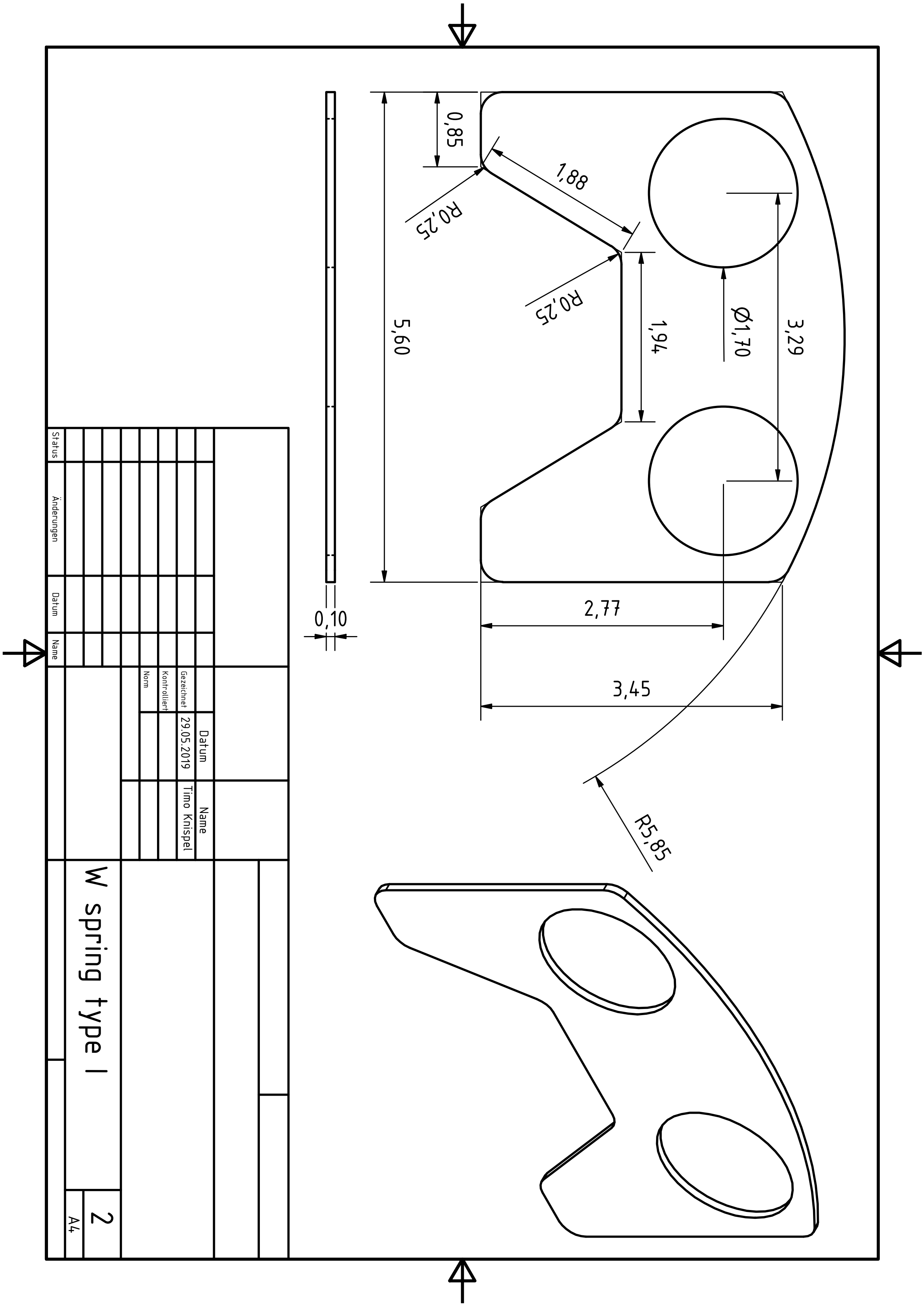

Figure B.3: W spring type I. Alternative for the Mo top plates for high temperatures.

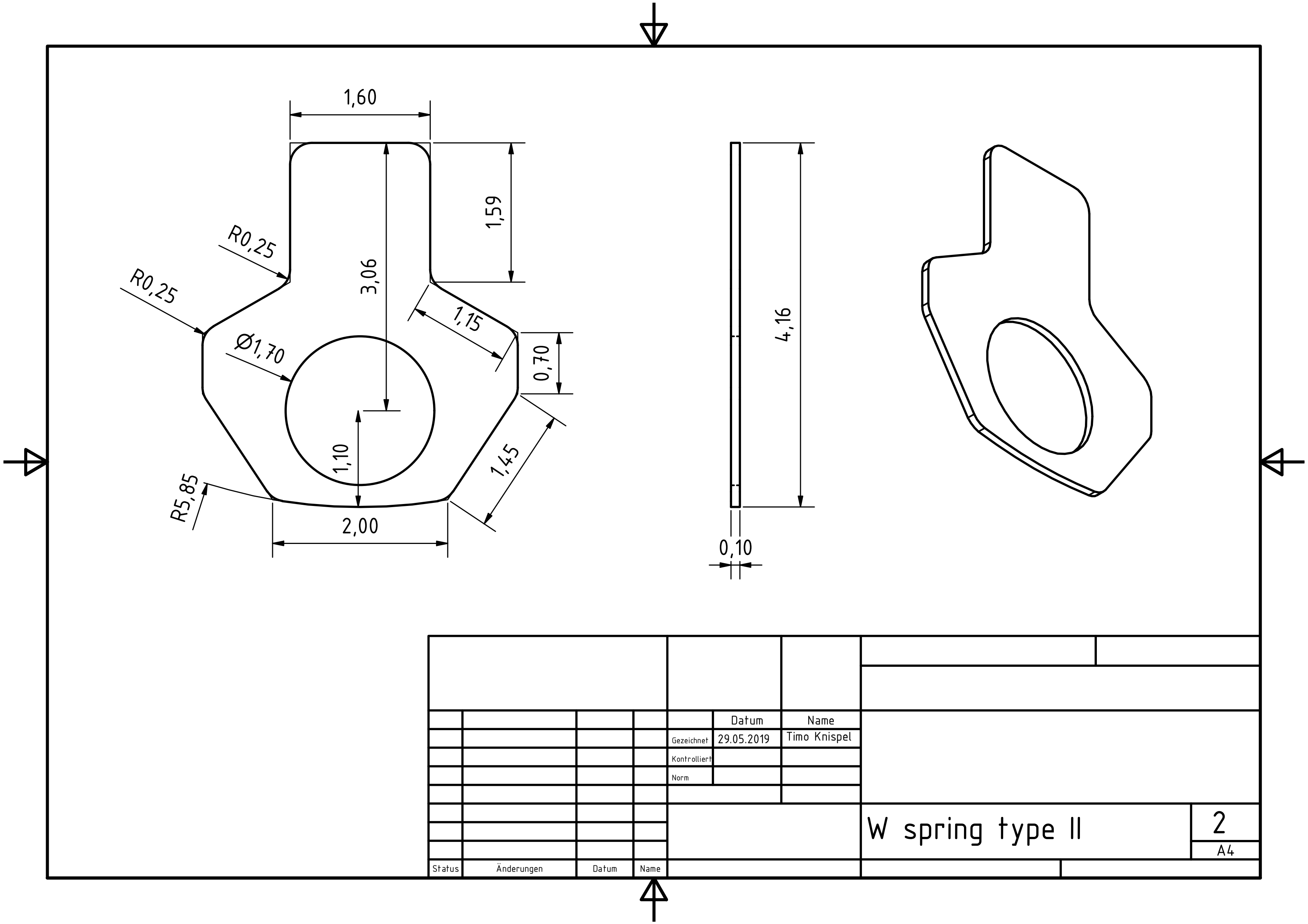

Figure B.4: W spring type II. Alternative for the Mo top plates for high temperatures.

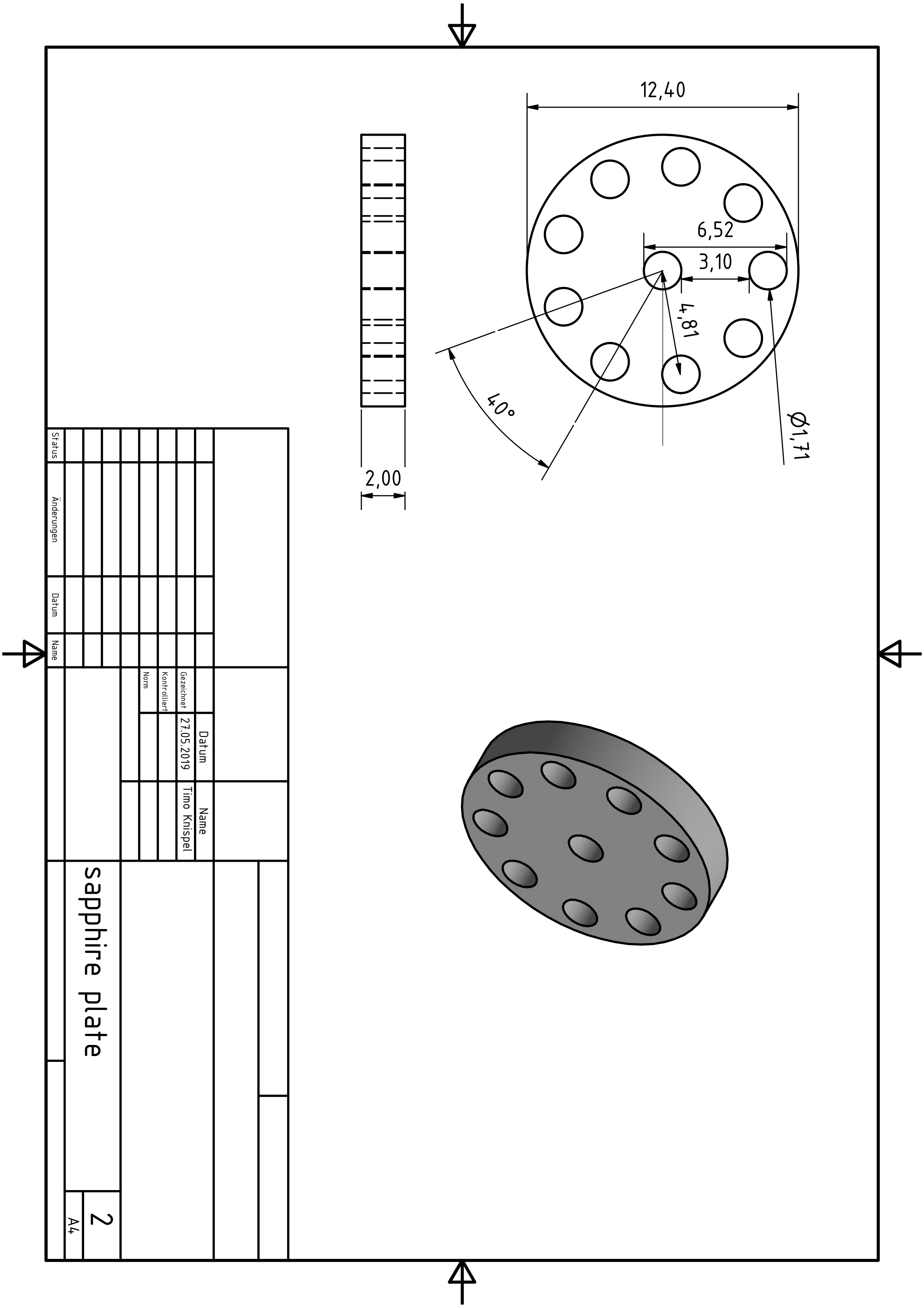

Figure B.5: Sapphire plate replacing the Al_2O_3 plates delivered by UNISOKU.

APPENDIX C

List of Publications
(Liste der Teilpublikationen)

The results presented in this thesis can be found in the following publications:
Teile dieser Arbeit wurden als Bestandteil der folgenden Artikel in Fachzeitschriften bereits veröffentlicht:

n/a **Timo Knispel**, Jeison Fischer, Jan Berges, Arne Schobert, Erik G. C. P. van Loon, Wouter Jolie, Timo Wehling, and Thomas Michely
Electronic structure and charge density wave order in monolayer NbS_2
manuscript in preparation phase

n/a **Timo Knispel**, Daniela Mohrenstecher, Carsten Speckmann, Yannic Falke, Alexander Grüneis, Nicolae Atodiresei, Jeison Fischer, and Thomas Michely
Post-growth intercalation at the interface of graphene and monolayer NbS_2
manuscript in preparation phase

n/a **Timo Knispel**, Vasily Tseplyaev, Markus Hoffmann, Stefan Blügel, Thomas Michely, and Jeison Fischer
Bloch spin helix in an ultrathin Fe film on Ir(110)
manuscript in preparation phase

Further publications:
Weitere Publikationen:

[340] Stefan Kraus, Felix Huttmann, Jeison Fischer, **Timo Knispel**, Ken Bischof, Alexander Herman, Marco Bianchi, Raluca-Maria Stan, Ann Julie Holt, Vasile Caciuc, Shigeru Tsukamoto, Heiko Wende, Philip Hofmann, Nicolae Atodiresei, Thomas Michely
Single-crystal graphene on Ir(110)
preprint in arXiv (2021), submitted to Physical Review B

[343] Wouter Jolie, **Timo Knispel**, Niels Ehlen, Konstantin Nikonov, Carsten Busse, Alexander Grüneis, and Thomas Michely
Charge density wave phase in VSe_2 *revisited*
Phys. Rev. B **99**, 115417 (2019)

[344] Wouter Jolie, Jonathan Lux, Mathias Pörtner, Daniela Dombrowski, Charlotte Herbig, **Timo Knispel**, Sabina Simon, Thomas Michely, Achim Rosch, and Carsten Busse
Suppression of Quasiparticle Scattering Signals in Bilayer Graphene Due to Layer Polarization and Destructive Interference
Phys. Rev. Lett. **120**, 106801 (2018)

[345] Sabina Simon, Elena Voloshina, Julia Tesch, Felix Förschner, Vivien Enenkel, Charlotte Herbig, **Timo Knispel**, Alexander Tries, Jörg Kröger, Yuriy Dedkov, and Mikhail Fonin
Layer-by-Layer Decoupling of Twisted Graphene Sheets Epitaxially Grown on a Metal Substrate
Small **14**, 1703701, (2018)

[346] **Timo Knispel**, Wouter Jolie, Nick Borgwardt, Jonathan Lux, Zhiwei Wang, Yoichi Ando, Achim Rosch, Thomas Michely, Markus Grüninger
Charge puddles in the bulk and on the surface of the topological insulator $BiSbTeSe_2$ *studied by scanning tunneling microscopy and optical spectroscopy*
Phys. Rev. B **96**, 195135, (2017)

[347] Charlotte Herbig, **Timo Knispel**, Sabina Simon, Ulrike A. Schröder, Antonio J. Martínez-Galera, Mohammad A. Arman, Christian Teichert, Jan Knudsen, Arkady V. Krasheninnikov, and Thomas Michely
From Permeation to Cluster Arrays: Graphene on Ir(111) Exposed to Carbon Vapor
Nano Lett. **17**, 3105 (2017)

Conference contributions as presenting author:
Konferenzbeiträge als präsentierender Autor:

2021 DPG SKM 2021, Online Conference , *Electronic structure and charge density wave order in monolayer* NbS_2. Poster

2021 Sol-SkyMag, Online Conference, *Bloch-type spin helix in bilayer iron islands on iridium(110) by spin polarized STM*. Talk

2021 DPG SurfaceScience21, Online Conference, *Electronic structure and charge density wave in monolayer* NbS_2. Poster

2018 DPG Spring Meeting, Berlin (DE), *Quantifying the charge density wave properties in* VSe_2. Poster

2017 DPG Spring Meeting, Dresden (DE), *Investigation of charge puddles at the surface of the compensated topological insulator* $BiSbTeSe_2$. Poster

Bibliography

[1] K. S. Novoselov, A. K. Geim, S. V. Morozov, D. Jiang, Y. Zhang, S. V. Dubonos, I. V. Grigorieva and A. A. Firsov, 'Electric Field Effect in Atomically Thin Carbon Films', *Science* **306**, 666 (2004). Cited on page(s) 1 and 18

[2] A. K. Geim and K. S. Novoselov, 'The rise of graphene', *Nature Materials* **6**, 183 (2007). Cited on page(s) 1

[3] K. S. Novoselov, E. McCann, S. V. Morozov, V. I. Fal'ko, M. I. Katsnelson, U. Zeitler, D. Jiang, F. Schedin and A. K. Geim, 'Unconventional quantum Hall effect and Berry's phase of 2π in bilayer graphene', *Nature Physics* **2**, 177 (2006). Cited on page(s) 1

[4] S. Z. Butler, S. M. Hollen, L. Cao, Y. Cui, J. A. Gupta, H. R. Gutiérrez, T. F. Heinz, S. S. Hong, J. Huang, A. F. Ismach, E. Johnston-Halperin, M. Kuno, V. V. Plashnitsa, R. D. Robinson, R. S. Ruoff, S. Salahuddin, J. Shan, L. Shi, M. G. Spencer, M. Terrones, W. Windl and J. E. Goldberger, 'Progress, Challenges, and Opportunities in Two-Dimensional Materials Beyond Graphene', *ACS Nano* **7**, 2898 (2013). Cited on page(s) 1 and 130

[5] K. S. Novoselov, A. Mishchenko, A. Carvalho and A. H. C. Neto, '2D materials and van der Waals heterostructures', *Science* **353**, 6298 (2016). Cited on page(s) 1

[6] J. Wilson, F. Di Salvo and S. Mahajan, 'Charge-density waves and superlattices in the metallic layered transition metal dichalcogenides', *Advances in Physics* **24**, 117 (1975). Cited on page(s) 1, 5, 7, 12, 13, and 17

[7] M. Van Maaren and G. Schaeffer, 'Superconductivity in group Va dichalcogenides', *Physics Letters* **20**, 131 (1966). Cited on page(s) 1, 15, 17, and 125

[8] S. Nagata, T. Aochi, T. Abe, S. Ebisu, T. Hagino, Y. Seki and K. Tsutsumi, 'Superconductivity in the layered compound 2H-TaS_2', *Journal of Physics and Chemistry of Solids* **53**, 1259 (1992). Cited on page(s) 1, 5, and 12

[9] E. Navarro-Moratalla, J. O. Island, S. Mañas-Valero, E. Pinilla-Cienfuegos, A. Castellanos-Gomez, J. Quereda, G. Rubio-Bollinger, L. Chirolli, J. A. Silva-Guillén, N. Agraït, G. A. Steele, F. Guinea, H. S. J. van der Zant and E. Coronado, 'Enhanced superconductivity in atomically thin TaS_2', *Nature Communications* **7**, 11043 (2016). Cited on page(s) 1, 12, and 13

[10] J. P. Tidman, O. Singh, A. E. Curzon and R. F. Frindt, 'The phase transition in 2H-TaS_2 at 75 K', *Philosophical Magazine* **30**, 1191 (1974). Cited on page(s) 1 and 12

[11] G. A. Scholz, O. Singh, R. F. Frindt and A. E. Curzon, 'Charge density wave commensurability in 2H-TaS_2 and Ag_xTaS_2', *Solid State Communications* **44**, 1455 (1982). Cited on page(s) 1 and 12

[12] S. C. de la Barrera, M. R. Sinko, D. P. Gopalan, N. Sivadas, K. L. Seyler, K. Watanabe, T. Taniguchi, A. W. Tsen, X. Xu, D. Xiao and B. M. Hunt, 'Tuning Ising superconductivity with layer and spin–orbit coupling in two-dimensional transition-metal dichalcogenides', *Nature Communications* **9**, 1427 (2018). Cited on page(s) 1 and 13

[13] Y. Yang, S. Fang, V. Fatemi, J. Ruhman, E. Navarro-Moratalla, K. Watanabe, T. Taniguchi, E. Kaxiras and P. Jarillo-Herrero, 'Enhanced superconductivity upon weakening of charge density wave transport in 2H-TaS_2 in the two-dimensional limit', *Physical Review B* **98**, 035203 (2018). Cited on page(s) 1 and 13

[14] D. Zhang, Y. Wu, Y.-H. Su, M.-C. Hsu, C. Ó Coileáin, J. Cho, M. Choi, B. S. Chun, Y. Guo, C.-R. Chang and H.-C. Wu, 'Charge density waves and degenerate modes in exfoliated monolayer 2H-TaS_2', *International Union of Crystallography Journal* **7**, 913 (2020). Cited on page(s) 1 and 13

[15] X. Zhu, Y. Cao, J. Zhang, E. W. Plummer and J. Guo, 'Classification of charge density waves based on their nature', *Proceedings of the National Academy of Sciences* **112**, 2367 (2015). Cited on page(s) 1

[16] X. Zhu, J. Guo, J. Zhang and E. W. Plummer, 'Misconceptions associated with the origin of charge density waves', *Advances in Physics: X* **2**, 622 (2017). Cited on page(s) 1, 5, 7, and 11

[17] W. G. Fisher and M. J. Sienko, 'Stoichiometry, structure, and physical properties of niobium disulfide', *Inorganic Chemistry* **19**, 39 (1980). Cited on page(s) 1, 15, 17, 22, and 125

[18] C. Witteveen, K. Górnicka, J. Chang, M. Månsson, T. Klimczuk and F. O. von Rohr, 'Polytypism and superconductivity in the NbS_2 system', *Dalton Transactions* **50**, 3216 (2021). Cited on page(s) 1, 15, 17, and 125

[19] I. Guillamón, H. Suderow, S. Vieira, L. Cario, P. Diener and P. Rodière, 'Superconducting Density of States and Vortex Cores of 2H-NbS_2', *Physical Review Letters* **101**, 166407 (2008). Cited on page(s) 1, 15, 17, and 125

[20] M. Leroux, M. Le Tacon, M. Calandra, L. Cario, M.-A. Méasson, P. Diener, E. Borrissenko, A. Bosak and P. Rodière, 'Anharmonic suppression of charge density waves in $2H$-NbS_2', *Physical Review B* **86**, 155125 (2012). Cited on page(s) 1, 15, 17, and 125

[21] H. Lin, W. Huang, K. Zhao, C. Lian, W. Duan, X. Chen and S.-H. Ji, 'Growth of atomically thick transition metal sulfide filmson graphene/6H-SiC(0001) by molecular beam epitaxy', *Nano Research* **11**, 4722 (2018). Cited on page(s) 1, 13, 15, 17, 18, 125, and 130

[22] E. A. Marseglia, 'Transition Metal Dichalcogenides and Their Intercalates', *International Reviews in Physical Chemistry* **3**, 177 (1983). Cited on page(s) 1, 6, 21, and 127

[23] D. Guerard and A. Herold, 'Intercalation of lithium into graphite and other carbons', *Carbon* **13**, 337 (1975). Cited on page(s) 1, 21, and 127

[24] M. S. Dresselhaus and G. Dresselhaus, 'Intercalation compounds of graphite', *Advances in Physics* **51**, 1 (2002). Cited on page(s) 1, 21, and 127

[25] R. Zhang, J. Waters, A. K. Geim and I. V. Grigorieva, 'Intercalant-independent transition temperature in superconducting black phosphorus', *Nature Communications* **8**, 15036 (2017). Cited on page(s) 1, 21, and 127

[26] N. L. Nair, E. Maniv, C. John, S. Doyle, J. Orenstein and J. G. Analytis, 'Electrical switching in a magnetically intercalated transition metal dichalcogenide', *Nature Materials* **19**, 153 (2020). Cited on page(s) 2, 24, and 127

[27] C. Riedl, C. Coletti, T. Iwasaki, A. A. Zakharov and U. Starke, 'Quasi-Free-Standing Epitaxial Graphene on SiC Obtained by Hydrogen Intercalation', *Physical Review Letters* **103**, 246804 (2009). Cited on page(s) 2, 21, and 127

[28] E. Grånäs, J. Knudsen, U. A. Schröder, T. Gerber, C. Busse, M. A. Arman, K. Schulte, J. N. Andersen and T. Michely, 'Oxygen Intercalation under Graphene on Ir(111): Energetics, Kinetics, and the Role of Graphene Edges', *ACS Nano* **6**, 9951 (2012). Cited on page(s) 2, 21, 127, 135, and 136

[29] M. Petrović, I. Šrut Rakić, S. Runte, C. Busse, J. T. Sadowski, P. Lazić, I. Pletikosić, Z.-H. Pan, M. Milun, P. Pervan, N. Atodiresei, R. Brako, D. Šokčević, T. Valla, T. Michely and M. Kralj, 'The mechanism of caesium intercalation of graphene', *Nature Communications* **4**, 2772 (2013). Cited on page(s) 2, 21, and 127

[30] M. Bosnar, V. Caciuc, N. Atodiresei, I. Lončarić and S. Blügel, ‘Se intercalation between $PtSe_2$ and the Pt surface during synthesis of $PtSe_2$ by direct selenization of Pt(111)’, *Physical Review B* **102**, 115427 (2020). Cited on page(s) 2, 21, and 127

[31] X. Zhou, X. Hu, S. Zhou, H. Song, Q. Zhang, L. Pi, L. Li, H. Li, J. Lü and T. Zhai, ‘Tunneling Diode Based on WSe_2/SnS_2 Heterostructure Incorporating High Detectivity and Responsivity’, *Advanced Materials* **30**, 1703286 (2018). Cited on page(s) 2, 24, and 127

[32] Z. Wang, D. A. Rhodes, K. Watanabe, T. Taniguchi, J. C. Hone, J. Shan and K. F. Mak, ‘Evidence of high-temperature exciton condensation in two-dimensional atomic double layers’, *Nature* **574**, 76 (2019). Cited on page(s) 2, 24, and 127

[33] M. Bode, M. Heide, K. von Bergmann, P. Ferriani, S. Heinze, G. Bihlmayer, A. Kubetzka, O. Pietzsch, S. Blügel and R. Wiesendanger, ‘Chiral magnetic order at surfaces driven by inversion asymmetry’, *Nature* **447**, 190 (2007). Cited on page(s) 2, 25, 26, 28, 37, and 128

[34] S. Mühlbauer, ‘Skyrmion lattice in a chiral magnet’, *Science* **323**, 915 (2009). Cited on page(s) 2, 25, 30, and 128

[35] S. Heinze, K. Von Bergmann, M. Menzel, J. Brede, A. Kubetzka, R. Wiesendanger, G. Bihlmayer and S. Blügel, ‘Spontaneous atomic-scale magnetic skyrmion lattice in two dimensions’, *Nature Physics* **7**, 713 (2011). Cited on page(s) 2, 25, 28, 29, and 128

[36] A. Fert, V. Cros and J. Sampaio, ‘Skyrmions on the track’, *Nature Nanotechnology* **8**, 152 (2013). Cited on page(s) 2, 26, 30, and 128

[37] F. Jonietz, S. Mulbauer, C. Pfleiderer, A. Neubauer, W. Munzer, A. Bauer, T. Adams, R. Georgii, P. Boni, R. A. Duine, K. Everschor, M. Garst and A. Rosch, ‘Spin Transfer Torques in MnSi’, *Science* 1648 (2010). Cited on page(s) 2, 28, and 30

[38] T. Schulz, R. Ritz, A. Bauer, M. Halder, M. Wagner, C. Franz, C. Pfleiderer, K. Everschor, M. Garst and A. Rosch, ‘Emergent electrodynamics of skyrmions in a chiral magnet’, *Nature Physics* **8**, 301 (2012). Cited on page(s) 2, 28, and 30

[39] N. Nagaosa and Y. Tokura, ‘Topological properties and dynamics of magnetic skyrmions’, *Nature Nanotechnology* **8**, 899 (2013). Cited on page(s) 2 and 28

[40] A. Fert, N. Reyren and V. Cros, ‘Magnetic skyrmions: Advances in physics and potential applications’, *Nature Reviews Materials* **2**, (2017). Cited on page(s) 2, 25, and 128

[41] S. Luo and L. You, ‘Skyrmion devices for memory and logic applications’, *APL Materials* **9**, (2021). Cited on page(s) 2, 25, 30, and 128

[42] S. Parkin and S. H. Yang, ‘Memory on the racetrack’, *Nature Nanotechnology* **10**, 195 (2015). Cited on page(s) 2, 25, and 128

[43] R. L. White, ‘The physical boundaries to high-density magnetic recording’, *Journal of Magnetism and Magnetic Materials* **209**, 1 (2000). Cited on page(s) 2 and 25

[44] W. A. Bhat, ‘Is a Data-Capacity Gap Inevitable in Big Data Storage?’, *Computer* **51**, 54 (2018). Cited on page(s) 2 and 25

[45] K. Litzius, I. Lemesh, B. Krüger, P. Bassirian, L. Caretta, K. Richter, F. Büttner, K. Sato, O. A. Tretiakov, J. Förster, R. M. Reeve, M. Weigand, I. Bykova, H. Stoll, G. Schütz, G. S. Beach and M. Klaüi, ‘Skyrmion Hall effect revealed by direct time-resolved X-ray microscopy’, *Nature Physics* **13**, 170 (2017). Cited on page(s) 2, 30, and 128

[46] W. Jiang, X. Zhang, G. Yu, W. Zhang, X. Wang, M. Benjamin Jungfleisch, J. E. Pearson, X. Cheng, O. Heinonen, K. L. Wang, Y. Zhou, A. Hoffmann and S. G. Te Velthuis, ‘Direct observation of the skyrmion Hall effect’, *Nature Physics* **13**, 162 (2017). Cited on page(s) 2, 30, and 128

[47] S. Huang, C. Zhou, G. Chen, H. Shen, A. K. Schmid, K. Liu and Y. Wu, 'Stabilization and current-induced motion of antiskyrmion in the presence of anisotropic Dzyaloshinskii-Moriya interaction', *Physical Review B* **96**, 144412 (2017). Cited on page(s) 2, 30, and 128

[48] A. A. Kovalev and S. Sandhoefner, 'Skyrmions and Antiskyrmions in Quasi-Two-Dimensional Magnets', *Frontiers in Physics* **6**, 98 (2018). Cited on page(s) 2, 30, and 128

[49] A. K. Nayak, V. Kumar, T. Ma, P. Werner, E. Pippel, R. Sahoo, F. Damay, U. K. Rößler, C. Felser and S. S. P. Parkin, 'Magnetic antiskyrmions above room temperature in tetragonal Heusler materials', *Nature* **548**, 561 (2017). Cited on page(s) 2, 30, and 128

[50] J. Jena, R. Stinshoff, R. Saha, A. K. Srivastava, T. Ma, H. Deniz, P. Werner, C. Felser and S. S. Parkin, 'Observation of Magnetic Antiskyrmions in the Low Magnetization Ferrimagnet $Mn_2Rh_{0.95}Ir_{0.05}Sn$', *Nano Letters* **20**, 59 (2020). Cited on page(s) 2, 30, and 128

[51] M. Hoffmann, B. Zimmermann, G. P. Müller, D. Schürhoff, N. S. Kiselev, C. Melcher and S. Blügel, 'Antiskyrmions stabilized at interfaces by anisotropic Dzyaloshinskii-Moriya interactions', *Nature Communications* **8**, 308 (2017). Cited on page(s) 2, 29, 30, and 128

[52] B. Sipos, A. F. Kusmartseva, A. Akrap, H. Berger, L. Forró and E. Tutiš, 'From Mott state to superconductivity in 1T-TaS_2', *Nature Materials* **7**, 960 (2008). Cited on page(s) 5

[53] Q. Yun, L. Li, Z. Hu, Q. Lu, B. Chen and H. Zhang, 'Layered Transition Metal Dichalcogenide-Based Nanomaterials for Electrochemical Energy Storage', *Advanced Materials* **32**, 1903826 (2020). Cited on page(s) 5, 21, and 127

[54] X. Zhang, S. Y. Teng, A. C. M. Loy, B. S. How, W. D. Leong and X. Tao, 'Transition Metal Dichalcogenides for the Application of Pollution Reduction: A Review', *Nanomaterials* **10**, (2020). Cited on page(s) 5

[55] Q. H. Wang, K. Kalantar-Zadeh, A. Kis, J. N. Coleman and M. S. Strano, 'Electronics and optoelectronics of two-dimensional transition metal dichalcogenides', *Nature Nanotechnology* **7**, 699 (2012). Cited on page(s) 5

[56] K. Thakar and S. Lodha, 'Optoelectronic and photonic devices based on transition metal dichalcogenides', **7**, 014002 (2020). Cited on page(s) 5

[57] J. Wilson and A. Yoffe, 'The transition metal dichalcogenides discussion and interpretation of the observed optical, electrical and structural properties', *Advances in Physics* **18**, 193 (1969). Cited on page(s) 5 and 6

[58] R. Lv, H. Terrones, A. L. Elías, N. Perea-López, H. R. Gutiérrez, E. Cruz-Silva, L. P. Rajukumar, M. S. Dresselhaus and M. Terrones, 'Two-dimensional transition metal dichalcogenides: Clusters, ribbons, sheets and more', *Nano Today* **10**, 559 (2015). Cited on page(s) 5

[59] A. Splendiani, L. Sun, Y. Zhang, T. Li, J. Kim, C.-Y. Chim, G. Galli and F. Wang, 'Emerging Photoluminescence in Monolayer MoS_2', *Nano Letters* **10**, 1271 (2010). Cited on page(s) 5 and 17

[60] K. F. Mak, C. Lee, J. Hone, J. Shan and T. F. Heinz, 'Atomically Thin MoS_2: A New Direct-Gap Semiconductor', *Physical Review Letters* **105**, 136805 (2010). Cited on page(s) 5, 17, and 130

[61] J. K. Ellis, M. J. Lucero and G. E. Scuseria, 'The indirect to direct band gap transition in multilayered MoS_2 as predicted by screened hybrid density functional theory', *Applied Physics Letters* **99**, 261908 (2011). Cited on page(s) 5 and 17

[62] K. Rossnagel, 'On the origin of charge-density waves in select layered transition-metal dichalcogenides', *Journal of Physics: Condensed Matter* **23**, 213001 (2011). Cited on page(s) 5, 7, 8, 12, 13, and 14

[63] J.Hall, 'Controlling Growth and Electronic Properties of Transition Metal Disulphide Layers via Molecular Beam Epitaxy', *Dissertation, University of Cologne* (2019). Cited on page(s) 6, 7, 8, 10, and 16

[64] S. Manzeli, D. Ovchinnikov, D. Pasquier, O. V. Yazyev and A. Kis, ‘2D transition metal dichalcogenides’, *Nature Reviews Materials* **2**, 17033 (2017). Cited on page(s) 6

[65] M. Chhowalla, H. S. Shin, G. Eda, L.-J. Li, K. P. Loh and H. Zhang, ‘The chemistry of two-dimensional layered transition metal dichalcogenide nanosheets’, *Nature Chemistry* **5**, 263 (2013). Cited on page(s) 6, 15, and 16

[66] R. E. Peierls, ‘Quantum theory of solids’ (Clarendon Press, 1955). Cited on page(s) 7

[67] M. D. Johannes and I. I. Mazin, ‘Fermi surface nesting and the origin of charge density waves in metals’, *Physical Review B* **77**, 165135 (2008). Cited on page(s) 7, 12, and 13

[68] F. Weber, S. Rosenkranz, J.-P. Castellan, R. Osborn, R. Hott, R. Heid, K.-P. Bohnen, T. Egami, A. H. Said and D. Reznik, ‘Extended Phonon Collapse and the Origin of the Charge-Density Wave in $2H-\mathrm{NbSe}_2$’, *Physical Review Letters* **107**, 107403 (2011). Cited on page(s) 7, 12, and 13

[69] J. Berges, E. G. Van Loon, A. Schobert, M. Rösner and T. O. Wehling, ‘Ab initio phonon self-energies and fluctuation diagnostics of phonon anomalies: Lattice instabilities from Dirac pseudospin physics in transition metal dichalcogenides’, *Physical Review B* **101**, 155107 (2020). Cited on page(s) 7 and 13

[70] S. K. Chan and V. Heine, ‘Spin density wave and soft phonon mode from nesting Fermi surfaces’, *Journal of Physics F: Metal Physics* **3**, 795 (1973). Cited on page(s) 7, 11, and 12

[71] H. Fröhlich, ‘Electrons in lattice fields’, *Advances in Physics* **3**, 325 (1954). Cited on page(s) 8

[72] G. Grüner, ‘Density Waves In Solids (1st ed.)’ (Taylor & Francis, 1994). Cited on page(s) 8, 10, and 11

[73] J. Lindhard, ‘ON THE PROPERTIES OF A GAS OF CHARGED PARTICLES’, *Dan. Mat. Fys. Medd* **28**, 8 (1954). Cited on page(s) 9

[74] J. Friedel, in ‘Electron-Phonon Interactions and Phase Transitions’, edited by T. Riste (Springer US, 1977), Pages 1–49. Cited on page(s) 9

[75] R. H. Friend and D. Jerome, ‘Periodic lattice distortions and charge density waves in one- and two-dimensional metals’, *Journal of Physics C: Solid State Physics* **12**, 1441 (1979). Cited on page(s) 9 and 10

[76] T. M. Rice and G. K. Scott, ‘New Mechanism for a Charge-Density-Wave Instability’, *Physical Review Letters* **35**, 120 (1975). Cited on page(s) 10 and 13

[77] M. Rice and S. Strässler, ‘Theory of a quasi-one-dimensional band-conductor’, *Solid State Communications* **13**, 125 (1973). Cited on page(s) 10

[78] W. Kohn, ‘Image of the Fermi Surface in the Vibration Spectrum of a Metal’, *Physical Review Letters* **2**, 393 (1959). Cited on page(s) 11

[79] P. Littlewood and V. Heine, ‘The effect of electron-electron interactions on the Peierls transition in metals with strong nesting of Fermi surfaces’, *Journal of Physics C: Solid State Physics* **14**, 2943 (2000). Cited on page(s) 11

[80] M. D. Johannes, I. I. Mazin and C. A. Howells, ‘Fermi-surface nesting and the origin of the charge-density wave in NbSe_2’, *Physical Review B* **73**, 205102 (2006). Cited on page(s) 12

[81] F. Weber, R. Hott, R. Heid, K.-P. Bohnen, S. Rosenkranz, J.-P. Castellan, R. Osborn, A. H. Said, B. M. Leu and D. Reznik, ‘Optical phonons and the soft mode in $2H$-NbSe_2’, *Physical Review B* **87**, 245111 (2013). Cited on page(s) 12 and 13

[82] P. Hofmann, M. M. Ugeda, A. Tamtögl, A. Ruckhofer, W. E. Ernst, G. Benedek, A. J. Martínez-Galera, A. Stróżecka, J. M. Gómez-Rodríguez, E. Rienks, M. F. Jensen, J. I. Pascual and J. W. Wells, ‘Strong-coupling charge density wave in a one-dimensional topological metal’, *Physical Review B* **99**, 035438 (2019). Cited on page(s) 12

[83] C. van Efferen, J. Berges, J. Hall, E. van Loon, S. Kraus, A. Schobert, T. Wekking, F. Huttmann, E. Plaar, N. Rothenbach, K. Ollefs, L. M. Arruda, N. Brookes, G. Schönhoff, K. Kummer, H. Wende, T. Wehling and T. Michely, 'A full gap above the Fermi level: the charge density wave of monolayer VS_2', *Nature Communications* **12**, 6837 (2021). Cited on page(s) 12 and 23

[84] M. D. Watson, O. J. Clark, F. Mazzola, I. Marković, V. Sunko, T. K. Kim, K. Rossnagel and P. D. C. King, 'Orbital- and k_z-Selective Hybridization of Se 4*p* and Ti 3*d* States in the Charge Density Wave Phase of $TiSe_2$', *Physical Review Letters* **122**, 076404 (2019). Cited on page(s) 12

[85] F. Weber, S. Rosenkranz, J.-P. Castellan, R. Osborn, G. Karapetrov, R. Hott, R. Heid, K.-P. Bohnen and A. Alatas, 'Electron-Phonon Coupling and the Soft Phonon Mode in $TiSe_2$', *Physical Review Letters* **107**, 266401 (2011). Cited on page(s) 12

[86] M. Holt, P. Zschack, H. Hong, M. Y. Chou and T.-C. Chiang, 'X-Ray Studies of Phonon Softening in $TiSe_2$', *Physical Review Letters* **86**, 3799 (2001). Cited on page(s) 12

[87] M. D. Watson, A. Rajan, T. Antonelli, K. Underwood, I. Marković, F. Mazzola, O. J. Clark, G.-R. Siemann, D. Biswas, A. Hunter, S. Jandura, J. Reichstetter, M. McLaren, P. L. Fèvre, G. Vinai and P. D. C. King, 'Strong-coupling charge density wave in monolayer $TiSe_2$', *2D Materials* **8**, 015004 (2020). Cited on page(s) 12

[88] J. Ying, H. Paudyal, C. Heil, X.-J. Chen, V. V. Struzhkin and E. R. Margine, 'Unusual Pressure-Induced Periodic Lattice Distortion in $SnSe_2$', *Physical Review Letters* **121**, 027003 (2018). Cited on page(s) 12

[89] Z. Shao, Z.-G. Fu, S. Li, Y. Cao, Q. Bian, H. Sun, Z. Zhang, H. Gedeon, X. Zhang, L. Liu, Z. Cheng, F. Zheng, P. Zhang and M. Pan, 'Strongly Compressed Few-Layered $SnSe_2$ Films Grown on a $SrTiO_3$ Substrate: The Coexistence of Charge Ordering and Enhanced Interfacial Superconductivity', *Nano Letters* **19**, 5304 (2019). Cited on page(s) 12

[90] S.-Z. Wang, Y.-M. Zhang, J.-Q. Fan, M.-Q. Ren, C.-L. Song, X.-C. Ma and Q.-K. Xue, 'Charge density waves and Fermi level pinning in monolayer and bilayer $SnSe_2$', *Physical Review B* **102**, 241408 (2020). Cited on page(s) 12

[91] R. V. Coleman, B. Giambattista, P. K. Hansma, A. Johnson, W. W. McNairy and C. G. Slough, 'Scanning tunnelling microscopy of charge-density waves in transition metal chalcogenides', *Advances in Physics* **37**, 559 (1988). Cited on page(s) 12

[92] C. Wang, B. Giambattista, C. G. Slough, R. V. Coleman and M. A. Subramanian, 'Energy gaps measured by scanning tunneling microscopy', *Physical Review B* **42**, 8890 (1990). Cited on page(s) 12

[93] C. Wang, 'Spectroscopy of dichalcogenides and trichalcogenides using scanning tunneling microscopy', *Journal of Vacuum Science & Technology B: Microelectronics and Nanometer Structures* **9**, 1048 (1991). Cited on page(s) 12

[94] W. C. Tonjes, V. A. Greanya, R. Liu, C. G. Olson and P. Molinié, 'Charge-density-wave mechanism in the 2*H*-$NbSe_2$ family: Angle-resolved photoemission studies', *Physical Review B* **63**, 235101 (2001). Cited on page(s) 12

[95] J. Inglesfield, 'Bonding and charge density wave phase transitions', *Physica B+C* **99**, 238 (1980). Cited on page(s) 12

[96] C. M. Varma and A. L. Simons, 'Strong-coupling theory of charge-density-wave transitions', *Physical Review Letters* **51**, 138 (1983). Cited on page(s) 12

[97] J. Dai, E. Calleja, J. Alldredge, X. Zhu, L. Li, W. Lu, Y. Sun, T. Wolf, H. Berger and K. McElroy, 'Microscopic evidence for strong periodic lattice distortion in two-dimensional charge-density wave systems', *Physical Review B* **89**, 165140 (2014). Cited on page(s) 12

[98] K. Wijayaratne, J. Zhao, C. Malliakas, D. Young Chung, M. G. Kanatzidis and U. Chatterjee, 'Spectroscopic signature of moment-dependent electron-phonon coupling in 2*H*-TaS_2', *Journal of Materials Chemistry C* **5**, 11310 (2017). Cited on page(s) 12

[99] J. Joshi, H. M. Hill, S. Chowdhury, C. D. Malliakas, F. Tavazza, U. Chatterjee, A. R. Hight Walker and P. M. Vora, 'Short-range charge density wave order in 2H-TaS_2', *Physical Review B* **99**, 245144 (2019). Cited on page(s) 12

[100] L. Fang, Y. Wang, P. Y. Zou, L. Tang, Z. Xu, H. Chen, C. Dong, L. Shan and H. H. Wen, 'Fabrication and superconductivity of Na_xTaS_2 crystals', *Physical Review B* **72**, 014534 (2005). Cited on page(s) 13

[101] X. Zhu, Y. Sun, S. Zhang, J. Wang, L. Zou, L. E. DeLong, X. Zhu, X. Luo, B. Wang, G. Li, Z. Yang and W. Song, ' Anisotropic intermediate coupling superconductivity in $Cu_{0.03}TaS_2$ ', *Journal of Physics: Condensed Matter* **21**, 145701 (2009). Cited on page(s) 13

[102] L. J. Li, X. D. Zhu, Y. P. Sun, H. C. Lei, B. S. Wang, S. B. Zhang, X. B. Zhu, Z. R. Yang and W. H. Song, 'Superconductivity of Ni-doping 2H-TaS_2', *Physica C: Superconductivity and its Applications* **470**, 313 (2010). Cited on page(s) 13

[103] H. Liu, S. Huangfu, X. Zhang, H. Lin and A. Schilling, 'Superconductivity and charge density wave formation in lithium-intercalated 2H-TaS_2', *Physical Review B* **104**, 065411 (2021). Cited on page(s) 13

[104] D. C. Freitas, P. Rodière, M. R. Osorio, E. Navarro-Moratalla, N. M. Nemes, V. G. Tissen, L. Cario, E. Coronado, M. García-Hernández, S. Vieira, M. Núñez Regueiro and H. Suderow, 'Strong enhancement of superconductivity at high pressures within the charge-density-wave states of $2H-TaS_2$ and $2H-TaSe_2$', *Physical Review B* **93**, 184512 (2016). Cited on page(s) 13

[105] K. Zhang, H. Jiang, J. Yang, J. Zhang, Z. Zeng, X. Chen and F. Su, 'Pressure effects on the lattice vibrations and ultrafast photocarrier dynamics in 2H-TaS_2', *Applied Physics Letters* **117**, (2020). Cited on page(s) 13

[106] X. M. Zhao, K. Zhang, Z. Y. Cao, Z. W. Zhao, V. V. Struzhkin, A. F. Goncharov, H. K. Wang, A. G. Gavriliuk, H. K. Mao and X. J. Chen, 'Pressure tuning of the charge density wave and superconductivity in 2H-TaS_2', *Physical Review B* **101**, 134506 (2020). Cited on page(s) 13

[107] J. Hall, N. Ehlen, J. Berges, E. van Loon, C. van Efferen, C. Murray, M. Rösner, J. Li, B. V. Senkovskiy, M. Hell, M. Rolf, T. Heider, M. C. Asensio, J. Avila, L. Plucinski, T. Wehling, A. Grüneis and T. Michely, 'Environmental Control of Charge Density Wave Order in Monolayer 2H-TaS_2', *ACS Nano* **13**, 10210 (2019). Cited on page(s) 13 and 130

[108] C. E. Sanders, M. Dendzik, A. S. Ngankeu, A. Eich, A. Bruix, M. Bianchi, J. A. Miwa, B. Hammer, A. A. Khajetoorians and P. Hofmann, 'Crystalline and electronic structure of single-layer TaS_2', *Physical Review B* **94**, 081404 (2016). Cited on page(s) 13

[109] O. R. Albertini, A. Y. Liu and M. Calandra, 'Effect of electron doping on lattice instabilities in single-layer 1H-TaS_2', *Physical Review B* **95**, 235121 (2017). Cited on page(s) 13

[110] H. M. Lefcochilos-Fogelquist, O. R. Albertini and A. Y. Liu, 'Substrate-induced suppression of charge density wave phase in monolayer 1H-TaS_2 on Au(111)', *Physical Review B* **99**, 174113 (2019). Cited on page(s) 13

[111] B. Shao, A. Eich, C. Sanders, A. S. Ngankeu, M. Bianchi, P. Hofmann, A. A. Khajetoorians and T. O. Wehling, 'Pseudodoping of a metallic two-dimensional material by the supporting substrate', *Nature Communications* **10**, 180 (2019). Cited on page(s) 13 and 24

[112] D. E. Moncton, J. D. Axe and F. J. DiSalvo, 'Neutron scattering study of the charge-density wave transitions in $2H - TaSe_2$ and $2H - NbSe_2$', *Physical Review B* **16**, 801 (1977). Cited on page(s) 13

[113] M. Naito and S. Tanaka, 'Electrical Transport Properties in 2H-NbS_2 , -$NbSe_2$, -TaS_2 and -$TaSe_2$', *Journal of the Physical Society of Japan* **51**, 219 (1982). Cited on page(s) 13

[114] Y. W. Li, J. Jiang, H. F. Yang, D. Prabhakaran, Z. K. Liu, L. X. Yang and Y. L. Chen, 'Folded superstructure and degeneracy-enhanced band gap in the weak-coupling charge density wave system $2H - TaSe_2$', *Physical Review B* **97**, 115118 (2018). Cited on page(s) 13

[115] T. Kumakura, H. Tan, T. Handa, M. Morishita and H. Fukuyama, 'Charge density waves and superconductivity in 2H-$TaSe_2$', *Czechoslovak Journal of Physics* **46**, 2611 (1996). Cited on page(s) 13

[116] A. H. Castro Neto, 'Charge density wave, superconductivity, and anomalous metallic behavior in 2D transition metal dichalcogenides', *Physical Review Letters* **86**, 4382 (2001). Cited on page(s) 13

[117] H. Ryu, Y. Chen, H. Kim, H. Z. Tsai, S. Tang, J. Jiang, F. Liou, S. Kahn, C. Jia, A. A. Omrani, J. H. Shim, Z. Hussain, Z. X. Shen, K. Kim, B. I. Min, C. Hwang, M. F. Crommie and S. K. Mo, 'Persistent Charge-Density-Wave Order in Single-Layer $TaSe_2$', *Nano Letters* **18**, 689 (2018). Cited on page(s) 13

[118] J. Shi, X. Chen, L. Zhao, Y. Gong, M. Hong, Y. Huan, Z. Zhang, P. Yang, Y. Li, Q. Zhang, Q. Zhang, L. Gu, H. Chen, J. Wang, S. Deng, N. Xu and Y. Zhang, 'Chemical Vapor Deposition Grown Wafer-Scale 2D Tantalum Diselenide with Robust Charge-Density-Wave Order', *Advanced Materials* **30**, 1804616 (2018). Cited on page(s) 13

[119] C. S. Lian, C. Heil, X. Liu, C. Si, F. Giustino and W. Duan, 'Coexistence of Superconductivity with Enhanced Charge Density Wave Order in the Two-Dimensional Limit of $TaSe_2$', *Journal of Physical Chemistry Letters* **10**, 4076 (2019). Cited on page(s) 13

[120] H. N. S. Lee, H. McKinzie, D. S. Tannhauser and A. Wold, 'The Low-Temperature Transport Properties of NbS_2', *Journal of Applied Physics* **40**, 602 (1969). Cited on page(s) 13

[121] B. Giambattista, A. Johnson, R. V. Coleman, B. Drake and P. K. Hansma, 'Charge-density waves observed at 4.2 K by scanning-tunneling microscopy', *Physical Review B* **37**, 2741 (1988). Cited on page(s) 13

[122] C. J. Arguello, S. P. Chockalingam, E. P. Rosenthal, L. Zhao, C. Gutiérrez, J. H. Kang, W. C. Chung, R. M. Fernandes, S. Jia, A. J. Millis, R. J. Cava and A. N. Pasupathy, 'Visualizing the charge density wave transition in $2H$-$NbSe_2$ in real space', *Physical Review B* **89**, 235115 (2014). Cited on page(s) 13

[123] S. V. Borisenko, A. A. Kordyuk, V. B. Zabolotnyy, D. S. Inosov, D. Evtushinsky, B. Büchner, A. N. Yaresko, A. Varykhalov, R. Follath, W. Eberhardt, L. Patthey and H. Berger, 'Two Energy Gaps and Fermi-Surface "Arcs" in $NbSe_2$', *Physical Review Letters* **102**, 166402 (2009). Cited on page(s) 13

[124] F. Flicker and J. van Wezel, 'Charge order from orbital-dependent coupling evidenced by NbS_2', *Nature Communications* **6**, 7034 (2015). Cited on page(s) 13

[125] M. Leroux, I. Errea, M. Le Tacon, S.-M. Souliou, G. Garbarino, L. Cario, A. Bosak, F. Mauri, M. Calandra and P. Rodière, 'Strong anharmonicity induces quantum melting of charge density wave in $2H - NbSe_2$ under pressure', *Physical Review B* **92**, 140303 (2015). Cited on page(s) 13

[126] F. Weber, R. Hott, R. Heid, L. L. Lev, M. Caputo, T. Schmitt and V. N. Strocov, 'Three-dimensional Fermi surface of $2H - \mathrm{NbSe}_2$: Implications for the mechanism of charge density waves', *Physical Review B* **97**, 235122 (2018). Cited on page(s) 13 and 14

[127] E. Revolinsky, E. Lautenschlager and C. Armitage, 'Layer structure superconductor', *Solid State Communications* **1**, 59 (1963). Cited on page(s) 13

[128] M. M. Ugeda, A. J. Bradley, Y. Zhang, S. Onishi, Y. Chen, W. Ruan, C. Ojeda-Aristizabal, H. Ryu, M. T. Edmonds, H.-Z. Tsai, A. Riss, S.-K. Mo, D. Lee, A. Zettl, Z. Hussain, Z.-X. Shen and M. F. Crommie, ‘Characterization of collective ground states in single-layer NbS_2’, *Nature Physics* **12**, 92 (2016). Cited on page(s) 14, 125, and 126

[129] J. Á. Silva-Guillén, P. Ordejón, F. Guinea and E. Canadell, ‘Electronic structure of 2H-$NbSe_2$ single-layers in the CDW state’, *2D Materials* **3**, 035028 (2016). Cited on page(s) 14

[130] F. Zheng and J. Feng, ‘Electron-phonon coupling and the coexistence of superconductivity and charge-density wave in monolayer $NbSe_2$’, *Physical Review B* **99**, 161119 (2019). Cited on page(s) 14

[131] X. Xi, L. Zhao, Z. Wang, H. Berger, L. Forró, J. Shan and K. F. Mak, ‘Strongly enhanced charge-density-wave order in monolayer NbS_2’, *Nature Nanotechnology* **10**, 765 (2015). Cited on page(s) 14

[132] D. Lin, S. Li, J. Wen, H. Berger, L. Forró, H. Zhou, S. Jia, T. Taniguchi, K. Watanabe, X. Xi and M. S. Bahramy, ‘Patterns and driving forces of dimensionality-dependent charge density waves in 2H-type transition metal dichalcogenides’, *Nature Communications* **11**, 2406 (2020). Cited on page(s) 14

[133] R. Bianco, L. Monacelli, M. Calandra, F. Mauri and I. Errea, ‘Weak Dimensionality Dependence and Dominant Role of Ionic Fluctuations in the Charge-Density-Wave Transition of $NbSe_2$’, *Physical Review Letters* **125**, 106101 (2020). Cited on page(s) 14

[134] R. F. Frindt, ‘Superconductivity in Ultrathin $NbSe_2$ Layers’, *Physical Review Letters* **28**, 299 (1972). Cited on page(s) 14

[135] Y. Xing, K. Zhao, P. Shan, F. Zheng, Y. Zhang, H. Fu, Y. Liu, M. Tian, C. Xi, H. Liu, J. Feng, X. Lin, S. Ji, X. Chen, Q.-K. Xue and J. Wang, ‘Ising Superconductivity and Quantum Phase Transition in Macro-Size Monolayer NbS_2’, *Nano Letters* **17**, 6802 (2017). Cited on page(s) 14

[136] F. Zheng, Z. Zhou, X. Liu and J. Feng, ‘First-principles study of charge and magnetic ordering in monolayer $NbSe_2$’, *Physical Review B* **97**, 081101 (2018). Cited on page(s) 14

[137] C.-S. Lian, C. Si and W. Duan, ‘Unveiling Charge-Density Wave, Superconductivity, and Their Competitive Nature in Two-Dimensional NbS_2’, *Nano Letters* **18**, 2924 (2018). Cited on page(s) 14

[138] F. Jellinek, G. Brauer and H. Müller, ‘Molybdenum and Niobium Sulphides’, *Nature* **185**, 376 (1960). Cited on page(s) 15, 22, and 23

[139] C. Heil, M. Schlipf and F. Giustino, ‘Quasiparticle *GW* band structures and Fermi surfaces of bulk and monolayer NbS_2’, *Physical Review B* **98**, 075120 (2018). Cited on page(s) 15, 16, and 17

[140] R. Bianco, I. Errea, L. Monacelli, M. Calandra and F. Mauri, ‘Quantum Enhancement of Charge Density Wave in NbS_2 in the Two-Dimensional Limit’, *Nano Letters* **19**, 3098 (2019). Cited on page(s) 15 and 17

[141] C. Heil, S. Poncé, H. Lambert, M. Schlipf, E. R. Margine and F. Giustino, ‘Origin of Superconductivity and Latent Charge Density Wave in NbS_2’, *Physical Review Letters* **119**, 087003 (2017). Cited on page(s) 15 and 17

[142] E. G. C. P. van Loon, M. Rösner, G. Schönhoff, M. I. Katsnelson and T. O. Wehling, ‘Competing Coulomb and electron–phonon interactions in NbS_2’, *npj Quantum Materials* **3**, 32 (2018). Cited on page(s) 15, 17, 20, 128, 132, 134, 137, 138, 146, and 147

[143] X. Wang, J. Lin, Y. Zhu, C. Luo, K. Suenaga, C. Cai and L. Xie, ‘Chemical vapor deposition of trigonal prismatic NbS_2 monolayers and 3R-polytype few-layers’, *Nanoscale* **9**, 16607 (2017). Cited on page(s) 15 and 19

[144] Z. Wang, C.-Y. Cheon, M. Tripathi, G. M. Marega, Y. Zhao, H. G. Ji, M. Macha, A. Radenovic and A. Kis, ‘Superconducting 2D NbS$_2$ Grown Epitaxially by Chemical Vapor Deposition’, *ACS Nano* **15**, 18403 (2021). Cited on page(s) 15, 18, 19, and 125

[145] E. Martino, C. Putzke, M. König, P. J. W. Moll, H. Berger, D. LeBoeuf, M. Leroux, C. Proust, A. Akrap, H. Kirmse, C. Koch, S. Zhang, Q. Wu, O. V. Yazyev, L. Forró and K. Semeniuk, ‘Unidirectional Kondo scattering in layered NbS$_2$’, *npj 2D Materials and Applications* **5**, 86 (2021). Cited on page(s) 15 and 23

[146] M. Leroux, L. Cario, A. Bosak and P. Rodière, ‘Traces of charge density waves in NbS$_2$’, *Physical Review B* **97**, 195140 (2018). Cited on page(s) 15 and 17

[147] C. J. Carmalt, T. D. Manning, I. P. Parkin, E. S. Peters and A. L. Hector, ‘Formation of a new (1T) trigonal NbS$_2$ polytype via atmospheric pressure chemical vapour deposition’, *Journal of Materials Chemistry* **14**, 290 (2004). Cited on page(s) 15

[148] C. Wen, Y. Xie, Y. Wu, S. Shen, P. Kong, H. Lian, J. Li, H. Xing and S. Yan, ‘Impurity-pinned incommensurate charge density wave and local phonon excitations in $2H-\mathrm{NbS}_2$’, *Physical Review B* **101**, 241404 (2020). Cited on page(s) 17 and 126

[149] C. Tresca and M. Calandra, ‘Charge density wave and spin 1/2 insulating state in single layer 1T-NbS$_2$’, *2D Materials* **6**, 035041 (2019). Cited on page(s) 17

[150] W. Wang, B. Wang, Z. Gao, G. Tang, W. Lei, X. Zheng, H. Li, X. Ming and C. Autieri, ‘Charge density wave instability and pressure-induced superconductivity in bulk $1T-\mathrm{NbS}_2$’, *Physical Review B* **102**, 155115 (2020). Cited on page(s) 17

[151] R.-M. Stan, S. K. Mahatha, M. Bianchi, C. E. Sanders, D. Curcio, P. Hofmann and J. A. Miwa, ‘Epitaxial single-layer NbS$_2$ on Au(111): Synthesis, structure, and electronic properties’, *Physical Review Materials* **3**, 044003 (2019). Cited on page(s) 18, 19, 20, and 130

[152] F. Güller, V. L. Vildosola and A. M. Llois, ‘Spin density wave instabilities in the NbS$_2$ monolayer’, *Physical Review B* **93**, 094434 (2016). Cited on page(s) 18, 23, 128, and 135

[153] Y. Zhou, Z. Wang, P. Yang, X. Zu, L. Yang, X. Sun and F. Gao, ‘Tensile Strain Switched Ferromagnetism in Layered NbS$_2$ and NbS$_2$’, *ACS Nano* **6**, 9727 (2012). Cited on page(s) 18, 23, and 128

[154] Y. Xu, X. Liu and W. Guo, ‘Tensile strain induced switching of magnetic states in NbS$_2$ and NbS$_2$ single layers’, *Nanoscale* **6**, 12929 (2014). Cited on page(s) 18, 23, and 128

[155] R. Yan, G. Khalsa, B. T. Schaefer, A. Jarjour, S. Rouvimov, K. C. Nowack, H. G. Xing and D. Jena, ‘Thickness dependence of superconductivity in ultrathin NbS$_2$’, *Applied Physics Express* **12**, 023008 (2019). Cited on page(s) 18, 19, and 125

[156] A. Devarakonda, H. Inoue, S. Fang, C. Ozsoy-Keskinbora, T. Suzuki, M. Kriener, E. K. L. Fu, D. C. Bell and J. G. Checkelsky, ‘Clean 2D superconductivity in a bulk van der Waals superlattice’, *Science* **370**, 231 (2020). Cited on page(s) 18

[157] W. Bai, P. Li, S. Ju, C. Xiao, H. Shi, S. Wang, S. Qin, Z. Sun and Y. Xie, ‘Monolayer Behavior of NbS$_2$ in Natural van der Waals Heterostructures’, *The Journal of Physical Chemistry Letters* **9**, 6421 (2018). Cited on page(s) 18

[158] R. Dong and I. Kuljanishvili, ‘Review Article: Progress in fabrication of transition metal dichalcogenides heterostructure systems’, *Journal of Vacuum Science & Technology B* **35**, 030803 (2017). Cited on page(s) 18

[159] J. R. Brent, N. Savjani and P. O’Brien, ‘Synthetic approaches to two-dimensional transition metal dichalcogenide nanosheets’, *Progress in Materials Science* **89**, 411 (2017). Cited on page(s) 18

[160] M. Wu, Y. Xiao, Y. Zeng, Y. Zhou, X. Zeng, L. Zhang and W. Liao, ‘Synthesis of two-dimensional transition metal dichalcogenides for electronics and optoelectronics’, *InfoMat* **3**, 362 (2021). Cited on page(s) 18

[161] K. S. Novoselov, D. Jiang, F. Schedin, T. J. Booth, V. V. Khotkevich, S. V. Morozov and A. K. Geim, 'Two-dimensional atomic crystals', *Proceedings of the National Academy of Sciences* **102**, 10451 (2005). Cited on page(s) 18

[162] C. Huo, Z. Yan, X. Song and H. Zeng, '2D materials via liquid exfoliation: a review on fabrication and applications', *Science Bulletin* **60**, 1994 (2015). Cited on page(s) 18

[163] C.-X. Hu, Y. Shin, O. Read and C. Casiraghi, 'Dispersant-assisted liquid-phase exfoliation of 2D materials beyond graphene', *Nanoscale* **13**, 460 (2021). Cited on page(s) 18

[164] A. Raza, J. Z. Hassan, M. Ikram, S. Ali, U. Farooq, Q. Khan and M. Maqbool, 'Advances in Liquid-Phase and Intercalation Exfoliations of Transition Metal Dichalcogenides to Produce 2D Framework', *Advanced Materials Interfaces* **8**, 2002205 (2021). Cited on page(s) 18

[165] J. Si, Q. Zheng, H. Chen, C. Lei, Y. Suo, B. Yang, Z. Zhang, Z. Li, L. Lei, Y. Hou and K. K. Ostrikov, 'Scalable Production of Few-Layer Niobium Disulfide Nanosheets via Electrochemical Exfoliation for Energy-Efficient Hydrogen Evolution Reaction', *ACS Applied Materials & Interfaces* **11**, 13205 (2019). Cited on page(s) 19

[166] Z. Cai, B. Liu, X. Zou and H.-M. Cheng, 'Chemical Vapor Deposition Growth and Applications of Two-Dimensional Materials and Their Heterostructures', *Chemical Reviews* **118**, 6091 (2018). Cited on page(s) 19

[167] S. Najmaei, M. Amani, M. L. Chin, Z. Liu, A. G. Birdwell, T. P. O'Regan, P. M. Ajayan, M. Dubey and J. Lou, 'Electrical Transport Properties of Polycrystalline Monolayer Molybdenum Disulfide', *ACS Nano* **8**, 7930 (2014). Cited on page(s) 19

[168] A. M. van der Zande, P. Y. Huang, D. A. Chenet, T. C. Berkelbach, Y. You, G.-H. Lee, T. F. Heinz, D. R. Reichman, D. A. Muller and J. C. Hone, 'Grains and grain boundaries in highly crystalline monolayer molybdenum disulphide', *Nature Materials* **12**, 554 (2013). Cited on page(s) 19

[169] X. Ling, Y.-H. Lee, Y. Lin, W. Fang, L. Yu, M. S. Dresselhaus and J. Kong, 'Role of the Seeding Promoter in MoS_2 Growth by Chemical Vapor Deposition', *Nano Letters* **14**, 464 (2014). Cited on page(s) 19

[170] A. Pisoni, J. Jacimovic, R. Gaál, B. Náfrádi, H. Berger, Z. Révay and L. Forró, 'Anisotropic transport properties of tungsten disulfide', *Scripta Materialia* **114**, 48 (2016). Cited on page(s) 19

[171] L. Tang, T. Li, Y. Luo, S. Feng, Z. Cai, H. Zhang, B. Liu and H.-M. Cheng, 'Vertical Chemical Vapor Deposition Growth of Highly Uniform 2D Transition Metal Dichalcogenides', *ACS Nano* **14**, 4646 (2020). Cited on page(s) 19

[172] S. Zhao, T. Hotta, T. Koretsune, K. Watanabe, T. Taniguchi, K. Sugawara, T. Takahashi, H. Shinohara and R. Kitaura, 'Two-dimensional metallic NbS_2: growth, optical identification and transport properties', *2D Materials* **3**, 025027 (2016). Cited on page(s) 19

[173] Y. Zhang, L. Yin, J. Chu, T. A. Shifa, J. Xia, F. Wang, Y. Wen, X. Zhan, Z. Wang and J. He, 'Edge-Epitaxial Growth of 2D NbS_2-WS_2 Lateral Metal-Semiconductor Heterostructures', *Advanced Materials* **30**, 1803665 (2018). Cited on page(s) 19

[174] Q. Lv, X. Qin and R. Lv, 'Controllable Growth of Few-Layer Niobium Disulfide by Atmospheric Pressure Chemical Vapor Deposition for Molecular Sensing', *Frontiers in Materials* **6**, 279 (2019). Cited on page(s) 19

[175] T. Yanase, S. Watanabe, M. Weng, M. Wakeshima, Y. Hinatsu, T. Nagahama and T. Shimada, 'Chemical Vapor Deposition of NbS_2 from a Chloride Source with H_2 Flow: Orientation Control of Ultrathin Crystals Directly Grown on SiO_2/Si Substrate and Charge Density Wave Transition', *Crystal Growth & Design* **16**, 4467 (2016). Cited on page(s) 19

[176] B. A. Joyce, 'Molecular beam epitaxy', *Reports on Progress in Physics* **48**, 1637 (1985). Cited on page(s) 19

[177] S. J. McDonnell and R. M. Wallace, 'Atomically-thin layered films for device applications based upon 2D TMDC materials', *Thin Solid Films* **616**, 482 (2016). Cited on page(s) 19 and 20

[178] A. Koma, K. Sunouchi and T. Miyajima, 'Fabrication and characterization of heterostructures with subnanometer thickness', *Microelectronic Engineering* **2**, 129 (1984), special Issue on Nanometer Structure Electronics. Cited on page(s) 20

[179] L. A. Walsh and C. L. Hinkle, 'van der Waals epitaxy: 2D materials and topological insulators', *Applied Materials Today* **9**, 504 (2017). Cited on page(s) 20

[180] J. Hall, B. Pielić, C. Murray, W. Jolie, T. Wekking, C. Busse, M. Kralj and T. Michely, 'Molecular beam epitaxy of quasi-freestanding transition metal disulphide monolayers on van der Waals substrates: a growth study', *2D Materials* **5**, 025005 (2018). Cited on page(s) 20 and 144

[181] M. S. Stark, K. L. Kuntz, S. J. Martens and S. C. Warren, 'Intercalation of Layered Materials from Bulk to 2D', *Advanced Materials* **31**, 1808213 (2019). Cited on page(s) 21

[182] J. Yao, K. J. Koski, W. Luo, J. J. Cha, L. Hu, D. Kong, V. K. Narasimhan, K. Huo and Y. Cui, 'Optical transmission enhacement through chemically tuned two-dimensional bismuth chalcogenide nanoplates', *Nature Communications* **5**, 5670 (2014). Cited on page(s) 21

[183] Y. Guo, J. Zhou, Y. Liu, X. Zhou, F. Yao, C. Tan, J. Wu, L. Lin, K. Liu, Z. Liu and H. Peng, 'Chemical Intercalation of Topological Insulator Grid Nanostructures for High-Performance Transparent Electrodes', *Advanced Materials* **29**, 1703424 (2017). Cited on page(s) 21

[184] M. S. Whittingham, 'Electrical Energy Storage and Intercalation Chemistry', *Science* **192**, 1126 (1976). Cited on page(s) 21 and 127

[185] J. Asenbauer, T. Eisenmann, M. Kuenzel, A. Kazzazi, Z. Chen and D. Bresser, 'The success story of graphite as a lithium-ion anode material - fundamentals, remaining challenges, and recent developments including silicon (oxide) composites', *Sustainable Energy Fuels* **4**, 5387 (2020). Cited on page(s) 21 and 127

[186] Y. Yu, F. Yang, X. F. Lu, Y. J. Yan, Y.-H. Cho, L. Ma, X. Niu, S. Kim, Y.-W. Son, D. Feng, S. Li, S.-W. Cheong, X. H. Chen and Y. Zhang, 'Gate-tunable phase transitions in thin flakes of 1T-TaS_2', *Nature Nanotechnology* **10**, 270 (2015). Cited on page(s) 21

[187] X. Zhao, P. Song, C. Wang, A. C. Riis-Jensen, W. Fu, Y. Deng, D. Wan, L. Kang, S. Ning, J. Dan, T. Venkatesan, Z. Liu, W. Zhou, K. S. Thygesen, X. Luo, S. J. Pennycook and K. P. Loh, 'Engineering covalently bonded 2D layered materials by self-intercalation', *Nature* **581**, 171 (2020). Cited on page(s) 21 and 22

[188] M. Rajapakse, B. Karki, U. O. Abu, S. Pishgar, M. R. K. Musa, S. M. S. Riyadh, M. Yu, G. Sumanasekera and J. B. Jasinski, 'Intercalation as a versatile tool for fabrication, property tuning, and phase transitions in 2D materials', *npj 2D Materials and Applications* **5**, 30 (2021). Cited on page(s) 21

[189] J. Zhou, Z. Lin, H. Ren, X. Duan, I. Shakir, Y. Huang and X. Duan, 'Layered Intercalation Materials', *Advanced Materials* **33**, 2004557 (2021). Cited on page(s) 21

[190] R. H. Friend, A. R. Beal and A. D. Yoffe, 'Electrical and magnetic properties of some first row transition metal intercalates of niobium disulphide', *The Philosophical Magazine: A Journal of Theoretical Experimental and Applied Physics* **35**, 1269 (1977). Cited on page(s) 21, 22, 23, 24, and 128

[191] R. Friend and A. Yoffe, 'Electronic properties of intercalation complexes of the transition metal dichalcogenides', *Advances in Physics* **36**, 1 (1987). Cited on page(s) 21

[192] B. Van Laar, H. Rietveld and D. Ijdo, 'Magnetic and crystallographic structures of Me_xNbS_2 and Me_xTaS_2', *Journal of Solid State Chemistry* **3**, 154 (1971). Cited on page(s) 21, 23, 24, and 128

[193] M. Mortazavi, C. Wang, J. Deng, V. B. Shenoy and N. V. Medhekar, ‘Ab initio characterization of layered MoS_2 as anode for sodium-ion batteries’, *Journal of Power Sources* **268**, 279 (2014). Cited on page(s) 21 and 22

[194] J. Rouxel, in ‘Intercalated Layered Materials’, edited by F. Lévy (Springer Netherlands, 1979), Pages 201–250. Cited on page(s) 21 and 22

[195] J. Yang, A. R. Mohmad, Y. Wang, R. Fullon, X. Song, F. Zhao, I. Bozkurt, M. Augustin, E. J. G. Santos, H. S. Shin, W. Zhang, D. Voiry, H. Y. Jeong and M. Chhowalla, ‘Ultrahigh-current-density niobium disulfide catalysts for hydrogen evolution’, *Nature Materials* **18**, 1309 (2019). Cited on page(s) 22 and 23

[196] S. Kim, J. Maassen, J. Lee, S. M. Kim, G. Han, J. Kwon, S. Hong, J. Park, N. Liu, Y. C. Park, I. Omkaram, J.-S. Rhyee, Y. K. Hong and Y. Yoon, ‘Interstitial Mo-Assisted Photovoltaic Effect in Multilayer $MoSe_2$ Phototransistors’, *Advanced Materials* **30**, 1705542 (2018). Cited on page(s) 22

[197] M. Zhang, C. Zhang, Y. You, H. Xie, H. Chi, Y. Sun, W. Liu, X. Su, Y. Yan, X. Tang and C. Uher, ‘Electron Density Optimization and the Anisotropic Thermoelectric Properties of Ti Self-Intercalated $Ti_{1+x}S_2$ Compounds’, *ACS Applied Materials & Interfaces* **10**, 32344 (2018). Cited on page(s) 22

[198] K. Lasek, P. M. Coelho, K. Zberecki, Y. Xin, S. K. Kolekar, J. Li and M. Batzill, ‘Molecular Beam Epitaxy of Transition Metal (Ti-, V-, and Cr-) Tellurides: From Monolayer Ditellurides to Multilayer Self-Intercalation Compounds’, *ACS Nano* **14**, 8473 (2020). Cited on page(s) 22

[199] Y. Yao, Y. Wen, F. Wang, N. Li, J. Wang, Y. Wang, J. Yang, X. Zhan, Z. Wang and J. He, ‘Self-intercalated two-dimensional magnetic semiconductor $V_8(S_{1-x}Se_x)_{15}$’, *Applied Physics Letters* **118**, 221903 (2021). Cited on page(s) 22 and 23

[200] A. Jain, S. P. Ong, G. Hautier, W. Chen, W. D. Richards, S. Dacek, S. Cholia, D. Gunter, D. Skinner, G. Ceder and K. a. Persson, ‘The Materials Project: A materials genome approach to accelerating materials innovation’, *APL Materials* **1**, 011002 (2013). Cited on page(s) 23

[201] F. Kadijk and F. Jellinek, ‘The system niobium-sulfur’, *Journal of the Less Common Metals* **19**, 421 (1969). Cited on page(s) 23 and 127

[202] D. Bansal, J. L. Niedziela, S. Calder, T. Lanigan-Atkins, R. Rawl, A. H. Said, D. L. Abernathy, A. I. Kolesnikov, H. Zhou and O. Delaire, ‘Magnetically driven phonon instability enables the metal–insulator transition in h-FeS’, *Nature Physics* **16**, 669 (2020). Cited on page(s) 23

[203] S. Tongay, S. S. Varnoosfaderani, B. R. Appleton, J. Wu and A. F. Hebard, ‘Magnetic properties of MoS_2: Existence of ferromagnetism’, *Applied Physics Letters* **101**, 123105 (2012). Cited on page(s) 23

[204] Z. Yang, D. Gao, J. Zhang, Q. Xu, S. Shi, K. Tao and D. Xue, ‘Realization of high Curie temperature ferromagnetism in atomically thin MoS_2 and WS_2 nanosheets with uniform and flower-like morphology’, *Nanoscale* **7**, 650 (2015). Cited on page(s) 23

[205] B. Liu, L.-J. Wu, Y.-Q. Zhao, L.-Z. Wang and M.-Q. Cai, ‘A first-principles study of magnetic variation via doping vacancy in monolayer’, *Journal of Magnetism and Magnetic Materials* **420**, 218 (2016). Cited on page(s) 23

[206] M. A. Khan, M. Erementchouk, J. Hendrickson and M. N. Leuenberger, ‘Electronic and optical properties of vacancy defects in single-layer transition metal dichalcogenides’, *Physical Review B* **95**, 245435 (2017). Cited on page(s) 23

[207] S.-C. Lu and J.-P. Leburton, ‘Electronic structures of defects and magnetic impurities in MoS_2 monolayers’, *Nanoscale Research Letters* **9**, 676 (2014). Cited on page(s) 23

[208] P. M. Coelho, H.-P. Komsa, K. Lasek, V. Kalappattil, J. Karthikeyan, M.-H. Phan, A. V. Krasheninnikov and M. Batzill, ‘Room-Temperature Ferromagnetism in $MoTe_2$ by Post-Growth Incorporation of Vanadium Impurities’, *Advanced Electronic Materials* **5**, 1900044 (2019). Cited on page(s) 23

[209] Y. Ma, Y. Dai, M. Guo, C. Niu, Y. Zhu and B. Huang, 'Evidence of the Existence of Magnetism in Pristine VX_2 Monolayers (X = S, Se) and Their Strain-Induced Tunable Magnetic Properties', *ACS Nano* **6**, 1695 (2012). Cited on page(s) 23

[210] D. Gao, Q. Xue, X. Mao, W. Wang, Q. Xu and D. Xue, 'Ferromagnetism in ultrathin nanosheets', *Journal of Materials Chemistry C* **1**, 5909 (2013). Cited on page(s) 23

[211] M. Zhong, Y. Li, Q. Xia, X. Meng, F. Wu and J. Li, 'Ferromagnetism in nanostructures: Nanoflowers versus ultrathin nanosheets', *Materials Letters* **124**, 282 (2014). Cited on page(s) 23

[212] M. Bonilla, S. Kolekar, Y. Ma, H. C. Diaz, V. Kalappattil, R. Das, T. Eggers, H. R. Gutierrez, M.-H. Phan and M. Batzill, 'Strong room-temperature ferromagnetism in VSe_2 monolayers on van der Waals substrates', *Nature Nanotechnology* **13**, 289 (2018). Cited on page(s) 23

[213] C. van Bruggen and C. Haas, 'Magnetic susceptibility and electrical properties of VSe_2 single crystals', *Solid State Communications* **20**, 251 (1976). Cited on page(s) 23

[214] S. Memarzadeh, M. R. Roknabadi, M. Modarresi, A. Mogulkoc and A. N. Rudenko, 'Role of charge doping and strain in the stabilization of in-plane ferromagnetism in monolayer VSe_2 at room temperature', *2D Materials* **8**, 035022 (2021). Cited on page(s) 23

[215] A. O. Fumega, M. Gobbi, P. Dreher, W. Wan, C. González-Orellana, M. Peña-Díaz, C. Rogero, J. Herrero-Martín, P. Gargiani, M. Ilyn, M. M. Ugeda, V. Pardo and S. Blanco-Canosa, 'Absence of Ferromagnetism in VSe_2 Caused by Its Charge Density Wave Phase', *The Journal of Physical Chemistry C* **123**, 27802 (2019). Cited on page(s) 23

[216] P. M. Coelho, K. Nguyen Cong, M. Bonilla, S. Kolekar, M.-H. Phan, J. Avila, M. C. Asensio, I. I. Oleynik and M. Batzill, 'Charge Density Wave State Suppresses Ferromagnetic Ordering in VSe_2 Monolayers', *The Journal of Physical Chemistry C* **123**, 14089 (2019). Cited on page(s) 23

[217] P. K. J. Wong, W. Zhang, F. Bussolotti, X. Yin, T. S. Herng, L. Zhang, Y. L. Huang, G. Vinai, S. Krishnamurthi, D. W. Bukhvalov, Y. J. Zheng, R. Chua, A. T. N'Diaye, S. A. Morton, C.-Y. Yang, K.-H. Ou Yang, P. Torelli, W. Chen, K. E. J. Goh, J. Ding, M.-T. Lin, G. Brocks, M. P. de Jong, A. H. Castro Neto and A. T. S. Wee, 'Evidence of Spin Frustration in a Vanadium Diselenide Monolayer Magnet', *Advanced Materials* **31**, 1901185 (2019). Cited on page(s) 23

[218] E. B. Isaacs and C. A. Marianetti, 'Electronic correlations in monolayer VS_2', *Physical Review B* **94**, 035120 (2016). Cited on page(s) 23

[219] F. Hulliger and E. Pobitschka, 'On the magnetic behavior of new 2H-NbS_2-type derivatives', *Journal of Solid State Chemistry* **1**, 117 (1970). Cited on page(s) 23

[220] S. S. P. Parkin and R. H. Friend, '3d transition-metal intercalates of the niobium and tantalum dichalcogenides. I. Magnetic properties', *Philosophical Magazine B* **41**, 65 (1980). Cited on page(s) 23

[221] M. Eibschütz, S. Mahajan, F. J. DiSalvo, G. W. Hull and J. V. Waszczak, 'Ferromagnetism in metallic intercalated compounds Fe_xTaS_2 ($0.20 \leq x \leq 0.34$)', *Journal of Applied Physics* **52**, 2098 (1981). Cited on page(s) 23

[222] J. G. Checkelsky, M. Lee, E. Morosan, R. J. Cava and N. P. Ong, 'Anomalous Hall effect and magnetoresistance in the layered ferromagnet $Fe_{1/4}TaS_2$: The inelastic regime', *Physical Review B* **77**, 014433 (2008). Cited on page(s) 23

[223] Y. J. Choi, S. B. Kim, T. Asada, S. Park, W. Wu, Y. Horibe and S.-W. Cheong, 'Giant magnetic coercivity and ionic superlattice nano-domains in $Fe_{0.25}TaS_2$', *Europhysics Letters* **86**, 37012 (2009). Cited on page(s) 23

[224] K.-T. Ko, K. Kim, S. B. Kim, H.-D. Kim, J.-Y. Kim, B. I. Min, J.-H. Park, F.-H. Chang, H.-J. Lin, A. Tanaka and S.-W. Cheong, 'RKKY Ferromagnetism with Ising-Like Spin States in Intercalated $Fe_{1/4}TaS_2$', *Physical Review Letters* **107**, 247201 (2011). Cited on page(s) 23

[225] Y. Horibe, J. Yang, Y.-H. Cho, X. Luo, S. B. Kim, Y. S. Oh, F.-T. Huang, T. Asada, M. Tanimura, D. Jeong and S.-W. Cheong, 'Color Theorems, Chiral Domain Topology, and Magnetic Properties of Fe_xTaS_2', *Journal of the American Chemical Society* **136**, 8368 (2014). Cited on page(s) 23

[226] S. Mankovsky, K. Chadova, D. Ködderitzsch, J. Minár, H. Ebert and W. Bensch, 'Electronic, magnetic, and transport properties of Fe-intercalated $2H-TaS_2$ studied by means of the KKR-CPA method', *Physical Review B* **92**, 144413 (2015). Cited on page(s) 23

[227] W. J. Hardy, C.-W. Chen, A. Marcinkova, H. Ji, J. Sinova, D. Natelson and E. Morosan, 'Very large magnetoresistance in $Fe_{0.28}TaS_2$ single crystals', *Physical Review B* **91**, 054426 (2015). Cited on page(s) 23

[228] T. Danz, Q. Liu, X. D. Zhu, L. H. Wang, S. W. Cheong, I. Radu, C. Ropers and R. I. Tobey, 'Structural and magnetic characterization of large area, free-standing thin films of magnetic ion intercalated dichalcogenides Mn0.25$TaS_2$and Fe0.25TaS_2', *Journal of Physics: Condensed Matter* **28**, 356002 (2016). Cited on page(s) 23

[229] S. Fan, I. Manuel, A. al Wahish, K. R. O'Neal, K. A. Smith, C. J. Won, J. W. Kim, S.-W. Cheong, J. T. Haraldsen and J. L. Musfeldt, 'Electronic chirality in the metallic ferromagnet $Fe_{1/3}TaS_2$', *Physical Review B* **96**, 205119 (2017). Cited on page(s) 23

[230] O. Gorochov, A. L. Blanc-soreau, J. Rouxel, P. Imbert and G. Jehanno, 'Transport properties, magnetic susceptibility and Mössbauer spectroscopy of Fe0.25NbS_2 and Fe0.33NbS_2', *Philosophical Magazine B* **43**, 621 (1981). Cited on page(s) 24

[231] S. Mankovsky, S. Polesya, H. Ebert and W. Bensch, 'Electronic and magnetic properties of $2H-NbS_2$ intercalated by $3d$ transition metals', *Physical Review B* **94**, 184430 (2016). Cited on page(s) 24

[232] S. Polesya, S. Mankovsky and H. Ebert, 'Electronic and magnetic properties of the 2H-NbS_2 intercalated by 3d transition metal atoms:', *Zeitschrift für Naturforschung B* **74**, 91 (2019). Cited on page(s) 24

[233] A. Little, C. Lee, C. John, S. Doyle, E. Maniv, N. L. Nair, W. Chen, D. Rees, J. W. F. Venderbos, R. M. Fernandes, J. G. Analytis and J. Orenstein, 'Three-state nematicity in the triangular lattice antiferromagnet $Fe_{1/3}NbS_2$', *Nature Materials* **19**, 1062 (2020). Cited on page(s) 24

[234] Y. Togawa, Y. Kousaka, S. Nishihara, K. Inoue, J. Akimitsu, A. S. Ovchinnikov and J. Kishine, 'Interlayer Magnetoresistance due to Chiral Soliton Lattice Formation in Hexagonal Chiral Magnet $CrNb_3S_6$', *Physical Review Letters* **111**, 197204 (2013). Cited on page(s) 24

[235] D. Braam, C. Gomez, S. Tezok, E. V. L. de Mello, L. Li, D. Mandrus, H.-Y. Kee and J. E. Sonier, 'Magnetic properties of the helimagnet $Cr_{1/3}NbS_2$ observed by μSR', *Physical Review B* **91**, 144407 (2015). Cited on page(s) 24

[236] S. N. Shirodkar and E. Kaxiras, 'Li intercalation at graphene/hexagonal boron nitride interfaces', *Physical Review B* **93**, 245438 (2016). Cited on page(s) 24

[237] D. T. Larson, I. Fampiou, G. Kim and E. Kaxiras, 'Lithium Intercalation in Graphene-MoS_2 Heterostructures', *Journal of Physical Chemistry C* **122**, 24535 (2018). Cited on page(s) 24

[238] D.-X. Song, Y.-Z. Du, W.-G. Ma and X. Zhang, 'High rate and capacity performances of functionalized MXene/graphene heterostructure anodes for magnesium-ion batteries', *International Journal of Energy Research* **45**, 3421 (2021). Cited on page(s) 24

[239] D.-X. Song, W.-G. Ma and X. Zhang, 'Correlated migration of ions in a 2D heterostructure anode: guaranteeing a low barrier for a high site occupancy', *Journal of Materials Chemistry A* **8**, 17463 (2020). Cited on page(s) 24

[240] D.-X. Song, L. Xie, Y.-F. Zhang, Y. Lu, M. An, W.-G. Ma and X. Zhang, ‘Multilayer Ion Load and Diffusion on TMD/MXene Heterostructure Anodes for Alkali-Ion Batteries’, *ACS Applied Energy Materials* **3**, 7699 (2020). Cited on page(s) 24

[241] J. Ma, J. Fu, M. Niu and R. Quhe, ‘MoO_2 and graphene heterostructure as promising flexible anodes for lithium-ion batteries’, *Carbon* **147**, 357 (2019). Cited on page(s) 24

[242] D. K. Bediako, M. Rezaee, H. Yoo, D. T. Larson, S. Y. F. Zhao, T. Taniguchi, K. Watanabe, T. L. Brower-Thomas, E. Kaxiras and P. Kim, ‘Heterointerface effects in the electrointercalation of van der Waals heterostructures’, *Nature* **558**, 425 (2018). Cited on page(s) 24 and 127

[243] S. Yazdani, J. V. Pondick, A. Kumar, M. Yarali, J. M. Woods, D. J. Hynek, D. Y. Qiu and J. J. Cha, ‘Heterointerface Effects on Lithium-Induced Phase Transitions in Intercalated MoS_2’, *ACS Applied Materials & Interfaces* **13**, 10603 (2021). Cited on page(s) 24 and 127

[244] S. Y. F. Zhao, G. A. Elbaz, D. K. Bediako, C. Yu, D. K. Efetov, Y. Guo, J. Ravichandran, K.-A. Min, S. Hong, T. Taniguchi, K. Watanabe, L. E. Brus, X. Roy and P. Kim, ‘Controlled Electrochemical Intercalation of Graphene/h-BN van der Waals Heterostructures’, *Nano Letters* **18**, 460 (2018). Cited on page(s) 24 and 127

[245] M. Hoffmann and S. Blügel, ‘Systematic derivation of realistic spin models for beyond-Heisenberg solids’, *Physical Review B* **101**, 024418 (2020). Cited on page(s) 25 and 27

[246] W. Heisenberg, ‘Zur Theorie des Ferromagnetismus’, *Zeitschrift für Physik* **49**, 619 (1928). Cited on page(s) 26

[247] J. A. Fischer, L. M. Sandratskii, S.-h. Phark, D. Sander and S. Parkin, ‘Atomic structure governed diversity of exchange-driven spin helices in Fe nanoislands: Experiment and theory’, *Physical Review B* **96**, 140407 (2017). Cited on page(s) 26 and 29

[248] I. Dzyaloshinsky, ‘A thermodynamic theory of “weak” ferromagnetism of antiferromagnetics’, *Journal of Physics and Chemistry of Solids* **4**, 241 (1958). Cited on page(s) 26

[249] T. Moriya, ‘Anisotropic Superexchange Interaction and Weak Ferromagnetism’, *Physical Review* **120**, 91 (1960). Cited on page(s) 26 and 28

[250] P. Ferriani, K. von Bergmann, E. Y. Vedmedenko, S. Heinze, M. Bode, M. Heide, G. Bihlmayer, S. Blügel and R. Wiesendanger, ‘Atomic-Scale Spin Spiral with a Unique Rotational Sense: Mn Monolayer on W(001)’, *Physical Review Letters* **101**, 027201 (2008). Cited on page(s) 26 and 29

[251] A. Fert and P. M. Levy, ‘Role of Anisotropic Exchange Interactions in Determining the Properties of Spin-Glasses’, *Physical Review Letters* **44**, 1538 (1980). Cited on page(s) 26

[252] T. Iwashita and N. Uryû, ‘Effects of biquadratic exchange in ferromagnets’, *Physical Review B* **14**, 3090 (1976). Cited on page(s) 27

[253] M. Takahashi, ‘Half-filled Hubbard model at low temperature’, *Journal of Physics C: Solid State Physics* **10**, 1289 (1977). Cited on page(s) 27

[254] J. Adler and J. Oitmaa, ‘The Heisenberg ferromagnet with higher-order exchange’, *Journal of Physics C: Solid State Physics* **12**, 575 (1979). Cited on page(s) 27

[255] P. Kurz, G. Bihlmayer, K. Hirai and S. Blügel, ‘Three-Dimensional Spin Structure on a Two-Dimensional Lattice: Mn/Cu(111)’, *Physical Review Letters* **86**, 1106 (2001). Cited on page(s) 27

[256] P. Ferriani, I. Turek, S. Heinze, G. Bihlmayer and S. Blügel, ‘Magnetic Phase Control in Monolayer Films by Substrate Tuning’, *Physical Review Letters* **99**, 187203 (2007). Cited on page(s) 27

[257] A. Al-Zubi, G. Bihlmayer and S. Blügel, ‘Modeling magnetism of hexagonal Fe monolayers on 4d substrates’, *physica status solidi (b)* **248**, 2242 (2011). Cited on page(s) 27

[258] A. Kartsev, M. Augustin, R. F. L. Evans, K. S. Novoselov and E. J. G. Santos, 'Biquadratic exchange interactions in two-dimensional magnets', *npj Computational Materials* **6**, 150 (2020). Cited on page(s) 27

[259] N. Romming, C. Hanneken, M. Menzel, J. E. Bickel, B. Wolter, K. von Bergmann, A. Kubetzka and R. Wiesendanger, 'Writing and Deleting Single Magnetic Skyrmions', *Science* **341**, 636 (2013). Cited on page(s) 28 and 129

[260] S. Meckler, N. Mikuszeit, A. Preßler, E. Y. Vedmedenko, O. Pietzsch and R. Wiesendanger, 'Real-space observation of a right-rotating inhomogeneous cycloidal spin spiral by spin-polarized scanning tunneling microscopy in a triple axes vector magnet', *Physical Review Letters* **103**, 157201 (2009). Cited on page(s) 29

[261] P. J. Hsu, A. Finco, L. Schmidt, A. Kubetzka, K. Von Bergmann and R. Wiesendanger, 'Guiding Spin Spirals by Local Uniaxial Strain Relief', *Physical Review Letters* **116**, 017201 (2016). Cited on page(s) 29

[262] G. Chen, J. Zhu, A. Quesada, J. Li, A. T. N'Diaye, Y. Huo, T. P. Ma, Y. Chen, H. Y. Kwon, C. Won, Z. Q. Qiu, A. K. Schmid and Y. Z. Wu, 'Novel chiral magnetic domain wall structure in Fe/Ni/Cu(001) Films', *Physical Review Letters* **110**, 177204 (2013). Cited on page(s) 29

[263] F. Ajejas, A. Gudín, R. Guerrero, A. Anadón Barcelona, J. M. Diez, L. De Melo Costa, P. Olleros, M. A. Niño, S. Pizzini, J. Vogel, M. Valvidares, P. Gargiani, M. Cabero, M. Varela, J. Camarero, R. Miranda and P. Perna, 'Unraveling Dzyaloshinskii-Moriya Interaction and Chiral Nature of Graphene/Cobalt Interface', *Nano Letters* **18**, 5364 (2018). Cited on page(s) 29

[264] R. Lo Conte, A. K. Nandy, G. Chen, A. L. Fernandes Cauduro, A. Maity, C. Ophus, Z. Chen, A. T. N'Diaye, K. Liu, A. K. Schmid and R. Wiesendanger, 'Tuning the Properties of Zero-Field Room Temperature Ferromagnetic Skyrmions by Interlayer Exchange Coupling', *Nano Letters* **20**, 4739 (2020). Cited on page(s) 29

[265] W. S. Wei, Z. D. He, Z. Qu and H. F. Du, 'Dzyaloshinsky–Moriya interaction (DMI)-induced magnetic skyrmion materials', *Rare Metals* **40**, 3076 (2021). Cited on page(s) 29

[266] S.-H. Phark, J. A. Fischer, M. Corbetta, D. Sander, K. Nakamura and J. Kirschner, 'Reduced-dimensionality-induced helimagnetism in iron nanoislands', *Nature Communications* **5**, 5183 (2014). Cited on page(s) 29

[267] N. Romming, H. Pralow, A. Kubetzka, M. Hoffmann, S. Von Malottki, S. Meyer, B. Dupé, R. Wiesendanger, K. Von Bergmann and S. Heinze, 'Competition of Dzyaloshinskii-Moriya and Higher-Order Exchange Interactions in Rh/Fe Atomic Bilayers on Ir(111)', *Physical Review Letters* **120**, 207201 (2018). Cited on page(s) 29

[268] A. Krönlein, M. Schmitt, M. Hoffmann, J. Kemmer, N. Seubert, M. Vogt, J. Küspert, M. Böhme, B. Alonazi, J. Kügel, H. A. Albrithen, M. Bode, G. Bihlmayer and S. Blügel, 'Magnetic Ground State Stabilized by Three-Site Interactions: Fe/Rh(111)', *Physical Review Letters* **120**, 207202 (2018). Cited on page(s) 29

[269] G. Chen, A. T. N'Diaye, S. P. Kang, H. Y. Kwon, C. Won, Y. Wu, Z. Q. Qiu and A. K. Schmid, 'Unlocking Bloch-type chirality in ultrathin magnets through uniaxial strain', *Nature Communications* **6**, (2015). Cited on page(s) 30

[270] M. J. Meijer, J. Lucassen, O. Kurnosikov, H. J. Swagten, B. Koopmans, R. Lavrijsen, F. Kloodt-Twesten, R. Frömter and R. A. Duine, 'Magnetic Chirality Controlled by the Interlayer Exchange Interaction', *Physical Review Letters* **124**, 207203 (2020). Cited on page(s) 30

[271] X. Z. Yu, Y. Onose, N. Kanazawa, J. H. Park, J. H. Han, Y. Matsui, N. Nagaosa and Y. Tokura, 'Real-space observation of a two-dimensional skyrmion crystal', *Nature* **465**, 901 (2010). Cited on page(s) 30

[272] M. Hayashi, L. Thomas, R. Moriya, C. Rettner and S. S. P. Parkin, 'Current-Controlled Magnetic Domain-Wall Nanowire Shift Register', *Science* **320**, 209 (2008). Cited on page(s) 30

[273] J. Sampaio, V. Cros, S. Rohart, A. Thiaville and A. Fert, 'Nucleation, stability and current-induced motion of isolated magnetic skyrmions in nanostructures', *Nature Nanotechnology* **8**, 839 (2013). Cited on page(s) 30

[274] S. Woo, K. M. Song, H. S. Han, M. S. Jung, M. Y. Im, K. S. Lee, K. S. Song, P. Fischer, J. I. Hong, J. W. Choi, B. C. Min, H. C. Koo and J. Chang, 'Spin-orbit torque-driven skyrmion dynamics revealed by time-resolved X-ray microscopy', *Nature Communications* **8**, 15573 (2017). Cited on page(s) 30

[275] X. Z. Yu, N. Kanazawa, W. Z. Zhang, T. Nagai, T. Hara, K. Kimoto, Y. Matsui, Y. Onose and Y. Tokura, 'Skyrmion flow near room temperature in an ultralow current density', *Nature Communications* **3**, 988 (2012). Cited on page(s) 30

[276] J. Iwasaki, M. Mochizuki and N. Nagaosa, 'Current-induced skyrmion dynamics in constricted geometries', *Nature Nanotechnology* **8**, 742 (2013). Cited on page(s) 30

[277] X. Zhang, J. Xia, Y. Zhou, X. Liu, H. Zhang and M. Ezawa, 'Skyrmion dynamics in a frustrated ferromagnetic film and current-induced helicity locking-unlocking transition', *Nature Communications* **8**, (2017). Cited on page(s) 30 and 128

[278] M. Pörtner, 'Spin-polarized scanning probe microscopy: tip preparation and different example cases', *Master thesis, University of Cologne* (2016). Cited on page(s) 33

[279] J. Bardeen, 'Tunnelling from a Many-Particle Point of View', *Physical Review Letters* **6**, 57 (1961). Cited on page(s) 33 and 34

[280] G. Binnig and H. Rohrer, 'Scanning tunneling microscopy–from birth to adolescence', *Reviews of Modern Physics* **59**, 615 (1987). Cited on page(s) 33

[281] D. Wortmann, S. Heinze, P. Kurz, G. Bihlmayer and S. Blügel, 'Resolving Complex Atomic-Scale Spin Structures by Spin-Polarized Scanning Tunneling Microscopy', *Physical Review Letters* **86**, 4132 (2001). Cited on page(s) 34 and 35

[282] R. Wiesendanger, 'Spin mapping at the nanoscale and atomic scale', *Reviews of Modern Physics* **81**, 1495 (2009). Cited on page(s) 34, 36, and 38

[283] J. Tersoff and D. R. Hamann, 'Theory and Application for the Scanning Tunneling Microscope', *Physical Review Letters* **50**, 1998 (1983). Cited on page(s) 34

[284] J. Tersoff and D. R. Hamann, 'Theory of the scanning tunneling microscope', *Physical Review B* **31**, 805 (1985). Cited on page(s) 34

[285] C. J. Chen, 'Tunneling matrix elements in three-dimensional space: The derivative rule and the sum rule', *Physical Review B* **42**, 8841 (1990). Cited on page(s) 34

[286] C. J. Chen, 'Origin of atomic resolution on metal surfaces in scanning tunneling microscopy', *Physical Review Letters* **65**, 448 (1990). Cited on page(s) 34

[287] C. J. Chen, 'Microscopic view of scanning tunneling microscopy', *Journal of Vacuum Science & Technology A* **9**, 44 (1991). Cited on page(s) 34

[288] P. M. Tedrow and R. Meservey, 'Spin-Dependent Tunneling into Ferromagnetic Nickel', *Physical Review Letters* **26**, 192 (1971). Cited on page(s) 35

[289] P. M. Tedrow and R. Meservey, 'Spin Polarization of Electrons Tunneling from Films of Fe, Co, Ni, and Gd', *Physical Review B* **7**, 318 (1973). Cited on page(s) 35

[290] M. Julliere, 'Tunneling between ferromagnetic films', *Physics Letters A* **54**, 225 (1975). Cited on page(s) 35

[291] M. Bode, ‘Spin-polarized scanning tunnelling microscopy’, *Reports on Progress in Physics* **66**, 523 (2003). Cited on page(s) 36

[292] R. Wiesendanger, H.-J. Güntherodt, G. Güntherodt, R. J. Gambino and R. Ruf, ‘Observation of vacuum tunneling of spin-polarized electrons with the scanning tunneling microscope’, *Physical Review Letters* **65**, 247 (1990). Cited on page(s) 36

[293] R. Wiesendanger, H. J. Güntherodt, G. Güntherodt, R. J. Gambino and R. Ruf, ‘Scanning tunneling microscopy with spin-polarized electrons’, *Zeitschrift für Physik B Condensed Matter* **80**, 5 (1990). Cited on page(s) 36

[294] R. Wiesendanger, D. Bürgler, G. Tarrach, T. Schaub, U. Hartmann, H. J. Güntherodt, I. V. Shvets and J. M. D. Coey, ‘Recent advances in scanning tunneling microscopy involving magnetic probes and samples’, *Applied Physics A* **53**, 349 (1991). Cited on page(s) 36 and 37

[295] R. Wiesendanger, ‘Vacuum tunneling of spin-polarized electrons detected by scanning tunneling microscopy’, *Journal of Vacuum Science & Technology B: Microelectronics and Nanometer Structures* **9**, 519 (1991). Cited on page(s) 36

[296] M. Morgenstern, ‘Probing the local density of states of dilute electron systems in differend dimensions’, *Surface Review and Letters* **10**, 933 (2003). Cited on page(s) 37

[297] M. Bode, M. Getzlaff, S. Heinze, R. Pascal and R. Wiesendanger, ‘Magnetic exchange splitting of the Gd(0001) surface state studied by variable-temperature scanning tunneling spectroscopy’, *Applied Physics A* **66**, S121 (1998). Cited on page(s) 37

[298] M. Bode, M. Getzlaff and R. Wiesendanger, ‘Quantitative aspects of spin-polarized scanning tunneling spectroscopy of Gd(0001)’, *Journal of Vacuum Science & Technology A: Vacuum, Surfaces, and Films* **17**, 2228 (1999). Cited on page(s) 37

[299] A. Minakov and I. Shvets, ‘On the possibility of resolving quantization axes of surface spins by means of a scanning tunneling microscope with a magnetic tip’, *Surface Science* **236**, L377 (1990). Cited on page(s) 37

[300] S. Murphy, J. Osing and I. Shvets, ‘Fabrication of submicron-scale manganese–nickel tips for spin-polarized STM studies’, *Applied Surface Science* **144-145**, 497 (1999). Cited on page(s) 37

[301] M. Bode, R. Pascal and R. Wiesendanger, ‘Scanning tunneling spectroscopy of Fe/W(110) using iron covered probe tips’, *Journal of Vacuum Science & Technology A: Vacuum, Surfaces, and Films* **15**, 1285 (1997). Cited on page(s) 37

[302] A. Kubetzka, P. Ferriani, M. Bode, S. Heinze, G. Bihlmayer, K. V. Bergmann, O. Pietzsch, S. Blügel and R. Wiesendanger, ‘Revealing antiferromagnetic order of the Fe monolayer on W(001): Spin-polarized scanning tunneling microscopy and first-principles calculations’, *Physical Review Letters* **94**, (2005). Cited on page(s) 37

[303] A. Kubetzka, M. Bode, O. Pietzsch and R. Wiesendanger, ‘Spin-Polarized Scanning Tunneling Microscopy with Antiferromagnetic Probe Tips’, *Physical Review Letters* **88**, 4 (2002). Cited on page(s) 37

[304] A. Wachowiak, J. Wiebe, M. Bode, O. Pietzsch, M. Morgenstern and R. Wiesendanger, ‘Direct Observation of Internal Spin Structure of Magnetic Vortex Cores’, *Science* **298**, 577 (2002). Cited on page(s) 37

[305] S.-h. Phark, J. A. Fischer, M. Corbetta, D. Sander and J. Kirschner, ‘Superparamagnetic response of Fe-coated W tips in spin-polarized scanning tunneling microscopy’, *Applied Physics Letters* **103**, 032407 (2013). Cited on page(s) 37

[306] UNISOKU, ‘Operating Manual USM1300S-He-3’, *Manual* . Cited on page(s) 45, 46, and 48

[307] B. Voigtländer, ‘Scanning Probe Microscopy Designs’ (Springer, 2015). Cited on page(s) 48 and 49

[308] K. Onabe, M. Naito and S. Tanaka, ‘Anisotropy of Upper Critical Field in Superconducting 2H-NbS_2’, *Journal of the Physical Society of Japan* **45**, 50 (1978). Cited on page(s) 126

[309] P. de Trey, S. Gygax and J.-P. Jan, ‘Anisotropy of the Ginzburg-Landau parameter κ in $NbSe_2$’, *Journal of Low Temperature Physics* **11**, 421 (1973). Cited on page(s) 126

[310] A. Nader and P. Monceau, ‘Critical field of 2H-$NbSe_2$ down to 50mK’, *SpringerPlus* **3**, 16 (2014). Cited on page(s) 126

[311] C. Rubio-Verdú, A. M. García-García, H. Ryu, D.-J. Choi, J. Zaldívar, S. Tang, B. Fan, Z.-X. Shen, S.-K. Mo, J. I. Pascual and M. M. Ugeda, ‘Visualization of Multifractal Superconductivity in a Two-Dimensional Transition Metal Dichalcogenide in the Weak-Disorder Regime’, *Nano Letters* **20**, 5111 (2020). Cited on page(s) 126

[312] P.-J. Hsu, L. Rózsa, A. Finco, L. Schmidt, K. Palotás, E. Vedmedenko, L. Udvardi, L. Szunyogh, A. Kubetzka, K. von Bergmann and R. Wiesendanger, ‘Inducing skyrmions in ultrathin Fe films by hydrogen exposure’, *Nature Communications* **9**, 1571 (2018). Cited on page(s) 129

[313] W. Han, R. K. Kawakami, M. Gmitra and J. Fabian, ‘Graphene spintronics’, *Nature Nanotechnology* **9**, 794 (2014). Cited on page(s) 129 and 148

[314] Y. S. Dedkov and M. Fonin, ‘Electronic and magnetic properties of the graphene–ferromagnet interface’, *New Journal of Physics* **12**, 125004 (2010). Cited on page(s) 129 and 148

[315] A. Chernikov, A. M. van der Zande, H. M. Hill, A. F. Rigosi, A. Velauthapillai, J. Hone and T. F. Heinz, ‘Electrical Tuning of Exciton Binding Energies in Monolayer WS_2’, *Physical Review Letters* **115**, 126802 (2015). Cited on page(s) 130

[316] D. Costanzo, S. Jo, H. Berger and A. F. Morpurgo, ‘Gate-induced superconductivity in atomically thin MoS_2 crystals’, *Nature Nanotechnology* **11**, 339 (2016). Cited on page(s) 130

[317] A. Raja, L. Waldecker, J. Zipfel, Y. Cho, S. Brem, J. D. Ziegler, M. Kulig, T. Taniguchi, K. Watanabe, E. Malic, T. F. Heinz, T. C. Berkelbach and A. Chernikov, ‘Dielectric disorder in two-dimensional materials’, *Nature Nanotechnology* **14**, 832 (2019). Cited on page(s) 130

[318] P. V. Nguyen, N. C. Teutsch, N. P. Wilson, J. Kahn, X. Xia, A. J. Graham, V. Kandyba, A. Giampietri, A. Barinov, G. C. Constantinescu, N. Yeung, N. D. M. Hine, X. Xu, D. H. Cobden and N. R. Wilson, ‘Visualizing electrostatic gating effects in two-dimensional heterostructures’, *Nature* **572**, 220 (2019). Cited on page(s) 130

[319] Z. Qiu, M. Trushin, H. Fang, I. Verzhbitskiy, S. Gao, E. Laksono, M. Yang, P. Lyu, J. Li, J. Su, M. Telychko, K. Watanabe, T. Taniguchi, J. Wu, A. H. C. Neto, L. Yang, G. Eda, S. Adam and J. Lu, ‘Giant gate-tunable bandgap renormalization and excitonic effects in a 2D semiconductor’, *Science Advances* **5**, eaaw2347 (2019). Cited on page(s) 130

[320] S. Schumacher, T. O. Wehling, P. Lazić, S. Runte, D. F. Förster, C. Busse, M. Petrović, M. Kralj, S. Blügel, N. Atodiresei, V. Caciuc and T. Michely, ‘The Backside of Graphene: Manipulating Adsorption by Intercalation’, *Nano Letters* **13**, 5013 (2013). Cited on page(s) 130 and 134

[321] S. Schumacher, F. Huttmann, M. Petrović, C. Witt, D. F. Förster, C. Vo-Van, J. Coraux, A. J. Martínez-Galera, V. Sessi, I. Vergara, R. Rückamp, M. Grüninger, N. Schleheck, F. Meyer zu Heringdorf, P. Ohresser, M. Kralj, T. O. Wehling and T. Michely, ‘Europium underneath graphene on Ir(111): Intercalation mechanism, magnetism, and band structure’, *Physical Review B* **90**, 235437 (2014). Cited on page(s) 130, 131, and 134

[322] W. Jolie, F. Craes, M. Petrović, N. Atodiresei, V. Caciuc, S. Blügel, M. Kralj, T. Michely and C. Busse, ‘Confinement of Dirac electrons in graphene quantum dots’, *Physical Review B* **89**, 155435 (2014). Cited on page(s) 130, 135, and 137

[323] U. A. Schröder, M. Petrović, T. Gerber, A. J. Martínez-Galera, E. Grånäs, M. A. Arman, C. Herbig, J. Schnadt, M. Kralj, J. Knudsen and T. Michely, ‘Core level shifts of intercalated graphene’, *2D Materials* **4**, 015013 (2016). Cited on page(s) 130, 134, and 137

[324] A. V. Fedorov, G. Poelchen, S. V. Eremeev, S. Schulz, A. Generalov, C. Polley, C. Laubschat, K. Kliemt, N. Kaya, C. Krellner, E. V. Chulkov, K. Kummer, D. Y. Usachov, A. Ernst and D. V. Vyalikh, ‘Insight into the Temperature Evolution of Electronic Structure and Mechanism of Exchange Interaction in EuS’, *The Journal of Physical Chemistry Letters* **12**, 8328 (2021). Cited on page(s) 132

[325] A. Mauger, ‘Indirect exchange in europium chalcogenides’, *physica status solidi (b)* **84**, 761 (1977). Cited on page(s) 132

[326] J. S. Moodera, T. S. Santos and T. Nagahama, ‘The phenomena of spin-filter tunnelling’, *Journal of Physics: Condensed Matter* **19**, 165202 (2007). Cited on page(s) 135

[327] C. Zhao, T. Norden, P. Zhang, P. Zhao, Y. Cheng, F. Sun, J. P. Parry, P. Taheri, J. Wang, Y. Yang, T. Scrace, K. Kang, S. Yang, G.-x. Miao, R. Sabirianov, G. Kioseoglou, W. Huang, A. Petrou and H. Zeng, ‘Enhanced valley splitting in monolayer WSe_2 due to magnetic exchange field’, *Nature Nanotechnology* **12**, 757 (2017). Cited on page(s) 135

[328] A. J. Martínez-Galera, U. A. Schröder, F. Huttmann, W. Jolie, F. Craes, C. Busse, V. Caciuc, N. Atodiresei, S. Blügel and T. Michely, ‘Oxygen orders differently under graphene: new superstructures on Ir(111)’, *Nanoscale* **8**, 1932 (2016). Cited on page(s) 135 and 136

[329] W. F. Avrin and R. P. Merrill, ‘Helium diffraction analysis of the microfaceted Ir(110) surface’, *Surface Science* **274**, 231 (1992). Cited on page(s) 138

[330] A. Ney, J. Schulz, M. Sturmat and R. Koch, ‘Stress-driven self-assembly on Ir: stripes, droplets, and missing-row-type reconstructions’, *Surface Science* **519**, 192 (2002). Cited on page(s) 138 and 139

[331] J. Kuntze, S. Speller and W. Heiland, ‘The Ir(110) surface studied by STM’, *Surface Science* **402**, 764 (1998). Cited on page(s) 138

[332] R. Koch, M. Borbonus, O. Haase and K. H. Rieder, ‘New aspects on the Ir(110) reconstruction: Surface stabilization on mesoscopic scale via (331) facets’, *Physical Review Letters* **67**, 3416 (1991). Cited on page(s) 138

[333] J. J. Schulz, M. Sturmat and R. Koch, ‘Illuminating structural transformation of Ir(110): A high-temperature scanning tunneling microscopy study’, *Physical Review B* **62**, 15402 (2000). Cited on page(s) 138

[334] C.-M. Chan, S. Cunningham, K. Luke, W. Weinberg and S. Withrow, ‘Determination of the atomic arrangement of the unreconstructed Ir (110) surface by low-energy electron diffraction a’, *Surface Science* **78**, 15 (1978). Cited on page(s) 139

[335] R. Koch, M. Borbonus, O. Haase and K. H. Rieder, ‘Applied Solids Physics A Surfaces Reconstruction Behaviour of fcc(llO) Transition Metal Surfaces and their Vicinals’, *Appl. Phys* **55**, 417429 (1992). Cited on page(s) 139

[336] P. Kaghazchi and T. Jacob, ‘First-principles studies on clean and oxygen-adsorbed Ir(110) surfaces’, *Physical Review B* **76**, (2007). Cited on page(s) 139

[337] K. Heinz, G. Schmidt, L. Hammer and K. Müller, ‘Dynamics of the reconstruction process Ir(100) 1×1→1×5’, *Physical Review B* **32**, 6214 (1985). Cited on page(s) 139

[338] M. Sicot, O. Kurnosikov, O. A. O. Adam, H. J. M. Swagten and B. Koopmans, ‘STM-induced desorption of hydrogen from Co nanoislands’, *Phys. Rev. B* **77**, 035417 (2008). Cited on page(s) 140

[339] 'Wolfram Research, ElementData, *https://reference.wolfram.com/language/ref/ElementData.html*', (2014, Accessed: 13-December-2021). Cited on page(s) 141

[340] S. Kraus, F. Huttmann, J. Fischer, T. Knispel, K. Bischof, A. Herman, M. Bianchi, R.-M. Stan, A. J. Holt, V. Caciuc, S. Tsukamoto, H. Wende, P. Hofmann, N. Atodiresei and T. Michely, 'Single-crystal graphene on Ir(110)', *arXiv* (2021). Cited on page(s) 143, 144, 145, 148, and 160

[341] J. Brede, J. Sławińska, M. Abadia, C. Rogero, J. E. Ortega, I. Piquero-Zulaica, J. Lobo-Checa, A. Arnau and J. I. Cerdá, 'Tuning the Graphene on Ir(111) adsorption regime by Fe/Ir surface-alloying', *2D Materials* **4**, 015016 (2016). Cited on page(s) 148

[342] A. Kuc, N. Zibouche and T. Heine, 'Influence of quantum confinement on the electronic structure of the transition metal sulfide TS_2', *Physical Review B* **83**, 245213 (2011). Cited on page(s) 151

[343] W. Jolie, T. Knispel, N. Ehlen, K. Nikonov, C. Busse, A. Grüneis and T. Michely, 'Charge density wave phase of VSe_2 revisited', *Phys. Rev. B* **99**, 115417 (2019). Cited on page(s) 160

[344] W. Jolie, J. Lux, M. Pörtner, D. Dombrowski, C. Herbig, T. Knispel, S. Simon, T. Michely, A. Rosch and C. Busse, 'Suppression of Quasiparticle Scattering Signals in Bilayer Graphene Due to Layer Polarization and Destructive Interference', *Phys. Rev. Lett.* **120**, 106801 (2018). Cited on page(s) 160

[345] S. Simon, E. Voloshina, J. Tesch, F. Förschner, V. Enenkel, C. Herbig, T. Knispel, A. Tries, J. Kröger, Y. Dedkov and M. Fonin, 'Layer-by-Layer Decoupling of Twisted Graphene Sheets Epitaxially Grown on a Metal Substrate', *Small* **14**, 1703701 (2018). Cited on page(s) 160

[346] T. Knispel, W. Jolie, N. Borgwardt, J. Lux, Z. Wang, Y. Ando, A. Rosch, T. Michely and M. Grüninger, 'Charge puddles in the bulk and on the surface of the topological insulator $BiSbTeSe_2$ studied by scanning tunneling microscopy and optical spectroscopy', *Phys. Rev. B* **96**, 195135 (2017). Cited on page(s) 160

[347] C. Herbig, T. Knispel, S. Simon, U. A. Schröder, A. J. Martínez-Galera, M. A. Arman, C. Teichert, J. Knudsen, A. V. Krasheninnikov and T. Michely, 'From Permeation to Cluster Arrays: Graphene on Ir(111) Exposed to Carbon Vapor', *Nano Letters* **17**, 3105 (2017). Cited on page(s) 160

Acknowledgements
(Danksagung)

Zum Gelingen dieser Arbeit haben eine Vielzahl von Personen beigetragen, denen ich an dieser Stelle meinen Dank aussprechen möchte.

Ich möchte mich an erster Stelle bei Prof. Dr. Thomas Michely bedanken, welcher mir die Durchführung meiner Promotion in seiner Arbeitsgruppe ermöglicht hat. Ich bedanke mich für die Vielzahl an Ratschlägen und Gesprächen sowohl auf wissenschaftlicher, als auch auf persönlicher Ebene. Ich danke für das jederzeit in mich gesetzte Vertrauen, auch in Zeiten in denen es mal nicht so gut lief.

Als nächstes bedanke ich mich bei Priv.-Doz. Dr. Daniel Bürgler für die Übernahme der Zweitkorrektur meiner Arbeit und der Einladung in das Forschungszentrum Jülich zum Gespräch über die Themen meiner Arbeit.

Mein Dank geht auch an Prof. Dr. Klas Lindfors, welcher sich sofort bereit erklärt hat den Vorsitz der Prüfungskommission für diese Arbeit zu übernehmen.

Vielen Dank an Dr. Wouter Jolie für die Übernahme des Beisitzes für die Disputation und die Betreuung meiner Masterarbeit in der Vergangenheit, im Rahmen welcher ich sehr viel gelernt habe.

Ich bedanke mich insbesondere für die hervorragende enge Zusammenarbeit mit Dr. Jeison Fischer, mit dem ich viele Messzeiten am MSTM geteilt habe und der jederzeit, auch in stressigen Phasen, mit Rat und Tat sowie einem offenen Ohr bereitstand.

Mein Dank geht hier auch an das MSTM-Team insgesamt (Dr. Jeison Fischer, Dr. Jens Brede und Mahasweta Bagchi), vielen Dank für die gute Zusammenarbeit im Rahmen des MSTM Aufbaus, vieler Reparaturphasen und Messungen. Auch die privaten Treffen wie zB. das Weihnachtsfondue bei Dr. Jeison Fischer halte ich in guter Erinnerung.

Die Betreuung von Daniela Mohrenstecher während ihrer Masterarbeit und die Betreuung von Felix Oberbauer im Rahmen seiner Bachelorarbeit haben mir großen Spaß bereitet und bleiben bei mir in guter Erinnerung.

Für das Korrekturlesen meiner Arbeit bedanke ich mich bei Dr. Jeison Fischer, Dr. Wouter Jolie, Camil van Efferen, Stefan Kraus und Philipp Warzanowski. Stefan Kraus möchte ich in diesem Zusammenhang auch noch einmal explizit für die teilweise gemeinsame Schreibphase im Großraumbüro 307/308 danken. Du hast mit der Beantwortung unendlich vieler Fragen und der Bereitstellung vieler Snacks maßgeblich zum Gelingen dieser Arbeit beigetragen.

Ich bedanke mich bei der gesamten Arbeitsgruppe Michely für die gemeinsame Zeit mit Dr. Jeison Fischer, Dr. Wouter Jolie, Dr. Pantelis Bampoulis, Dr. Clifford Murray, Dr. Moritz Will, Dr. Philipp Valerius, Dr. Joshua Hall, Tobias Hartl, Camiel van Efferen, Stefan Kraus, Christian Krämer, Daniela Mohrenstecher, Jason Bergelt, Nicolas Georgopoulos, Felix Oberbauer, Ken Bischof und Pascal Hurth.

Bei Pascal Hurth und den Mitgliedern der mechanischen und elektrischen Werkstätten bedanke ich mich für die Vielzahl an technischen Lösungen. Besonders bei Pascal Hurth mit vielen "Last-Minute"-Lösungen.

Ich bedanke mich für die Kollaboration mit Dr. Nicolae Atodiresei, Vasily Tseplayaev, Dr. Markus Hoffmann und Prof. Dr. Stefan Blügel am Forschungszentrum Jülich, mit Dr. Jan Berges und Arne Schobert an der Universität Bremen, Prof. Dr. Tim Wehling an der Universität Bremen und Universität Hamburg, Dr. Erik van Loon an der Universität Bremen und Universität Lund und Yannik Falke sowie Prof. Dr. Alexander Grüneis an der Universität zu Köln.

Ich bedanke mich bei meiner Kölner (und teilweise nicht mehr Kölner) Truppe mit Bahareh Ghannad, Philipp Warzanowski, Daniel Jose-Tüns, Gereon Hackenberg, Felix Gerick und Mathias Kleppel, die mich durch mein gesamtes Studium und bis heute als Freunde begleitet haben.

Zu guter Letzt möchte ich mich hier bei meinen Eltern Sandra und Norbert Knispel, sowie meine Schwester Alena Knispel bedanken. Ich bin unendlich dankbar für die nie endende Unterstützung und die Ermutigung meinen Weg zu gehen.

Erklärung zur Dissertation

gemäß der Promotionsordnung vom 12. März 2020

Hiermit versichere ich an Eides statt, dass ich die vorliegende Dissertation selbstständig und ohne die Benutzung anderer als der angegebenen Hilfsmittel und Literatur angefertigt habe. Alle Stellen, die wörtlich oder sinngemäß aus veröffentlichten und nicht veröffentlichten Werken dem Wortlaut oder dem Sinn nach entnommen wurden, sind als solche kenntlich gemacht. Ich versichere an Eides statt, dass diese Dissertation noch keiner anderen Fakultät oder Universität zur Prüfung vorgelegen hat; dass sie - abgesehen von unten angegebenen Teilpublikationen und eingebundenen Artikeln und Manuskripten - noch nicht veröffentlicht worden ist sowie, dass ich eine Veröffentlichung der Dissertation vor Abschluss der Promotion nicht ohne Genehmigung des Promotionsausschusses vornehmen werde. Die Bestimmungen dieser Ordnung sind mir bekannt. Darüber hinaus erkläre ich hiermit, dass ich die Ordnung zur Sicherung guter wissenschaftlicher Praxis und zum Umgang mit wissenschaftlichem Fehlverhalten der Universität zu Köln gelesen und sie bei der Durchführung der Dissertation zugrundeliegenden Arbeiten und der schriftlich verfassten Dissertation beachtet habe und verpflichte mich hiermit, die dort genannten Vorgaben bei allen wissenschaftlichen Tätigkeiten zu beachten und umzusetzen. Ich versichere, dass die eingereichte elektronische Fassung der eingereichten Druckfassung vollständig entspricht.

Teilpublikationen:

n/a **Timo Knispel**, Jeison Fischer, Jan Berges, Arne Schobert, Erik G. C. P. van Loon, Wouter Jolie, Timo Wehling, and Thomas Michely
Electronic structure and charge density wave order in monolayer NbS_2
manuscript in preparation phase

n/a **Timo Knispel**, Daniela Mohrenstecher, Carsten Speckmann, Yannic Falke, Alexander Grüneis, Nicolae Atodiresei, Jeison Fischer, and Thomas Michely
Post-growth intercalation at the interface of graphene and monolayer NbS_2
manuscript in preparation phase

n/a **Timo Knispel**, Vasily Tseplyaev, Markus Hoffmann, Stefan Blügel, Thomas Michely, and Jeison Fischer
Bloch spin helix in an ultrathin Fe film on Ir(110)
manuscript in preparation phase

Köln, den 31.03.2022 Timo Knispel T. Knispel

Datenverfügbarkeit:
Die in dieser Dissertation gezeigten Primärdaten sind bei der Arbeitsgruppe von Prof. Dr. Thomas Michely am II. Physikalischen Institut der Universität zu Köln hinterlegt.

Lebenslauf *(Curriculum Vitae)*

Persönliche Daten

Timo Knispel	
Geburtstag	13.05.1992
Geburtsort	Köln
Staatsangehörigkeit	deutsch

Ausbildung

10/2017 – heute	Promotionsstudium II. Physikalisches Institut, Universität zu Köln Arbeitsgruppe Prof. Dr. Thomas Michely
10/2014 – 09/2017	M. Sc. Physik Universität zu Köln Durchschnittsnote: 1,2 Masterarbeit: “STM and STS on in situ cleaved bulk crystals: Charge puddles and charge density waves” (Note: sehr gut 1,0) II. Physikalisches Institut, Universität zu Köln Arbeitsgruppe Prof. Dr. Thomas Michely
10/2011 – 09/2014	B. Sc. Physik Universität zu Köln Durchschnittsnote: 2,1 Bachelorarbeit: “Bilagen-Graphen auf Ir(111)” (Note: sehr gut 1,0) II. Physikalisches Institut, Universität zu Köln Arbeitsgruppe Prof. Dr. Thomas Michely
07/2011	Allgemeine Hochschulreife, Max-Ernst-Gymnasium, Brühl (Rheinland) Durchschnittsnote: 2,1